

Surface Science Investigations on Structure and Binding Centers of Intermetallic PdGa Surfaces

THÈSE N° 6337 (2014)

PRÉSENTÉE LE 25 AOÛT 2014

À LA FACULTÉ DES SCIENCES DE BASE
LABORATOIRE DE NANOSTRUCTURES SUPERFICIELLES
PROGRAMME DOCTORAL EN PHYSIQUE

ÉCOLE POLYTECHNIQUE FÉDÉRALE DE LAUSANNE

POUR L'OBTENTION DU GRADE DE DOCTEUR ÈS SCIENCES

PAR

Jan PRINZ

acceptée sur proposition du jury:

Prof. O. Schneider, président du jury
Prof. H. Brune, Dr R. Widmer, directeurs de thèse
Prof. K.-H. Ernst, rapporteur
Prof. M. Grioni, rapporteur
Prof. G. Rupprechter, rapporteur



ÉCOLE POLYTECHNIQUE
FÉDÉRALE DE LAUSANNE

Suisse
2014

Abstract

Intermetallic compounds present a promising class of materials for the development of novel catalysts. Due to the partially covalent character of their atomic bonds and their structural properties, they offer potentially higher stability and selectivity compared to the elemental constituents, or surface alloys containing the active element. Although these advantageous properties are surely present in the bulk of intermetallic compounds, it is the structure and composition of the surface that determine the energetics and kinetics of possible reaction processes. Recent experiments revealed remarkable catalytic properties for Palladium-Gallium (Pd_1Ga_4) intermetallic compound as a selective acetylene semi-hydrogenation catalyst, which is assigned to its intrinsic material properties. In this thesis, low-Miller index surfaces of PdGa were investigated experimentally with respect to surface atomic structure and adsorption properties of small molecules using a wide variety of surface analytical methods.

By application of quantitative low energy electron diffraction (LEED-I(V)) in combination with dynamic LEED simulations, the atomic structures of PdGa(111), (-1-1-1), (110), (100), and (210) surfaces were determined. High resolution scanning tunneling microscopy (STM) and density functional theory (DFT) calculations corroborate the results. On the outermost layers, the threefold PdGa(111) and (-1-1-1) surfaces exhibit well-separated single Pd atoms, and trimers of Pd, respectively, while the (100), (110), and (210) surfaces terminate with chain-like arrangements of alternating Pd and Ga atoms. These pronounced difference in the local atomic arrangement of the Pd, as potentially catalytically active, and Ga, as spacer atom, make the PdGa surfaces highly attractive to study the impact of the local atomic structure on molecular adsorption and reaction properties.

To identify the preferred adsorption sites and investigate the effect of the Pd ensemble size and -separation, carbon monoxide (CO) was used as a test molecule on PdGa(111), (-1-1-1), (100), and (110). In a combined approach using infrared spectroscopy, low temperature STM (LT-STM), density functional theory (DFT), and temperature-programmed desorption (TPD) the CO binding configuration was found to be governed by the structure of the Pd ensembles of the respective surface terminations. Experimental and computational results revealed that binding to surface Pd is preferred by CO, while no binding to Ga atoms was observed. The adsorption of acetylene, molecular hydrogen, and ethylene, which represent the reactants and product of acetylene semi-hydrogenation, was studied on the threefold PdGa surfaces by means of LT-STM, TPD and DFT. Acetylene forms a weak π -bond to isolated Pd atoms, and a strong σ -bond to Pd trimers, respectively, revealing a strong influence of the Pd ensemble structure on acetylene binding. In contrast, binding of molecular hydrogen and ethylene is less affected by the local structure of the Pd atoms, since weak π -bonded configurations were observed on both Pd single atoms and trimers.

PdGa belongs to space group $P2_13$, and therefore has a chiral bulk structure despite its cubic lattice. As no significant reconstructions are observed, all investigated surface structures show chiral configurations. In some cases this chirality is expressed in sub surface atomic planes, therefore, the degree to which the chirality is expressed for a given surface orientation can vary. To investigate the influence of the PdGa surface

chirality on enantioselective adsorption, the adsorption of prochiral 9-Ethynylphenanthrene (9-EP, C₁₆H₁₀) molecules was followed using LT-STM. 9-EP is a planar molecule and as such is achiral in three dimensions, but forms chiral adsorbate complexes or enantiomers upon deposition on a surface. Adsorption of 9-EP on the threefold PdGa(111) and (-1-1-1) surfaces led to a temperature-, and structure-dependent enantiomeric excess (*ee*), with remarkable high values of up to *ee* = 0.98 for deposition at room temperature.

Our results on the PdGa single crystal surfaces demonstrate the importance of the surface atomic structure on binding geometry and -energy of small molecules on intermetallic surfaces. They also demonstrate the extraordinary suitability of PdGa and its crystalline surfaces to act as model systems to understand the role of intermetallic bonding and specific, structural atomic ensembles in catalytic processes. Therefore, these findings pave the way for the use of well-defined crystal facets as templates to catalyze specific surface reactions with high selectivity.

Keywords: Scanning tunneling microscopy, low energy electron diffraction, Fourier transform infrared spectroscopy, X-ray photoelectron spectroscopy, intermetallic compounds, PdGa, heterogeneous catalysis, molecular adsorption, site-isolation concept, ensemble effect, acetylene semi-hydrogenation, enantioselectivity

Zusammenfassung

Die Materialgruppe der intermetallischen Verbindungen bietet vielversprechende Eigenschaften für die Entwicklung neuer Katalysatoren. Aufgrund ihres teilkovalenten Bindungscharakters und der wohldefinierten Kristallstruktur bieten diese „geordneten Legierungen“ potentiell höhere chemische Stabilität und katalytische Selektivität als ihre Aufbaustoffe in elementarer Form, oder als ungeordnete Oberflächenlegierungen. In Hinblick auf die Katalyse stellt sich jedoch die Frage ob diese besonderen Eigenschaften auch an der Oberfläche des Materials erhalten sind. Die chemische Zusammensetzung und die atomare Struktur der Katalysatoroberfläche sind entscheidend für den Reaktionsablauf, da die Edukte lediglich mit den äussersten atomaren Lagen der Oberfläche interagieren. Vor kurzem wurde die intermetallische Verbindung Palladium-Gallium (Pd_1Ga_1) als höchst selektiver und stabiler Katalysator für die Semi-Hydrogenierung von Acetylen vorgestellt. Die hier vorliegende Doktorarbeit beinhaltet eine experimentelle Oberflächenstudie an Einkristallen dieser Verbindung, in der die atomare Oberflächenstruktur bestimmt, und die Adsorption von Molekülen untersucht wurde.

Mittels Vergleich von experimenteller und simulierter niederenergetischer Elektronenstreuung (LEED-I(V)) wurden die atomaren Strukturen von fünf PdGa Oberflächen mit den Millerschen Indizes (111), (-1-1-1), (100), (110) und (210) bestimmt. Atomar aufgelöste rastertunnelmikroskopische Aufnahmen (STM) und theoretische Untersuchungen mittels Dichte-Funktional-Theorie (DFT) bestätigten die Ergebnisse. Die dreifach rotationssymmetrischen (111) und (-1-1-1) Oberflächen zeigen eine starke Separierung der Oberflächenpalladiumatome und sind durch isolierte Pd Atome, respektive atomare Pd Trimere, terminiert. Die (100), (110) und (210) Oberflächen weisen eine weniger starke Separierung von Oberflächenpalladiumatomen auf, welche kettenförmig angeordnet sind. Diese charakteristischen atomaren Strukturen aus potentiell katalytisch aktiven Pd Atomen und Ga Separierungsatomen, bilden ideale Modellsysteme um den Einfluss der lokalen atomaren Struktur auf die Bindungseigenschaften von Adsorbaten zu erforschen.

Für die Untersuchung der Separierung der Bindungsplätze wurde Kohlenstoffmonoxid als Test-Molekül auf den verschiedenen PdGa Oberflächen adsorbiert, und der Einfluss der unterschiedlichen atomaren Pd Ensembles auf das Adsorptionsverhalten untersucht. Die Kombination aus Infrarot Spektroskopie, Tieftemperatur-STM, DFT und temperatur-programmierter Desorption (TPD) zeigte, dass die Struktur der unterschiedlichen Pd Oberflächenensemble die Adsorptionskonfiguration von CO bestimmt, während keine Bindung auf Ga Atomen der Oberflächen beobachtet wurde. Die Adsorption von Acetylen, Wasserstoff und Ethylen wurde auf den dreifach symmetrischen PdGa Oberflächen mittels Tieftemperatur-STM, TPD und DFT untersucht. Acetylen bindet mit einer starken σ -Bindung auf den Pd Trimeren und mit einer schwachen π -Bindung auf den isolierten Pd Atomen. Dahingegen hat die lokale atomare Struktur der Pd Ensembles einen vergleichsweise geringen Einfluss auf die Bindung von molekularem Wasserstoff und Ethylen. Auf den isolierten Pd Atomen und Trimeren bilden beide Moleküle jeweils eine schwache π -Bindung zur Oberfläche.

Die Kristallstruktur von PdGa gehört zur Raumgruppe $P2_13$ und besitzt daher eine intrinsische Händigkeit, trotz des kubischen Gitters. Die auf allen Oberflächen vorhandene Chiralität ist auf den verschiedenen Kristalloberflächen unterschiedlich stark ausgeprägt. Um den Einfluss der chiralen Struktur der Bindungszentren auf Oberflächenadsorbate zu untersuchen, wurden prochirale 9-Ethynylphenanthren (9-EP) Moleküle auf den dreifach rotationssymmetrischen Oberflächen abgeschieden. 9-EP ist ein planares Molekül und daher achiral im dreidimensionalen Raum. Wird das Molekül jedoch auf einer Oberfläche adsorbiert, geht diese Symmetrie verloren und es bildet sich einer von zwei möglichen chiralen Adsorbatkomplexen. In unseren Experimenten wurde das Vorkommen der dabei gebildeten Enantiomere mittels Tieftemperatur-STM untersucht und statistisch ausgewertet. Dabei wurde ein bemerkenswert hoher Überschuss von einem der beiden möglichen Adsorptionskomplexe festgestellt, mit einem Enantiomereüberschuss von bis zu 0.98 bei Raumtemperaturadsorption.

Die hier dokumentierten Ergebnisse an PdGa Einkristalloberflächen demonstrieren den Einfluss der atomaren Struktur der Oberflächenbindungsplätze auf die Bindungsgeometrie und –Energie von Molekülen auf intermetallischen Oberflächen. Es hat sich ausserdem gezeigt, dass PdGa ein hervorragendes Model-System darstellt, um Bindungs- oder Reaktionseigenschaften verschiedener Pd Ensembles mit spezifischer Struktur und atomarer Koordination zu untersuchen. Die präsentierten Resultate bilden den ersten Schritt auf dem Weg zur Verwendung von wohldefinierten Kristallfacetten als atomare Schablone für spezifische katalytische Reaktionen mit hoher Selektivität.

Schlüsselwörter: Rastertunnelmikroskopie, niederenergetische Elektronenbeugung, Fourier-Transform-Infrarotspektroskopie, Photoelektronenspektroskopie, intermetallische Verbindungen, PdGa, heterogene Katalyse, molekulare Adsorption, Separation der Adsorptionsplätze, Ensemble-Effekt, Acetylen semi-Hydrogenierung, Enantioselektivität

Contents

Abstract	iii
Zusammenfassung	v
List of Figures	ix
Chapter 1 Introduction	13
Chapter 2 Materials and Methods.....	21
2.1 The bulk structure of the intermetallic compound PdGa	21
2.2 Preparation of the single crystal surfaces in UHV.....	23
2.3 Quantitative LEED analysis, LEED-I(V)	24
2.4 Scanning tunneling microscopy	33
2.5 Infrared Spectroscopy.....	38
2.6 Temperature-programmed Desorption.....	41
2.7 X-ray Photoelectron Spectroscopy	43
Chapter 3 Structure determination of intermetallic PdGa single crystal surfaces.....	45
3.1 Publication: “Isolated Pd Sites on the Intermetallic PdGa(111) and PdGa (-1-1-1) Model Catalyst Surfaces”	45
3.2 Determination of the PdGa(100), (110) and (210) surface terminations	60
3.3 Comparison of the determined surface atomic structures	65
Chapter 4 CO as a test molecule for the identification of binding sites	69
4.1 Publication: “Ensemble Effect Evidenced by CO Adsorption on the 3-Fold PdGa Surfaces”	69
4.2 Temperature-programmed desorption of CO on the threefold PdGa Surfaces.....	81
4.3 Binding sites of the PdGa(100) and (110) surfaces probed by CO.....	84
Chapter 5 Reaction centers for acetylene semi-hydrogenation on Pd₃ and Pd₁.....	89
5.1 Publication (in print): “Adsorption of Small Hydrocarbons on Pd Reaction Centers: The Road to Selective Hydrogenation on PdGa (111)”	89

5.2	The C ₂ H ₂ molecular rotor on Pd ₃	105
5.3	XPS studies of acetylene and ethylene on the threefold PdGa surfaces	108
Chapter 6	Exploring enantioselectivity on intrinsically chiral intermetallic PdGa surfaces	113
6.1	Publication (in preparation): “Room Temperature Enantioselective Adsorption on a Chiral Intermetallic Surface”	115
6.2	Adsorption of 9-Ethynylphenanthrene on the threefold Pd ₃ termination	127
Chapter 7	Conclusions and Outlook	131
References	133
Curriculum Vitae	139
Acknowledgements	141

List of Figures

Figure 1.1 <i>In-situ</i> CO oxidation on Pt(111).	15
Figure 1.2 The site-isolation concept realized in different ways.	16
Figure 1.3 Van der Waals radii of adsorbed molecules of ethyne and acetylene	16
Figure 1.4 Conversion and selectivity of PdGa comparison to supported Pd.....	17
Figure 2.1 Cubic unit cell ($a = 4.89 \text{ \AA}$) of the PdGa bulk crystal structure containing eight atoms.	22
Figure 2.2 Local atomic structure in bulk PdGa.	22
Figure 2.3 LEED setup and threefold LEED pattern.....	24
Figure 2.4 The muffin-tin approximation.....	26
Figure 2.5 Plane wave scattering on a spherical potential.	27
Figure 2.6 Energy-dependent phase shifts for electron scattering	28
Figure 2.7 Angular distribution of the scattering amplitude	28
Figure 2.8 “Universal curve” for electron scattering	30
Figure 2.9 Schematic diagram of energy distribution of electrons backscattered from a solid.	30
Figure 2.10 Working principle of an STM. The tip trajectory for a constant tunnel current yields a profile line of constant electronic density.	33
Figure 2.11 The evolution of STM in the last decades.	33
Figure 2.12 Principle of tip-sample tunneling.	34
Figure 2.13 Main components of an STM setup	36
Figure 2.14 Experimental principle of RAIRS.....	38
Figure 2.15 Working principle of a Fourier transform spectrometer.	39
Figure 2.16 Photo of the TPD sample holder and calibration curves using CO/Cu(111).	42
Figure 2.17 Energy level in the XPS experiment	44
Figure 3.1 Pendry R_p factors from the LEED-I(V) analysis of all structure models.....	52
Figure 3.2 Experimental (dashed) and theoretical I(V) profiles	53
Figure 3.3 Lateral view of two slabs used in the calculation of the surface free energies.	54

Figure 3.4 Perspective view of a slab used to compute the STM profile of a surface with vacancies.	56
Figure 3.5 The pDOS of the Pd <i>4d</i> -bands of the two threefold PdGa surfaces.....	57
Figure 3.6 The DOS projected on the <i>d</i> -bands of selected Pd surface atoms and on the <i>s</i> -band of hydrogen atoms.....	59
Figure 3.7 Side view of the orthorhombic (100), (110) and (210) unit cells of PdGa.	60
Figure 3.8 STM images of stepped terraces and height profiles of the PdGa(100), (110) and (210) surfaces.....	61
Figure 3.9 LEED patterns of PdGa:A(100), PdGa:A(110), and PdGaA:(210) surfaces.....	61
Figure 3.10 Comparison of LEED-I(V) and STM results for PdGa(100), (110) and (210).	62
Figure 3.11 STM image of a PdGa:A(110) step edge showing an enlarged defect area.	63
Figure 3.12 Chiral motives of the PdGa surfaces.	67
Figure 4.1 Contrast inversion of CO in STM.	76
Figure 4.2 Series of images STM images of CO/Pd ₁ for different tunnel voltages.....	76
Figure 4.3 Various tested adsorption sites for CO on the threefold PdGa surfaces	77
Figure 4.4 LEED-I(V) results for the suggested Ga terminated surfaces.	79
Figure 4.5 STM images of individual CO molecules adsorbed on PdGa(111) and PdGa(-1-1-1).	80
Figure 4.6 Desorption curves of CO adsorbed on Cu(111), PdGa:A(111)Pd ₁ and PdGa:A(-1-1-1)Pd ₃	81
Figure 4.7 Series of TPD experiments for the two threefold PdGa surfaces	82
Figure 4.8 Coverage as a function of CO exposure	82
Figure 4.9 RAIRS adsorption spectra for CO on PdGa:B(100) and (110).	84
Figure 4.10 STM images of the (100) terminations after small (left) and large (right) exposure of CO	85
Figure 4.11 Identification of the adsorption site for CO on PdGa:A(100)Pd _α	85
Figure 4.12 STM images of PdGa:A(110) after exposure to CO.	86
Figure 4.13 Identification of the adsorption site for CO on PdGa:A(110)Ga _α	87
Figure 5.1 Hopping of H ₂ molecules on the Pd ₃ surfaces at 5K.....	97
Figure 5.2 STM images of the collective alignment of C ₂ H ₂ molecules at 5K.	97
Figure 5.3 Tip induced relaxation of C ₂ H ₂ adsorbed in the interstitial adsorption site on Pd ₁	98
Figure 5.4 Steric repulsion of neighboring C ₂ H ₄ molecules adsorbed on the same Pd trimer	98

Figure 5.5 DFT optimized geometries of C_2H_2 on Pd_3	99
Figure 5.6 DFT optimized geometries of C_2H_2 on Pd_1	100
Figure 5.7 DFT optimized geometries of C_2H_3 on Pd_3	100
Figure 5.8 DFT optimized geometries of C_2H_3 on Pd_1	100
Figure 5.9 DFT reaction barrier for $H_2 \rightarrow H + H$ on Pd_3	101
Figure 5.10 DFT reaction barrier for $H_2 \rightarrow H + H$ on Pd_1	101
Figure 5.11 DFT reaction barrier for $C_2H_2 \rightarrow C_2H_3$ on Pd_3	102
Figure 5.12 DFT reaction barrier for $C_2H_2 \rightarrow C_2H_3$ on Pd_1	102
Figure 5.13 Alternative reaction pathway for $C_2H_2 \rightarrow C_2H_3$ on Pd_1	102
Figure 5.14 DFT reaction barrier for $C_2H_3 \rightarrow C_2H_4$ on Pd_3	103
Figure 5.15 DFT reaction barrier for $C_2H_3 \rightarrow C_2H_4$ on Pd_1	103
Figure 5.16 DFT reaction barrier for $C_2H_4 \rightarrow C_2H_5$ on Pd_3	104
Figure 5.17 DFT reaction barrier for $C_2H_4 \rightarrow C_2H_5$ on Pd_1	104
Figure 5.18 Rotational motion of the acetylene on the Pd_3 trimer.	106
Figure 5.19 XPS spectra of the C1s peak as a function time for exposure of Pd_3 to C_2H_4	108
Figure 5.20 XPS spectra (round markers, same colors as in Figure 5.19) of the C1s level...	109
Figure 5.21 XPS of Pd 3d and Ga 3p core levels before and after adsorption of C_2H_2 at 80 K	111
Figure 6.1 Different approaches to chiral synthesis of molecules.....	114
Figure 6.2 Surface structure of $PdGa:A(111)Pd_1$ and its enantiomorph $B(-1-1-1)Pd_1$	118
Figure 6.3 STM images (10x20 nm, 0.02 V, 2 nA, T = 5 K) of 9-EP adsorbed at room temperature	119
Figure 6.4 STM images (T=5 K, 20x20 nm, 0.2 V, 2 nA) of 9-EP	121
Figure 6.5 Phase diagram based on statistical evaluation of 9-EP molecules on Pd_1	122
Figure 6.6 STM topography in overlay with the DFT optimized structure of a R^* and S^* adsorbate	124
Figure 6.7 STM images of 9-EP on Pd_1 at room temperature, and after cooling to 77K (left: 0.5 V, 2 nA; right: -0.8 V, 0.05 nA).	124
Figure 6.8 Evolution of the different 9-EP species upon annealing of the same sample. ...	125
Figure 6.9 Adsorption of prochiral 9-EP on $PdGa:A(-1-1-1)Pd_3$	127
Figure 6.10 Identification of the adsorption site for 9-EP on Pd_3 by STM.	129

Chapter 1 Introduction

Knowledge-based catalysts

Catalytic reactions are involved in a large number of technological processes, ranging from chemical synthesis, exhaust gas treatment and fuel refining to food processing and production of pharmaceuticals. Optimization of large scale catalytic processes is of importance to the reduction of resources- and energy demands, both of which potentially lower production costs and environmental impact. One such large scale process is the production of polyethylene from ethylene with a total annual volume of 80 Mt¹, which heavily relies on an efficient polymerization reaction. The Ziegler-Natta polymerization catalysts used today suffer from poisoning by traces of acetylene in the ethylene feed.² Therefore, pretreatment of the gaseous ethylene precursor stream is required in order to remove the pollutant. Most often, this purification is achieved by Pd-based catalysts, which convert the acetylene (C₂H₂) to the desired ethylene (C₂H₄) through its selective semi-hydrogenation: $C_2H_2 + H_2 \rightarrow C_2H_4$.³⁻⁴ A common problem encountered for these catalysts is their deactivation with increasing time-on-stream, which is due to the formation of carbon deposits through unselective processes. These circumstances demand regular replacement of the catalyst and shut-down of the chemical reactor.² Generally, the suitability of a good catalyst is characterized by an optimal combination of activity, stability and selectivity to which the economical cost needs to be added.

Improvement in selectivity has been made for the catalytic process of acetylene semi-hydrogenation by dilution of the active Pd species with other elements, such as Ag, and proper choice of the support material,³⁻⁴ but there is still a large interest to develop catalysts of higher stability and selectivity.² Achieving high selectivity is of particular interest in the production of fine chemicals and pharmaceuticals, where compound purity is vital. The main problem to accomplish a paradigm change from the trial and error based catalyst development to a truly knowledge based approach is the lack of a detailed understanding of the chemical reaction pathways on the atomic scale, and the specific influence of the single catalysts components on the catalytic process. A detailed understanding of the role of the atomic surface structure and composition of the catalysts, allows for specific suggestions of how a catalyst should be prepared, or how the reaction should be run (temperature, pressure, gas flow).⁵

An obvious starting point to gather this knowledge would be the detailed study of modern heterogeneous catalysts, which are often composed of different metallic species and supported by oxides. Unfortunately, most of today's experimental techniques, yielding information on the reaction pathway on the atomic scale, do not allow for *in-situ* studies on technologically applied catalysts under industrially relevant process conditions.⁵ A further complication arises from the morphological and structural properties of technical catalysts which are mostly applied in form of milled powders. Recent advances in experimental equipment overcome these problems partially,⁶⁻⁷ but the ability to study the precise structural configurations and reaction pathways of the catalytic surface and the involved molecules is still lacking.

Insights provided by surface science

The surface science approach to heterogeneous catalysis is based on the concept to study catalysis in an idealized environment, focusing on particular aspects or selected steps of the process and extrapolation of the findings to real world catalysts.^{5, 8} In practice, the applied idealizations often include atomically clean single crystal surfaces, ultra-high vacuum (UHV) surface preparation and characterization, low reactant pressures, and low temperatures of adsorption, representing a “model system” of the technological catalyst. As all these parameters are extreme with respect to industrial process conditions, there exists a risk of oversimplification, introducing “gaps” between the research results and industrial application; like the so-called materials gap and the pressure gap. Efforts to mitigate this risk are ongoing, with the goal to extend the range of surface analytical tools to high pressures and temperatures.^{7, 9} However, experiments on ideal model systems offer a much wider range of applicable analytical techniques to study the elementary processes in catalysis, as for example the precise atomic structure of the catalysts surface, or reactant adsorption and -diffusion. In particular real space imaging of molecules on surfaces, by high resolution scanning probe techniques, provides access to the local structure on the atomic length scale. To suppress the fast thermal diffusion of the adsorbates, which is certainly present under real reaction conditions, these techniques require low temperatures. Also scattering techniques take advantage of cryogenic temperatures, as the thermal motion of the atomic scattering centers is reduced to obtain diffraction over more extended regions in reciprocal space.

Maybe the most prominent example for the application of an idealized model system that is used to understand an important technical catalytic process is the oxidation of carbon monoxide on different transition metals, nowadays widely applied in exhaust gas treatment of automobiles. Early studies by Somorjai⁸ and Ertl¹⁰, focused on the first step of the reaction, which is the binding, or adsorption, of CO on clean, single crystal metal surfaces. Using low energy electron diffraction, different binding sites were identified, *e.g.* “on-top” of surface atoms, or in between two (“bridge”), three or four (“hollow”) surface atoms. These adsorption sites bind the CO molecules with different strengths and their occupation depends on surface structure and CO coverage.⁸ Such information from simplified model systems contributes to an in-depth understanding of catalytic reactions, which is necessary for the rational design of novel catalysts.

A further example in this line, also from the group of Ertl¹¹, is the CO oxidation reaction, studied at reduced temperatures on (111) single crystal metal surfaces by co-adsorption of CO and O₂. For Rh(111), the dissociative adsorption of the oxygen molecule was found to require a low coverage of CO on the surface to make the Rh threefold hollow sites accessible for O₂ adsorption. In addition, two neighboring free hollow sites are required for the O₂ dissociation, revealing that the low CO coverage is essential to the oxidation reaction.¹¹ In an additional example by Winterlin *et al.*¹², the kinetics of the CO oxidation reaction on Pt(111) could be monitored *in-situ* by scanning tunneling microscopy, revealing that the oxidation reaction occurs at the boundary between CO and O adsorbate islands. The series of STM images in Figure 1.1 visualizes this process, showing the growth of CO islands on the previously oxygen-covered surface, as a function of time. The reaction product, CO₂, desorbs immediately after reaction at the borders between the CO and oxygen islands.

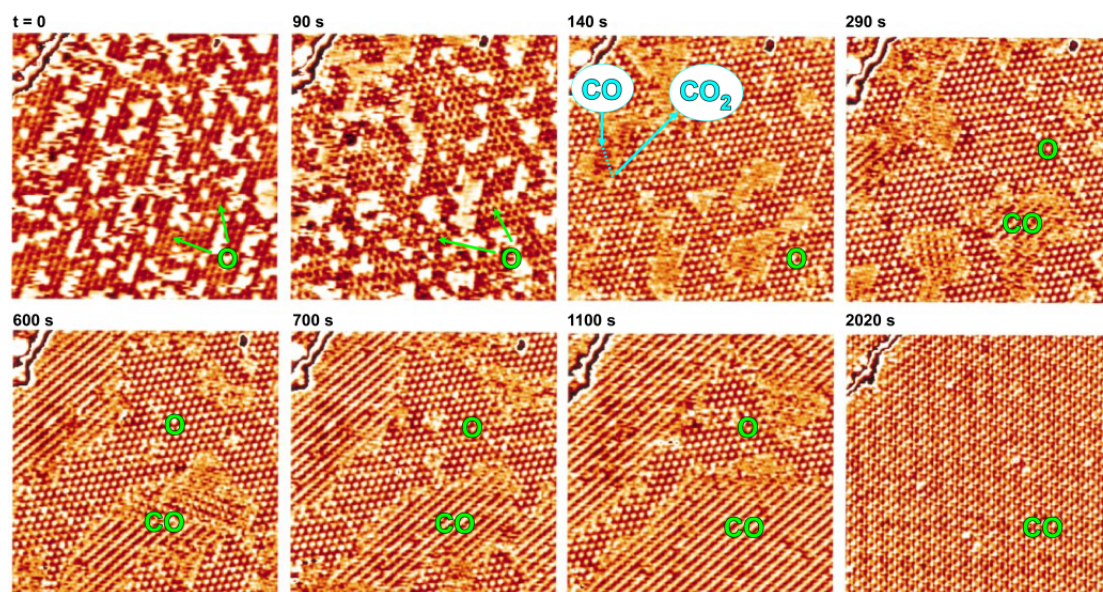


Figure 1.1 *In-situ* CO oxidation on Pt(111). Series of STM images, recorded during reaction of pre-adsorbed oxygen atoms with CO molecules at 247 K, all from the same area of a Pt(111) crystal. At $t > 0$, the partially O (dark) covered surface is continuously exposed to CO. As time increases, the O islands become smaller. The reaction pathway (blue in the image at 140 s) includes CO adsorption on clean surface parts, diffusion to O-covered surface, reaction to CO_2 and immediate desorption. At $t = 290$ s, the previously clean areas become occupied by CO. At $t = 2020$ s, all oxygen has reacted to CO_2 . (Figure adapted from Ref. ¹²)

Another well-studied example, and of particular interest to this work, is the investigations on Pd single crystal surfaces with regard to the selective hydrogenation of acetylene to ethylene,¹³⁻¹⁶ whose technological importance has already been discussed at the start of this chapter. As Pd generally performs well as a hydrogenation catalyst, modified oxide-supported Pd catalysts are the most widely applied systems to achieve this conversion.³⁻⁴ Increased selectivity towards semi- instead of full hydrogenation is observed after exposure of the Pd catalysts to gaseous hydrocarbons, which is believed to originate from carbonaceous deposits on the Pd surface. These deposits form during the catalyst stabilization phase, prior to steady-state reaction conditions and cover most of the Pd surface. The carbonaceous layer exhibits small vacancies of atomic dimensions, which allow for specific adsorption of acetylene onto exposed Pd sites and subsequent conversion to ethylene. The increased selectivity in this case is believed to be associated with the size reduction and spatial isolation of the reaction centers. This strategy to enhance selectivity is generally called site-isolation concept. Figure 1.2a shows different strategies how such reaction site-isolation can be achieved.

It was suggested that the small size of the isolated Pd sites is responsible for the high selectivity, due to several reasons:³ Firstly, the larger van der Waals radii of ethylene leads to a stronger reduction of the binding strength to the isolated Pd sites than for acetylene, promoting desorption of ethylene instead of further hydrogenation (the van der Waals radii of the two molecules are depicted in Figure 1.3). Secondly, also the acetylene is weaker bonded and less coordinated with Pd surface atoms as compared to adsorption on an extended Pd surface, which might reduce the hydrogenation barrier and thus lead to higher activity.

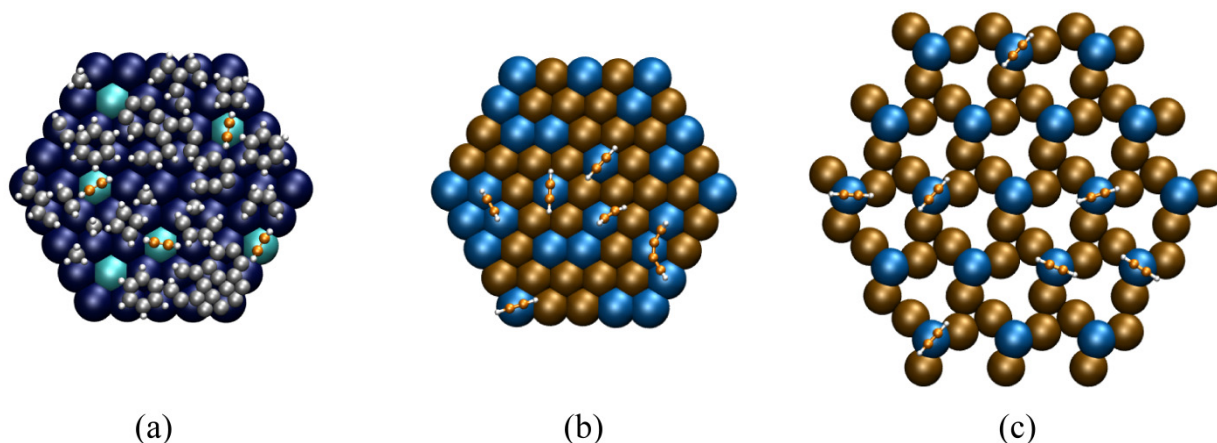


Figure 1.2 The site-isolation concept realized in different ways. (a) On the pure Pd catalyst (dark blue and cyan), carbonaceous deposits (gray) leave available isolated sites (cyan) for acetylene adsorbates (orange and white). (b) Dilution of Pd (blue) with an inert element (brown) in surface alloys leads to small Pd ensembles which serve as isolated binding centers for acetylene. (c) Site-isolation on a surface of an intermetallic compound; due to the crystal structure, the active adsorption sites (blue) are well-defined and of high areal density, while at the same time being separated by an inert atomic species (brown).

Hence, it is concluded that the key ingredient to obtain increased selectivity for semi-hydrogenation is the provision of spatially separated, single or few atom Pd adsorption sites leading to π -bonded acetylene.³ Consequently, the aim is to reduce the size of the active site and the coordination of the molecules with the surface atoms for this reaction. This can be obtained by alloying of the Pd surface with Ag, leading to the creation of small reaction centers of Pd, as shown in Figure 1.2b. Indeed, the Ag-diluted Pd catalysts exhibit higher initial selectivity than pure Pd.¹⁷ However, long-term stability of the catalyst is reduced, as segregation can lead to structural and compositional changes at the surfaces causing a loss of selectivity and/or activity under reaction conditions.¹⁸

An alternative approach to achieve more stable site-isolation is based on using intermetallic compounds as novel catalyst materials. This class of materials is distinct from standard metallic alloys by ordered crystal structures, which are markedly different from those of their single elemental constituents. Additionally, the interatomic bonding has a partial covalent character which can lead to beneficial materials properties like increased corrosion resistance and hardness.¹⁹ In contrast to surface alloys, an intermetallic compound can be expected to exhibit well-ordered and -defined catalytic sites (Figure 1.2c), which is the ideal condition for selective reaction pathways by site-isolation and long-term stability due to the directional bonding character.

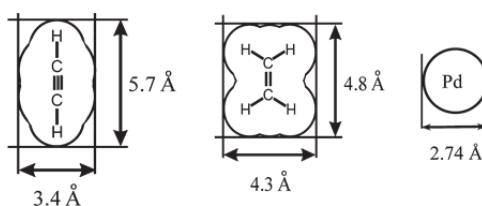


Figure 1.3 Van der Waals radii of adsorbed molecules of ethyne and acetylene and plane view of palladium atom for comparison (Figure reprinted from Ref. ³)

The Palladium-Gallium catalyst

The present study on intermetallic PdGa is motivated by the particular crystalline bulk structure of the compound, which bears two geometrical features that are highly interesting for heterogeneous catalysis. The first is the intrinsic isolation of the Pd atoms, which are surrounded by a shell of Ga as nearest neighbor atoms, and exhibit a 10% larger Pd-Pd distance compared to metallic Pd.²⁰ The second intrinsic feature of PdGa is the bulk chirality of the intermetallic compound, which originates from its crystal structure belonging to the space group $P2_13$. This results in a chiral basis of the unit cell even though the lattice is cubic. This bulk chirality is expected to result in chiral atomic arrangements on the surfaces. We will discuss both these structural properties in greater detail in Chapter 2.

Outstanding properties have been demonstrated for PdGa as a selective catalyst in the semi-hydrogenation of acetylene by the group of Armbrüster *et al.*, which was assigned to the intrinsic site-isolation and stability.²¹⁻²⁵ Figure 1.4 shows the enhanced stability of the compound in comparison to an oxide-supported Pd catalyst. The bulk properties of PdGa were studied in detail by experimental²⁶ and computational techniques²², revealing the partial covalent character of the intermetallic bonds. In contrast to metallic Pd, no hydrogen uptake was observed for PdGa,^{23, 26} which is advantageous in order to favor semi- instead over full-hydrogenation of reactants. By application of surface-sensitive analytical techniques in earlier studies, the separation of adsorption sites was demonstrated on PdGa powder samples using CO as a test molecule in infrared absorption experiments.²²⁻²³ However, the detailed atomic structures of the active catalytic sites remained unresolved.

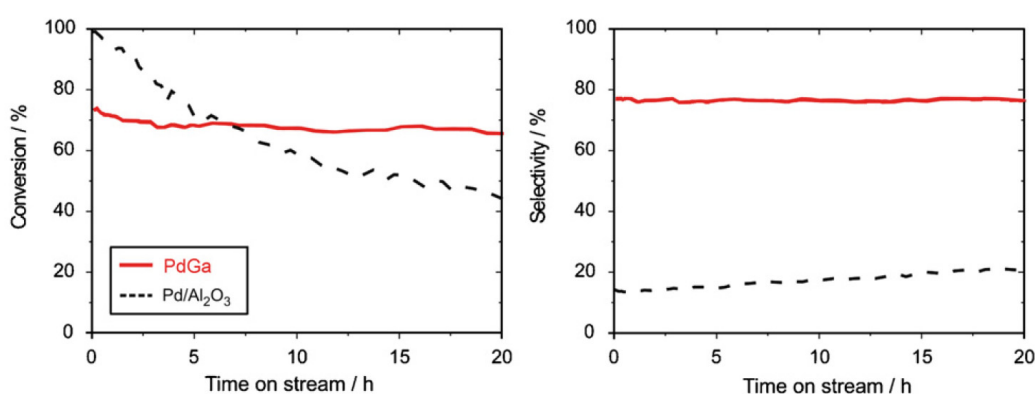


Figure 1.4 Conversion and selectivity of PdGa comparison to supported Pd in the semi-hydrogenation of acetylene. (Adapted from Ref. ²²)

To obtain an adequate picture on the presence, distribution and structural nature of Pd sites on the atomic scale, the surface structures of several low-Miller index facets of PdGa were determined in this study, using surface science techniques. The main goal was to obtain a detailed understanding of binding and adsorption of molecules on site-isolated surfaces. Therefore, we aimed to answer the following questions: Which atomic ensembles are present on the intermetallic surface? How does the structure of the sites influence the adsorption of molecules? Which types of ensembles should be present to obtain a strong, or weak bond of a certain molecule to the substrate?

To approach these questions, we apply well-defined, crystalline and reproducible sample surfaces, which require preparation in UHV. Only under these conditions an unambiguous interpretation of the experimental data is possible. It is clear, that it is not straight forward to relate the findings, obtained from UHV

prepared model surfaces, to the PdGa material used in high pressure experiments to assess its catalytic properties. Here usually powder material of polycrystalline nature is used. However, it can be expected that the equilibrium crystallite shape of PdGa exhibits these terminating low-Miller index facets,²⁷ even though their size might be small and the step density high. Leaving aside the role of step edges and surface defect, which certainly should not be neglected generally, the molecular adsorption mechanism on the single crystal facets compares to the one on the powder samples, such that information on the active metallic species and the preferred bonding geometries can be retrieved from the single crystal model catalysts.

In addition to the Pd site-isolation, we studied the surface chirality of this intermetallic compound, which originates from the chiral basis of the unit cell. The expression of intrinsic bulk chirality of an intermetallic compound on its surfaces has not been studied so far, although, this bears great potential for chiral synthesis, which is important to the pharmaceutical industry and biotechnology. Here, we conducted a first approach to this topic by investigating the enantioselective adsorption of prochiral molecules on PdGa, which is the first step to enantioselective catalysis.

Structure of the thesis and personal contribution

Chapter 2 gives an overview on the bulk crystal structure of PdGa and the features that are relevant to this study. The experimental methods are discussed subsequently. Further chapters of this thesis discuss the experimental findings, focusing on selected aspects of the PdGa surfaces. Each chapter starts with short introduction to the topic, followed by a publication summarizing the most important results (with some of them being in preparation for publication). Supporting information and additional experimental data provide deeper insight and may raise new questions. In Chapter 3 we report on the surface atomic structures of five low-Miller index surfaces. This information is pivotal for the interpretation of the subsequently presented adsorption experiments. In Chapter 4, the CO adsorption sites are identified and characterized for four surfaces. To approach the semi-hydrogenation reaction, we studied acetylene, hydrogen and ethylene adsorption on the two threefold surfaces, which is the content of Chapter 5. The influence of surface chirality on enantioselective adsorption of prochiral molecules is presented in Chapter 6.

In the course of the PhD project, the consortium of several collaborators, which was meeting on a regular basis in the frame of the “Pd-days”, initiated by the Fritz-Haber Institute Berlin, has led to a review article on selective hydrogenation catalysis on Pd- based catalysts:

Armbrüster, M., Behrens, M., Cinquini, F., Föttinger, K., Grin, Y., Haghofer, A., Klötzer, B., Knop-Gericke, A., Lorenz, H., Ota, A., Penner, S., Prinz, J., Rameshan, C., Révay, Z., Rosenthal, D., Rupprechter, G., Sautet, P., Schlögl, R., Shao, L., Szentmiklósi, L., Teschner, D., Torres, D., Wagner, R., Widmer, R. and Wowsnick, G. *How to Control the Selectivity of Palladium-based Catalysts in Hydrogenation Reactions: The Role of Subsurface Chemistry*. ChemCatChem (2012), 4: 1048–1063

My contributions to the publications discussed in this thesis are the collection of all experimental data, simulation of low energy electron diffraction, data analysis, and large contribution in the writing of the paper texts. All measurements were conducted at the Federal Laboratories for Materials Science and Technology (Empa), in Dübendorf Switzerland, in collaboration with the École Polytechnique Fédérale de Lausanne (EPFL). Fourier-transform infrared spectroscopy was performed in the laboratories of Empa section 203. *Ab-initio* calculations were performed by Roberto Gaspari, Carlo Pignedoli, and Daniele Passerone. PdGa single crystals were grown and provided by Prof. Peter Gille (LMU Munich) and Prof. Yuri Grin (MPI Dresden), respectively. A second set of samples was purchased from Mateck GmbH (Juelich).

The research project was funded by the Swiss National Science Foundation under the contract 200021-129511.

Chapter 2 Materials and Methods

This chapter provides background information on the crystal structure of the intermetallic compound PdGa and gives an introduction to the methods that were used in the experimental surface analysis. The intrinsic bulk site-isolation and chirality of PdGa are addressed in Chapter 2.1. Preparation of the single crystal surfaces in UHV is shortly described in Chapter 2.2. The following Chapters 2.3 and 2.4 contain an introduction to quantitative low energy electron diffraction (LEED-I(V)) and scanning tunneling microscopy (STM). The two were used in combination to determine the atomic surface structures of the single crystals, while the latter was also applied to study the local structure of molecules on the surfaces. In Chapter 2.5, a short introduction to reflection absorption infrared spectroscopy (RAIRS) is given, which was used for identification and characterization of the adsorption sites. Temperature-programmed desorption (TPD) yields information on binding strength of adsorbates and is discussed in Chapter 2.6. To investigate the electronic structure of adsorbates, X-ray photoelectron spectroscopy was applied. The method's basic working principle is explained in Chapter 2.7.

2.1 The bulk structure of the intermetallic compound PdGa

The crystal structure of PdGa belongs to the $P2_13$ space group, *i.e.* it is of FeSi type. The cubic unit cell shown in Figure 2.1, with lattice parameter $a = 4.897 \text{ \AA}$ ²⁰ contains 8 atoms. As depicted in Figure 2.2, each Pd atom is embedded in a cage of Ga atoms, such that the seven nearest neighbors to each Pd atom are Ga atoms. The nearest Pd-Pd distance in the bulk amounts to 3.00 \AA , which is about 10% larger than in elemental Pd. Therefore, isolation of Pd atoms is already present to some extent in the bulk of the intermetallic compound. The question to be addressed is whether and in which form it is expressed at the surfaces. Another peculiarity regarding the crystal structure is its chirality, which is illustrated in the right panel of Figure 2.2. The view along the $\langle 111 \rangle$ direction on the 7 atom Ga cage of the centered Pd atom reveals the absence of any mirror symmetry plane, as the triangle formed by the topmost three Ga atoms is rotated by about 23° clockwise or counter-clockwise, with respect to the triangle formed by the lower three Ga atoms, with the direction depending on the enantiomer form. This chirality of the crystal is reflected in the intensity pattern of the Bragg-spots in LEED, which is shown for a threefold PdGa surface in Figure 2.3. The surface chirality of the different low-Miller index samples will be discussed in Chapter 3.3, after the determination of the surface atomic structures. To distinguish the two enantiomorphs, a capital A or B, separated by colon punctuation, is following the chemical formula (PdGa:A and PdGa:B), as introduced in Refs²⁸⁻²⁹.

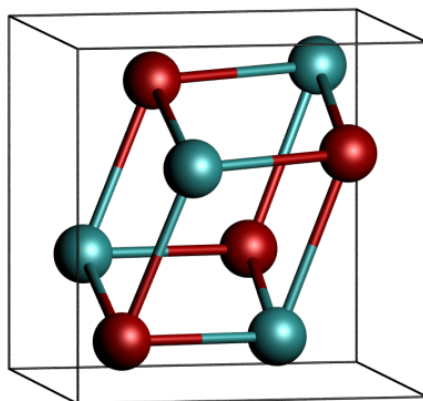


Figure 2.1 Cubic unit cell ($a = 4.89 \text{ \AA}$) of the PdGa bulk crystal structure containing eight atoms. (Pd: cyan, Ga: red)

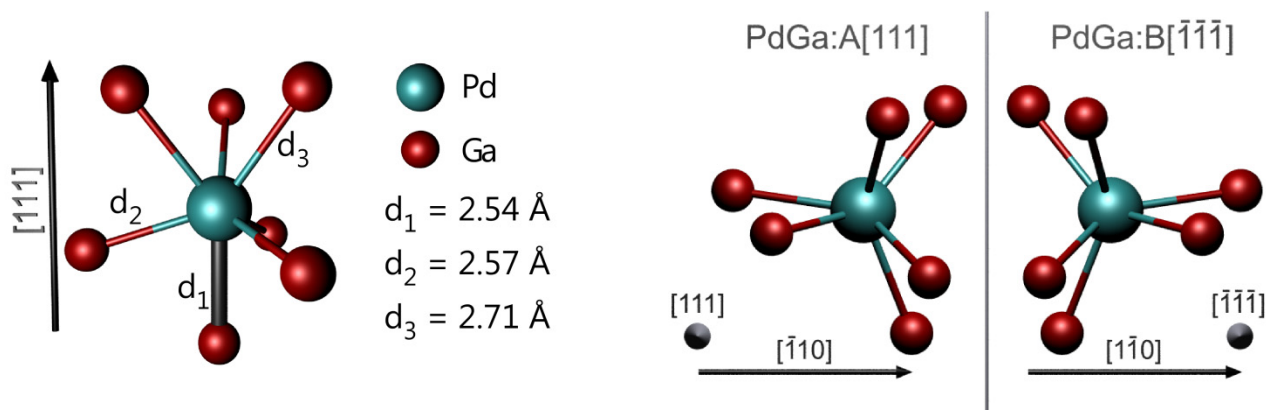


Figure 2.2 Local atomic structure in bulk PdGa. Left: In the bulk crystal structure of PdGa each Pd atom (cyan) is surrounded by 7 Ga nearest neighbors (red). The closest bond d_1 (black) is parallel to the threefold symmetric direction. The graphic shows a section of the PdGa:A structure. Right: Top view on the same cluster in the two enantiomer forms PdGa:A and PdGa:B, revealing the chiral atomic arrangement in the PdGa unit cell.

The PdGa surfaces studied in the course of this thesis are obtained from precise cutting of a PdGa single crystal parallel to the principal crystal planes that are defined by the Miller indices (111), $(-1-1-1)$, (100), (110), (210). Please note, that we distinguish the (111) and the $(-1-1-1)$ surfaces, which are non-equivalent since the crystal is build up out of 4 different atomic layers along this direction, Pd3-Ga3-Pd1-Ga1. Care must be taken in the comparison of the threefold symmetric surfaces of the two enantiomers, as by convention the crystalline directions are switched when going from Form A to Form B. Thus, PdGa:A(111) and PdGa:B(111) show an inverted layer stacking, and in order to compare surfaces that are exact mirror images of one another, one needs to compare the PdGa:A(111) surface to the PdGa:B $(-1-1-1)$ surface (or: PdGa:A $(-1-1-1)$ to PdGa:B(111)).

2.2 Preparation of the single crystal surfaces in UHV

In this study, PdGa single crystals of several cm³ grown by the Czochralski method have been used.³⁰ The enantiomer form of the final crystal can be controlled by choice of a PdGa seed crystal of either enantiomer form A or B. The determination of the crystal orientation has been achieved by Laue diffraction. Subsequently, the crystal has been cut perpendicular to the desired crystal direction to better than 0.1° accuracy and mechanically polished to mirror-like surface finish. For the experiments we rely on a reproducible method to prepare atomically clean surfaces, which is achieved by sputtering-annealing cycles in a UHV chamber (pressure < 5*10⁻¹⁰ mbar). Argon or Neon ion sputtering at 1kV acceleration voltage was used in all studies. Annealing was performed by resistive heating or electron bombardment from the backside of the crystal. An annealing temperature of 850 ± 30 K results in large, atomically flat terraces. Temperature monitoring was performed using optical pyrometers by Raytek (emissivity = 0.1).

2.3 Quantitative LEED analysis, LEED-I(V)

Low energy electron diffraction (LEED) is an analytical technique that allows the determination of the atomic structure of crystalline surfaces. It is not only one of the most widely applied, but also one of the earliest techniques with encompasses the scientific discipline of surface science. After the prediction of electron diffraction in 1924 by de Broglie, the effect was shown experimentally in 1927 by Davidson and Germer³¹, being one of the first experimental confirmations of de Broglie's postulation of the electrons particle-wave duality. It wasn't until the early 1960s, that LEED was introduced as analytical tool in surface science, which is due to the advances and availability of high vacuum techniques in this period, allowing for preparation and characterization of atomically clean surfaces.

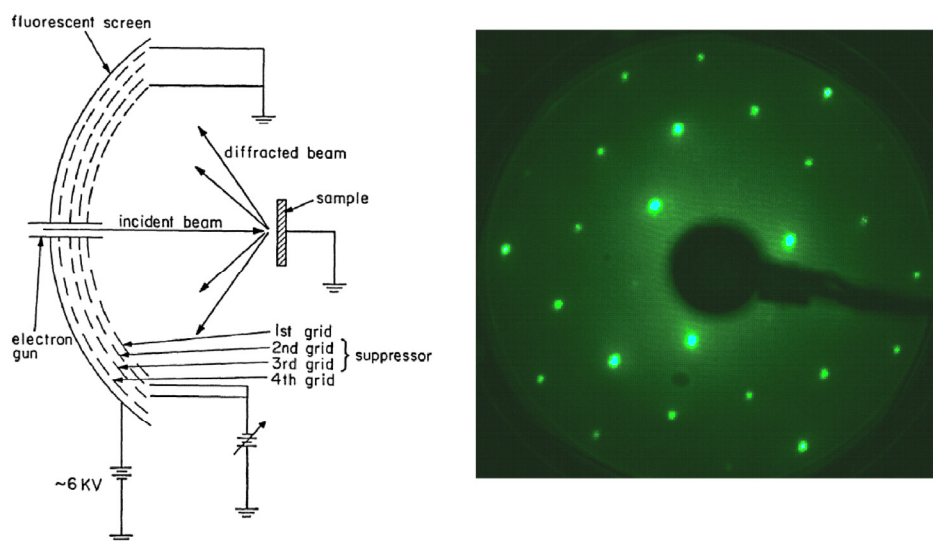


Figure 2.3 LEED setup and threefold LEED pattern. Left: Schematic of a four grid LEED display system. (Figure adapted from Ref. ³²) Right: LEED pattern of a threefold symmetric PdGa:B(-1-1-1) surface showing different spot intensities, using an electron kinetic energy of 54 eV.

The basic LEED experiment setup is comparably simple; a collimated mono-energetic electron beam is incident on a sample surface, from which it is back-scattered towards a hemispherical fluorescent screen. A series of spherical grid electrodes repels secondary electrons and accelerates the elastically scattered (i.e. diffracted) ones on the screen to produce visible spots. A sketch of the experimental setup and an image of a LEED-pattern are shown in Figure 2.3. If the sample shows a two-dimensional periodic structure on the length scale of the de Broglie wavelength of the impinging electrons and a sufficiently extended structural coherence, the back-scattered electron waves interfere, resulting in a pattern of Bragg spots on the screen. By this fast and reliable method a direct image of the reciprocal space of the two-dimensional surface structure is obtained, which is one of the strength of the method. From back transformation into real space, the 2D lattice parameter(s) of the surface and/or adsorbate phases are accessible.

Based on this principle, many derived techniques have developed that make use of different aspects of the electron diffraction process, like for example "spot profile analysis-" (SPA-) LEED, and "reflection high energy electron diffraction" (RHEED). The method applied within this thesis is LEED-I(V), in which the intensity (I) of a set of diffraction spots is analyzed as a function of the electron kinetic energy, which is given by the acceleration voltage (V). By exploiting the intensity information of the Bragg beams, the three-dimensional

structure of the first few atomic layers of the sample's surface can be determined with high precision through comparison with simulated intensity data. This very powerful approach requires a complex dynamical scattering theory, to obtain high accuracy, and an initial model structure which is close to the real one, to get convergence. In this introduction, a conceptual overview of the main theoretical concepts of LEED-I(V) analysis is given. As a full description of the theory and its implementation into the simulation would go beyond the scope of the thesis, the interested reader is referred to Refs ³² and ³³.

The necessary ingredients for the LEED-I(V) analysis and the simulation of the electronic scattering will be treated in the following subchapters. As the surface will be approximated to be built up of non-interacting single atoms, we start with the scattering of electrons on isolated spherical potentials (2.3.1). Thereafter, the problem of multiple electron scattering is treated, which is vital for the quantitative simulation of LEED (2.3.2). The next subchapter (2.3.3) is on the conceptual implementation of multiple scattering in the three-dimensional atomic lattice. At this stage, we are in principle able to simulate the LEED beam intensities. However, in order to practically determine the atomic position of the surfaces atoms, an iterative structure refinement has to be performed, which is done here by the Tensor-LEED approach (2.3.4). In the last subchapter (2.3.5) we comment on the use of LEED-I(V) on the intermetallic compound PdGa.

2.3.1 Electron scattering on a spherical potential

The main task in the computation of the Bragg beams intensities in LEED, is to simulate the scattering process of an incident electron with the surface. This is a complex, multi-particle problem, where the incident electron is scattered by all coulomb charges that are present in the sample. These are core- and valence electrons, as well as the positively charged atomic nuclei. The problem is described comprehensively through the following Hartree-Fock Type equation³², including interaction with the atomic nuclei (Z_j), screening charges (V_{sc}) and the exchange interaction:

$$\left(-\frac{\hbar^2}{2m} \vec{\nabla}_j^2 - \sum_j \frac{Z_j e^2}{|\vec{r} - \vec{r}_j^n|} + V_{sc}(\vec{r}) + \sum_i \int \frac{e^2 |\Psi_i(\vec{r}_i)|^2}{|\vec{r} - \vec{r}_i|} d^3 r_i \right) \varphi(\vec{r}) - \sum_i \left(\int \frac{e^2 \Psi_i^*(\vec{r}_i) \varphi(\vec{r}_i)}{|\vec{r} - \vec{r}_i|} d^3 r_i \right) \Psi_i(\vec{r}) = E \varphi(\vec{r}) \quad (2-1)$$

Here $\varphi(\mathbf{r})$ describes the wave function of the scattering electron, and $\psi_i(\mathbf{r})$ that of the electrons of the surface ($i=1, \dots, N$). While the first term includes the kinetic energy and the local interactions of the scattering electron with the charges of the sample, the second term describes the non-local exchange interaction between all the electrons of the system. The complete description of the problem in this form is unpractical due to the appearance of $\varphi(\mathbf{r})$ in the integral of the exchange term and the consideration of all surface electrons. Consequently, several approximations are applied to allow for a solution with a reasonable computational effort.

Instead of simplifying equation (2-1) for the entire surface, a different approach is followed to solve the electronic scattering process at the basis of LEED. The starting point is the description of the sample as being built up of independent atoms, represented by spherical potentials specific to their element type, *i.e.* the materials related features of the valence electronic structure are neglected. This so called muffin-tin

approximation is schematically depicted in Figure 2.4. The shape of the potentials is determined by the atomic charges and their cut-off radius is chosen as half the distance between nearest neighbors. The “empty” space between the spheres is set to a constant potential background (muffin-tin constant), leading to the muffin-tin shape of the electron potential landscape. As shown in Figure 2.4, this potential landscape exhibits steps, *e.g.* between the vacuum and the surface, which have to be considered in the description of electron scattering.

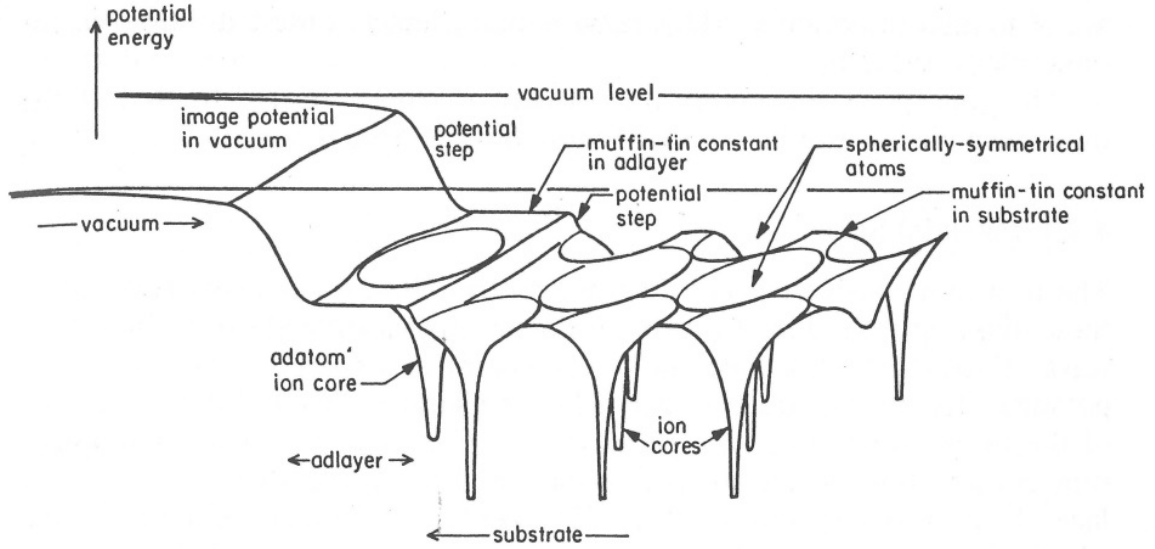


Figure 2.4 The muffin-tin approximation. The potential landscape of the sample is approximated as being built up of potential steps and spherical scattering potentials (muffin-tin potential landscape). (Image adapted from Ref. ³²)

The spherical potentials are defined by the charge of the atomic nuclei and the electronic charge distribution given the well-known atomic orbitals and their occupation. Once the scattering process is solved for such an element specific, spherical atomic potential, the atom can be treated as a point scatterer described by a phase shift and an angle-dependent scattering amplitude. This is a legitimate approximation outside the spherical potential which can be proven by scattering theory.³²

In order to solve equation (2-1) for a single spherical potential, the incoming electron plane wave is expanded in terms of spherical waves of angular momentum l . This allows for separating the above equation into a radial and an angular part, resulting in the following, one-dimensional Schrödinger equation for scattering on a spherical potential:

$$-\frac{\hbar^2}{2m}\left(\frac{1}{r^2}\right)\frac{d}{dr}\left(r^2\frac{dR_l(r)}{dr}\right) + \frac{\hbar^2 l(l+1)}{2mr^2}R_l(r) + \left(-\frac{Ze^2}{r} + V_{sc}(r) + V_{ex}(r)\right)R_l(r) = ER_l(r) \quad (2-2)$$

The solution of the scattering problem is given by the sum of an incoming plane wave and a set of outgoing spherical waves of different angular momentum l . Since the direction of the incoming wave breaks the spherical symmetry of the system, the outgoing spherical waves show a dependency on θ , the scattering angle, which is reflected in the complex scattering amplitude $f(\theta)$.

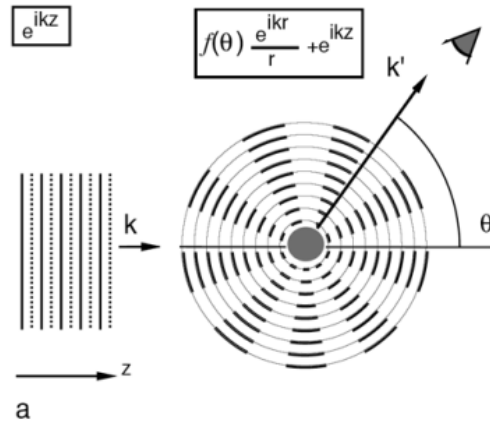


Figure 2.5 Plane wave scattering on a spherical potential. The outgoing wave is a superposition of the incoming plane wave and an angle-dependent spherical wave. (Image adapted from Ref. ³⁴)

Within this partial wave approach to elastic electron scattering, the influence of the spherical scattering potential, and thus of the atomic species, is completely described by the energy-dependent phase shifts δ_l between the incoming and the outgoing waves. The resulting wave functions are given by:

$$\begin{aligned}\Psi_l(r, \theta) &= e^{i\vec{k}\vec{r}} + f(\theta) \frac{e^{ikr}}{r} \\ f(\theta) &= -4\pi \sum_l (2l+1) t_l P_l(\cos \theta) \\ t_l &= -\frac{\hbar^2}{2m} \left(\frac{1}{k} \right) \sin \delta_l \exp(i\delta_l)\end{aligned}\tag{2-3}$$

In the scope of this thesis the Barbieri/Van Hove phase shift program was used for the computation of the phase shifts.³⁵ As described above, atomic orbitals are used and their electronic occupation is an input parameter to the program. In this way, a solution for each atomic species is determined individually. For the PdGa intermetallic compound, the bulk structure was input to compute the potential step to the vacuum (muffin-tin-zero) and the atomic (muffin-tin) radii, which were defined as the half of the nearest neighbor atomic distances (a test in which this parameter was varied showed that the influence of the muffin-tin radius on the overall LEED-I(V) results is small). The following peaks shifts were computed for the two atomic species:

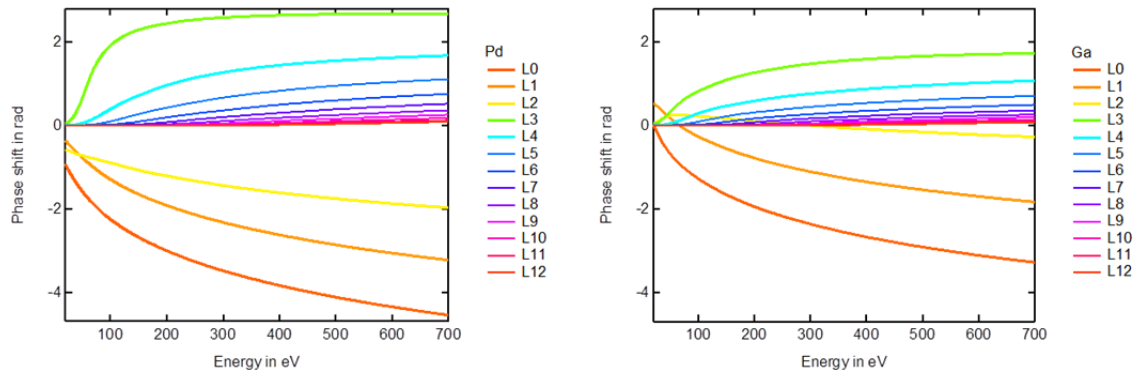


Figure 2.6 Energy-dependent phase shifts for electron scattering on Pd (left) and Ga (right) atomic cores in the PdGa compound, obtained by the program by Barbieri and Van Hove.

The comparison of the phase shifts in Figure 2.6 reveals that the average values for Pd are larger than those of Ga, which is reasonable, as electron and nuclei charges of Pd are larger than those of Ga. To visualize the scattering amplitudes of the two atomic species the values are applied in above equations to compute $f(\theta)$. Figure 2.7 displays $|f(\theta)|^2$ (i.e. the scattering probability) in a polar graph as a function of scattering angle θ for different incident electron energies.

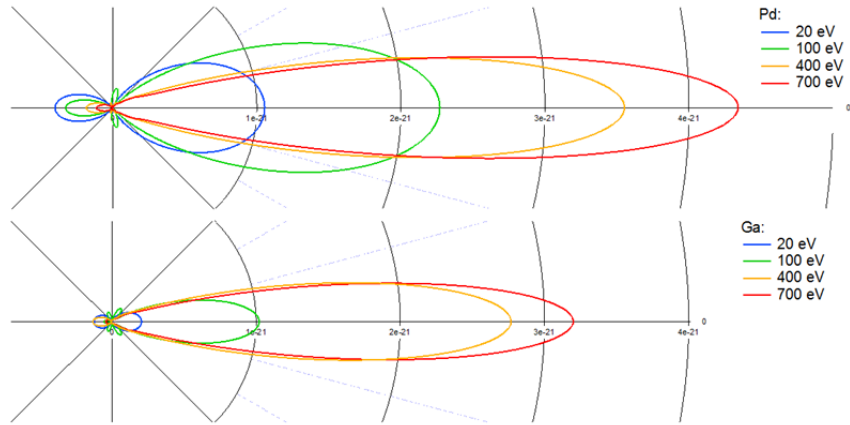


Figure 2.7 Angular distribution of the scattering amplitude $|f(\theta)|^2$ of a plane wave on the spherical potentials of the Pd and Ga atomic potentials with the incident electron direction from the left.

For all energies computed, the forward scattering of electrons is predominant, with increasing importance at higher energies. The larger scattering strength of Pd in comparison with Ga is observed in the scattering amplitudes.

The scattering on the isolated atomic potentials described so far is an essential ingredient to simulate the elastic scattering of LEED electrons from the whole surface. The next step is to assemble the spherical atomic potentials, which can now be approximated as point scatterers, to form the surface structure. This requires consideration of additional effects that are treated within the dynamical scattering theory as discussed in the next subchapter.

2.3.2 Kinematic and Dynamic Theory

Before discussing the scattering of LEED electron on a three-dimensional lattice of atomic potentials, the concept of the dynamic scattering theory is introduced, which is needed to describe LEED comprehensively. Single scattering phenomena and weak scattering interactions, as in X-ray or neutron diffraction, are well explained by the kinematic theory. In contrast, the scattering of an electron in a solid involves strong electronic interaction. Therefore, the “dynamic theory” extends the kinematic one by including multiple scattering effects. Multiple scattering can occur between the atoms of a structure, but also within single atomic potentials, causing large energy-dependent phase shifts. Indeed, this consequence of intra-atomic multiple scattering was already taken into account in Figure 2.6 for Pd and Ga. The second point is multiple scattering between different atoms of the surface, which requires a self-consistent treatment of a large number of possible scattering pathways within the surface. In this context, the term “self-consistent” refers to the requirement of current conservation of the scattering process, *i.e.* current of the incident electron beam equals the one of the sum of the outgoing, multiply scattered beams plus inelastic losses (discussed below). The consequence is a large increase of computational effort in comparison to simulations based on the kinematic theory. The simulation of the Bragg spot positions in the two-dimensional LEED pattern does not require information on the scattering potential, nor consideration of multiple scattering, and therefore can be achieved using purely kinematic theory. However, to describe electron energy dependence of the Bragg beam intensities, the quantitative, self-consistent approach has to be applied, yielding information on the near surface, three-dimensional and chemically resolved surface atomic structure.

The reason why multiple scattering has to be considered for electron scattering is the Coulomb interaction of the scattering electrons with the charges in the surface, namely electrons and ionic cores. This interaction between charged particles is much stronger than for example interactions of X-rays with Coulomb charges. Consequently, the probability of an incident electron undergoing a scattering event is much larger than for example for an incident photon, which is traveling the same distance within a solid. Accordingly, electrons/photons that have already scattered once are more/less likely to undergo a second scattering event on their way back to the detector. Therefore, all possible pathways involving the nearby atoms in the crystal have to be considered in the LEED simulation, including multiple forward and backward scatterings, with the different path lengths leading to different phases of the wave amplitudes.

Even though it seems like an overwhelming number of possible pathways has to be taken into account, one can make use of two circumstances, which reduce the computational effort. First, only those pathways have to be considered that fulfill the two-dimensional Bragg condition of the surface crystal structure, and thereby contribute to the coherent scattering. Second, very long scattering paths carry only very small wave amplitudes and thus don't need to be taken into account, as inelastic, *i.e.* incoherent, scattering events become more probable. This is reflected in the so-called “universal curve” of the electron inelastic mean free path as a function of energy, shown in Figure 2.8. This curve also represents the surface sensitivity of analysis methods based on elastically scattered electrons, and especially that of LEED, as typical LEED energies are of 50 - 500 eV. The minimum indicates that electrons with kinetic energies of 50 eV are most surface sensitive, while at larger LEED energies, electrons can penetrate deeper into, and out of, the surface, since the probability for an inelastic scattering event is smaller.

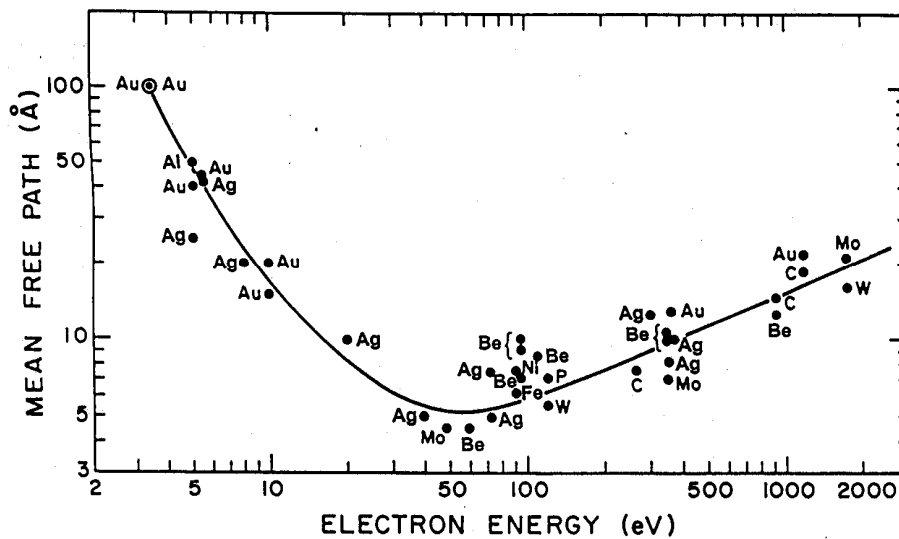


Figure 2.8 “Universal curve” for electron scattering, describing the electron mean free path in different solids as a function of kinetic electron energy. (Figure adapted from Ref. ³⁶)

In a LEED experiment, only the elastically scattered electrons are observed. Nevertheless, the loss of intensity through inelastic scattering events has to be considered in the simulation. This is obvious when looking at the energy spectrum of backscattered electrons from a surface under irradiation with a mono-energetic electron beam, shown in Figure 2.9. Indeed, only about 1 or 2 % of the incident electrons are backscattered elastically,³³ which explains the need for consideration of the inelastic events as a part of the quantitative self-consistent treatment of the scattering amplitudes.

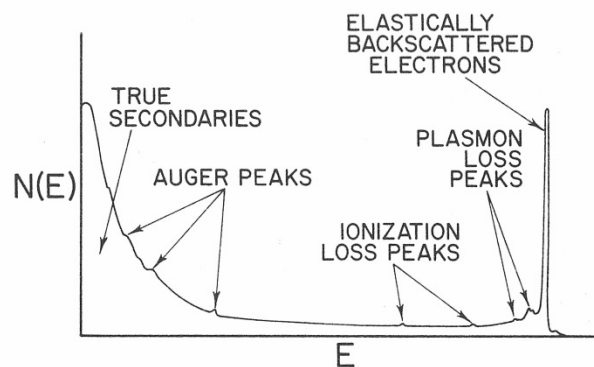


Figure 2.9 Schematic diagram of energy distribution of electrons backscattered from a solid. The sharp peak at the right contains the elastically scattered electrons. (Figure adapted from Ref. ³³)

In the frame of the computational simulation, this is taken care of by the definition of an imaginary part of the inner potential which is present between the atomic point scatterers. The consequence is an exponential decay of the wave amplitude with the propagation length in the solid. Scattering paths that carry amplitudes that are smaller than a certain threshold value are neglected.

Additionally to the effects discussed above, vibrations of the atomic positions due to temperature are taken into account in the dynamical LEED theory, as vibrations increase the incoherency of non-forward scattering events. A complete description of the theory can be found in Chapter 4 and 5 of Ref. ³² and in Ref ³³. After this short description of the most important aspects of the dynamical approach to LEED, their technical realization is summarized in the following chapter.

2.3.3 Electron scattering on the crystal lattice

The inclusion of multiple scattering is performed on various levels in a LEED calculation. In Chapter 2.3.1, we discussed the energy-dependent phase shifts which incorporate multiple scattering within the atomic spherical potentials. To treat interatomic multiple scattering, the structure is separated into different composite layers parallel to the surface. A composite layer, in turn can contain several atomic planes, while each plane contains one atom of the surface unit cell. The program that was used here for the dynamical simulation of the LEED curves is the “symmetrized automated tensor LEED”, or SATLEED, program by Barbi-eri and Van Hove.³⁵

When an electron wave is incident on the first composite layer, it is treated as a plane wave that is scattered into spherical waves at the atoms of the crystal. The incident electron energy and the phase shifts (Figure 2.6), characteristic for the scattering atoms, define the angular dependence (Figure 2.7) of the waves that are emerging from each scatterer. Subsequently, these spherical waves will propagate to all other atoms in the composite layer and perform additional scattering events. Following this procedure, all possible scattering pathways over multiple scattering events are taken into account. The self-consistency is preserved through the quantitative treatment of the scattering amplitudes between all scatterers. Inelastic effects are treated as wave attenuation as a function of wave propagation length. Mathematically, this self-consistency is described in a matrix notation, resulting in a layer diffraction matrix for each composite layer. By stacking these layers parallel to the surface plane, the complete surface structure is simulated. Wave propagation in between the composite layers is treated in the plane wave representation. In practice, only the amplitudes of the Bragg beams corresponding to the in-plane lattice structure of the layer are transmitted from one composite layer to the next. Ultimately, the intensities of the recorded Bragg beams are computed for the stack of layer diffraction matrices, and for each incident electron energy. The next step is to compare the computed intensity vs. energy profiles, or I(V) profiles, with experimentally measured ones and determine the precise atomic structure.

2.3.4 Iterative structure refinement by Tensor LEED

As the diffraction is very sensitive to the surface structure geometry, small deviations in the atomic coordinates may cause a disagreement in the comparison of the computed beam intensities with experiment. This means, one would have to compute the spot intensities for a large range of structure parameters, which is a rather large computational effort as soon as the coordinates of a few atoms should be optimized. Alternatively, a perturbation theory based approach can be followed, which allows for a more efficient search for the optimized structure model.

In order to allow reasonably fast optimization of the structure coordinates, the Tensor – LEED method is applied.³⁷ Based on the wave-field that was computed by dynamical means for an initial guess of the atomic

structure, the weak modification of this wave-field caused by a small displacement of the atoms is considered as a first order perturbation. To this end, the derivatives of the diffraction amplitudes with respect to the atomic positions are computed and stored in a tensor file. From this starting point, trial structures are produced by displacing the atoms in the structure slightly (up to ± 0.4 Å) which results in a modification of the simulated Bragg beam intensities. From comparison to experiment, the new agreement is evaluated. In an automated fashion, a multi-dimensional search is performed, using search-algorithms to optimize the agreement between simulation and experiment by changing the atomic coordinates slightly. A detailed discussion of the Tensor – LEED method is given in Ref. ³⁸.

The agreement between the computed and the measured Bragg beam intensities, or $I(V)$ curves, is expressed by terms of reliability, or R -, factors. For LEED- $I(V)$, the R -factor introduced by Pendry³⁹ (R_p) is used in the structure refinement carried out in this work. The comparison of experimental data and simulation is expressed in a single value of R_p , which is computed as the sum of the differences in the logarithmic derivatives of the computed and measured $I(V)$ profiles over all energy values. In this way, the R_p is sensitive to peak positions (in energy) rather than absolute peak heights.

2.3.5 The application of LEED- $I(V)$ to the intermetallic compound PdGa

The automated structure refinement-algorithms and the application of Tensor LEED enabled surface scientists to determine a broad range of surface structures. Indeed, LEED- $I(V)$ was the method used to determine the majority of the atomic surface structures known today.⁴⁰⁻⁴¹ The first LEED- $I(V)$ structure determinations were those of low-Miller-indexed pure metal single crystals and due to the purely metallic binding within those samples, the muffin-tin potential approximation discussed above is perfectly suited to describe the surface. For covalently bonded materials, the validity of this approximation might be more questionable, as directional bonds might lead to non-spherical charge distributions around the ion cores. Surprisingly, the spherical potential approximation yields acceptable agreement also for the determination of oxide structures and covalent molecular adsorbates.⁴²⁻⁴³ Even though the R -factors for pure materials are generally lower than those of partially covalent compounds, the latter still allows for an identification of the best fit structure from a set of model structures, which is the approach that is applied in the case of PdGa within the scope of this study.

2.4 Scanning tunneling microscopy

Scanning tunneling microscopy (STM) is part of the broader field of scanning probe techniques which allows for real space topographic imaging down to the atomic length scale. Due to its ability to resolve single molecules and atoms on surfaces, it has evolved to one of the major tools of modern surface science. STM is based on the quantum-mechanical tunneling effect between a small conductive tip that is brought in close

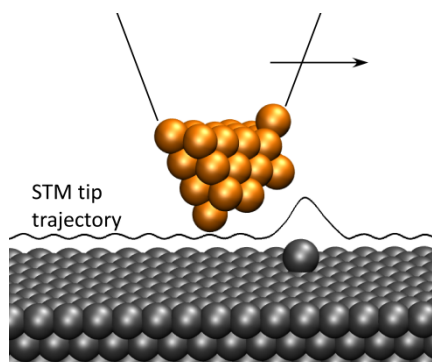


Figure 2.10 Working principle of an STM. The tip trajectory for a constant tunnel current yields a profile line of constant electronic density.

distance to a conductive sample.⁴⁴ If a voltage is applied between the two components, quantum tunneling allows for an electric current across this tunnel gap, while the magnitude of the current is strongly dependent on the width of this gap and therefore the spacing between tip and sample. By moving the tip parallel to the surface plane, and keeping the tunnel current constant through a regulation of the height of the tip above the sample, a profile line of the surface topography is obtained, as shown in Figure 2.10. Likewise, scanning a two-dimensional area yields a topographic image of a surface. In fact, the “topography” of the sample in terms of atomic positions is not directly probed, but the measured data represents in first approximation a surface of constant electronic density which depends on the applied tunnel voltage (cf. right panel in Figure 2.11). More details on the theory of STM and the experimental setup are given in the next subchapters.

After its invention in 1982 by Binnig and Rohrer at the IBM Lab in Rüschlikon⁴⁵, STM has experienced an enormous growth in terms of installed instrumentation and application range. Starting with the first images of the atomically resolved Si(111) 7x7 reconstruction⁴⁶ (cf. left panel in Figure 2.11), latest developments allow to visualize the precise shape of molecular orbitals on surfaces.⁴⁷

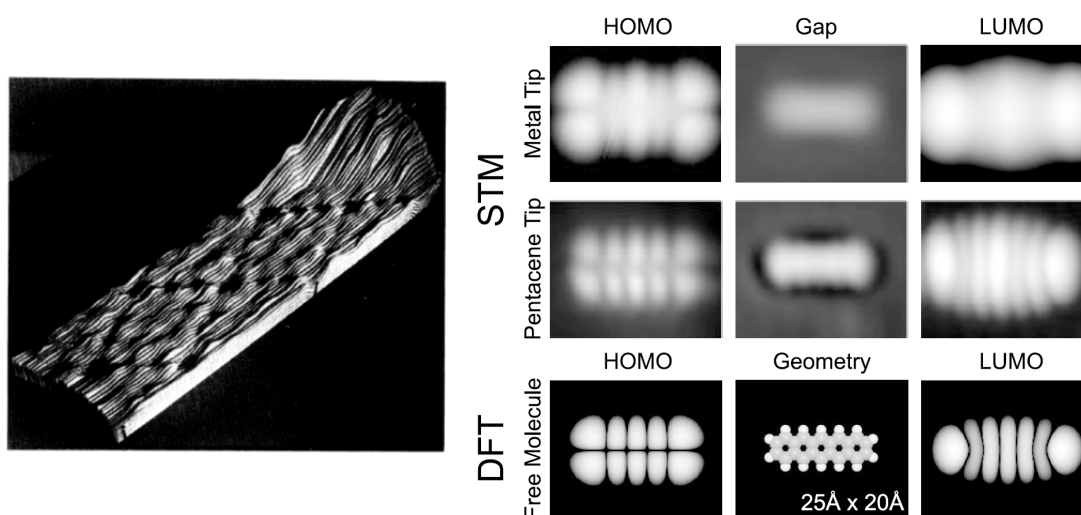


Figure 2.11 The evolution of STM in the last decades. Left: First STM images of the Si 7x7 reconstruction from 1982 by Binnig and Rohrer. (Figure adapted from Ref. ⁴⁶) The cardboard model visualizes an area of about 10x4 nm in size. Right: HOMO and LUMO orbitals of pentacene adsorbed on a non-conductive surface, imaged by STM in 2005. Nodes and maxima of the different molecular orbitals are visible in the STM topography. The size of the images are 2.5 x 2.0 nm, yielding sub-nm lateral resolution. (Figure adapted from Ref. ⁴⁸)

2.4.1 The theory of STM

The theoretical concept behind STM is visualized in Figure 2.12. A DC bias voltage V_T is applied between tip and sample which are made of conductive materials. If the distance d is small enough, electrons can tunnel across the vacuum. It is important to distinguish between the regimes of quantum tunneling and field emission.

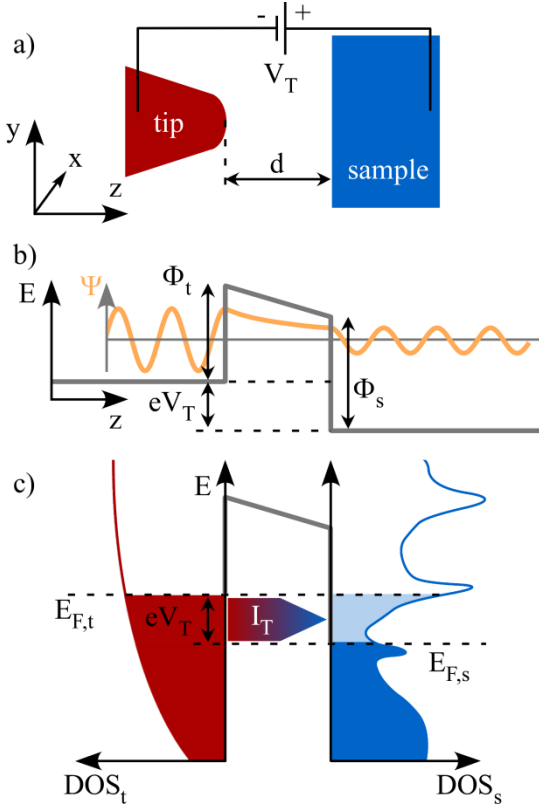


Figure 2.12 Principle of tip-sample tunneling.

a) Schematic view of the STM. A tunnel voltage V_T is applied between a metallic tip and the sample which are separated by a distance d ($\approx 0.5 - 10$ Å). b) The electron wave functions (yellow) decay exponentially over the tunnel barrier. The barrier shape is defined by the workfunctions of tip and sample materials, the tunnel voltage, and the distance d . c) Diagram of the tip and sample DOS when a bias voltage is applied.

In the latter case, a much higher voltage is applied and electrons can overcome the workfunction of the material, leading to an emission current of free- electrons traveling through the vacuum. In the case of quantum tunneling, the applied voltage does not suffice to overcome the workfunction of the material, but the small distance leads to an overlap of the atomic orbitals of tip and sample. In a simplified, one-dimensional picture, quantum tunneling can be understood through the decay of the electron wave function amplitude within the potential barrier of the vacuum gap, as shown in Figure 2.12 b). The non-zero amplitude at the right end of the barriers gives rise to a coupling of the tip electronic state to the counter electrode, and thus a probability of tunneling through the gap. The trapezoidal shape and height of the potential barrier $\phi(z)$ are defined by the workfunctions of the tip Φ_t and the sample Φ_s and by the applied tunnel voltage V_T .⁴⁹ In the solution of the Schrödinger equation for tunneling through a one-dimensional barrier, the resulting tunnel current I_T is exponentially dependent on the tip-sample separation:

$$I_T(d) \propto \exp(-2\kappa d)$$

$$\kappa = \sqrt{\frac{2m\phi}{\hbar^2}}; \quad \phi = \frac{\Phi_t + \Phi_s - eV_T}{2} \quad (2-4)$$

where m is the electron mass and \hbar the reduced Planks constant. Here, ϕ is approximated as the average barrier height.⁴⁹ This exponential relation allows a very precise measurement of variations in the tip-sample distance d by monitoring the tunnel current I_T .

Additionally to the tip-sample separation, the electronic structure has a major influence on the tunnel current. A scheme of the energetic levels and the density of states (DOS) in STM is shown in Figure 2.12 c). Due to the applied tunnel voltage, the Fermi levels of tip and sample are energetically offset by eV_T with respect to each other. In the case of positive sample voltage shown in the Figure, electrons from the occupied states of the tip tunnel into the unoccupied states of the sample. Consequently, electronic states of the tip in the range of $E_{F,t}$ to $E_{F,t} - eV_T$, and those of the sample in the range of $E_{F,s}$ to $E_{F,s} + eV_T$ contribute to the tunnel current. In fact the current I_T is a convolution of the density of states of tip and sample, as described by Bardeen's theory for tunnel between two planar electrodes (see equation (2-5)).⁵⁰⁻⁵¹

$$I_T \propto \int_{-\infty}^{\infty} DOS_s(\varepsilon + eV_T) \cdot DOS_T(\varepsilon) |M(\varepsilon)|^2 [f(\varepsilon) - f(\varepsilon - eV_T)] d\varepsilon \quad (2-5)$$

$$M_{nm} = \int \Psi_0^* H_{nm} \Psi_{nm} dz \quad (2-6)$$

$$f(\varepsilon) = \frac{1}{(1 + \exp(\varepsilon / (k_b T)))} \quad (2-7)$$

The transition matrix element M_{nm} describes the probability of an electron in the state n of the tip, to tunnel into state m of the sample, while H_{nm} is the transfer Hamiltonian and $f(\varepsilon)$ the Fermi distribution. Ψ_0 and Ψ_{nm} are the initial and final wave functions of the entire system, respectively, differing by the one electron which is transferred from tip to sample (or vice-versa). The spatial integration in the matrix element (equation (2-6)), incorporates the exponential dependence of the tunnel current on the tip-sample separation (cf. equation (2-4)). In most cases of STM and particularly scanning tunneling spectroscopy, a close to constant DOS of the tip is preferred, in order to minimize the influence of the tip states on the tunnel current.

Based on Bardeen's formalism of 1961, Tersoff and Hamann refined the theory towards the application of STM by modeling the tip as an s-orbital of a single atom, leading to the current dependence shown in equation (2-8).⁵²

$$I_T \propto V_T DOS_t(E_F) R^2 \exp(2\kappa R) \sum_m |\varphi_m(\vec{r}_0)|^2 \delta(E_m - E_F) \quad (2-8)$$

where R and \vec{r}_0 denotes the radius and the center of curvature of the tip and the sum is over all states m of the sample, with wave functions φ_m , that are in the range of the delta function. This result is obtained by substituting the s-type wave function of the tip into equation (2-6) and evaluating equation (2-5) for states near the Fermi level. This limits the validity of Equation (2-8) to small tunnel voltages $V_T \ll \phi$. The exponential decay of the tunnel current with tip-sample separation d that holds for the one-dimensional case in (2-4) is preserved in (2-8), since the sample wave function is evaluated at the tip position \vec{r}_0 and thus $|\varphi_m(\vec{r}_0)|^2 \propto \exp[-2\kappa(R+d)]$. Equation (2-8) is the basis of most STM simulations based on density functional theory (DFT).

2.4.2 The main components of an STM setup

The main components of an STM experimental setup are shown in Figure 2.13. The high resolution of STM is based on the ability to control the lateral position of the tip (or sample) in the pm range. While in early STM setups three separate piezos for x,y and z motion were applied, respectively, more recent STM designs use single piezo tube scanners for positioning.

To avoid electronic noise, the tunnel current is pre-amplified close to the sample-scanner assembly, and after that input to the scan control electronics. Typical tunnel current values are in the range of a few pA to a few hundred nA, while gap voltages of a few mV to V are used. The choice of the optimal current and gap voltage depends strongly on the stability of the sample and the tip, as adsorbates might move or degrade under the influence of high tunnel currents. On the other hand, if a clean substrate is imaged, high tunnel currents are useful to decrease the tip-sample separation and achieve high resolution.

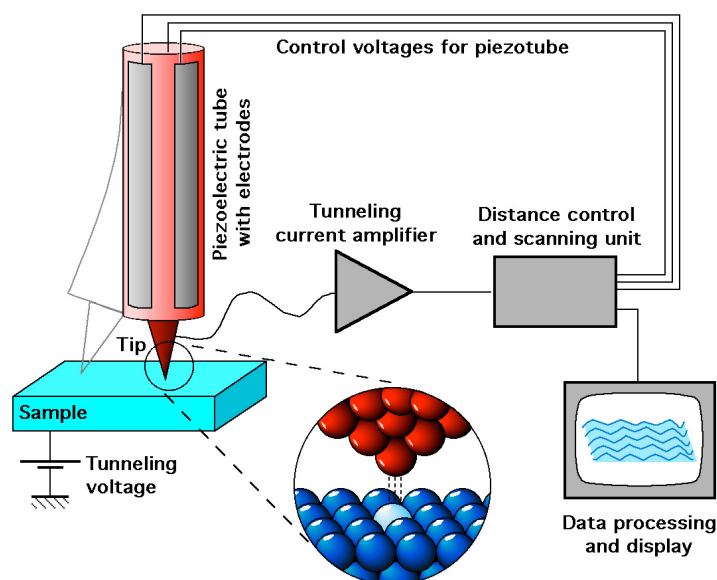


Figure 2.13 Main components of an STM setup. (figure by Michael Schmid, TU Wien)

As discussed above, the exponential dependency of the tunnel current I_T on the tip sample separation allows for a very precise measurement of height variations. The accuracy of this measurement however critically depends on the positional stability of the system with regard to mechanical vibrations and drift, as well as the reduction of electronic noise. Accordingly, the improvements in resolution and stability which took place over the last 30 years are mainly due to the sophistication of both electronic and mechanical damping systems.

The mechanical stability is especially important if the instrument is to be used at reduced temperatures. Due to thermal expansion, the design of a combined cryostat and STM experiment has to be in a way to minimize deformations of the tip-sample positioning which would lead to an enduring distortion of the recorded images, also known as “thermal drift”. A good thermal, i.e. mechanical, contact of the STM stage with the cryostat is needed, which is a problem as vibration would couple to the tunnel gap. In modern designs, this problem is solved by pressing the STM stage to the bottom of a cryostat during cool-down, and releasing it into a suspended position for measurement. In the suspended position, vibrations are inhibited by springs and eddy current damping, while cooling is provided only from a bunched wire connection to the cryostat. It is necessary to shield the suspended parts from thermal radiation, to maintain the low tempera-

ture. Measurements in this thesis were performed using variable temperature (VT-) and low temperature (LT-) STM by Omicron (<http://www.omicron.de>).

The most commonly applied operational mode in STM is the constant-current mode, where the user defines the tunnel current as the set-point to a feedback loop, which regulates the z-piezo voltage and consequently the separation of tip and sample to stabilize the tunnel current. By recording the regulated tip height z as a function of the lateral position, an iso-surface of the electronic density is measured, which is then processed and displayed. Data processing and analysis was performed using the `matrixfilereader` package by Thomas Braun (<http://www.byte-physics.de>), and several home-made procedures based on Wavemetrics Igor Pro.

2.5 Infrared Spectroscopy

A powerful technique to study the state of an adsorbate bound to a surface comprises the analysis of its vibrational modes. The most important property in this context is the vibrational frequency, or vibrational energy, as it provides information on the strength of a certain bond within an adsorbed molecule associated with the vibrational mode considered. A free di-atomic molecule can be approximated as a spring connecting two masses, yielding a harmonic oscillator with a defined vibrational eigenfrequency corresponding to its normal mode. This frequency depends on the two masses and the spring constant. In the molecular picture, the spring constant is defined by the bond strength between the two atoms. For an adsorbed molecule, (at least) one of the atoms forms a bond with the surface, which, in the case of a chemisorption type of situation, leads to a significant mixing of the molecular- with the surface electronic states.⁵³⁻⁵⁴ Within this adsorption process, the di-atomic bond within the molecule is altered and consequently also the vibrational frequency of the oscillator which is accessible experimentally. The assignment of a measured vibrational mode frequency to a specific binding configuration is not trivial and is best performed through comparison to experimental reference data of the adsorbate in the gas phase and adsorbed on a comparable surface, or *ab-initio* simulation of the adsorbate configuration and the bond strength.

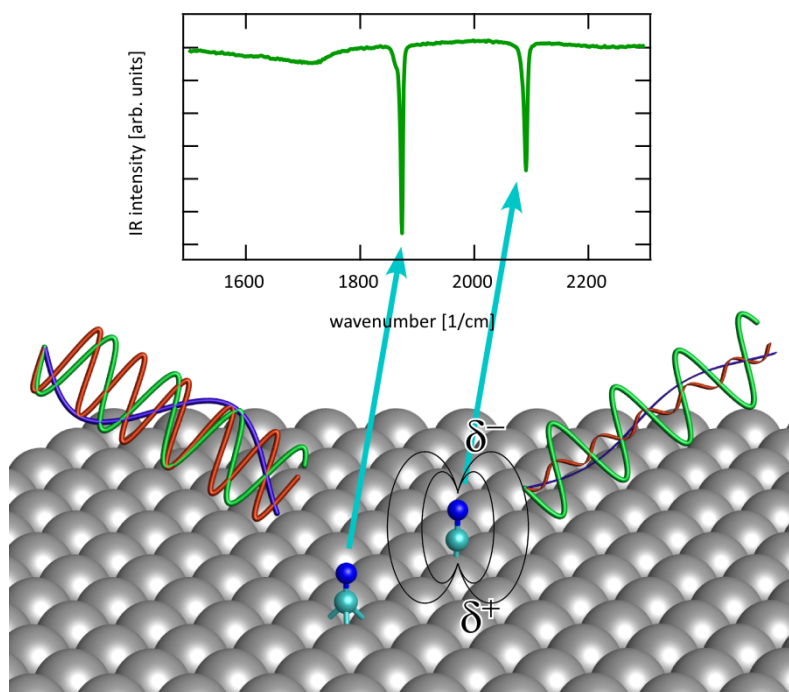


Figure 2.14 Experimental principle of RAIRS. Molecular dipoles adsorb specific wavelengths of IR light (incident from the left in the graphics). The outgoing spectrum exhibits sharp peaks at energies that correspond to the vibrational modes of molecule. These depend, for instance, on the adsorption site, as shown in the example for hollow and on-top sites.

A well-suited technique to measure vibrational modes of adsorbed molecules is the absorption of infrared (IR) radiation as a function of wavelength. As IR frequencies are in the range of typical vibrational mode frequencies, the photons interact with, or excite vibrations in free or adsorbed molecules, leading to sharp absorption peaks for IR light passing through a sample. However, the molecule requires a non-zero electric dipole moment that is coupled to the vibration, to be able to absorb electromagnetic radiation, and be “IR-

active". In the case of IR spectroscopy on single crystal surfaces (see Figure 2.14), the IR light is reflected from the adsorbate covered surface with low incident angle, which is known as Reflection Absorption Infrared Spectroscopy (RAIRS). If weakly absorbing, sub-monolayer coverages are investigated, a reference spectrum of the clean surface is required for background subtraction.

An enormous improvement in the detection of the outgoing IR light spectra has been achieved by the implementation of an interferometric analysis technique. To detect the intensity as a function of wavelength, the incident beam is split in two, and for one of the two branches the beam path length is modulated by a movable mirror. The principle of the setup is very similar to that of the Michelson Interferometer and a schematic diagram is shown in Figure 2.15.

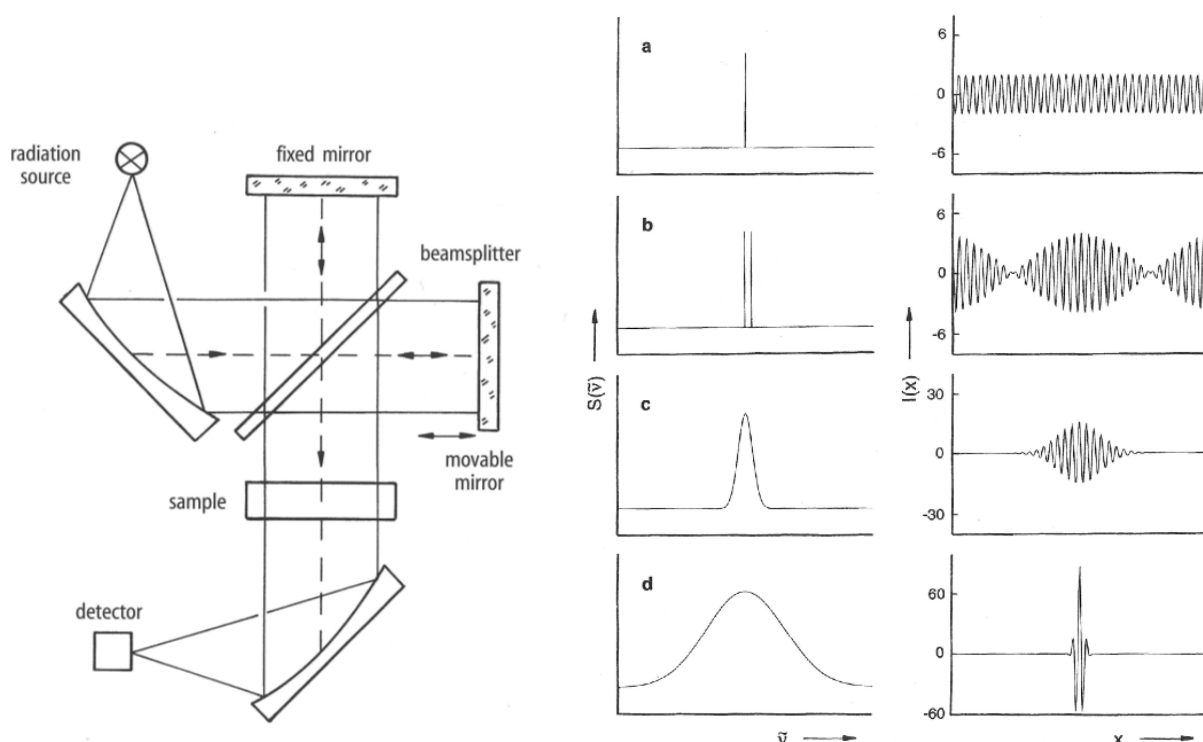


Figure 2.15 Working principle of a Fourier transform spectrometer. Left: Schematic view of the setup. The intensity at the detector is a function of the pathlength difference, i.e. of the position (x) of the movable mirror. Right: Interferograms ($I(x)$) and Spectra $S(\tilde{\nu})$ for different spectral distributions: from a) monochromatic light (laser), to d) broad wavelength distribution (FTIR experiment). (Figures adapted from Ref. ⁵⁵)

After recombining the two beams of different paths they interfere at the detector. The measured total intensity is recorded as a function of the displacement of the movable mirror x , which generates a path length difference and consequently a phaseshift between the two beams. In this way an interferogram $I(x)$ is recorded and examples for different cases are given in the right panel of Figure 2.15. The case d) is closest to the experimental case of FTIR, where a broad wavelength distribution is used. Evidently, a precise determination of the path length difference x is vital to a high precision measurement. To this aim, a monochromatic laser beam is guided in parallel to the broadband IR radiation and a second interferogram is recorded simultaneously as reference, yielding a sine signal as function of x (see case "a" in Figure 2.15) with a periodicity of the well-known laser wavelength. The zero-crossings of this laser interferogram are used as sampling points for the IR interferogram, allowing for a recording at equidistant points of path length dif-

ference. In this way, more accurate spectra with better signal-to-noise ratios are obtained compared to the formerly applied dispersive spectrometers.

The computed Fourier transformation of this interferogram yields the intensity as a function of reciprocal path length and therefore photon energy, usually expressed in units of $\text{cm}^{-1} = 0.12398 \text{ meV}$, which is the intensity vs. wavenumber spectrum. A more detailed description of the mathematical transformation is given in Ref. ⁵⁶. As the computational effort involved in the Fourier transformation is easily accomplished by modern personal computers, FTIR has developed the most applied technique for infrared spectroscopy.

Within the present PhD thesis, FTIR was used to study the different binding sites on PdGa surfaces by analyzing the vibrational modes of carbon monoxide adsorbates. As CO is a commonly applied test molecule a large dataset for comparison of vibrational mode frequencies is provided by literature.

2.6 Temperature-programmed Desorption

Temperature-programmed desorption (TPD), is an experimental technique to study desorption processes of adsorbates (molecules or adatoms). After UHV preparation of the sample surface, the adsorbate is dosed at low temperatures, to achieve a desired coverage and the sample is subsequently heated with a well-defined heating rate. While the sample temperature is increased, the desorbed molecules or atoms are most commonly detected with a quadrupole mass spectrometer (QMS), where the partial pressures for one, or several characteristic masses are monitored as a function of sample temperature. The desorption rate ($d\sigma/dt$) vs. temperature (T) graph allows insight into the binding energy of the desorbed species and the kinetics of the desorption process by analysis of desorption peak position and shape, respectively.

The basis of all analysis methods for the study of desorption experiments is the Polanyi-Wigner equation⁵⁷,

$$-\frac{d\sigma}{dt} = \nu(\sigma, T) \sigma^n \exp(-E(\sigma, T)/k_B T) \quad (2-9)$$

where ν is the rate constant, or "attempt frequency", σ is the coverage, E is the binding energy of the adsorbate, and n the order of the desorption process. Zero order desorption yields coverage independent rates of desorption and can be used to describe evaporation of substrate material. First order desorption implies desorption of the adsorbates directly from their preferred binding sites on the surface. A second order desorption process is a two-step process, involving for example a recombination of two atoms into a di-atomic molecule before desorption, for instance for O_2 on Pd(100).⁵⁸

For the analysis of the CO desorption data presented in this work, several data analysis methods were tested. Due to the low signal to noise ratio of the desorption curves, advanced analysis methods⁵⁹⁻⁶⁰ were not applicable to the data and a simple desorption simulation by kinetic Monte-Carlo methods yields good results through comparison of experimental and simulated desorption peaks. These simulations are based on the Boltzmann factor for overcoming an energy barrier as a function of temperature and binding energy. The probability per simulation time-, respectively temperature step, for a desorption event then reads in the Monte-Carlo computation:

$$P = \nu_0 N \exp(-E/k_B T), \quad (2-10)$$

where N is the total number of simulated adsorbates ($N \geq 10^5$). The resulting simulated desorption curves are equivalent to those simulated using the well-known Redhead theory.⁶¹ For the determination of the desorption parameters, binding energy and desorption frequency were fitted to match the measured peak shape and position. A frequent controversial point in desorption simulations is the attempt frequency, which is commonly assumed to be on the order of $\nu_0 = 10^{13}$ Hz. However, in particular for CO, very different, and strongly coverage-dependent values are reported for desorption from different transition metal surfaces ranging from 10^6 to 10^{19} Hz. (See Ref. ⁶² and references therein). Even though advanced methods allow for determination of this pre-factor, quality and quantity of the data presented here does not suffice to allow for this analysis. Instead, we compare the data of different samples and molecular coverages to determine relative adsorption energies and orders of desorption.

To increase the accuracy of the TPD experiments conducted within this study, an appropriate heating setup was installed and thoroughly calibrated. A specially designed sample holder was used, in which the single crystal sample is held only by the heating wires, as shown in Figure 2.16. This design allows fast heating ramps and reduced temperature gradients on the sample surface. The temperature is monitored using a type K thermocouple, which is pressed to the back of the sample by a ceramic piece. A thin wire diameter was chosen for the thermocouple such that it adds little thermal mass to the system, and excessive cooling through the wires is suppressed. Since the heat source is closer to the sample surface than to the thermocouple and the ceramic piece is not heated, one can expect a lower temperature reading with respect to the real temperature of the surface. To quantify the offset, calibration measurements of CO desorption from Cu(111) were conducted. The curves in the top of Figure 2.16 show the CO desorption signal from Cu(111), obtained in the employed setup, in comparison to literature data⁶³. The calibration curve reproduces the characteristic shape and desorption temperatures reported in literature.

For the detection of desorbing molecules, the sample was placed in close proximity (1-2 cm) of the QMS (Hiden, HAL 511/3F) with the surface normal pointing towards its opening aperture. As no shielding of the heating wires or sample holder was available, CO desorption from metallic parts, touching the heating wires, and from the heating wires themselves, can contribute to the detected signal. This may result in an increased background, or smeared-out peaks. To detect CO molecules with a large temporal- (and thereby thermal-) resolution, the signal for mass 28 was measured, exclusively.

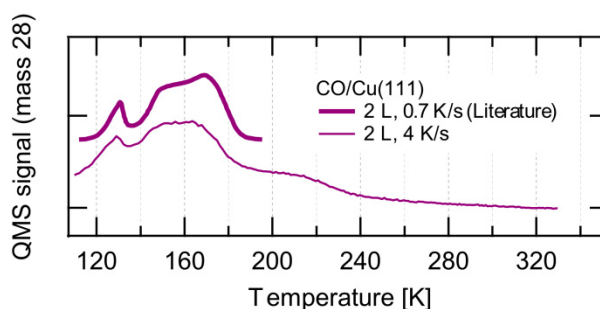
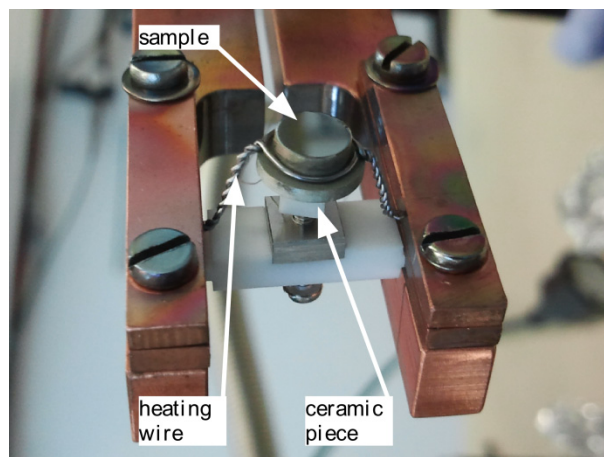


Figure 2.16 Photo of the TPD sample holder and calibration curves using CO/Cu(111).

The sample is contacted only the heating wires, such that there is no heat sink during a temperature ramp, except for the small thermocouple which is pushed to the sample from the bottom. Calibration using CO desorption from Cu(111) yields agreement with literature data.⁶³

2.7 X-ray Photoelectron Spectroscopy

X-ray photoelectron spectroscopy is one of the most frequently used methods for chemical surface characterization, yielding information on the electronic structure, elemental composition and chemical state of near surface atoms. The technique, also known as “electron spectroscopy for chemical analysis” (ESCA), is based on the photoelectric effect, which describes electron emission from a sample upon illumination with high energy photons. The possibility to selectively detect emitted photoelectrons according to their kinetic energy allows for recording of emission spectra as a function of electron binding energy, if the photon energy ($h\nu$) is known. The energy resolution of the method depends on the analyzer resolving power and most importantly on the energy spread of the excitation photon source. For laboratory use the characteristic x-ray emission lines of specific elements Al- K_α or Mg- K_α , are used for this purpose. By using Bragg crystal monochromators the line width of such characteristic emission lines can be significantly reduced. X-rays of high brilliance, low energy spread and variable energy can be produced at synchrotron facilities.

The photoelectron kinetic energy (KE) is related to the binding energy of the electron (E_B) through the Einstein equation for the emission of photoelectrons:

$$E_B^F = h\nu - KE - \phi \quad (2-11)$$

The Einstein relation holds true for the full path of the electron from the sample surface to the electron counting detector, if ϕ is viewed as the vacuum potential at the position where the kinetic energy is considered. As the kinetic energy is measured in the analyzer, the correct workfunction to be introduced in the Einstein equation is the analyzer work function ϕ_{sp} , which might be different from the one of the sample. A diagram of the different energy levels is shown in Figure 2.17. As sample and analyzer are in electrical contact, their Fermi levels are aligned. The measured kinetic energy and the binding energy of the sample electrons are connected through the adapted Einstein equation⁶⁴ (2-12).

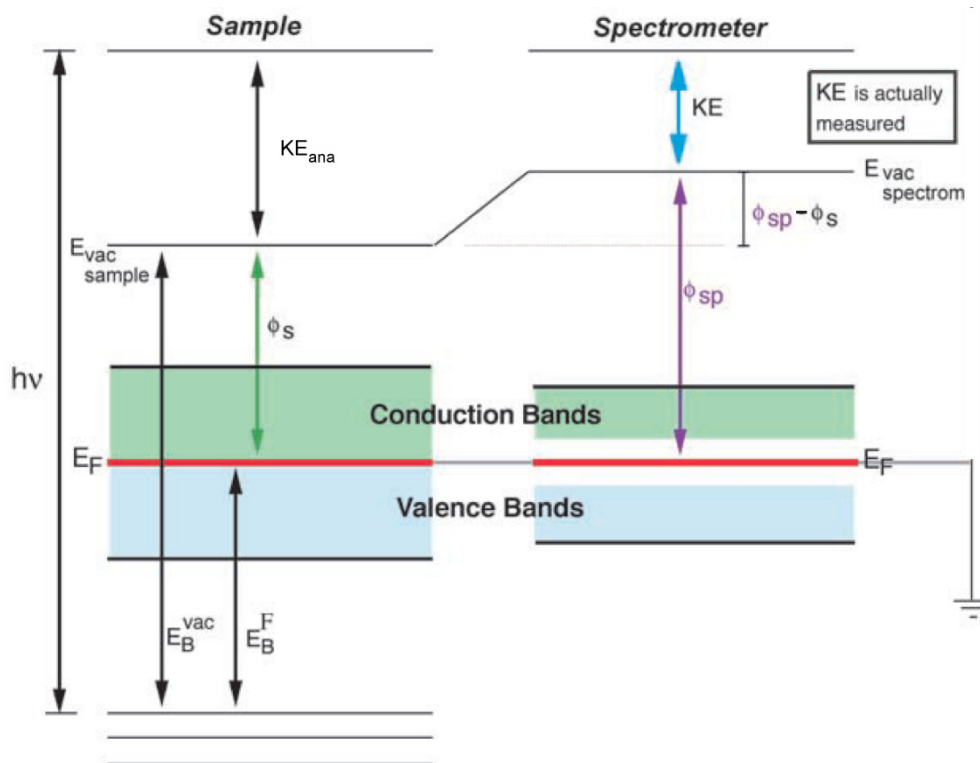


Figure 2.17 Energy level in the XPS experiment for conductive samples. The Fermi levels of sample and analyzer are aligned. To determine the electron binding energy with respect to the Fermi level, the work function of the analyzer has to be taken into account. (Figure adapted and modified from Ref. ⁶⁴)

$$KE_{ana} = h\nu - E_B^F - \phi_s ; \quad KE = KE_{ana} - (\phi_{sp} - \phi_s) \quad (2-12)$$

$$E_B^F = h\nu - KE - \phi_{sp}$$

For the experiments presented in this work, a monochromatized Al K_{α} X-ray source was used for excitation and a VG Scienta Analyzer R3000 with a 2D detector was applied in sweep mode. XPS was used to determine the shifts of atomic core level energies upon molecule deposition on PdGa surfaces. Primarily, carbon C1s peaks are analyzed to study the amount of adsorbed carbon and the bond of the molecule to the surface. To ensure temperature stability during molecule deposition, samples were cooled for 1h using liquid nitrogen before deposition. XPS measurements were started on the clean sample and C_2H_x was then exposed by backfilling of the chamber to a defined pressure and time (differences in hydrocarbon ionizability for pressure determination were neglected).

The Wavemetrics Igor Pro routines provided by the manufacturer were used for data processing and display. For peak fitting and quantitative spectra evaluation CasaXPS was employed. C1s peak shapes were fitted using Gaussian-Lorentzian (50:50) peak shapes with asymmetric tail function (T0.9).

Chapter 3 Structure determination of inter-metallic PdGa single crystal surfaces

The pivotal step in the study of model catalyst systems is to develop a detailed knowledge of the structural properties of the catalyst and the catalyst's surface. In the present case, this knowledge includes surface chemical composition and morphology on the atomic length scale. This detailed structural information enables the correct interpretation of experimental results on adsorption sites and molecular binding configurations, from which in turn a deeper understanding of the interactions between the surface and the reactants can be obtained. Furthermore, the knowledge of the precise atomic surface structure opens the door to treat the model catalyst system by means of *ab-initio* calculations and study physical properties and reaction pathways.

This chapter begins with the structure determination of the threefold PdGa surface, which was published as a "Communication" in the journal *Angewandte Chemie-International Edition* (Chapter 3.1). Thereafter, investigations on the (110), (210) and (100) PdGa surface structures are presented (Chapter 3.2), while a comparative summary is given for the five investigated structures in the last part of the chapter (Chapter 3.3).

3.1 Publication: "Isolated Pd Sites on the Intermetallic PdGa(111) and PdGa (-1-1-1) Model Catalyst Surfaces" in *Angewandte Chemie - International Edition*

(Article reprinted with permission. Copyright © 2012 WILEY-VCH Verlag GmbH & Co. KGaA, Weinheim)

Isolated Pd Sites on the Intermetallic PdGa(111) and PdGa($\bar{1}\bar{1}\bar{1}$) Model Catalyst Surfaces**

Jan Prinz, Roberto Gaspari, Carlo A. Pignedoli, Jochen Vogt, Peter Gille, Marc Armbrüster, Harald Brune, Oliver Gröning, Daniele Passerone, and Roland Widmer*

Catalytic reactions are of highest technological and economic importance, especially in the field of chemical synthesis and exhaust gas treatment.^[1] About 80% of the reactions in chemical industry rely on catalysts, thus giving motivation for research in this area.^[2,3] There has been enormous progress in heterogeneous catalysis through the understanding of reaction mechanisms and the relation of catalyst surface structures to the reaction rate and selectivity.^[3–7] A major step forward has been achieved by comparing single-crystal model catalysts to real catalysts and by combining the ultrahigh-vacuum (UHV) surface-science approach with high-pressure studies of the reaction kinetics.^[2–4] This development has led to a paradigm shift in catalyst development.^[8]

Amongst the most ingenious and innovative catalyst materials are intermetallic compounds (IMCs) as they enable spatial separation of the catalytically active sites^[9] and thus the achievement of both high activity and selectivity.^[10] Additionally, it is also possible to tune the electronic properties of IMCs by changing their chemical composition. Recent results revealed that this new class of catalytic materials might be of industrial relevance, and outperform known catalysts, especially when highly selective processes are demanded.^[11]

PdGa IMCs have shown remarkable catalytic properties for an important reaction in polyethylene production, namely the partial hydrogenation of acetylene to ethylene.^[11,13–15] However, the reaction pathway is largely unknown. We address this question on single-crystal IMC PdGa model systems.^[4] Their bulk crystal and electronic structure have been reported earlier.^[11–14,16–18] Herein, we determine and explore the stable surface terminations because they define the activity and selectivity of the catalyst.^[8]

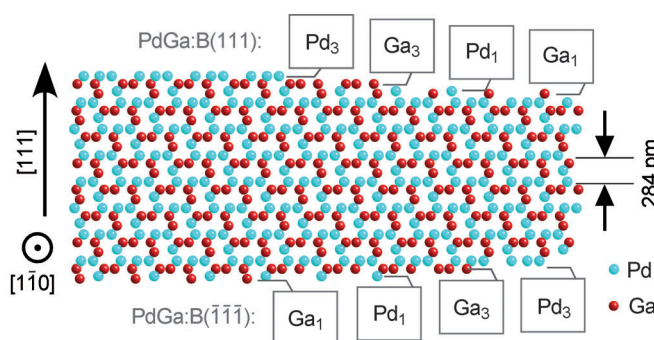


Figure 1. Bulk-truncated surface terminations of the PdGa:B(111) and PdGa:(111) surfaces. The surfaces are named according to Ref. [12], including the chemical composition, the enantiomeric form, and the surface direction.

We combine quantitative low-energy electron diffraction (LEED), high-resolution scanning tunneling microscopy (STM), and ab initio thermodynamics calculations to unequivocally identify the surface terminations of PdGa(111) and PdGa($\bar{1}\bar{1}\bar{1}$) surfaces. These surfaces exhibit significant differences in catalytic activity that are exemplified by calculations of hydrogen dissociation.

The crystal structure of PdGa belongs to the $P2_13$ space group and therefore exhibits two enantiomeric forms (labeled A and B in Refs. [12,19]). Figure 1 displays a side view onto a (110) surface of the structure model of form B that was derived from X-ray diffraction.^[16] The stacking sequence involves four nonequivalent atomic planes. As a consequence, the top and bottom surfaces are different, and each can exhibit four possible terminations. Recent STM investigations^[12] revealed that there is only one step height, and its value of 284 pm corresponds to four atomic planes, thus implying that only one of the four terminations is realized. LEED and X-ray photoelectron diffraction have shown that the surfaces are chiral and unreconstructed.^[12] Herein, we identify which of the four bulk terminations is realized and discuss the structure–reactivity relation.

[*] J. Prinz,^[†] Dr. R. Gaspari,^[†] Dr. C. A. Pignedoli, Dr. O. Gröning, Dr. D. Passerone, Dr. R. Widmer
Empa, Swiss Federal Laboratories for Materials Science and Technology
Überlandstrasse 129, 8600 Dübendorf (Switzerland)
E-mail: roland.widmer@empa.ch
Homepage: <http://www.surfaces.ch>

Dr. J. Vogt
Chemisches Institut, Otto-von-Guericke-Universität
39106 Magdeburg (Germany)

Prof. Dr. P. Gille
Dept. für Geo- und Umweltwissenschaften
Ludwig-Maximilians-Universität, 80333 München (Germany)

Dr. M. Armbrüster
Max-Planck-Institut für Chemische Physik fester Stoffe
01187 Dresden (Germany)

J. Prinz,^[†] Prof. Dr. H. Brune
Institute of Condensed Matter Physics, EPFL, Station 3
1015 Lausanne (Switzerland)

[†] These authors contributed equally to this work.

[**] This work was supported by the Swiss National Science Foundation under the contract 200021-129511. We kindly acknowledge D. Rosenthal, R. Schlögl (FHI Berlin), and Y. Grin (MPI Dresden) for fruitful discussions, and the Swiss Supercomputing Center (CSCS) for computational resources.

Supporting information for this article is available on the WWW under <http://dx.doi.org/10.1002/anie.201203787>.

Our initial approach to determining the surface terminations was by using LEED. This technique is intrinsically surface sensitive because of the small mean-free path of low-energy electrons. In addition to the diffraction images of the surface unit cells, information on the vertical structure was acquired from the variation of the diffraction spot intensities with incident electron energy owing to the interference of electrons scattered from lower-lying layers. Comparison of these I - V curves with simulated ones allows the determination of the atomic positions of the first atomic layers. The quality of this comparison is quantified by the Pendry reliability factor R_p ^[20] which is 0 for perfect agreement and 1 for uncorrelated profiles. The agreement is acceptable when R_p is less than 0.3.^[20,21]

We compared experimental results to the theoretical results for the 32 possible structures that result from both enantiomeric forms of the crystal, the four bulk truncations, the two nonequivalent close-packed surfaces, that is, (111) and $(\bar{1}\bar{1}\bar{1})$, and both possible in-plane orientations of the sample. Density functional theory (DFT) was used to compute the atomic positions of the relaxed bulk-surface terminations. The SATLEED code was applied to calculate the LEED curves from these model structures.^[21,22] The atomic positions were further fine-tuned to minimize the R_p factor for a given termination. The R_p factors for the model structures that were closest to the experimental structures are presented in Figure 2. The best fit was found for the PdGa:B(111)Pd₃ and PdGa:B($\bar{1}\bar{1}\bar{1}$)Pd₁ surface structures of the respective samples.

The difference in the R_p factor between the proposed structures is larger for the (111) surface than for the $(\bar{1}\bar{1}\bar{1})$ surface because of the much lower atomic density of the latter, and the weaker scattering cross section when Pd₁ terminated. Nevertheless, the difference remains significant also in that case, and the best fit for both structures give $R_p = 0.22$. To get an impression of the agreement between experimental and theoretical results, in Figure 2 we show for each surface the I - V curves for the structures with the lowest and highest R_p factors. Notably, the atomic displacements from the DFT relaxed structure that was used for the

optimization of the R_p factor are very small, being less than 7 pm in the vertical and less than 27 pm in the lateral direction. Finally, our LEED patterns confirm the formerly found absence of a surface reconstruction.^[12]

The surface terminations found by LEED are confirmed by the atomic resolution STM images shown in Figure 3. The unit cells are imaged as a trimer for the (111) surface and as a single atomic protrusion for the $(\bar{1}\bar{1}\bar{1})$ surface. In both cases,

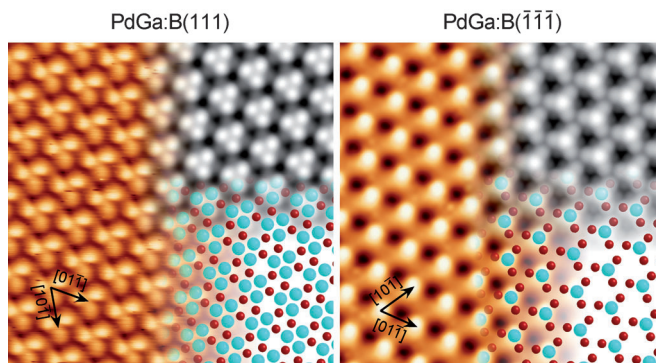


Figure 3. Atomically resolved STM images ($T = 77$ K) overlaid with simulated STM images (top right inset) and the respective structure models (bottom right inset; Pd = aqua, Ga = red). STM parameters (PdGa:B(111)Pd₃)/(PdGa:B($\bar{1}\bar{1}\bar{1}$)Pd₁): $V_T = 80/100$ mV; $I_T = 0.73/0.4$ nA; $\Delta z = 32/51$ pm; scan size = 6×6 nm².

the periodicity corresponds to the bulk value of 0.693 nm.^[16] This atomic contrast was found for all terraces of the respective surfaces, thus confirming that only one stable termination exists. The STM simulations shown in the top right insets agree with the experimental results. These simulations were obtained by applying the Tersoff-Hamann (TH) formalism^[23] to the DFT computed local density of states (LDOS; see the Supporting Information), the isovalue of which is matched to give good agreement with the experiment.

We addressed the physical origin of the stability of the identified terminations with DFT calculations. The relative stability of all PdGa terminations were computed in the grand canonical ensemble, where the different surfaces are at equilibrium with external sources of Pd and Ga atoms, and the equilibrium state is determined by the minimum of the Gibbs surface energy, G_s . The chemical potentials of the Pd and Ga atoms, μ_{Pd} and μ_{Ga} , depend on external parameters, such as pressure and temperature, and their individual values are generally unknown. However, the range of allowed μ_{Pd} and μ_{Ga} values can be determined by thermodynamic considerations.^[24] The upper limit of the chemical potential of Pd and Ga in the alloy is given by the respective bulk values. Moreover, when the sources of Pd and Ga atoms are in equilibrium with the PdGa bulk, μ_{PdGa} is a function of μ_{Pd} and μ_{Ga} . This gives an interval of [Eq. 1]:

$$\begin{aligned} \mu_{Ga}^{bulk} + \frac{\Delta H_f}{4} &\leq \mu_{Ga} \leq \mu_{Ga}^{bulk} \\ \mu_{Pd}^{bulk} + \frac{\Delta H_f}{4} &\leq \mu_{Pd} \leq \mu_{Pd}^{bulk} \end{aligned} \quad (1)$$

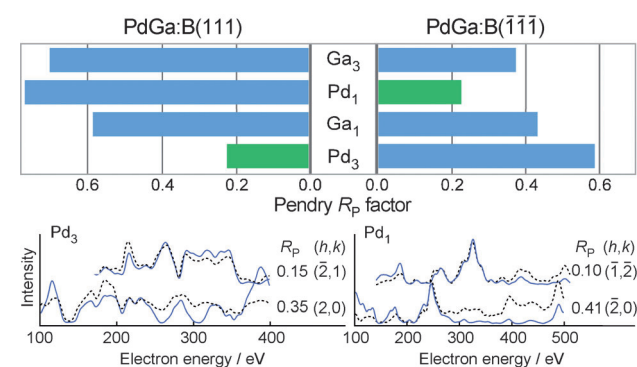


Figure 2. Top: R_p factors for the surface terminations that are shown in Figure 1. The experimental I - V data is derived from an average of 12 nonequivalent diffraction spots for each sample. The terminations giving best agreement are marked in green. Bottom: Experimental (dashed black line) and theoretical I - V curves (full blue line) for the two spot profiles that are in best and worst agreement among those of Pd₃ and Pd₁ (see also the Supporting Information).

where ΔH_f is the enthalpy of formation of PdGa per unit cell, containing four Pd and four Ga atoms. For the bulk cohesive energies we find $\mu_{\text{Pd}}^{\text{bulk}} = -3.69$ eV and $\mu_{\text{Ga}}^{\text{bulk}} = -2.78$ eV, which are in agreement with previous results.^[25,26] For the heat of formation per PdGa unit cell we obtain $\Delta H_f = -5.48$ eV, which is close to the experimental value of -5.96 eV.^[27]

For both surface orientations, Figure 4 displays the resulting $\Delta G_s(\mu_{\text{Ga}})$ curves, computed using periodic slab calculations.^[28] ΔG_s is expressed relative to PdGa:B(111)Ga₃

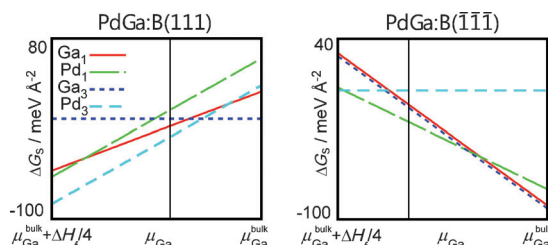


Figure 4. Change in Gibbs surface energy as a function of μ_{Ga} for the different terminations. Vertical lines refer to the actual value of the surface chemical potential estimated for the respective PdGa surfaces.

and PdGa:B($\bar{1}\bar{1}\bar{1}$)Pd₃, respectively (see the Supporting Information). The graphs shown reveal which surfaces can be expected over the whole range of external parameters. Clearly, the surface terminations determined by experiment have the widest stability ranges with a $\Delta\mu_{\text{Ga}}$ value of 1 eV and 0.8 eV in the two cases. This finding confirms the experimental results for both surfaces. Moreover, the actual values of the chemical potentials can be estimated under the assumptions that the Pd and Ga sources are in equilibrium with kink sites of the crystal surface and that the two opposite surfaces of the same sample equilibrate independently. The explicit calculation (see the Supporting Information) gives values of $\mu_{\text{Ga}}^{(111)} = \mu_{\text{Ga}}^{\text{bulk}} - 0.57$ eV and $\mu_{\text{Ga}}^{(\bar{1}\bar{1}\bar{1})} = \mu_{\text{Ga}}^{\text{bulk}} - 0.90$ eV, which are indicated in the energy profiles (Figure 4) as vertical lines. Again, for these specific values Pd₃(111) and Pd₁($\bar{1}\bar{1}\bar{1}$) are found to be the most stable terminations, in agreement with the experimental results.

STM images of surface vacancies provide an additional and very sensitive test of the determined surface terminations. The distance from the surface as well as the chemical composition of the underlying layer varies strongly with the surface termination, thus giving rise to termination specific STM contrast between the surface and vacancies. Figure 5 shows a comparison of measured and calculated constant-current STM images and apparent height profiles going from regular surface areas to vacancies and back. The surface layer is identified from the simulated STM vacancy profiles for all bulk terminations, by comparison of the calculated vacancy depths with the experimental value.

For both surfaces, the measured apparent-vacancy heights agree well with the calculated ones for the two identified terminations, and differ significantly from all other terminations. This result gives us additional confidence that PdGa:B(111)Pd₃ and PdGa:B($\bar{1}\bar{1}\bar{1}$)Pd₁ are the actual surface

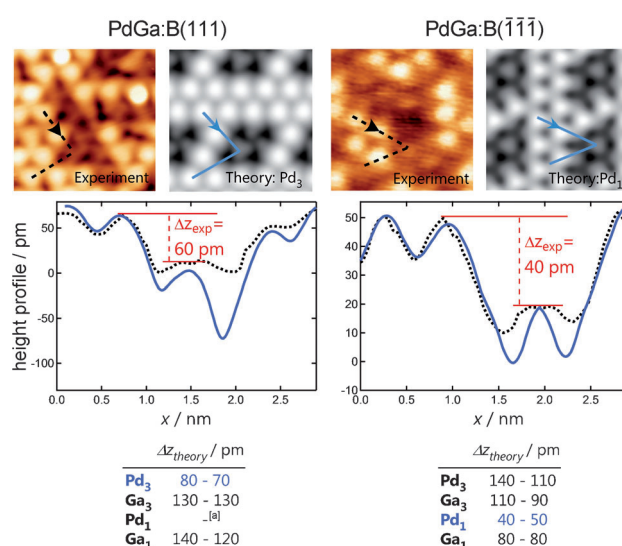


Figure 5. Top: Measured and calculated constant-current STM images. Middle: Apparent height profiles for experimental (dashed black line) and simulated (full blue line) STM images of surface vacancies. Bottom: The tables show simulated values of the apparent vacancy depths (Δz) for all DFT relaxed model terminations. The values that have best agreement between simulation and experiment are marked in blue. [a] In the DFT-optimized structure for (111)Pd, the underlying Ga layer relaxes towards the surface and becomes the top layer.

structures. The STM simulations were obtained using the TH^[23] model and DFT relaxed surface structures displaying patterns of 2×2 vacancies with monoatomic steps. The comparison of experimental and theoretical results is particularly robust, as the vacancy depth is rather stable against changes of simulated isocurrent or tip radius. A large range of tip-sample distances was covered by simulating STM images for integrated LDOS values of 10^{-7} and 10^{-11} e³. For a pointlike tip, these values correspond to tip-sample distances of 0.45 nm and 0.9 nm, respectively. The vacancy depth intervals given in Figure 5 come from these two extreme tip-sample distances and provide a conservative error margin of the STM simulation.

An initial indication of the catalytic activity of the two surface terminations can be obtained from the position of the metal d-band center with respect to E_{F} , an indicator for the bonding strength of adsorbates to metallic surfaces.^[29] However, this simple d-band-center rule has to be taken with care, both, because covalent bonding plays a role in this system, and in case molecular adsorption modifies considerably the band shape (as seen in the Supporting Information, this is the case for hydrogen adsorption).^[30] For high catalytic activity, the bond to a reactant molecule should be of intermediate strength, this is known as the Sabatier principle.^[31] In comparison to Pd(111), (for details see the Supporting Information) the Pd d-band edge of both PdGa surfaces is found at lower energy, which is an indication (with the above caveats) of a weaker binding of the adsorbed molecules on the IMC surfaces, in agreement with thermal desorption spectroscopy (TDS) results.^[12] Additionally, the PdGa surfaces exhibit a sharper d-band, and thus a stronger localization of electronic states. In spite of their electronic similarity, as seen

by the projected density of states (pDOS; see the Supporting Information), the two PdGa terminations allow for different adsorption conformations as single Pd atoms or Pd trimers terminate the surface. This site separation is particularly evident for Pd₁, where the surface atomic Pd–Pd distance is 2.5 times larger than for Pd(111), and more than twice the bulk value of PdGa.^[14]

A more elaborate assessment of the catalytic properties can be obtained by DFT calculations of the binding energies and adsorption sites; we performed these calculations for molecular and atomic hydrogen adsorbed onto both surfaces (Figure 6) while no hydrogen uptake into the bulk is expected.^[32] On PdGa:B($\bar{1}\bar{1}\bar{1}$)Pd₁ the most favorable adsorp-

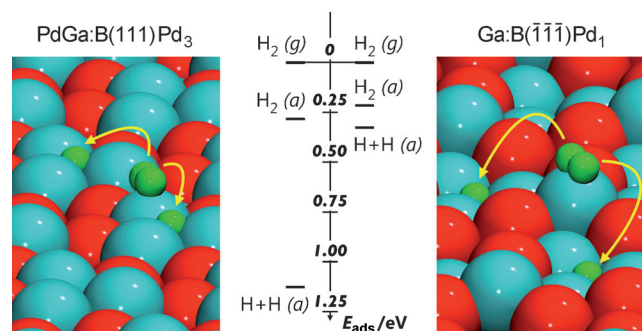


Figure 6. Adsorption sites and binding energies for H₂ and H on the investigated surfaces. Energies are given in eV per H atom couple with respect to the molecule in the gas phase.

tion site for H₂ is the Pd₁ on-top position with an adsorption energy of 0.22 eV per H₂ molecule. From this site H₂ dissociation is exothermic with 0.11 eV and the most favorable site for atomic hydrogen is the threefold coordinated hollow site on the Pd₃ trimer (Figure 6, right). This position is 70 pm below the Pd₃ surface plane, and 13 pm below the first Ga₃ plane, a site that is sufficiently close to the surface for the adsorbate to remain available for the hydrogenation of other molecules.

The adsorption energy of H₂ on PdGa:B(111)Pd₃ is 0.28 eV, and thus comparable to PdGa:B($\bar{1}\bar{1}\bar{1}$)Pd₁. Furthermore, similar adsorption positions for H₂ and H are identified for both surfaces, that is, Pd top site and Pd threefold hollow site, respectively. However, H₂ dissociation is associated with a larger energy gain of 0.85 eV on the Pd₃ termination. This comparison reveals that both surface orientations with their terminations determined in the present study show mostly quantitative differences in their behavior towards H₂ dissociation. Although the binding energies of the molecular precursor are quite similar, one surface has more strongly bound dissociation products than the other. The different bonding mechanisms of both surfaces are also highlighted by the projected densities of states. Hybridization of the H s level with the Pd d bands shows a different fine structure at around 6 eV below the Fermi energy (see the Supporting Information), which is where there is maximum overlap between H and Pd orbitals participating in the bonding (as it results from a bond-order analysis performed within Bader's topological theory of atoms in molecules,^[33] see Supporting Information.

This analysis also confirms the stronger bonding of H atoms on the surface trimer on the PdGa:B(111)Pd₃.

In conclusion, we have determined the surface terminations of the IMC PdGa:B(111)Pd₃ and PdGa:B($\bar{1}\bar{1}\bar{1}$)Pd₁. The structural details revealed in this work and their implications on the binding of adsorbates will serve as the essential basis for understanding chemical reactions on the PdGa surfaces and help develop high performance catalysts from intermetallic compounds. The structural dissimilarities of the two surface terminations lead to significant energetic differences in the catalytic dissociation of a molecule as simple as hydrogen, an essential reagent in many relevant reactions. We expect similar or even larger differences for organic molecules, a topic to be addressed in a forthcoming publication. Moreover, the structural dissimilarity of the (111) and ($\bar{1}\bar{1}\bar{1}$) surfaces makes the IMC PdGa a prototype model system, which allows the study of the effect of active-site separation in heterogeneous catalysis.

Experimental Section

Methods: The single-crystal samples used in this study originate from one large PdGa crystal grown by the Czochralski method.^[34] After cutting and polishing, reflective energy dispersive X-ray diffraction determined the surface orientations to be within 0.3° precise.

STM measurements were performed with an Omicron low-temperature STM at 77 K and at a base pressure below 5×10^{-11} mbar with a mechanically cut Pt/Ir-tip. STM data were analyzed using the WSxM software.^[35]

Sample preparation in UHV consists of several sputter-annealing cycles (sputtering: Ar⁺, 1 keV; annealing: 20 min at 870 K) until a sharp (1×1) LEED pattern was obtained. During preparation, no change in the surface stoichiometry of PdGa was observed.^[12] The LEED investigations were carried out with an Omicron multi-channelplate Spectra-LEED and acquired with a CCD camera at 1 eV/frame. Video analysis was performed using the Spectaview software from Omicron. *I*-*V* profiles for the single spots were background corrected. The angle of incidence was perpendicular to the surface, thus allowing for averaging over the symmetry equivalent spot profiles leading to an improved signal to noise ratio.^[21–22]

Relative surface energies have been computed using DFT slab calculations, employing the PWSCF^[36] code. Simulated STM vacancy heights have been computed using supercell DFT slab calculations employing the CP2K^[37] code (for further details see the Supporting Information).

Received: May 16, 2012

Revised: June 8, 2012

Published online: August 22, 2012

Keywords: density functional calculations · electron diffraction · heterogeneous catalysis · intermetallic compounds · surface chemistry

[1] U. Dingerdissen, A. Martin, D. Herein, H. J. Wernicke in *Handbook of Heterogeneous Catalysis* (Eds.: G. Ertl, H. Knözinger, F. Schüth, J. Weitkamp), VCH, Weinheim, **2008**.

[2] J. A. Dumesic, G. W. Huber, M. Boudart in *Handbook of Heterogeneous Catalysis* (Eds.: G. Ertl, H. Knözinger, F. Schüth, J. Weitkamp), VCH, Weinheim, **2008**.

- [3] G. Kyriakou, M. B. Boucher, A. D. Jewell, E. A. Lewis, T. J. Lawton, A. E. Baber, H. L. Tierney, M. Flytzani-Stephanopoulos, E. C. H. Sykes, *Science* **2012**, 335, 1209–1212.
- [4] G. A. Somorjai, *Science* **1985**, 227, 902–908.
- [5] H. J. Freund, N. Ernst, T. Risse, H. Hamann, G. Rupprechter, *Phys. Status Solidi A* **2001**, 187, 257–274.
- [6] G. Ertl, H. J. Freund, *Phys. Today* **1999**, 52, 32–38.
- [7] M. Ortega Lorenzo, C. J. Baddeley, C. Muryn, R. Raval, *Nature* **2000**, 404, 376–379.
- [8] J. K. Nørskov, T. Bligaard, J. Rossmeisl, C. H. Christensen, *Nat. Chem.* **2009**, 1, 37–46.
- [9] W. M. H. Sachtler, *Catal. Rev. Sci. Eng.* **1976**, 14, 193–210.
- [10] M. Armbrüster in *Encyclopedia of Catalysis* (Ed.: I. T. Horvath), VCH, Weinheim, **2011**.
- [11] J. Osswald, K. Kovnir, M. Armbrüster, R. Giedigleit, R. E. Jentoft, U. Wild, Y. Grin, R. Schlögl, *J. Catal.* **2008**, 258, 219–227.
- [12] D. Rosenthal, R. Widmer, R. Wagner, P. Gille, M. Armbrüster, Y. Grin, R. Schlögl, O. Gröning, *Langmuir* **2012**, 28, 6848–6856.
- [13] J. Osswald, R. Giedigkeit, R. E. Jentoft, M. Armbrüster, F. Girgsdies, K. Kovnir, T. Ressler, Y. Grin, R. Schlögl, *J. Catal.* **2008**, 258, 210–218.
- [14] K. Kovnir, M. Armbrüster, D. Teschner, T. V. Venkov, F. C. Jentoft, A. Knop-Gericke, Y. Grin, R. Schlögl, *Sci. Technol. Adv. Mater.* **2007**, 8, 420–427.
- [15] M. Armbrüster, K. Kovnir, M. Behrens, D. Teschner, Y. Grin, R. Schlögl, *J. Am. Chem. Soc.* **2010**, 132, 14745–14747.
- [16] M. Armbrüster, H. Borrmann, M. Wedel, Y. Prots, R. Giedigkeit, P. Gille, *Z. Kristallogr. New Cryst. Struct.* **2010**, 225, 617–618 (please consider the accidental interchanging of crystal form “A” and “B” in this reference).
- [17] B. H. Verbeek, P. K. Larsen, W. M. Gerits, *Vacuum* **1983**, 33, 813–814.
- [18] K. Kovnir, M. Armbrüster, D. Teschner, T. V. Venkov, L. Szentmiklosi, F. C. Jentoft, A. Knop-Gericke, Y. Grin, R. Schlögl, *Surf. Sci.* **2009**, 603, 1784–1792.
- [19] J. C. H. Spence, J. M. Zuo, M. Okeeffe, K. Marthinsen, R. Hoier, *Acta Crystallogr. Sect. A* **1994**, 50, 647–650.
- [20] J. B. Pendry, *J. Phys. C* **1980**, 13, 937–944.
- [21] M. A. Van Hove, W. H. Weinberg, C. M. Chan, *Low-Energy Electron Diffraction*, Springer, Heidelberg, **1986**.
- [22] A. Barbieri, M. A. Van Hove, private communication (<http://www.ap.cityu.edu.hk/personal-website/Van-Hove.htm>) ed.
- [23] J. Tersoff, D. R. Hamann, *Phys. Rev. B: Condens. Matter Mater. Phys.* **1985**, 31, 805–813.
- [24] G. X. Qian, R. M. Martin, D. J. Chadi, *Phys. Rev. B: Condens. Matter Mater. Phys.* **1988**, 38, 7649–7663.
- [25] D. D. Wagman, W. H. Evans, V. B. Parker, R. H. Schumm, I. Halow, S. M. Bailey, K. L. Churney, R. L. Nuttall, *J. Phys. Chem. Ref. Data* **1982**, 11, 1–405.
- [26] C. Kittel, *Introduction to Solid State Physics*, Wiley, New York, **1971**.
- [27] S. V. Meschel, O. J. Kleppa, *Thermochim. Acta* **1997**, 292, 13–17.
- [28] W. E. Pickett, *Comput. Phys. Rep.* **1989**, 9, 115–197.
- [29] B. Hammer, J. K. Nørskov, *Surf. Sci.* **1995**, 343, 211–220.
- [30] A. Roudgar, A. Gross, *J. Electroanal. Chem.* **2003**, 548, 121–130.
- [31] P. Sabatier, *Ber. Dtsch. Chem. Ges.* **1911**, 44, 1984–2001.
- [32] M. Klanjsek, et al., *J. Phys.: Condens. Matter* **2012**, 24, 085703.
- [33] J. G. Angyan, M. Loos, I. Mayer, *J. Phys. Chem.* **1994**, 98, 5244–5248.
- [34] P. Gille, T. Ziemer, M. Schmidt, K. Kovnir, U. Burkhardt, M. Armbrüster, *Intermetallics* **2010**, 18, 1663–1668.
- [35] I. Horcas, R. Fernandez, J. M. Gomez-Rodriguez, J. Colchero, J. Gomez-Herrero, A. M. Baro, *Rev. Sci. Instrum.* **2007**, 78, 013705.
- [36] P. Giannozzi, et al., *J. Phys.: Condens. Matter* **2009**, 21, 395502.
- [37] J. VandeVondele, M. Krack, F. Mohamed, M. Parrinello, T. Chassaing, J. Hutter, *Comput. Phys. Commun.* **2005**, 167, 103–128.

3.1.1 Supporting information for the publication "Isolated Pd Sites on the Intermetallic PdGa(111) and PdGa(-1-1-1) Model Catalyst Surfaces"

Table of Contents

1. LEED-I(V) calculation part
2. Surface energy calculation part
3. Estimation of the chemical potential from kink energy considerations
4. DFT vacancy simulation part
5. Projected density of states of the clean surfaces
6. Hydrogen adsorption and projected density of states
7. References

1. LEED-I(V) calculation part:

In the first step of simulating the I(V) profiles, the potential landscape within the material is approximated as a muffin-tin potential, where the individual atomic cores are assumed to form symmetric spherical potentials with the muffin-tin radius, embedded in a region of constant potential, the "muffin-tin zero", or "inner potential". For the PdGa structure, the radii of the respective atoms were chosen as half the distance to the nearest neighbor. By solving the Schrödinger equation for an electron scattered on an individual atom, i.e. a certain spherical potential, the energy dependent phase shifts for the scattering process were obtained. For these calculations, the phase shift package of Barbieri and Van Hove³⁵ was used.

The next steps are the calculations of the intensity vs. energy profiles for different reference model structures and the optimization of the atomic coordinates via comparison to the experiment. For this, the reliability factor R_p was used, as defined by Pendry.³⁹ A value of $R_p = 0$ would result from a perfect correlation of experiment and theory, whereas $R_p = 1$ means uncorrelated profiles. If $R_p < 0.3$, the agreement is considered to be acceptable. The SATLEED code used throughout this study makes use of the tensor LEED approximation.⁶⁵⁻⁶⁶ Within tensor LEED, the time consuming solution of the multiscattering problem in LEED is limited to the reference structure only, while the I(V) profiles of a large number of test structures deviating moderately from this reference structure are calculated efficiently by means of a perturbation treatment.

In the main article, we present only the comparisons for structure models of the enantiomer form B, the correct sample in-plane rotation (explained later in the text) and the surface directions according to the respective sample ((111) and (-1-1-1)). However, within the analysis, a total of 32 sets of profiles originating from 32 model structures were compared to both sets of I(V) profile, for the (111) and the (-1-1-1) surface. This number arises from 4 different layers in the surface unit cell (Pd_3 , Ga_3 , Pd_1 , Ga_1), 2 non-equivalent surfaces ((111) and (-1-1-1)), 2 enantiomeric forms and 2 possible rotational directions of the sample in the LEED setup. The latter originates from the unknown in-plane direction of the threefold symmetric sample. This problem is equal to the question of how to assign Miller's indices to the experimental spots for the

hexagonal pattern with a threefold rotational symmetry. A summary of the R-factors is shown as a bar-chart in Figure 3.1.

The R_p values shown in Figure 3 of the main article and Figure 3.1 were obtained after fitting out-of-plane and in-plane lattice parameters of the top 9-12 atomic layers, depending on the respective structure model, and the real part of the inner potential.⁶⁷ Calculations for obtaining the R_p factors presented in Figure 3.1 were carried out using a low maximum angular momentum ($L_{\max} = 6$) in the simulated scattering process to increase convergence stability. For the precise determination of the atomic arrangement, the computation was optimized for the two identified structures using $L_{\max} = 8$ and a repetitive optimization of the model structure, using the previous best-fit structure as a new reference structure.⁶⁷ Starting from the DFT relaxed structure models, this optimization procedure involved shifts of the atoms from their initial positions not larger than 7 pm in the direction perpendicular to the surface with respect to the lowest layer of the fitted stack. The in-plane shifts of the structure optimization were less than 27 pm.

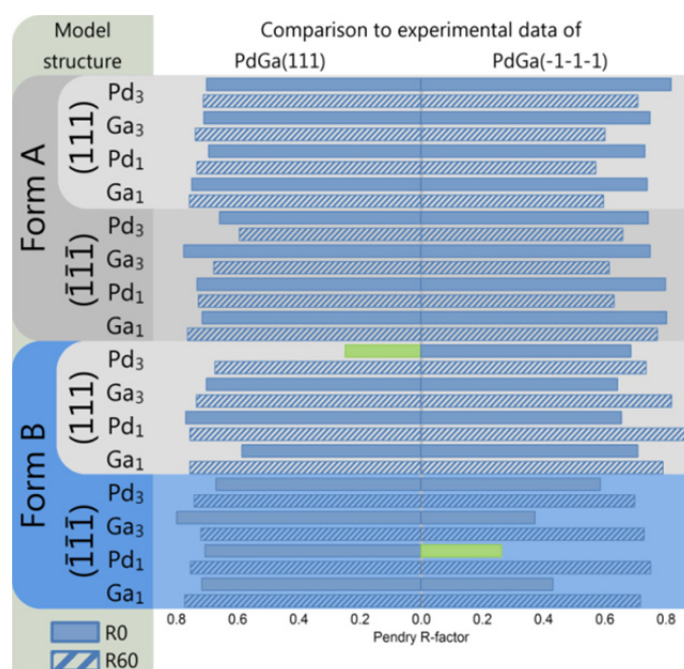


Figure 3.1 Pendry R_p factors from the LEED-I(V) analysis of all structure models taken into account in the comparison of experimental and theoretical I(V) profiles. For each surface termination, two possible rotations of the surface had to be considered (R0 and R60).

Resulting I(V) profiles for the best fit structures are shown in Figure 3.2 and in the lower part of Figure 3 of the main article.

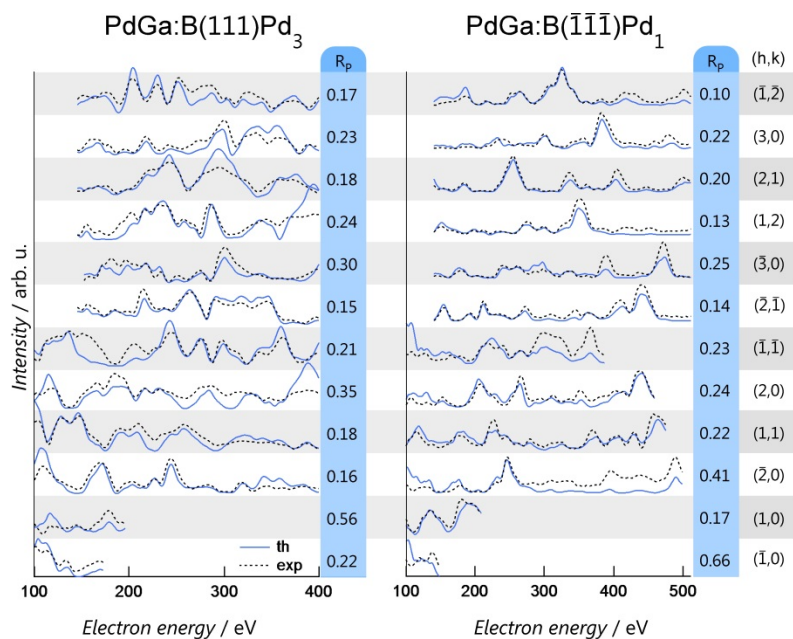


Figure 3.2 Experimental (dashed) and theoretical I(V) profiles (drawn, blue) for the best fit structures showing visual agreement for both surfaces. To the right of each profile, the respective spot indices (h,k) and the individual R_p is given. The overall R_p are 0.22 for both surfaces.

The model structures consisted of two, so called composite layers⁶⁷: a substrate part of 12 layers, where the atoms were kept fixed and the coordinates were determined by DFT bulk relaxation and on top of this, a surface part, composed of 9 to 12 layers, depending on the surface model. Here, the initial atomic structure was taken from the DFT relaxation described later. In general, the error bars determined according to Pendry³⁹ are larger than the actual shift, meaning that the precision of the initial DFT relaxed structure was already good.

2. Surface energy calculation part:

PdGa surface stability was calculated in the framework of periodic slab simulations. For all the slabs considered, the unit cell is primitive along the surface plane. In the direction perpendicular to the surface, 20 Å of vacuum have been added in order to decouple the two surfaces of the slab (see Figure 3.3).

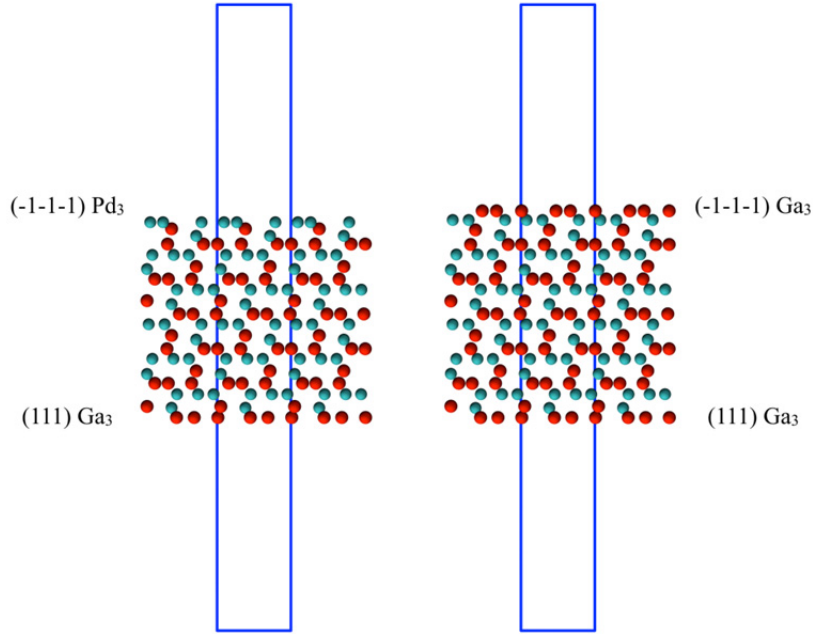


Figure 3.3 Lateral view of two slabs used in the calculation of the surface free energies. The lower surface (111) Ga₃ is the same in both slabs, allowing to subtract the contribution of the latter face, and to obtain the difference between the surface energies of the surfaces (-1-1-1)Pd₃ and (-1-1-1)Ga₃. Shown are also the simulation box (in blue) including a vacuum region below and above the slab, and two repetition units in the lateral direction.

We prepared two stoichiometric slabs of 24 layers (two bulk units) and 36 layers (three bulk units), respectively, both terminated (111)Ga₃ and (-1-1-1)Pd₃. We computed the bulk energy of PdGa as the energy difference of the two relaxed slabs, following the prescription of Ref. ⁶⁸⁻⁶⁹. By adding layers on the (111)Ga₃/(-1-1-1)Pd₃ slab (24 layers), according to the stacking sequence, we obtained the (111)X/(-1-1-1)Pd₃, (111)Ga₃/(-1-1-1)X slabs, X being any of the 4 bulk terminations (Ga₁, Ga₃, Pd₁, Pd₃). In the (111) direction the OK DFT energy of each slab, $E_{slab}^{(111)X, (-1-1-1)Pd_3}$ is approximately related to the surface energies $G^{(111)X}(\mu_{Ga})$ and $G^{(-1-1-1)Pd_3}(\mu_{Ga})$ by the relationship

$$G_{surf}^{(111)X}(\mu_{Ga}) + G_{surf}^{(-1-1-1)Pd_3}(\mu_{Ga}) \approx E_{slab}^{(111)X/(-1-1-1)Pd_3} - (n_{Pd}^{(111)X/(-1-1-1)Pd_3} \mu_{Pd} + n_{Ga}^{(111)X/(-1-1-1)Pd_3} \mu_{Ga}) \quad (3-1)$$

n_{Pd} and n_{Ga} being the number of Pd and Ga atoms contained in the slab. By repeating the calculation for another slab (111)X'/(-1-1-1)Pd₃ we obtain the surface free energy difference between the termination X and X' as:

$$G_{surf}^{(111)X}(\mu_{Ga}) - G_{surf}^{(111)X'}(\mu_{Ga}) \approx E_{slab}^{(111)X/(-1-1-1)Pd_3} - n_{Pd}^{(111)X/(-1-1-1)Pd_3} \mu_{Pd} - n_{Ga}^{(111)X/(-1-1-1)Pd_3} \mu_{Ga} \\ - E_{slab}^{(111)X'/(-1-1-1)Pd_3} + n_{Pd}^{(111)X'/(-1-1-1)Pd_3} \mu_{Pd} + n_{Ga}^{(111)X'/(-1-1-1)Pd_3} \mu_{Ga} \quad (3-2)$$

The dependency of G_{surf} on μ_{Pd} can be dropped, since μ_{Ga} and μ_{Pd} are related by the relationship given by the chemical equilibrium between the sources and the PdGa bulk.

$$4\mu_{Ga} + 4\mu_{Pd} = \mu_{PdGa(bulk)} \quad (3-3)$$

It must be noted that the free energy of the slab should in principle be used instead of the OK DFT total energy. However the influence of zero point vibrational effects and entropic contributions can be neglected in many cases, especially when surface energy differences are concerned.⁷⁰⁻⁷²

The same procedure was applied to obtain the surface energy differences for the (-1-1-1) termination. As reference terminations in Figure 4 of the main article we used (111)Ga₃, and (-1-1-1)Pd₃ which therefore appear constant in the respective graph.

Calculations on bulk Pd, bulk Ga (α phase) and bulk PdGa have been performed using the primitive bulk unit cells of the two systems. For all the systems considered the PWSCF package⁷³ was used for the calculations. The structural optimization has been performed until the largest forces on the atoms were as small as $5 \cdot 10^{-4}$ Ry/Å. We used PBE exchange-correlation functional⁷⁴, ultrasoft pseudopotential⁷⁵ for all elements and a plane wave cutoff of 30 Ryd. A convergence test was carried out using a plane wave cutoff of 40 Ryd. With respect to a 30 Ryd cutoff calculation the change in cohesive energy of PdGa gives a difference of about 1 meV/atom. K-points sampling was performed using a 3x3x1 Monkhorst pack grid for the PdGa slabs and a 4x4x4 grid for the bulks of Pd and Ga.

Figure 3.3 shows the typical setup for the calculation of G_{surf} : two slabs showing one similar surface are optimized.

3. Estimation of the chemical potential from kink energy considerations:

Because of the peculiar structure of PdGa, Pd and Ga units lack lateral interaction at the surface. This becomes clear from the comparison of in-plane and out-of-plane nearest neighbor distances (in-plane: 0.43/0.69 nm for trimer/atomic distance; out-of-plane: 0.25 nm). Hence the lateral bonding of atoms on the (111) and (-1-1-1) surfaces is weak compared to the out-of-plane bonding and consequently the energy of a surface unit does not depend on the position in the sample: adatom, kink, step, and surface sites are energetically equivalent. The energy of kink units has therefore been computed as the energy difference between slabs with a contiguous number of layers, in the two orientations.

For the estimation of chemical potentials it was assumed that the sources of Pd and Ga are in equilibrium with kink units of the crystal and that the two surfaces equilibrate independently. In this case the following set of equations holds for both orientations:

$$\begin{aligned} 4\mu_{Ga} &= \mu_{Ga1}^{kink} + \mu_{Ga3}^{kink} \\ 4\mu_{Pd} &= \mu_{Pd1}^{kink} + \mu_{Pd3}^{kink} \end{aligned} \quad (3-4)$$

where μ^{kink} is the change in energy of the system upon removal of a kink unit (which can be either a monomer or a trimer, according to the kink type). In simple crystals the kink energy has the special property of being equal to the cohesive energy. In the PdGa sample kink energies are related to the bulk energy by the relationship:

$$\mu_{Ga1}^{kink} + \mu_{Ga3}^{kink} + \mu_{Pd1}^{kink} + \mu_{Pd3}^{kink} = \mu_{PdGa(bulk)} \quad (3-5)$$

The relationships in Equation 3 and Equation 4 hold separately for both the (111) and (-1-1-1) orientations and can be combined to recover the equilibrium condition between the bulk and the sources as expressed in the previous paragraph. Therefore the values of the surface chemical potentials given by Equation (3-4) and (3-5) are compatible with the more general conditions under which the Gibbs surface energy profiles (Equations (3-1) and (3-2)) were obtained.

4. DFT vacancy simulation part:

Electronic structure calculations were performed in the framework of density functional theory (DFT) using the mixed plane wave-gaussian (GPW) basis set approach implemented in CP2K.⁷⁶ Kohn-Sham equations were solved using the PBE exchange correlation functional, Goedecker-Teter-Hutter (GTH) pseudopotentials and contracted gaussian basis sets⁷⁷ for all elements. The Poisson equation was solved by expanding the charge density in plane waves using a cutoff of 280 Rydberg. The surface unit cell of each PdGa slab is rectangular, corresponding to the 3x(2x√3) primitive hexagonal surface unit cell. After the electronic optimization was carried out, the individual states have been analytically extrapolated into the vacuum region using the matching procedure described in⁷⁸ and STM images have been computed using the Tersoff-Hamann (TH) approximation, with a negative bias of 0.5 eV. It must be observed that the original TH approximation only considers tunneling from states at Fermi level; however, if the bias voltage is small compared to the work functions of the tip and the sample, the approximation can be easily modified to account for non-zero bias voltages.⁷⁹

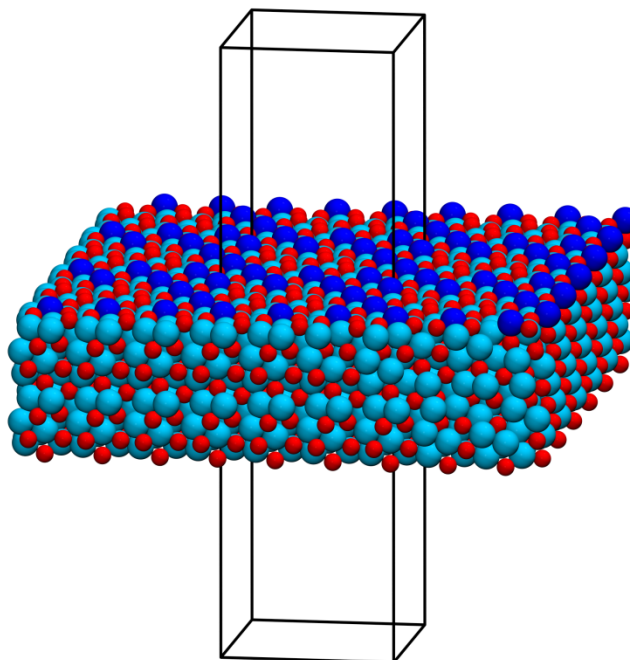


Figure 3.4 Perspective view of a slab used to compute the STM profile of a surface with vacancies. In this case, a Pd₁ surface is shown, with the Pd atoms at the surface highlighted in blue, to underline the presence of a 2x2 vacancy pattern. 3x3 lateral simulation cells are shown.

5. Projected density of states of the clean surfaces:

For the discussed surfaces, the pDOS (based on calculations done with q-Espresso⁷³) is plotted together with PdGa(bulk) and Pd(111) in Figure 11, in line with ultra-violet photoemission spectroscopy results.⁸⁰ In comparison to Pd(111) the PdGa surfaces exhibit a sharper d-band, and thus a stronger localization of electronic states. In addition, the Pd *d*-band edge of both PdGa surfaces is found at lower energies, a hint for a weaker binding of adsorbed molecules on the IMC surface, in agreement with TDS results.⁸⁰ Furthermore, the center of the Pd *d*-band shifts remarkably, depending on the distance of the projection layer from the surface as shown in Figure 11. A strong peak can be found around 2 eV below the Fermi energy for the projection on Pd *d*-bands of both PdGa surfaces which is absent in bulk PdGa. The overall shape differs only slightly for PdGa:B(111)Pd₃ and PdGa:B(-1-1-1)Pd₁, and thus the catalytic activity of the two surface terminations is expected similar by the *d*-band model.

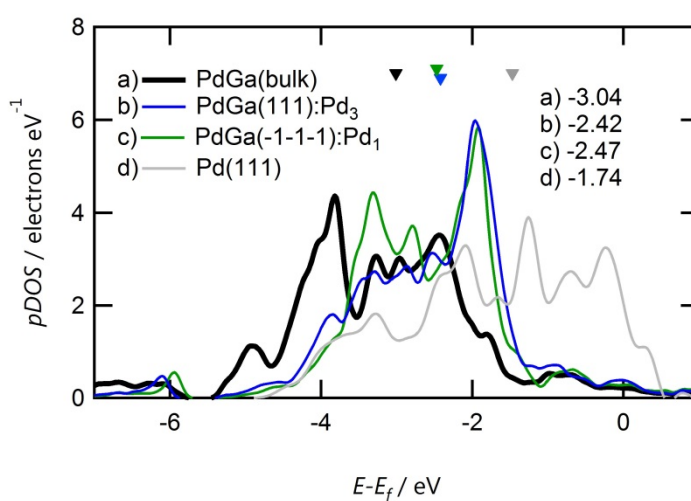


Figure 3.5 The pDOS of the Pd 4*d*-bands of the two threefold PdGa surfaces in comparison with that of Pd(111) and PdGa(bulk). The center of the *d*-band (colored triangles in the top) is shifted towards lower energies for the PdGa surfaces with respect to Pd(111). Values of the positions of the *d*-band centers with respect to E_f are given in the top right part of the graph.

6. Hydrogen adsorption and projected density of states

In order to test the adsorption properties of the available sites on the two most stable surface terminations (PdGa:B(111)Pd₃ and PdGa:B(-1-1-1)Pd₁) we performed *ab-initio* simulations using cp2k, using similar cells as the ones described above. We choose cp2k because it allows a large supercell where adsorbed species can be considered as isolated even with boundary conditions. In order to screen a large number of molecular and atomic adsorption sites, we first adopted thin slabs with 8 layers (192 atoms) in the substrate (12 or 36 atoms per layer), then we fully optimized the best configurations using thicker slabs with 24 layers, which were also used to compute the adsorption energies. Basis set superposition error (BSSE) was verified in a specific case to amount to less than 0.02 eV, thus not affecting considerably our results.

For each case (H₂ on Pd₁, H₂ on Pd₃, H on Pd₁, H on Pd₃) we started from a grid of initial configurations. We could draw the following conclusions for the four cases:

1. H_2 on Pd_1 . The best configuration is an on-top adsorption site ($E_{\text{ads}}=-0.22$ eV). The second best site is an on-top site on a subsurface trimer, already almost not bound.
2. H_2 on Pd_3 . Also in this case, the best configuration is an on-top adsorption site ($E_{\text{ads}}=-0.28$ eV). The second best site is a bridge site on the trimer, less bound by 0.15 eV
3. H on Pd_1 . In this case the best configuration is a hollow site on the subsurface Pd_3 trimer ($E_{\text{ads}}=-0.33$ eV per H couple, with respect to the molecule in gas phase). The second best site is barely bound, with an energy worse by 0.23 eV.
4. H on Pd_3 . In this case the best configuration is a hollow site on the surface Pd_3 trimer ($E_{\text{ads}}=-1.13$ eV per H couple, with respect to the molecule in gas phase). The second best configuration, a hollow site on the same trimer, is less bound by 0.54 eV.

We show in Figure 3.6 the projected density of states on the d -bands of surface and subsurface Pd atoms, together with the projection on the H s -bands, upon adsorption of molecular and atomic hydrogen. As mentioned in the main text, hydrogen uptake of PdGa is not expected.²⁶

A modification of the d -bands upon adsorption is clearly noticeable. For example, in a), we note that the on-top adsorption on the Pd_1 makes the peak at -2 eV disappear. The same happens on the Pd_3 (panel c)). But also in the case of atomic adsorption (panels b) and d)), a downward shift of the band is observed. The observation done for H adsorption on Pd(111) in⁸¹ thus remains valid, the authors recognize that the correlation between band-center position and molecular adsorption is able to explain several observed phenomena in reactivity but that... "This analysis shows that the d -band model is only appropriate if the interaction between adsorbate and substrate is not too strong. If there is a strong coupling, then the response of the local d -band to the presence of the adsorbate has to be taken into account in addition to the d -band position in order to understand the reactivity."²⁶

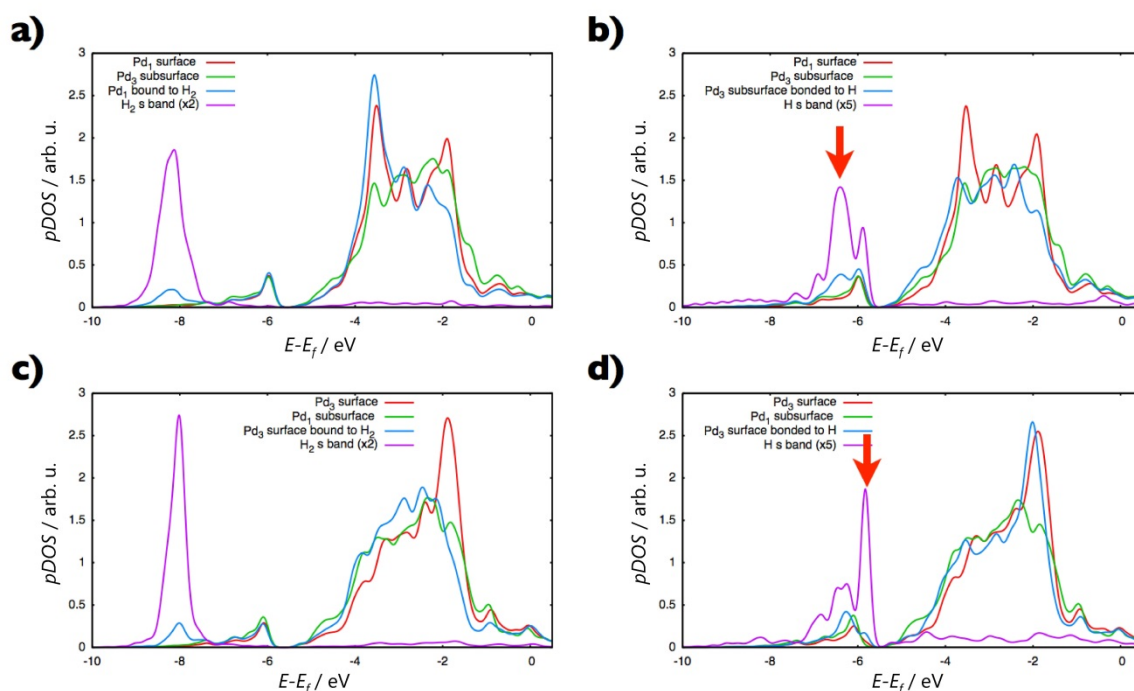


Figure 3.6 The DOS projected on the d -bands of selected Pd surface atoms and on the s -band of hydrogen atoms.

Additionally, we performed a Bader analysis in order to study the bonding of hydrogen atoms to the surface trimer (Pd_3 case) and to the subsurface trimer (Pd_1 case). We use the procedure described in ⁸². First, the boundaries of atomic basins are determined by a zero-flux condition applied to the electronic density. Then, the atomic overlap matrix of the molecular orbitals is obtained by integration over Bader domains of a given atom. The idea is then that if two orbitals will overlap significantly in the basin of an atom A and in the basin of an atom B, this overlap will contribute to the bonding between A and B. The bond-order between two atoms A and B is then obtained by summing all such products of overlaps on basins A and B for all orbital pairs. The C-C triple bond in acetylene leads for example to a bond order of 2.885, the C-C double bond in ethylene to 1.984, the C-C single bond in ethane to 1.013, and the bond in the HF molecule to 0.480.

In our case, the adsorption to the trimer leads to a bond order of 0.48 (summed over all Pd atoms) for the Pd_1 subsurface trimer, and to a bond order of 0.52 for the Pd_3 surface timer.

3.2 Determination of the PdGa(100), (110) and (210) surface terminations

In the present chapter, we discuss the surface structure determination of three low-Miller index surfaces exhibiting rectangular unit cells, namely PdGa(100), (110) and (210). The goal is to reveal if the Pd site-isolation is present and how it is realized on the surfaces. We follow the same approach as applied in the previous chapter, combining LEED-I(V) with STM and DFT.

Figure 3.7 shows the PdGa bulk structure in viewing directions perpendicular to the [100], [110] and [210] crystal directions. The vertical lattice parameters for the orthorhombic three-dimensional unit cells are given ($a = 489$ pm, $b = a \cdot \sqrt{2} = 692$ pm, $c = a \cdot \sqrt{5} = 1095$ pm). The non-equivalent atomic layers are named independently for the different facets (e.g. (100) $\text{Pd}_\alpha \neq (110)\text{Pd}_\alpha$). The (100) surface unit cell contains 8 atoms and is identical to the cubic unit cell of bulk PdGa (cf. Figure 2.1). However, when considering a bulk truncation at each of the four atoms of the upper half of the unit cell, an energetically identical truncation is found in the lower half of the unit cell and therefore we identify 4 non-equivalent atomic layers for this surface direction. This originates from the atomic coordination of the surface atoms after truncation, and is due to the $P2_13$ crystal structure. Accordingly, surface terminations constructed from truncation at distances of $a/2$ have the same surface energy. Comparison of the atomic structures reveals that the truncations are identical after in plane rotation of 180° . This will be important for the LEED-I(V) analysis, as the LEED data will be an average of both domains appearing with equivalent abundances. The presence of half unit cell steps is confirmed by the STM step heights shown in Figure 3.8 which correspond to $a/2$.

Also for the (110) surface unit cell of 16 atoms (cf. Figure 3.7) we find the layers of the top half of the orthorhombic (110) unit cell repeated in the lower half. Here, a simple lateral shift along the $\langle 1-10 \rangle$ direction exists between the structurally and energetically equivalent terminations, such that there is no domain averaging needed in the LEED-I(V) analysis shown below. Again, the terrace step heights measured in the STM topography confirm the existence of truncations at a layer distance of $b/2$. Additionally, STM reveals the existence of enlarged, row-like intrusions on the surface, with a depth of about 100 pm. A model for these surface vacancies is given later in this chapter, after the determination of the atomic surface structure by LEED-I(V).

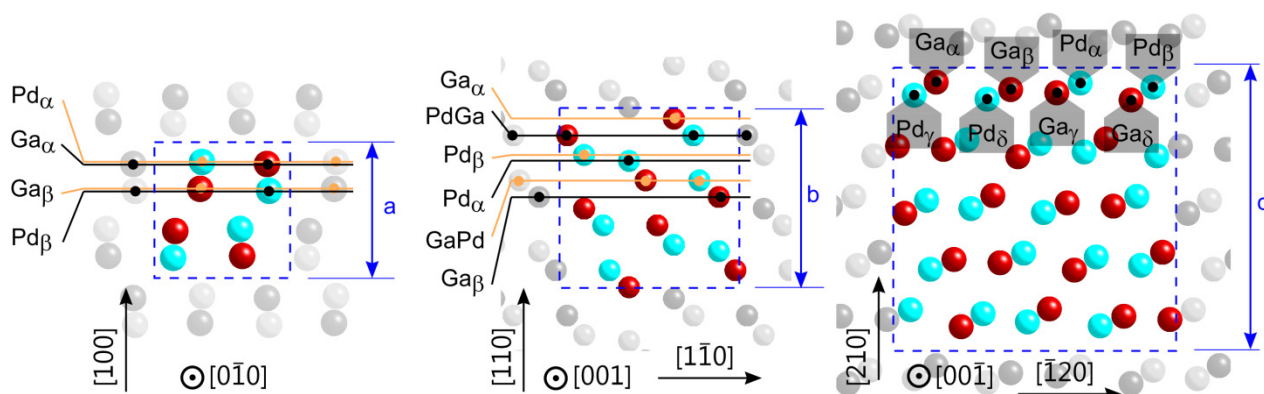


Figure 3.7 Side view of the orthorhombic (100), (110) and (210) unit cells of PdGa. Names for atomic layers are given, corresponding to bulk truncations. Unlike for the threefold surfaces, the layer stacking sequences (not the chirality!) are independent of the enantiomer form, for the unit cells presented here.

For the (210) surface unit cell, containing 40 atoms, energetically equivalent truncations are in a distance of $c/5$ perpendicular to the surface, as shown in Figure 3.7. The side-view shows that layers are rather compact and well-separated with each containing eight atoms per surface unit cell. There is a lateral registry

shift along the $\langle -120 \rangle$ direction for subsequent layers and the STM topography shows step heights corresponding to $c/5$, confirming the energy equivalent layers.

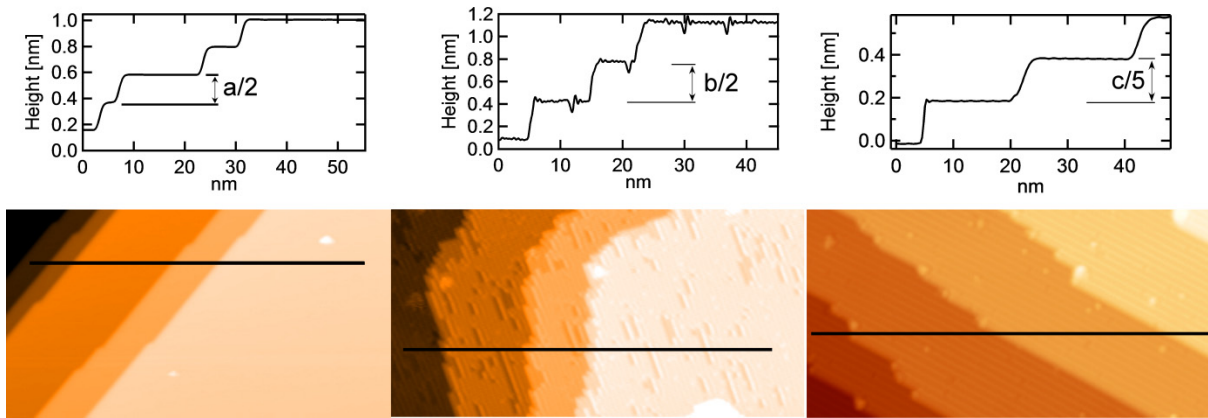


Figure 3.8 STM images of stepped terraces and height profiles of the PdGa(100), (110) and (210) surfaces (from left to right). The STM image of the (110) surface shows linear surface defects. (tunnel parameters, I_T, V_T from left to right: 3V, 1 nA ; 1V, 0.2 nA ; 0.6V, 0.75 nA)

The different symmetries of the three different facets are visible in the LEED patterns at selected electron beam energies shown in Figure 3.9. From the Bragg spot intensities, the two-fold rotational symmetry can be recognized for the (100) surface. In contrast, the (110) and the (210) surfaces exhibit no symmetries in the spot intensities. None of the three surfaces exhibits mirror symmetry, indicating that the bulk chirality of PdGa is perpetuated to the surface.

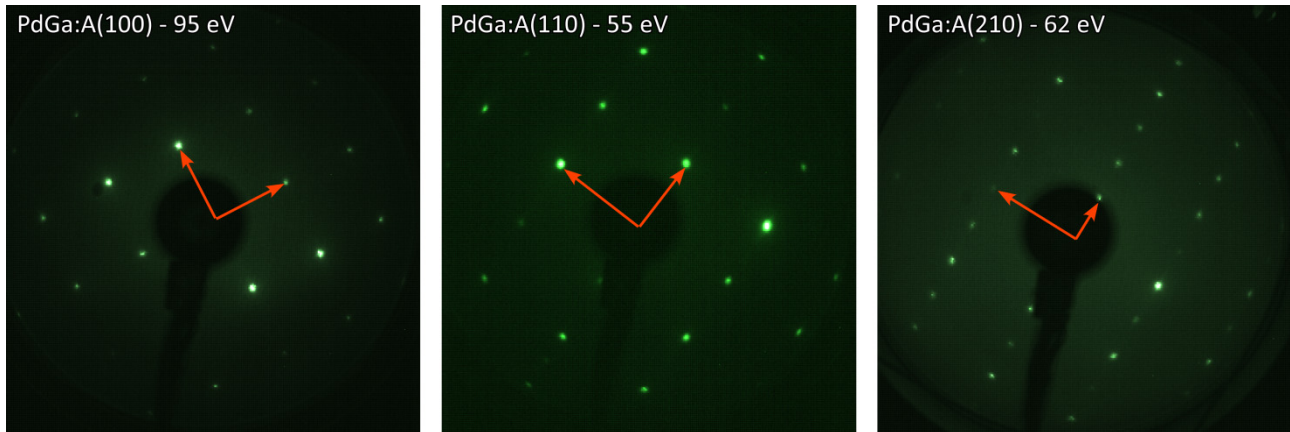


Figure 3.9 LEED patterns of PdGa:A(100), PdGa:A(110), and PdGa:A(210) surfaces. Reciprocal unit vectors are shown in red. The Bragg spot intensities at the selected energies reveal the different symmetries of the surfaces (see text for details).

The distinct step heights seen in the STM images reveal that the surfaces are well-defined and bulk-truncated. However, similar to the analysis of the threefold surfaces, it remains unclear which atomic layer terminates the surface. To approach this question, LEED-I(V) analysis was performed, using the DFT optimized bulk truncations shown in Figure 3.7 as model structures for the simulation of the I(V) profiles. Similar to the study on the threefold PdGa surfaces, possible rotations and mirror inversions (enantiomer form A and B) were taken into account. The phase shifts shown in Figure 2.6 were used to simulate the electronic scattering on Pd and Ga. The Pendry R-factors obtained from the comparison of the simulated and experi-

mental I(V) profiles are presented in Figure 3.10. For clarity, only the results for those sets of model structures that yield the best agreement are shown (same enantiomeric form and rotational orientation).

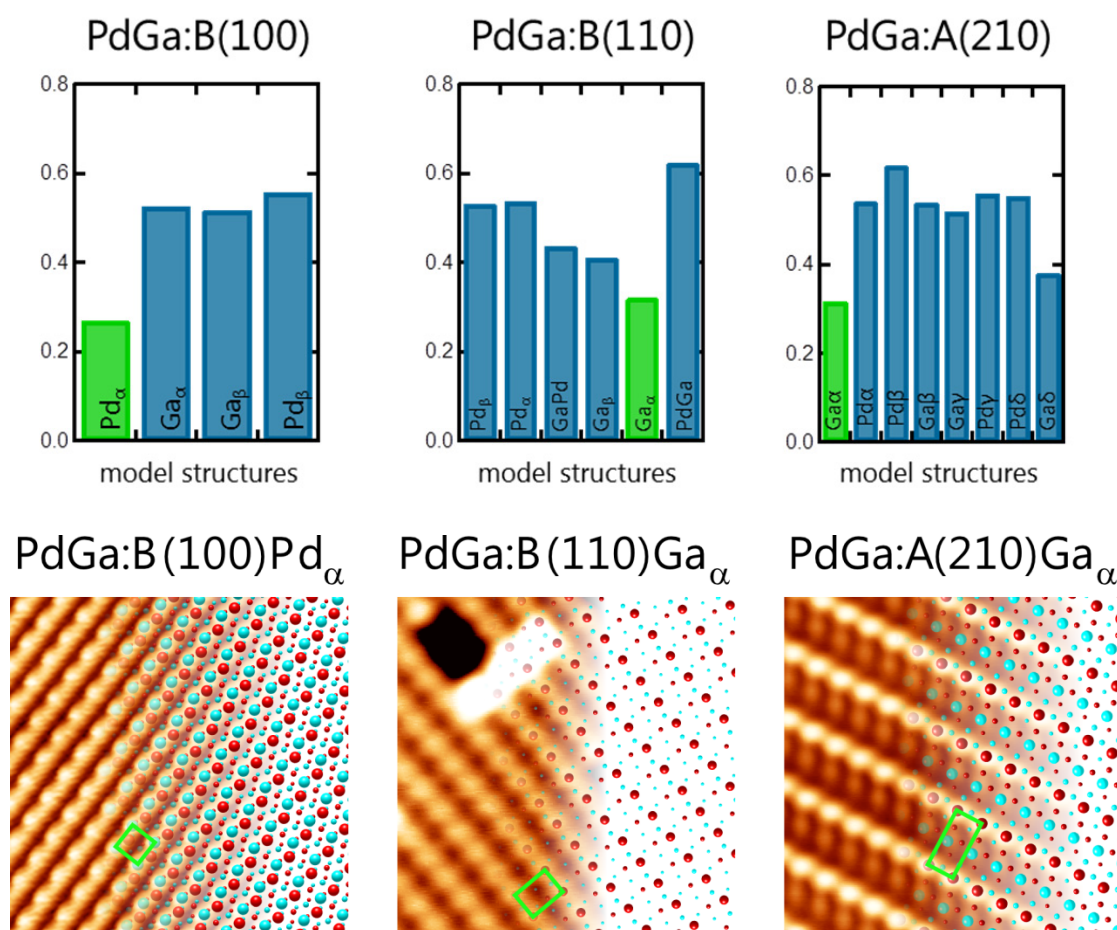


Figure 3.10 Comparison of LEED-I(V) and STM results for PdGa(100), (110) and (210). Top: Pendry R-factors from the comparison of the experimental LEED-I(V) spot profiles to the model structures for the three PdGa samples. Bottom: STM images (6 x 6 nm) of the clean surfaces in overlay with a ball model of the best fit structure from the LEED-I(V) comparison (Pd: cyan, Ga: red, tunnel parameters: I_T, V_T from left to right: 8 mV, 100 nA; 1.5 V, 3 nA; 0.8 V, 2 nA). The two-dimensional surface unit cells are shown in green.

For the (100) surface, LEED-I(V) results clearly indicate agreement of the Pd_α termination with experiment ($R_p=0.23$). The comparisons for the (110) and (210) surfaces show minimum R-Factors of 0.30 and 0.32, respectively. The agreement factors obtained here are not completely satisfactory, but compared to the other tested model structures they still yield an acceptable agreement of the bulk truncations being Ga_α in both cases. An additional confirmation for the identified structures can be found in recent publications by Gaspari⁸³, for PdGa(100) and (110), and by Krajci⁸⁴, on PdGa(210). In both studies, the most stable bulk-truncated surface terminations were determined using DFT, and the conclusions reach by the authors are compatible with those of LEED-I(V) presented in Figure 3.10. However, considering the open structure of the (110) and (210) surfaces, an evaporation of sub-surface atoms during preparation of the samples cannot be excluded. A more extensive study on possible non-bulk-truncated surface structures is currently undertaken, by taking into account a possible evaporation of sub-surface atomic layers.

The STM images shown in Figure 3.10 reveal the squared and rectangular unit cells of the (100) and the (110) and (210) surfaces, respectively. The surface terminations determined by LEED-I(V) are superimposed

as ball models in the right hand side of each image. The STM images of the PdGa(110) termination shown in Figure 3.8 and Figure 3.10 reveal that the surface termination exhibits irregularly, but frequently appearing surface defects with mostly linear shape, in parallel to the short axis of the unit cell. The defects are often found on step edges that are parallel to the long axis of the unit cell, as shown in Figure 3.11. The image shows three distinct height levels, the top layer in blue, the intermediate defect layer in gray, and the bottom layer in orange.

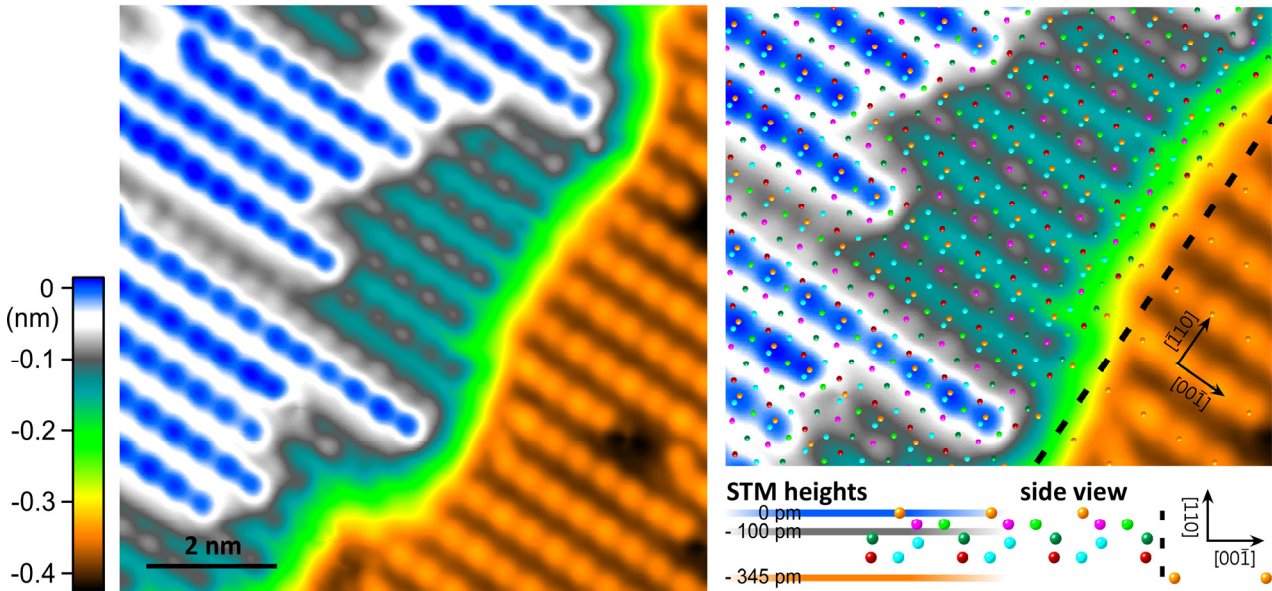


Figure 3.11 STM image of a PdGa:A(110) step edge showing an enlarged defect area. The rectangular lattice is visible in each of the three layers (top terrace: blue, defect layer: gray, bottom terrace: orange). Right: Section of the STM image in overlay with a structure model of the Ga_α termination, exhibiting a step edge at the dashed line. The side view given below shows the color code used for the atomic ball model (Ga_α : orange; PdGa: purple(Ga) and light-green(Pd); Pd_β : dark-green; lower layers: Pd: cyan, Ga: red; compare layer names Figure 3.7). The STM heights of the three layers are drawn next to the side view of the step edge model, revealing that the defect step appears at about 1/3 of the total step height.

The height difference between top and bottom terrace corresponds to the characteristic step height for the PdGa(110) surface. The intermediate defect layer (gray) appears 100 pm below the top terrace. This suggests that one or several atomic layers of the intact surface have desorbed, leading to the formation of this defect layer. To determine which atoms are absent, a surface structure model including a step edge (dashed line) is shown in overlay with the STM topography in the right of Figure 3.11. The side view of the atomic model structure below the image shows the color code that is used to represent different heights. In the overlay with the STM image, the topmost atoms of the model (orange) are aligned with the protrusions in the STM topography of the intact surface. Between the top and bottom of the step edge, a registry shift of $\frac{1}{2}$ unit cell is present along the $[-110]$ direction, which is visible in the STM topography and the atomic model.

The overlay shows that the atoms drawn in purple coincide with the protrusions of the defect layer, while no feature is visible at the position of the orange atoms or the light green atoms. Slight differences in the lateral positioning might be due to surface relaxation (the step model is constructed from the bulk structure without DFT relaxation). Therefore, we identify the defect structures as vacancies in the PdGa:A(111) Ga_α termination in which the topmost Ga atoms (orange) and the Pd atoms of the mixed PdGa

layer (light-green) are missing. At one end of the linear defect, the neighboring topmost layer atom appears misplaced with respect to the row of topmost atoms. This can be seen for the small defect in the bottom right corner of Figure 3.11.

The frequent appearance of the linear vacancy defects suggests that the surface energy of the respective termination must be similar to that of the Ga_α surface termination. Consequently, due to entropy, the defective termination contributes partially to the total surface area of the sample. An explanation for the vacancy structure can be derived from bond strength considerations. As described in Figure 2.2, each Pd(Ga) atom is surrounded by seven nearest neighbors of Ga(Pd), while the bond to one of the neighbors is shorter than to the others. Interestingly, the missing Pd-Ga pair of atoms is connected through this shortest Pd-Ga bond. It is thus reasonable, that the Ga_α termination is stabilized by this most stable bond, acting like an anchor to the topmost Ga atom.

In conclusion, we have identified the surface terminations of the PdGa(100), (110) and (210) by STM and LEED-I(V) using bulk truncations as model structures. The resulting surface geometries are discussed and summarized in the following Chapter 3.3, together with previously shown structures of the threefold surfaces.

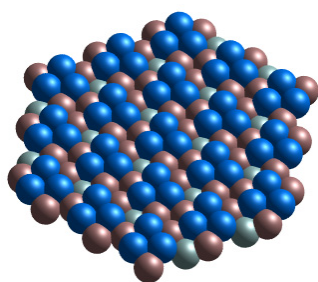
3.3 Comparison of the determined surface atomic structures

The previous subchapters have shown a comprehensive determination of the low-Miller index surfaces (111), (-1-1-1), (100), (110) and (210) structures of the intermetallic compound PdGa after preparation in UHV at high temperatures (870 K). Here, we summarize the results and compare the structures with regard to Pd site-isolation and symmetry. The following table shows the structure models of the five surfaces, together with the most important geometrical parameters.

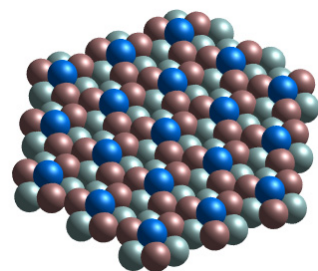
The facets exhibit Pd site separations of very different extents. In comparison, the most isolated sites are those of the threefold Pd₁ termination. The isolated Pd atoms are at the same time the ones with the lowest coordination with the bulk, as only 4 of the 7 bonds to the nearest neighbors of Ga remain after bulk truncation. Furthermore, these Pd atoms have a hexagonal arrangement, with a comparably large lattice constant of 0.69 nm, which results in an open surface structure for Pd₁, where even the 3rd outermost atomic layer seems accessible. The Pd₃ termination on the other hand exhibits a denser topmost layer, such that only the 2nd outermost atoms of Ga are accessible. The Pd trimers show the same hexagonal pattern, but they offer Pd hollow sites for adsorption of molecules. Therefore, the two surfaces are prototypical model systems to study the Pd site-isolation and the catalytic ensemble effect.

For the rectangular surfaces PdGa(100), (110) and (210), the smallest Pd separation in the outermost Pd layer is given by the bulk lattice parameter, and is therefore lower than on the threefold Pd₁ surface, while at the same time the coordination of the topmost Pd atoms is higher (5/7). Going from (100) to (110) to (210), the area of the surface unit cell increases, which results in more open surface structures. On the PdGa(210) surface, for example, four differently coordinated Pd atoms are accessible from the vacuum, potentially offering four different adsorption sites. In contrast, for the (100) surface, the 2nd topmost Pd layer is well below the topmost atomic layer, such that only one type of Pd adsorption site seems available. Furthermore, on the (210) surface the Pd atoms of various surface layers form continuous chains, while on PdGa(100) and (110) the Pd atoms appear in alternating chains of Pd and Ga atoms. Depending on the dimension of the respective unit cell, the chains show a different separation from each other. This leads to the question of how these chain-like atomic arrangements affect the steric hindrance of adsorbed molecules and if it is possible to exploit the atomic patterning of the substrates to catalyze chemical reactions with specific geometrical reaction pathways.

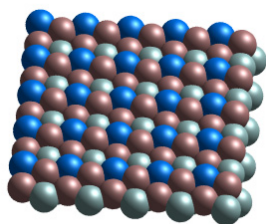
With regard to Pd site-isolation, all these surfaces can be compared to low-Miller index surfaces of clean Pd, where a large dataset of adsorption studies is available in literature. However, one has to keep in mind the electronic influence of Ga in the intermetallic compound, which alters the electronic structure considerably.²²

**PdGa:A(-1-1-1)Pd₃**

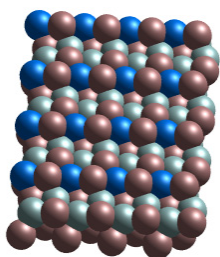
Symmetry: threefold rotational, no mirror symmetry
 Surface periodicity: hexagonal, lattice constant: 695 pm
 Topmost atomic layer: Pd₃ – trimers of Pd atoms
 2nd topmost atomic layer: Ga₃ – trimers of Ga (53 pm below Pd₁ layer)
 Site-isolation: d_{trimer-trimer} = 695 pm
 d_{Pd-Pd} = 301 pm (within trimer)
 Top Pd to bulk coordination: 4/7*
 Symmetry equivalent faces: PdGa:A(-111), (11-1), (1-11) → multiplicity: 3

**PdGa:A(111)Pd₁**

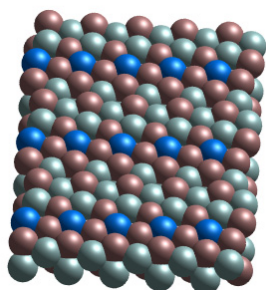
Symmetry: threefold rotational, no mirror symmetry
 Surface periodicity: hexagonal, lattice constant: 695 pm
 Topmost atomic layer: Pd₁ – single atoms of Pd
 2nd topmost atomic layer: Ga₃ – trimers of Ga (56 pm below Pd₁ layer)
 Site-isolation: d_{Pd-Pd} = 695 pm
 d_{Pd-Pd(3rd layer)} = 303 pm
 Top Pd to bulk coordination: 4/7
 Symmetry equivalent faces: PdGa:A(-1-11), (1-1-1), (-11-1) → multiplicity: 3

**PdGa:A(100)Pd_α**

Symmetry: no rotational or mirror symmetry
 subsequent terraces are rotated by 180°
 Surface periodicity: square, lattice constant: 489 pm
 Topmost atomic layer: Ga_α – single atoms of Ga
 2nd topmost atomic layer: Pd_α – single atoms of Pd (5 pm below Ga_α layer)**
 Site-isolation: d_{Pd-Pd} = 489 pm
 Top Pd to bulk coordination: 5/7
 Symmetry equivalent faces: PdGa:A(100), (010), (001), (-100), ... → multiplicity: 6

**PdGa:A(110)Ga_α**

Symmetry: no rotational or mirror symmetry
 Surface periodicity: rectangular, lattice constants: 489 pm, 695 pm
 Topmost atomic layer: Ga_α – single atoms of Ga
 2nd topmost atomic layer: PdGa – mixed layer of Pd and Ga (67 pm below Ga_α layer)
 Site-isolation: d_{Pd-Pd} = 489 pm (rows in distance of 695 pm)
 d_{Pd-Pd(3rd layer)} = 303 pm
 Top Pd to bulk coordination: 5/7
 Symmetry equivalent faces: PdGa:A(110), (-1-10), (-110), (1-10), ... → multiplicity: 12

**PdGa:A(210)Ga_α**

Symmetry: no rotational or mirror symmetry
 Surface periodicity: rectangular, lattice constants: 489 pm, 1095 pm
 Topmost atomic layer: Ga_α – single atoms of Ga
 2nd topmost atomic layer: PdGa – mixed layer of Pd and Ga (17 pm below Ga_α layer)
 Site-isolation: d_{Pd-Pd} = 489 pm, (rows in distance of 1095 pm)
 d_{Pd-Pd(3rd layer)} = 305 pm
 Top Pd to bulk coordination: 5/7
 Symmetry equivalent faces: PdGa:A(210), (-2-10), (-210), (2-10), ... → multiplicity: 12
 (not equivalent to PdGa:A(120) !)



* The value indicates how many of the seven nearest neighbors of the Ga cage (see Figure 2.2) remain after bulk truncation.

** In the DFT relaxation, the initially outermost atomic layer Pd_α relaxed towards the bulk. The energetically most favorable position is 5 pm below the 2nd layer Ga_α.

A final point to discuss is the structural manifestation of the bulk chirality of the PdGa intermetallic compound on the different low-Miller index faces. The chiral motives are depicted in Figure 3.12 for each surface. For the Pd₁ termination, the chirality is defined by the arrangement of the Ga and Pd trimers of the 2nd and 3rd outermost layers, respectively. This comprises a slight in-plane rotation of the triangles formed by Ga and Pd with respect to the hexagonal lattice of the surface unit cell (see Chapter 2 for a more detailed discussion). For the Pd₃ termination, an identical structural argument and manifestation of chirality holds for the outermost Pd trimers and 2nd outermost Ga trimers. In Chapter 6, the threefold surface structures are analyzed with respect to their ability to enantioselectively adsorb prochiral molecules.

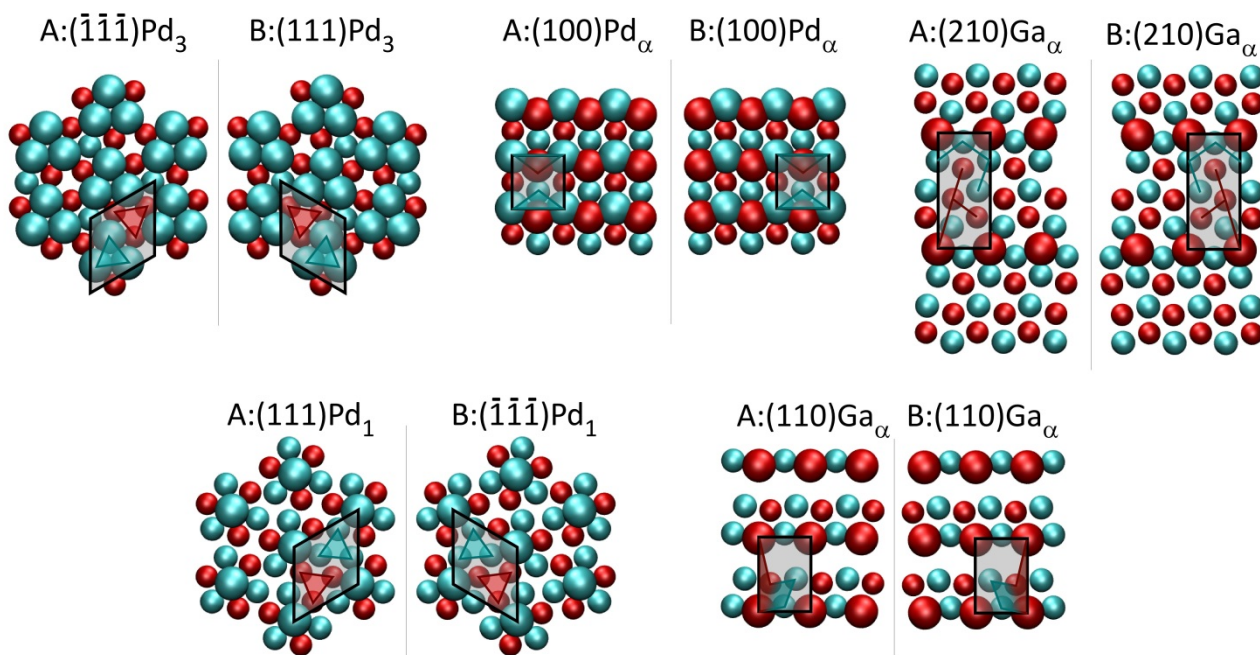


Figure 3.12 Chiral motives of the PdGa surfaces. Pd: cyan, Ga: red. Surface unit cells are drawn in black.

While the handedness of the threefold surfaces can be seen from the ball models shown in Figure 3.12, the (100) surface appears almost mirror symmetric with respect to a plane perpendicular to the surface and along one of the main crystal directions. However, a closer look on atomic distances reveals that also for this surface chirality is present. This is manifested in the Pd-Ga distance which is different for the [001] and the [00-1] directions, with 257 and 271 pm, respectively. To which extent this can lead to enantioselective adsorption has to be determined in experiment. A more obvious chiral arrangement of surface atoms is seen on the (110) and (210) surfaces, exhibiting open, more corrugated structures. For PdGa(210), the outermost Pd atoms are arranged in well-separated zig-zag lines, exhibiting a chiral pattern. Therefore, it would be highly interesting to investigate this surface with respect to the formation of chiral molecular polymers along these adsorption sites, which was recently demonstrated for non-chiral chains of alkanes on Au(110).⁸⁵

In summary, the surface structures of PdGa offer a wealth of differently coordinated and well-defined Pd surface sites which allow for studying the ensemble effect and chiral recognition in adsorption and catalysis. The determination of the atomic surface structures, presented here, is pivotal for studying molecules on the prototypal catalytic surfaces by experimental and computational means.

Chapter 4 CO as a test molecule for the identification of binding sites

The knowledge on the precise atomic surface structures allows extending the study on the PdGa surfaces towards the emerging question of which atoms or atomic ensembles of the determined surfaces offer the most stable adsorption configurations. Or in other words; which are the active adsorption sites? To this end, we investigated the binding of carbon monoxide to the PdGa single crystal surfaces. As CO is a frequently used probe molecule, a large set of reference data for comparison to different materials is available in literature.⁸⁶⁻⁸⁸

In a combined approach of STM, RAIRS and DFT, we determine the local morphology of the adsorbates and characterize the active sites by analysis of the vibrational modes of the CO molecules. The IR absorption peak positions and shapes allow to retrieve information on the CO binding configurations (on-top, bridge, hollow-site) and nearest neighbor interactions as a function of CO coverage, while the precise position of the molecule on the surface unit cell is resolved by STM. This powerful combination enabled us to evidence the site-isolation concept which is attributed to PdGa.

In Chapter 4.1, adsorption of CO on the threefold PdGa surfaces at low temperatures is investigated. This work is summarized in a publication as an article in *The Journal of Physical Chemistry C*. Chapter 4.2 shows additional data on very recent TPD experiments on CO desorption from the two surfaces. Thereafter, in Chapter 4.3, we focus on CO interactions on the structures showing less site-isolation, namely the (100) and (110) surfaces. CO adsorption on the PdGa(210) surface is subject to future studies and therefore not discussed here.

4.1 Publication: “Ensemble Effect Evidenced by CO Adsorption on the 3-Fold PdGa Surfaces” in *The Journal of Physical Chemistry C*

(Article reprinted with permission. Copyright © 2014, American Chemical Society)

Ensemble Effect Evidenced by CO Adsorption on the 3-Fold PdGa Surfaces

Jan Prinz,^{†,‡} Roberto Gaspari,^{†,§} Quirin S. Stöckl,^{||} Peter Gille,[⊥] Marc Armbrüster,[#] Harald Brune,[‡] Oliver Gröning,[†] Carlo A. Pignedoli,[†] Daniele Passerone,[†] and Roland Widmer^{*,†}

[†]Empa, Swiss Federal Laboratories for Materials Science and Technology, nanotech@surfaces Laboratory, Ueberlandstrasse 129, 8600 Dübendorf, Switzerland

^{||}Empa, Swiss Federal Laboratories for Materials Science and Technology, Nanoscale Materials Science, Ueberlandstrasse 129, 8600 Dübendorf, Switzerland

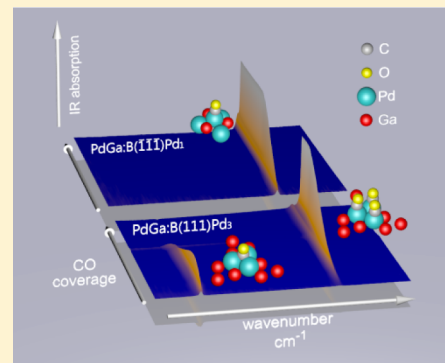
[⊥]Dept. für Geo- und Umweltwissenschaften, Ludwig-Maximilians-Universität, 80333 München, Germany

[#]Max-Planck-Institut für Chemische Physik fester Stoffe, 01187 Dresden, Germany

[‡]Institute of Condensed Matter Physics, Station 3, Ecole Polytechnique Fédérale de Lausanne (EPFL), 1015 Lausanne, Switzerland

S Supporting Information

ABSTRACT: The atomic structure and composition of a catalyst's surface have a major influence on its performance regarding activity and selectivity. In this respect, intermetallic compounds are promising future catalyst materials, as their surfaces exhibit small and well-defined ensembles of active metal atoms. In this study, the active adsorption sites of the 3-fold-symmetric surfaces of the PdGa intermetallic compound were investigated in a combined experimental and computational approach using CO as a test molecule. The PdGa(111) and $(-1-1-1)$ surfaces exhibit very similar electronic structures, but have Pd sites with very different, well-defined atomic coordination and separation. They thereby serve as prototypical model systems for studying ensemble effects on bimetallic catalytic surfaces. Scanning tunneling microscopy and Fourier transform infrared spectroscopy show that the CO adsorption on both surfaces is solely associated with the topmost Pd atoms and Ga acts only as an inactive spacer. The different local configurations of these Pd atoms dictate the CO adsorption sites as a function of coverage. The experimental results are corroborated by density functional theory and illustrate the site separation and ensemble effects for molecular adsorption on intermetallic single crystalline surfaces.



1. INTRODUCTION

Surface science methods allow for studying the structure of catalytic surfaces on the atomic level, and in some cases even under reaction pressures.^{1,2} This ability expanded the understanding of heterogeneous catalysis and led to many ideas on how to structure catalyst surfaces to improve their performance.^{3–6} An important aspect of research in catalysis, besides achieving high activity, is improving selectivity. One proposed enhancement is the dilution of the active (metal) species with less active spacer atoms. This site isolation concept consists of forming isolated catalytic centers of reduced size, leading to a limited number of adsorption configurations for the reactants, which is called the “ensemble effect”.^{7–9} The number of reaction pathways emerging from these active centers is thereby reduced, resulting in an increased selectivity, as compared to metal surfaces consisting of a single element.

In addition to this ensemble effect, the electronic structure of the active species is influenced by the nature and concentration of the spacer atoms, which is known as the “ligand effect”.^{7,9} Since atomic and electronic structure of a surface are always interconnected, it is difficult to unambiguously impute a given

experimental observation purely to the ligand-, and/or to the ensemble effect of a catalytic surface.

One model system in this respect is bimetallic surface alloys, which have a random spatial distribution of active sites.^{3,7–11} Intermetallic compounds (IMCs) are a second model system, which have an ordered crystal structure. Additionally, they exhibit a higher energy of formation, which potentially increases surface stability.^{3,10–12} In this respect, the PdGa IMC has recently received considerable interest due to its high activity, stability, and selectivity in the semihydrogenation of acetylene.^{12,13} This reaction is industrially important,¹⁴ as it is a crucial step in polyethylene production, where currently Ag–Pd alloy catalysts are applied. In the context of the site isolation concept, also for PdGa, Pd is supposed to take the role of the catalytically active species and Ga the role of the spacer atom.

In a recent publication,¹⁵ we reported on the 3-fold surfaces of the PdGa IMC. The two crystallographically opposed

Received: February 13, 2014

Revised: May 14, 2014

Published: May 14, 2014

surfaces, (111) and $(-1-1-1)$, exhibit equal surface symmetry, equal lattice parameters, and very similar electronic structure, but different atomic configurations of the Pd atoms. On one surface separated Pd trimers are present, while the other is terminated by isolated, single Pd atoms. This particular situation allows for investigating the pure structural ensemble effect, while the influences from the ligand effect can be neglected.

On the other hand, studying the ligand effect can be accomplished by exchanging the chemical species of the spacer atoms, while keeping the atomic surface structure unchanged. Whereas the realization of this concept is experimentally challenging, it has been used in theoretical studies, such as in quantum chemical calculations performed by Nørskov et al.¹⁶ This computational screening for improved catalysts reveals trends for the selection of the most promising constituent materials.

In this study, we present experimental and computational results of CO adsorption on the PdGa:B $(-1-1-1)$ Pd₁ and PdGa:B(111)Pd₃ surfaces.¹⁵ These two surfaces serve as prototypical system to study the ensemble effect because they expose two different terminations. One consisting of single palladium atoms (Pd₁) and the second of palladium trimers (Pd₃). The effects of the Pd site structure are directly observed in the vibrational frequency of the adsorbed CO as a function of coverage as measured by Fourier transform infrared spectroscopy (FTIR). Scanning tunneling microscopy (STM) provides local information on the adsorption geometry and allows an unambiguous interpretation of the vibrational spectroscopy. Density functional theory (DFT) calculations agree with the experimental results and allow for an in depth understanding of the bonding situation of CO to the single atomic and trimer Pd sites.

We observe strong site isolation effects on both PdGa surfaces, which are most clearly expressed on the PdGa:B $(-1-1-1)$ Pd₁ surface, where the full CO coverage at low-temperature (77 K) and pressure (10^{-6} mbar range) is about 15% of that of Pd(111). To the best of our knowledge, this is the first experimental demonstration of the ensemble effect on well-defined intermetallic compound surfaces, which is a promising class of materials for the development of future catalysts.

2. METHODS

Experiments. The growth and surface preparation of the PdGa single crystals has been described in detail previously, so that only a brief summary is given.^{17,18} The PdGa single crystal surfaces were cleaned by Ar-ion sputtering and high temperature annealing (870 K) cycles.^{15,19} The STM measurements were performed with an Omicron low-temperature (LT-) STM at a base pressure below 5×10^{-11} mbar using a mechanically cut Pt/Ir-tip.

FTIR absorption spectroscopy measurements were recorded with a Bruker Vertex 70v/80v spectrometer in reflection-absorption mode (RAIRS). CO (purity 4.7, CANGas) was dosed on the sample at 90 K (± 10 K) by backfilling the main chamber.

Simulations. All simulations were performed within DFT in the mixed Gaussian Plane Waves framework as implemented in the CP2K code (see SI for further details).²⁰ We used the Perdew–Burke–Ernzerhof (PBE)²¹ parametrization for the exchange correlation functional.

PdGa slabs were simulated in the repeated slab geometry.²² Orthorhombic simulation cells of 23 and 24 atomic PdGa layers were used for simulations of the PdGa:B(111) and PdGa:B $(-1-1-1)$ surface, respectively. The positions of the lowest eight layers were fixed in the structure optimization. About 3 nm of vacuum was added above the adsorbate atoms. The lateral dimension of the cell corresponds to 12 hexagonal surface unit cells. The ground state adsorption energies and structures were computed by relaxing all atomic positions until forces were lower than 0.05 eV/nm. IR spectra were calculated using finite differences starting from the equilibrium adsorption geometries.²⁰

3. RESULTS AND DISCUSSION

A first approach to determine the adsorption sites of CO on PdGa:B(111)Pd₃ and $(-1-1-1)$ Pd₁ was performed by LT-STM measurements. Figure 1 shows STM images of both

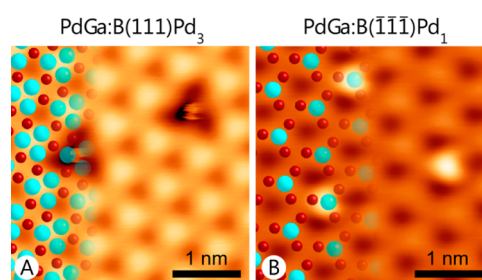


Figure 1. STM images of CO adsorbed on Pd₃ (A) and Pd₁ (B). The atomic surface structure is overlaid on the left-hand side of each image (Pd: cyan, large; Ga: red, small). The top layer consists of Pd trimers, for Pd₃ (A), and single Pd atoms for Pd₁ (B). The second layer consists of Ga trimers for both surface orientations. On Pd₃ (A), two CO molecules are present, appearing as triangular depressions. On Pd₁ (B), three CO molecules are present, appearing as protrusions (Tunneling parameters: A: -7 mV, 2 nA; B: -1 V, 35 nA).

surfaces at very low CO coverage. The surface Pd atoms are imaged as protrusions.¹⁵ In combination with low energy electron diffraction (LEED) measurements and STM simulations, the atomic structure of the clean surface is identified with regard to lateral position and orientation,¹⁵ and overlaid on the left-hand side of each image for the two surfaces. The samples were exposed to CO during imaging at 78 K, which allowed for identifying single adsorbed CO molecules. On Pd₃, CO molecules appear as triangular depressions with a central maximum, whereas on Pd₁, they are imaged as bright protrusions. According to the atomic structure overlay, individual CO molecules adsorb in the 3-fold Pd hollow site on Pd₃, and at the on-top Pd site on Pd₁.

To complement these atomic scale observations and to study the adsorption kinetics, RAIRS experiments as a function of CO coverage were carried out. As shown in Figure 2, a single, CO coverage independent, absorption peak is observed for the Pd₁ surface. For the Pd₃ surface, two separate, coverage dependent peaks are observed. Comparison of the peak positions with RAIRS of CO on Pd(111) allows for an assignment of the peaks at higher and lower wavenumbers found for CO/Pd₃ to on-top and hollow site adsorption, respectively.^{3,23} This assignment is substantiated by the sequence of binding energies of the optimized adsorption configurations found by DFT for adsorption of one, two, and three CO per Pd trimer (see Table 1 and Supporting

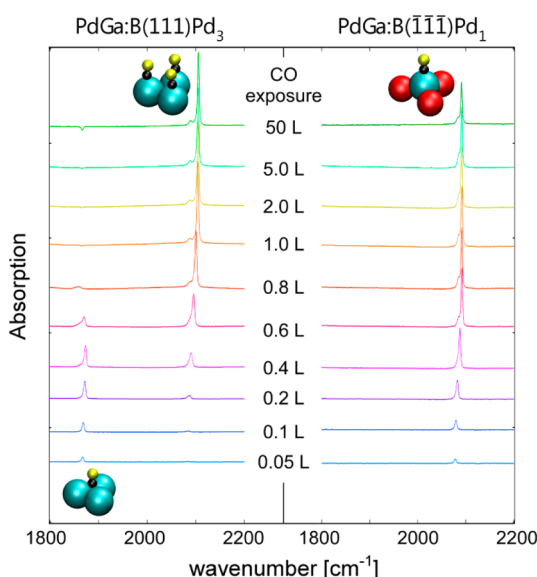


Figure 2. IR absorption spectra as a function of wavenumber and CO exposure at 90 K on Pd₃ (left) and Pd₁ (right). Insets next to the peaks show the respective adsorption configuration (C in black, O in yellow).

Information). Therefore, the series of RAIRS spectra for the CO/Pd₃ can be interpreted as a transition from hollow to on-top site with increasing exposure.^{3,23} A qualitative comparison to similar experiments of CO/Pd(111) reveals that peak shapes are sharper and coverage-dependent peak shifts are much smaller for the CO/PdGa system presented here. Indeed, on

Table 1. Experimental and Theoretical IR Absorption Peak Positions for CO on the Different Sites of the PdGa Surfaces and Calculated Binding Energies^a

	CO/Pd ₃ (hollow site)	CO/Pd ₃ (on-top site)	CO/Pd ₁ (on-top site)
ν_{exp} (cm ⁻¹)	1868–1874	2084–2105	2078–2092
ν_{th} (cm ⁻¹)	1822	2039 (2 CO) 2047 (3 CO)	2032
E_{b}/CO (eV)	1.59	1.28 (2 CO) 1.25 (3 CO)	1.37
Pd–C bond order	1.34 (3 × 0.45)	0.82	0.83
C–O bond order	0.91	0.98	0.95

^aThe covalent bond orders are computed according to Angyan.²⁹ For a CO molecule in the gas phase the theory predicts a value of 1.51, accounting for the polar character of the C–O bond (2.89 for the covalent triple bond in C₂H₂).

CO/Pd(111), a full hierarchy of bonding sites is observed (hollow, bridge, and on-top sites), with a coverage-dependent spectrum influenced by long-ranged intermolecular interactions,^{23–25} leading to broadened IR-absorption features. Accordingly, our RAIRS data clearly indicates a suppression of CO–CO interactions on both PdGa surfaces. This is most pronounced in the CO/Pd₁ case, where the on-top sites are separated by 0.69 nm, but is also seen for CO/Pd₃, where at full coverage, the interaction is mainly reduced to the three neighboring CO molecules on the same trimer. Additionally, the Pd–Pd nearest neighbor distance of 0.3 nm within such a Pd trimer is 10% larger than in Pd(111).¹²

A summary of the experimental IR vibration frequencies is shown in Table 1, together with simulated frequencies from DFT for the most stable adsorption geometries, which corroborate the experimental vibrational assignments. The ranges given for the experimental frequencies represent the coverage-dependent variations in peak positions. The computed vibration frequencies underestimate the experimental values by a constant scaling of $2.80 \pm 0.02\%$. This is a common problem in DFT with PBE approximation (see refs 11 and 26) and can vary according to the parametrization employed.²⁷ However, the agreement of the relative frequencies by less than 0.5% confirms the hypothetical structure model used in DFT.

The combined experimental and theoretical data enables us to interpret the CO/PdGa(111) and (–1–1–1) systems as follows: On Pd₃, the adsorption site is coverage dependent, the 3-fold hollow site is occupied at low coverage, and the on-top site is occupied if two or three CO are present on one Pd trimer. Pd₁ allows only for on-top adsorption on the terminating Pd atom. According to DFT, in all CO binding conformations the molecular axis is oriented perpendicular to the surface (see insets in Figure 2).

Along with this interpretation, details in the RAIRS results shown in Figure 2 can be explained. The frequency shift from initial to full coverage of the peaks originating from on-top site species amounts to 14 cm⁻¹ for CO/Pd₁ and 21 cm⁻¹ for CO/Pd₃. The full coverage is obtained after exposure to 0.6 and 1.2 L for Pd₁ and Pd₃, respectively. On Pd₁, the shift is assigned to interactions with the nearest neighbor adsorbates (1–6 CO) separated by 0.69 nm. For CO adsorbed at the on-top site on Pd₃, the main contribution to the shift is attributed to the occupancy increase from two to three CO per trimer at a mutual distance of 0.31 nm.

Both on-top site peaks exhibit a shoulder at lower wavenumbers, which for CO/Pd₁ shifts along with the main peak, but for CO/Pd₃, remains at a fixed position. These side peaks are assigned to CO molecules neighboring, for example, a surface vacancy¹⁵ or a step edge.²⁸

The coverage-dependent transition from hollow to on-top site adsorption and the small vibrational shifts due to weak CO–CO interactions are in agreement with high resolution electron energy loss spectroscopy (HREELS) of CO adsorbed on PdAg surface alloys of different Pd concentrations.¹⁰

Additionally, the CO binding energies shown in Table 1 are comparable to those computed for PdAg/Pd(111) surface alloys.¹¹ Using the same PBE functionals, Mancera et al.¹¹ found on-top site binding energies of 1.37 and 1.29 eV for CO on single Pd atoms and trimers, respectively. These energies are in very good agreement with our calculations (1.37 and 1.25 eV) for PdGa. On the other hand, the hollow site adsorption energy deviates with 1.97 eV for PdAg from the value of 1.59 eV found for PdGa. This difference might be a consequence of the reduced Pd–Pd distance in the trimer of the surface alloy, and/or of the different ligand effects of Ag and Ga.

To get a broader insight into the adsorption energy landscape, the binding energies for other possible sites were calculated using DFT. A summary of all tested configurations is given in the Supporting Information. On Pd₁, the trimers of Pd atoms, lying 143 pm below the Pd₁ termination, are found less favorable for CO adsorption ($E_{\text{b}} = 0.88$ eV), since the atoms of this third-outermost layer are almost completely coordinated with bulk atoms. Furthermore, CO adsorbed on the hollow site of the Ga trimers of the second-outermost layer (53 and 56 pm below the surface layer on Pd₃ and Pd₁, respectively) was

computed to have a weaker binding energy on both terminations ($E_b = 0.08$ eV for Pd₃ and 0.56 eV for Pd₁). To investigate the absence of CO bridge site bonding on Pd₃, the binding energies for two CO molecules in “top-and-bridge” and “top-and-top” configuration on the Pd trimer were computed. For both situations, a local energetic minimum was found, with the “top-and-top” configuration being preferred by 63 meV per CO molecule. A single molecule located on the trimer in a Pd–Pd bridge site was found unstable in the DFT optimization. The large relative differences in binding energies between the first and the second preferred adsorption sites found by DFT confirms the experimental observation that both surfaces exhibit saturation after adsorption of one and three CO molecules per surface unit cell, respectively.

Krajci and Hafner conducted a computational study on the structure and adsorption properties of the 3-fold PdGa surface.³⁰ Their adsorption energies for CO on the Pd₁ and Pd₃ surface are in agreement with our DFT derived values summarized in Table 1, with a shift to lower binding energies, which is consistent with the different parametrization for the PBE approximation. However, in their study they concluded Ga surface terminations to be energetically more favorable than the Pd ones, which we find to be incompatible with experiment (see Supporting Information).^{15,19}

We studied the coverage dependence for CO/Pd₃ in more detail by LT-STM. Images at higher coverage than in Figure 1 reveal four different CO occupations per Pd-trimer, namely, one, two, three, and no CO molecules per trimer (cf. Figure 3). As already shown in Figure 1, we find that one CO per Pd trimer appears as a single protrusion that is centered on the Pd₃ trimer. If two CO molecules are adsorbed on a Pd trimer, the imaged adsorbate has a larger apparent height and an elliptical shape (Figure 3A). The center of the protrusion is found slightly off the Pd₃ hollow sites located at the intercepts of the red grid (Figure 3B). Additionally, their long semiaxis is not oriented along the $\langle 1-10 \rangle$ directions, but along the lines connecting two of the three Pd atoms in the trimer. The sketch in Figure 3C shows the orientation of trimers as determined by LEED-I(V).¹⁵ Together with the change in IR-absorption frequency, we conclude that adding one more CO molecule per Pd₃ converts the 3-fold hollow site to three on-top sites of which two are occupied. Higher coverage leads to wider, 3-fold symmetric protrusions (Figure 3D), exhibiting the same orientation as the Pd₃ trimers, which is consistent with the hypothesis of three CO molecules in the on-top site configuration on the topmost Pd atoms. Accordingly, STM confirms on a local scale the adsorption site sequence derived from RAIRS and DFT simulations for CO/Pd₃. As seen from the STM topographies for CO on Pd₃ and Pd₁, shown in Figures 1 and 3, CO molecules are found exclusively at the positions of the protrusions on the clean surfaces. As these protrusions coincide with the outermost Pd atoms,¹⁵ we find no indication for bonding of CO to Ga.

The presented data show different expression of the active site separation on the Pd₃ and Pd₁ terminations. At low coverage, the adsorption sites have the same separation on both surfaces (one CO per unit cell), but are of a different type, namely, on-top site for Pd₁ and hollow site for Pd₃. However, the Pd₃ surface also has three adjacent Pd on-top adsorption sites that are populated at high coverage; therefore it can accommodate three times as many CO than the Pd₁ surface. This means that at full CO coverage the minimum CO–CO

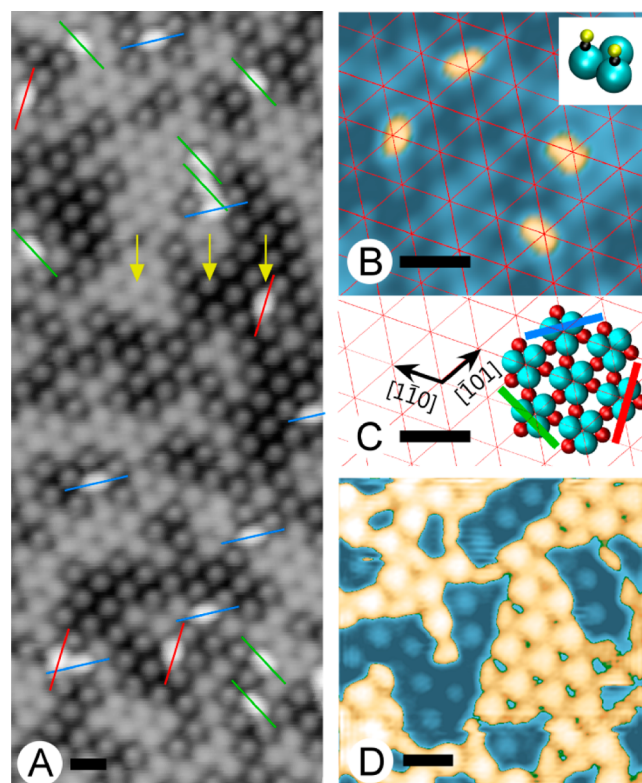


Figure 3. (A) LT-STM image of a partially CO covered PdGa:B(111)-Pd₃ surface. A Pd₃ trimer with no CO (left arrow) appears in light-gray. A trimer with one CO (center arrow) appears as a well localized protrusion with lower apparent height, and a trimer with two CO (right arrow) as elongated white protrusion. The different elongated protrusions appear in three distinct directions indicated by the colored lines. These directions coincide with the “edges” of a Pd trimer (see C). (B) Detail showing that elliptical protrusions are off center with respect to the Pd₃ lattice. (C) Surface atomic structure derived from LEED-I(V).¹⁵ (D) Increased CO exposure leads to protrusions with triangular envelopes, that is, fully occupied trimers. Scale bars correspond to 1.0 nm. In B and C, a different color-scale was chosen to emphasize the shape of the CO protrusions (beige; tunneling parameters: (A, B) 0.2 V, 0.5 nA; (D) −2.5 V, 0.5 nA).

separation is 0.69 nm for the Pd₁ surface and only 0.31 nm for the Pd₃ surface.

To investigate the chemical behavior of the active sites we characterized the nature of the binding of CO to the Pd sites by computing the covalent bond-order index, following the approach by Angyan et al.²⁹ in the framework of Bader’s topological theory. The method is basis-set independent and takes into account bond ionicities, leading to reduced bond orders for polar covalent bonds. For CO adsorbed on PdGa, the computed covalent Pd–C bond order reveals that the bonding character in the case of one CO molecule per surface unit cell is remarkably different on the two surfaces, whereas the on-top site bond configuration for high coverage is very similar. In the Pd₁ case, our analysis indicates a bond order of 0.83 for the Pd–C bond (where a value of 2.89 would correspond to C–C triple bond, as in acetylene). In the Pd₃ case, when CO is adsorbed at the hollow site of the trimer, each Pd atom contributes a bond order of 0.45, for a total bond order of 1.34. Indeed, the calculated adsorption energy in this configuration is higher compared to Pd on-top and the IR active CO vibrational mode has a lower frequency due to the weakened C–O bond, which is indicated by a small reduction

of the C–O covalent bond order (cf. Table 1). In the case of three CO per Pd₃, the situation is again similar to CO on Pd₁, which is reflected in binding energy, vibrational mode frequency and a comparable bond-order of 0.82 and 0.83, respectively.

For both 3-fold PdGa surfaces the site isolation concept is realized for the CO adsorption. This can be seen in particular by comparing it to CO adsorption on Pd(111). In the case of the Pd₁ surface, full CO coverage is obtained at a much lower molecular density of 2.41 CO/nm² compared to 15.26 CO/nm² for Pd(111), with both cases having on-top Pd adsorption. In the case of the Pd₃ surface the CO adsorption proceeds from hollow site adsorption on the Pd trimer to on-top site adsorption with increasing coverage, reaching a maximum CO density of 7.23 CO/nm². Although the CO density on the Pd₃ surface is a factor of 2 lower compared to Pd(111), the nearest CO–CO distance is only 10% different (Pd₃, 0.31 nm; Pd(111), 0.275 nm). The reason for the very different molecular saturation densities is the large separation between the trimers on Pd₃. While the local Pd trimers on Pd₃ do not show bridge site adsorption for CO, this is observed on Pd(111). Therefore, Pd(111) exhibits an almost continuous transition from hollow to bridge to on-top site adsorption with increasing coverage.^{23,24}

This transition was also reported for Pd ensembles on PdAu and PdAg surface alloys.^{3,8,10} In these alloys, the Pd ensemble size depends on the random local Pd concentration at the surface, whereas in the PdGa (111) and (–1–1–1) surfaces, size and separation are given by the crystal structure and do not allow for CO bridge site adsorption. However, the Pd ensembles found in the partially covalently bound IMC retain their adsorption properties, as adsorption sites, energy, and vibrational modes compare for CO adsorbed on the IMC and on the surface alloys, for Pd ensembles of equal size.

4. CONCLUSIONS

We compared the two 3-fold-symmetric surfaces of the PdGa IMC with regard to active adsorption site separation and ensemble effect. CO was used as a test molecule, confirming the active site isolation¹² and revealing differences in the ensemble effect for the two surface structures exhibiting single atoms (Pd₁) and trimers (Pd₃). Our combined analysis of STM, RAIRS, and DFT shows that Pd₁ provides, independent of coverage, only one on-top site for CO, whereas Pd₃ allows for hollow site adsorption at low coverage and on-top site adsorption at high coverage. This leads to a maximum occupancy of one and three CO molecules per surface unit cell for Pd₁ and Pd₃, respectively, while no adsorption is taking place on Ga related sites. This observation underlines the hypothesis that the Ga indeed only assumes the role of a spacer atom with regard to the CO adsorption properties.

Due to the similar electronic structure of these surfaces, the differences in their bonding properties are mainly attributed to the geometric ensemble effect. Furthermore, the comparison with CO adsorption studies on Pd-containing surface alloys supports the argument of a dominating ensemble- over the ligand effect in this IMC. This concept of the ensemble effect in PdGa combined with the active site isolation represents a paradigm for the study of selective catalytic reactions.

■ ASSOCIATED CONTENT

Supporting Information

Data on STM topography contrast of CO, details on the computations, and a verification of the PdGa:B(111)Pd₃ and PdGa:B(–1–1–1)Pd₁ surface structures with respect to ref 30. This material is available free of charge via the Internet at <http://pubs.acs.org>.

■ AUTHOR INFORMATION

Corresponding Author

*E-mail: roland.widmer@empa.ch. Tel.: +41 58 765 4745.

Present Address

[§]Drug Discovery and Development, Italian Institute of Technology, Via Morego 30, 16163 Genova, Italy (R.G.).

Notes

The authors declare no competing financial interest.

■ ACKNOWLEDGMENTS

We gratefully acknowledge funding by the Swiss National Science Foundation under Contract 200021-129511 and support by the Swiss National Supercomputing Center (CSCS).

■ REFERENCES

- (1) Bocklein, S.; Gunther, S.; Wintterlin, J. High-Pressure Scanning Tunneling Microscopy of a Silver Surface During Catalytic Formation of Ethylene Oxide. *Angew. Chem., Int. Ed.* **2013**, *52*, 5518–5521.
- (2) Herbschleb, C. T.; Bobaru, S. C.; Frenken, J. W. M. High-Pressure STM Study of NO Reduction by CO on Pt(100). *Catal. Today* **2010**, *154*, 61–67.
- (3) Chen, M. S.; Kumar, D.; Yi, C. W.; Goodman, D. W. The Promotional Effect of Gold in Catalysis by Palladium–Gold. *Science* **2005**, *310*, 291–293.
- (4) Somorjai, G. A. Surface Science and Catalysis. *Science* **1985**, *227*, 902–908.
- (5) Ertl, G.; Freund, H. J. Catalysis and Surface Science. *Phys. Today* **1999**, *52*, 32–38.
- (6) Kyriakou, G.; Boucher, M. B.; Jewell, A. D.; Lewis, E. A.; Lawton, T. J.; Baber, A. E.; Tierney, H. L.; Flytzani-Stephanopoulos, M.; Sykes, E. C. H. Isolated Metal Atom Geometries as a Strategy for Selective Heterogeneous Hydrogenations. *Science* **2012**, *335*, 1209–1212.
- (7) Sachtler, W. M. H. Chemisorption Complexes on Alloy Surfaces. *Catal. Rev.: Sci. Eng.* **1976**, *14*, 193–210.
- (8) Ruff, M.; Takehiro, N.; Liu, P.; Norskov, J. K.; Behm, R. J. Size-specific Chemistry on Bimetallic Surfaces: A Combined Experimental and Theoretical Study. *ChemPhysChem* **2007**, *8*, 2068–2071.
- (9) Gao, F.; Goodman, D. W. Pd–Au Bimetallic Catalysts: Understanding Alloy Effects from Planar Models and (Supported) Nanoparticles. *Chem. Soc. Rev.* **2012**, *41*, 8009–8020.
- (10) Ma, Y. S.; Diemant, T.; Bansmann, J.; Behm, R. J. The Interaction of CO with PdAg/Pd(111) Surface Alloys: A Case Study of Ensemble Effects on a Bimetallic Surface. *Phys. Chem. Chem. Phys.* **2011**, *13*, 10741–10754.
- (11) Mancera, L. A.; Behm, R. J.; Gross, A. Structure and Local Reactivity of PdAg/Pd(111) Surface Alloys. *Phys. Chem. Chem. Phys.* **2013**, *15*, 1497–1508.
- (12) Kovnir, K.; Armbrüster, M.; Teschner, D.; Venkov, T. V.; Szentmiklosi, L.; Jentoft, F. C.; Knop-Gericke, A.; Grin, Y.; Schlögl, R. In Situ Surface Characterization of the Intermetallic Compound PdGa: A Highly Selective Hydrogenation Catalyst. *Surf. Sci.* **2009**, *603*, 1784–1792.
- (13) Osswald, J.; Kovnir, K.; Armbrüster, M.; Giedigkeit, R.; Jentoft, R. E.; Wild, U.; Grin, Y.; Schlögl, R. Palladium–Gallium Intermetallic Compounds for the Selective Hydrogenation of Acetylene, Part II: Surface Characterization and Catalytic Performance. *J. Catal.* **2008**, *258*, 219–227.

- (14) Borodzinski, A.; Bond, G. C. Selective Hydrogenation of Ethyne in Ethene-Rich Streams on Palladium Catalysts, Part 2: Steady-State Kinetics and Effects of Palladium Particle Size, Carbon Monoxide, and Promoters. *Catal. Rev.: Sci. Eng.* **2008**, *50*, 379–469.
- (15) Prinz, J.; Gaspari, R.; Pignedoli, C. A.; Vogt, J.; Gille, P.; Armbrüster, M.; Brune, H.; Gröning, O.; Passerone, D.; Widmer, R. Isolated Pd Sites on the Intermetallic PdGa(111) and PdGa(−1−1−1) Model Catalyst Surfaces. *Angew. Chem., Int. Ed.* **2012**, *51*, 9339–9343.
- (16) Norskov, J. K.; Bligaard, T.; Rossmeisl, J.; Christensen, C. H. Towards the Computational Design of Solid Catalysts. *Nat. Chem.* **2009**, *1*, 37–46.
- (17) Gille, P.; Ziemer, T.; Schmidt, M.; Kovnir, K.; Burkhardt, U.; Armbrüster, M. Growth of Large PdGa Single Crystals from the Melt. *Intermetallics* **2010**, *18*, 1663–1668.
- (18) Armbrüster, M.; Borrmann, H.; Wedel, M.; Prots, Y.; Giedigkeit, R.; Gille, P. Refinement of the Crystal Structure of Palladium Gallium (1:1), PdGa. *Z. Kristallogr.: New Cryst. Struct.* **2010**, *225*, 617–618.
- (19) Rosenthal, D.; Widmer, R.; Wagner, R.; Gille, P.; Armbrüster, M.; Grin, Y.; Schlögl, R.; Gröning, O. Surface Investigation of Intermetallic PdGa(−1−1−1). *Langmuir* **2012**, *28*, 6848–6856.
- (20) VandeVondele, J.; Krack, M.; Mohamed, F.; Parrinello, M.; Chassaing, T.; Hutter, J. QUICKSTEP: Fast and Accurate Density Functional Calculations Using a Mixed Gaussian and Plane Waves Approach. *Comput. Phys. Commun.* **2005**, *167*, 103–128.
- (21) Perdew, J. P.; Burke, K.; Ernzerhof, M. Generalized Gradient Approximation Made Simple. *Phys. Rev. Lett.* **1997**, *78*, 1396–1396.
- (22) Pickett, W. E. Pseudopotential Methods in Condensed Matter Applications. *Comput. Phys. Rep.* **1989**, *9*, 115–197.
- (23) Hoffmann, F. M. Infrared Reflection-Absorption Spectroscopy of Adsorbed Molecules. *Surf. Sci. Rep.* **1983**, *3*, 107–192.
- (24) Morkel, M.; Rupprechter, G.; Freund, H. J. Ultrahigh Vacuum and High-pressure Coadsorption of CO and H₂ on Pd-(111): A Combined SFG, TDS, and LEED Study. *J. Chem. Phys.* **2003**, *119*, 10853–10866.
- (25) Tüshaus, M.; Berndt, W.; Conrad, H.; Bradshaw, A. M.; Persson, B. Understanding the Structure of High Coverage CO Adlayers. *Appl. Phys. A* **1990**, *51*, 91–98.
- (26) Yudanov, I. V.; Sahnoun, R.; Neyman, K. M.; Rosch, N.; Hoffmann, J.; Schauer mann, S.; Johane k, V.; Unterhalt, H.; Rupprechter, G.; Libuda, J.; et al. CO Adsorption on Pd Nanoparticles: Density Functional and Vibrational Spectroscopy Studies. *J. Phys. Chem. B* **2003**, *107*, 255–264.
- (27) Hammer, B.; Hansen, L. B.; Norskov, J. K. Improved Adsorption Energetics within Density-Functional Theory Using Revised Perdew-Burke-Ernzerhof Functionals. *Phys. Rev. B* **1999**, *59*, 7413–7421.
- (28) Armbrüster, M.; Behrens, M.; Cinquini, F.; Föttinger, K.; Grin, Y.; Haghofer, A.; Klötzer, B.; Knop-Gericke, A.; Lorenz, H.; Ota, A.; et al. How to Control the Selectivity of Palladium-based Catalysts in Hydrogenation Reactions: The Role of Subsurface Chemistry. *ChemCatChem* **2012**, *4*, 1048–1063.
- (29) Angyan, J.; Loos, M.; Mayer, I. Covalent Bond Orders and Atomic Valence Indexes in the Topological Theory of Atoms in Molecules. *J. Phys. Chem.* **1994**, *98*, 5244–5248.
- (30) Krajci, M.; Hafner, J. Structure and Chemical Reactivity of the Polar Three-Fold Surfaces of GaPd: A Density-functional Study. *J. Chem. Phys.* **2013**, *138*, 124703.

4.1.1 Supporting information for the publication "Ensemble Effect Evidenced by CO Adsorption on the Threefold PdGa Surfaces"

In the following supporting information we will define the PdGa:B(111)Pd₃ terminated by three Pd atoms as Pd₃ and the PdGa:B(-1-1-1)Pd₁ terminated by one Pd atom as Pd₁.

1. Tunneling voltage dependence of the contrast of CO molecules on PdGa(111) surfaces

The STM appearance of CO adsorbed on-top site of the Pd₁ surface atoms was found to depend strongly on the tunnel voltage. A contrast inversion from a protruding appearance to an intrusion is observed when going from a tunnel bias of -2 V to +2 V. This effect was not found for CO adsorbed on the Pd atoms of the Pd₃ termination, as demonstrated in Figure 4.1.

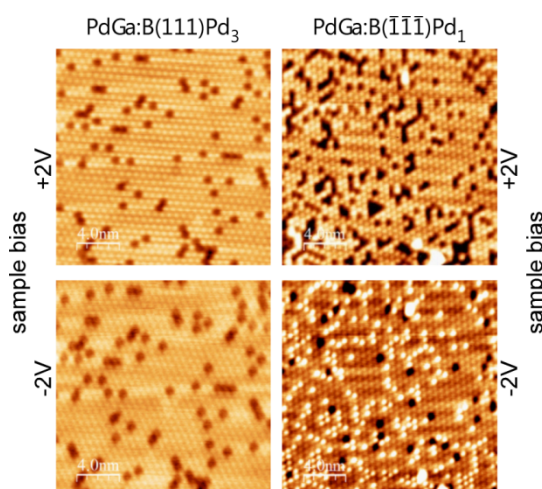


Figure 4.1 Contrast inversion of CO in STM. STM images of the same sample positions at different voltages for the two investigated samples. On Pd₃ (left panels), CO appears as dark intrusions for positive and negative sample bias. On Pd₁, the apparent height of CO changes when changing the polarity of the bias. The dark spots that are visible at -2 V for CO/Pd₁, are surface vacancies, as described in an earlier publication.²⁹

A series of images at different scanning voltages is shown in Figure 4.2. The change in contrast seems to take place around +0.5 V tunnel voltage.

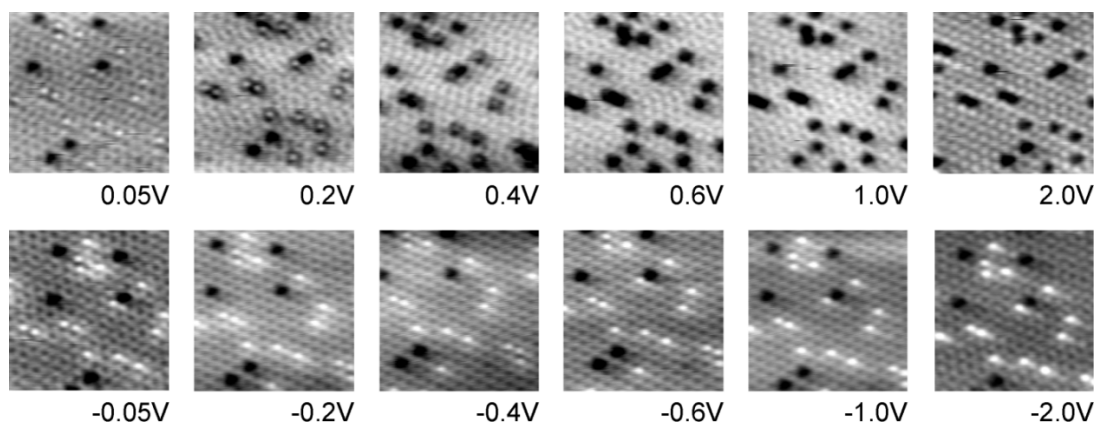


Figure 4.2 Series of images STM images of CO/Pd₁ for different tunnel voltages at the same position. All images were taken with a tunnel current of 0.2 nA.

2. Details on bonding conformations calculated by DFT

Details on the computational methods:

All calculations were performed in the mixed Gaussian plane wave approach as implemented in the CP2K code (<http://www.cp2k.org>). The substrate was modeled in the repeated slab geometry. Tests performed on slabs thicker than 23/24 atomic layers confirm that the thickness of our slab is appropriate. Norm conserving pseudopotentials of the Goedecker type were employed.⁸⁹ Semicore *4s* and *4p* states of Pd, as well as *3d* semicore states of Ga, were treated in the valence. A cutoff of 600 Ry was used for the representation of the charge density in plane waves. We used the PBE parameterization for the exchange correlation functional.⁹⁰

CO adsorption energies for the tested adsorption sites:

To test the different adsorption sites on Pd₃ and Pd₁, the structures shown in the graph below were optimized using DFT. The structures yielding the lowest binding energy per CO molecule are in agreement with the STM topographies and FTIR results presented in the main text of the publication.

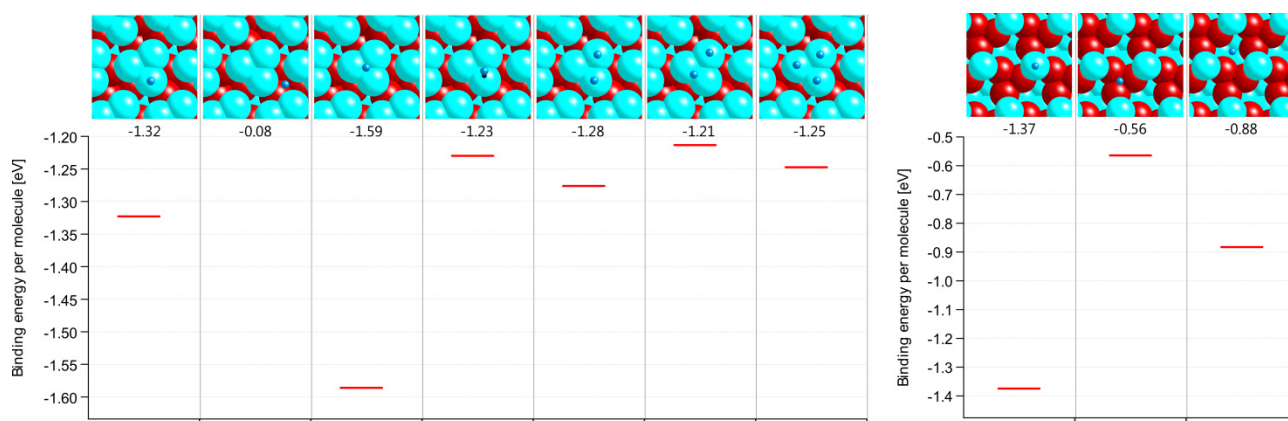


Figure 4.3 Various tested adsorption sites for CO on the threefold PdGa surfaces Pd₃ (left) and Pd₁ (right) (Pd: cyan, Ga: red, C: black, O: dark blue).

3. Experimental corroboration of the Pd-terminations of the PdGa(111) and PdGa(-1-1-1) surfaces

In a recent publication by Krajci and Hafner⁹¹ the termination of the PdGa(111) and PdGa(-1-1-1) surfaces as well as the CO adsorption on these surfaces has been investigated by a computational approach. From this theoretical investigation it has been concluded that both surfaces are Ga-terminated. These findings are in contrast to our findings of a topmost Pd layer.²⁹ In view of the importance to correctly assign the surface termination we have taken the terminations suggested by Krajci and Hafner into consideration and compared them with our LEED-I(V) and CO adsorption data.

In the following Table S1 we summarize the structure of the different proposed terminations. For the nomenclature of the denotation of the layers, see Ref.²⁹. In short: Pd_x (resp. Ga_x) represents a layer of Pd (resp. Ga) atoms with a density of x atoms per surface unit cell. The sequence of the layers from left to right corresponds to the order of layers from the surface into the bulk, the bulk part in parenthesis, is perpetuated.

Table S1: Layer structure of the different proposed PdGa surface termination.

	PdGa:B(-1-1-1)	PdGa:B(111)
Prinz, <i>et al</i> ²⁹ :	$\text{Pd}_1 - (\text{Ga}_3 - \text{Pd}_3 - \text{Ga}_1 - \text{Pd}_1) - (\dots)$ or „pG“	$\text{Pd}_3 - (\text{Ga}_3 - \text{Pd}_1 - \text{Ga}_1 - \text{Pd}_3) - (\dots)$ or „PG“
Krajci and Hafner ⁹¹ :	$\text{Ga}_3 - (\text{Pd}_3 - \text{Ga}_1 - \text{Pd}_1 - \text{Ga}_3) - (\dots)$ or „GP“ Alternative, after annealing to 870K: $\text{Ga}_1 - \text{Ga}_3 - (\text{Pd}_3 - \text{Ga}_1 - \text{Pd}_1 - \text{Ga}_3) - (\dots)$ or „gG“	$\text{Ga}_3 - (\text{Pd}_1 - \text{Ga}_1 - \text{Pd}_3 - \text{Ga}_3) - (\dots)$ or „GM“

In Table S1 all the terminations except “gG” are bulk terminations, i.e. truncations of the bulk crystal structure. The “gG” termination has been proposed by Krajci and Hafner as possible high temperature phase, where preferential desorption of Pd leads to a Ga rich surface.

Figure 4.4 shows the Pendry R-factors for all possible bulk terminations found by Tensor LEED optimization as described in detail in Ref. ²⁹. The Palladium “pG” and “PG” terminations show the best agreement, whereas the suggested Gallium bulk-truncated terminations “GP” and “GM” show no particularly low R-factors, except for the “GP”/B(-1-1-1) Ga_3 case (compared to the PdGa(-1-1-1) dataset). The R-factor in this case is just 33% higher than for the “PG” case, which is easily understood as the “pG” termination can be regarded as the “GP” termination topped with a low density Pd_1 layer. Nevertheless the low R-factor, the “GP” termination can be discarded on the basis of high resolution STM images, as these show that the PdGa(-1-1-1) surface terminates in single atoms and not in trimers as the “GP” termination would show. The suggested high temperature “gG” termination, which would show single Ga atoms at the topmost surface layer, shows no particularly low R-factor (120% larger than for the “pG”).

Concerns have been raised that LEED-I(V) calculation may not be valid for a partly covalently bonded crystal like PdGa.⁹¹ It is true that the muffin-tin potentials, which were used to calculate the scattering phase shifts, are not an ideal approximation, due to the partial covalent character of the bonds. It is however well-known, that the scattering event is mostly occurring at the ionic core of the atoms, and thus only weakly influenced by those (considerably few) electrons taking part in the chemical bond. Since the method has been used for IMCs before⁹² and can even be applied to most covalently bond materials, such as diamond⁹³, the application to PdGa is absolutely legitimate.

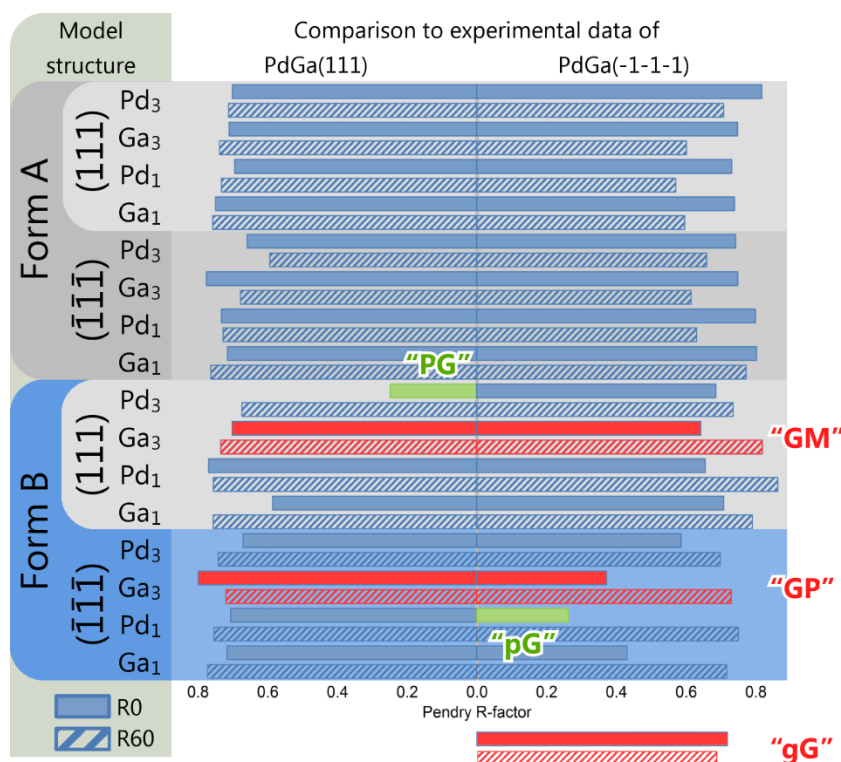


Figure 4.4 LEED-I(V) results for the suggested Ga terminated surfaces. Pendry R-factors for the LEED-I(V) analysis based on the procedure described in Ref. ²⁹. The experimental dataset for the analysis consists on the LEED-I(V) spot profiles of 24 diffraction spots (12 are symmetrically inequivalent) recorded over several hundred eV in energy. The hatched bars correspond to a 60° rotation of the LEED pattern as compared to the solid bars. Adapted from Ref. ²⁹. Copyright 2012, Wiley.

We have also considered the suggested CO adsorption sites on the Ga terminations and compared it with our available STM data. As discussed above, the "GP" termination can be discarded and therefore we have considered the "GM" and the "gG" for this comparison. Figure 4.5 shows the superposition of experimental STM images with the suggested "GM" and "gG" Ga termination of the (-1-1-1) and the (111) PdGa surface, respectively. The alignment of model structure and STM topography has been made by identifying the protrusions in the experimental STM image with the Ga trimers in the case of "GM", and with the individual Ga for the "gG" termination. There remains a rotational uncertainty of 60° as the threefold hollow sites between the protrusions in the STM image cannot be unambiguously attributed to the corresponding site in the model structure. As described in the paper, the isolated depressions and protrusions correspond to individual CO molecules. For the (111) case we find from the STM the CO centered in an on-top position, whereas the positions found by Krajci and Hafner for the "gG" termination would be bridge sites between two Ga atoms. For the (-1-1-1) surface the energetically most favorable CO adsorption site would be on-top the subsurface Pd, which is not seen in STM. Here the CO is centered in the hollow trimer site. The energetically second most favorable adsorption site is a bridge site on the trimer and not the hollow-site, although it is not easy to distinguish the two in the STM image.

In summary, the comparison of the experimental LEED-I(V) and STM/CO adsorption data with the suggested Ga terminations of the PdGa(111) and (-1-1-1) yields no compelling agreement.

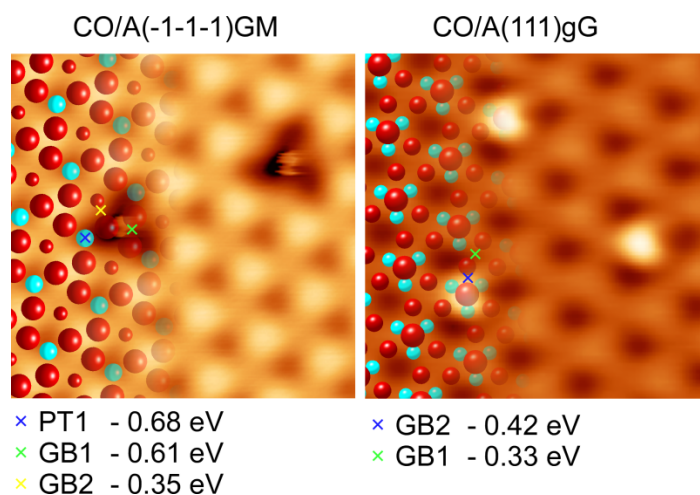


Figure 4.5 STM images of individual CO molecules adsorbed on PdGa(111) and PdGa(-1-1-1). The atomic model structure corresponds to the suggested “GM” (for the (111) surface) and the “gG” (for the (-1-1-1) surface) Ga termination. The markers denote the different CO adsorption sites found by Krajci and Hafner.⁹¹

4.2 Temperature-programmed desorption of CO on the threefold PdGa Surfaces

An experimental approach to the binding strength of the CO molecules to the threefold PdGa surfaces PdGa:A(-1-1-1)Pd₃ and PdGa:A(111)Pd₁ is achieved by TPD experiments. Desorption curves of CO are shown in Figure 4.6 for two different exposures of 0.2 and 1.0 Langmuir (L). On both surfaces, only one single desorption peak is observed at 278 and 289 K for Pd₃ and Pd₁, respectively. The background signal is ascribed to desorption from the sample holder. For exposures up to 0.2 L of CO, the peak areas are very similar for the two samples, indicating a comparable amount of desorbed CO from the two samples. At higher CO exposures (5 L), the peak area for Pd₃ becomes larger, while the one for Pd₁ remains constant, which is in agreement with the FTIR and STM data, showing maximum occupation of 3 vs. 1 CO per surface unit cell for Pd₃ and Pd₁, respectively.

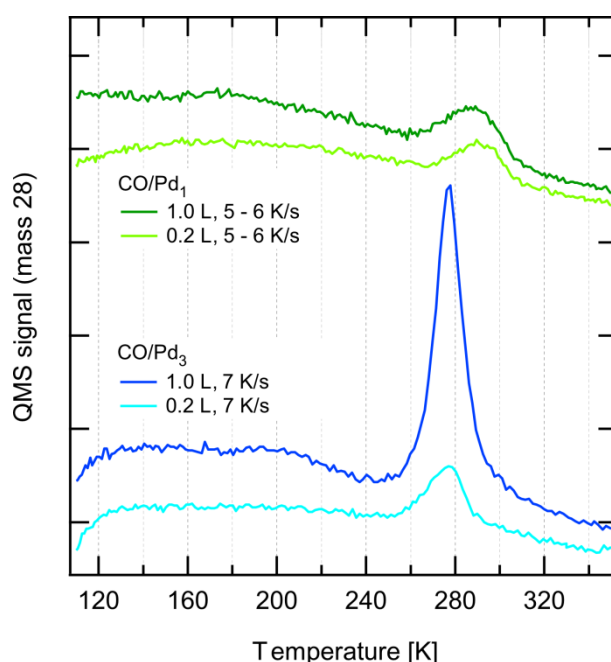


Figure 4.6 Desorption curves of CO adsorbed on Cu(111), PdGa:A(111)Pd₁ and PdGa:A(-1-1-1)Pd₃ in purple, green and blue, respectively. The thick purple line for Co/Cu(111) is adapted from Ref. ⁶³. The legends show the CO exposure and heating ramp speed for each curve.

To obtain a deeper insight into the coverage dependency of the desorption process, series of desorption curves were measured for various exposures shown in Figure 4.7. Before we turn our attention towards the peak shapes, we discuss the background subtracted peak areas as a function of coverage, which is presented in Figure 4.8. The peak areas were obtained by integration after subtraction of a linear background (see inset in Figure 4.8). For the CO saturation coverages of Pd₃ to Pd₁, a ratio of 3.64 is computed, which is in reasonable agreement with the 3:1 ratio that is expected from the STM results (cf. Chapter 4.1). The desorption peak area increases linearly as a function of exposure, up to about 85 % of the saturation coverage for Pd₃. This indicates, that impinging CO molecules are not repelled from the almost saturated surface, but rather enter a weakly bound precursor state.⁹⁴⁻⁹⁵ In this physisorbed state, the molecule is highly mobile, which enables diffusion to a nearby free Pd adsorption sites and subsequent chemisorption.

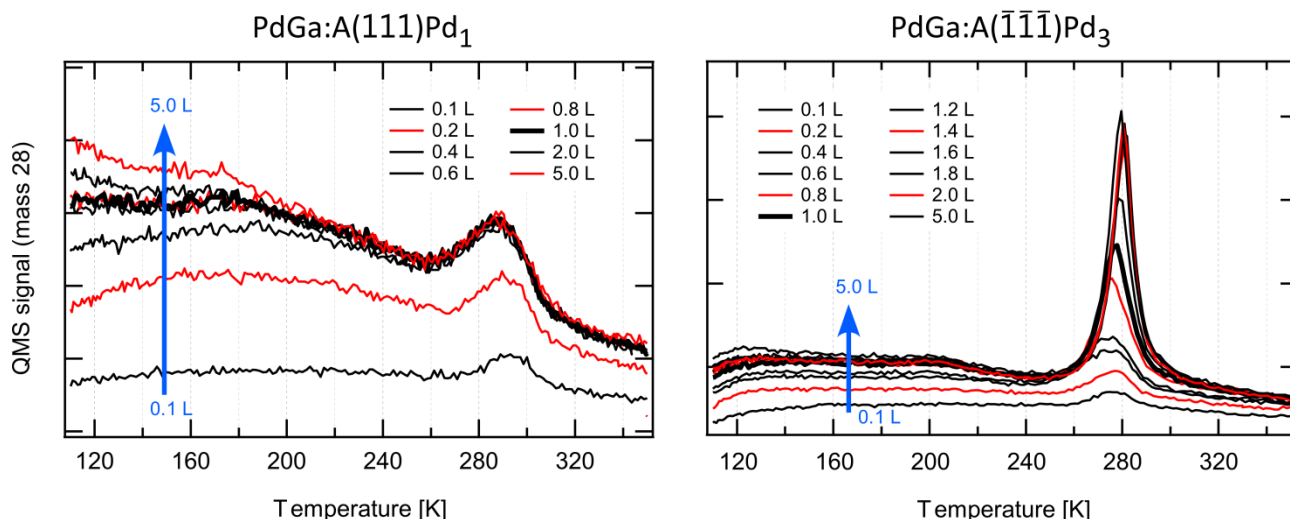


Figure 4.7 Series of TPD experiments for the two threefold PdGa surfaces after different exposures of CO (vertical scales are different in the two graphs). The ramp speed is 6 K/s (± 1 K/s) for all desorption curves. While the peak shape in the left graph remains asymmetric for all coverages, the shape is almost symmetrical for intermediate coverages of about 1.0 L in the right graph.

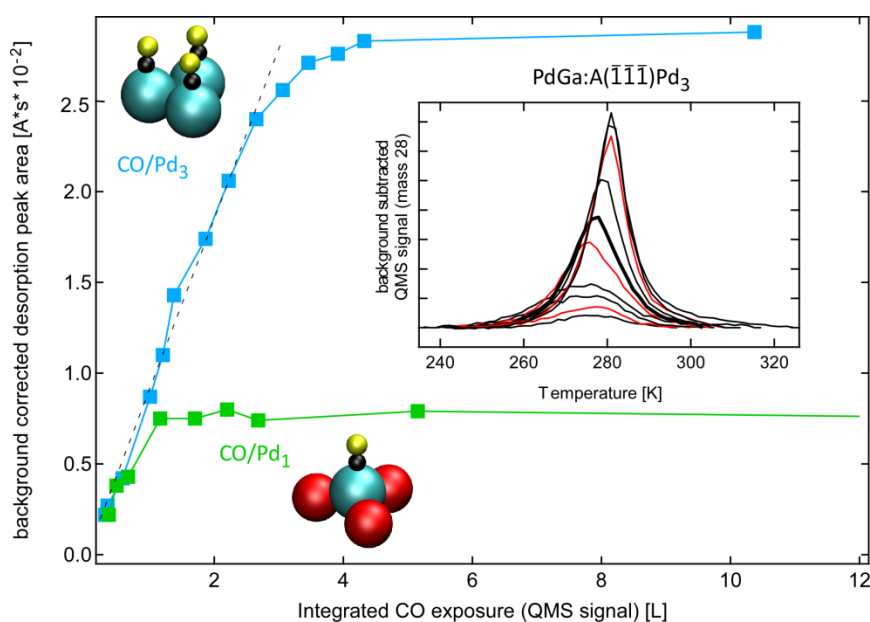


Figure 4.8 Coverage as a function of CO exposure for the Pd₁ and Pd₃ sample, computed from the CO desorption peak areas after background subtraction. The linear increase is indicated by a dashed line for Pd₃. The inset shows the series of desorption curves, corrected by a linear background for CO/Pd₃.

The exposure series shown in Figure 4.7 reveal that the peak shape for CO desorption from Pd₁ is asymmetric for all exposures, which is typical for a first order desorption mechanism.⁶¹ For Pd₃, the peak shape is also asymmetric for low coverage, but symmetric for intermediate exposures of about 1 L, which can also be seen from the background subtracted peaks in the inset in Figure 4.8). Even though this might indicate a 2nd order desorption mechanism, a more plausible explanation is a superposition of two nearby peaks, indicating the presence of two different binding sites of similar energies. This scenario is also supported by the STM and FTIR experiments, showing a threefold hollow site and on-top site adsorption for CO on Pd₃.

The desorption temperatures of 280 - 290 K for CO from Pd₁ and Pd₃ surfaces indicate a binding energy of 0.8-0.9 eV. This is in disagreement with the adsorption energies calculated by DFT (Pd₃ : 1.59 eV (hollow site), 1.25 eV (on-top site), Pd₁ : 1.37 eV (on-top site)). Discrepancies between experimental and theoretical determined binding energies for CO on transition metals have been reported earlier, *e.g.* for CO/Pt(111)⁹⁶ and for CO on Pd-Ag surface alloys.^{87, 97} In general, the *ab-initio* methods result in an overestimation of the bond strength, but trends in experimental desorption- and occupation sequences are reproduced by theory.

For the PdGa surfaces investigated here, we find the Pd₁ desorption peak at slightly higher temperatures than the Pd₃ peak, in agreement with the binding energies for on-top adsorption of CO on Pd (Pd₃ : 1.25 eV (on-top site), Pd₁ : 1.37 eV (on-top site)). At low CO coverages, the findings presented in Chapter 4.1 show the occupation of the threefold Pd hollow site which also yields a larger binding energy in DFT. Accordingly, for low CO coverages on Pd₃, a higher desorption temperature is expected. However, desorption from the Pd hollow site on Pd₃, also leads to a single desorption peak around 280 K, in disagreement with the DFT results (Pd₃ : 1.59 eV (hollow site)). The reason for this discrepancy might be an overestimation of the binding energy for CO in the threefold Pd hollow site by the computational method. An alternative explanation is desorption from the threefold Pd hollow site via a weakly bonded precursor state, which the CO molecules enter at increased temperatures prior to desorption.^{95, 98} This might lead to a reduced desorption temperature.

In a previous study, Rosenthal *et al.*²⁸ reported on CO desorption from the Pd₁ surface. The desorption peak was observed around 210 K, with a shoulder towards lower temperatures. The offset of 90 K with respect to our measurements might originate from a not accurately calibrated temperature reading in one of the two experiments. In order to validate the correct temperature scale, the experiment should be repeated in a separate dedicated setup. However, the calibration measurements for the setup employed in this study using CO desorption from Cu(111) (cf. Chapter 2.6) are in agreement with literature.

The Pd site separation of PdAg/Pd(111) surface alloys was recently investigated as a function of Pd concentration on the surface.⁸⁷ For highly dispersed Pd, (2% Pd, 98% Ag on the surface) the CO adsorption sites are single Pd atoms, embedded in a Ag matrix. TPD experiments from this surface yielded a weak desorption signal at T = 316 K, which is close to the 290 K observed for the intermetallic Pd₁. Increasing the Pd concentration of the surface alloys to 7 and 10 % leads to peak positions of 364 and 380 K for desorption from the saturated surfaces, respectively. This indicates, that already at these low amounts of Pd on the surface, Pd dimers have formed and the single atom site-isolation is compromised. A quantitative comparison of the number of Pd sites per surface area reveals that the Pd₁ surface offers about double as many Pd sites per nm² which are well-defined and isolated, as compared to the Pd-Ag alloy with 7% Pd and 93% Ag on the surface.

In summary, the TPD experiments for CO on the threefold PdGa surfaces confirm the different saturation coverages that are seen in STM, FTIR and DFT results. The desorption temperatures are very similar on the Pd₃ and Pd₁ surfaces. Analysis, by using a first order desorption theory, results in disagreement between the experimental and DFT computed binding energies, especially for desorption of CO from the threefold hollow site on the Pd trimers on Pd₃. The reason for this discrepancy might be found in the precise pathway for desorption, which so far is not fully understood.

4.3 Binding sites of the PdGa(100) and (110) surfaces probed by CO

In addition to the threefold surfaces, also the binding sites of the (100) and (110) surfaces were investigated using CO as a probe molecule. While the threefold surfaces exhibit a hexagonal pattern of the Pd binding sites, the (100) and (110) surfaces show a chain-like arrangement of alternating Pd and Ga atoms as outermost layers, as shown in the comparison in Chapter 3.3.

The coverage-dependent RAIRS spectra for CO adsorption on the (100) and (110) surface is shown in Figure 4.9 in panel A and B, respectively. For comparison, the RAIRS data from the four CO covered surfaces is shown as an overview in Figure 4.9C. For the PdGa:B(100)Pd_α surface we find a single sharp peak. With increasing coverage, a peak shift of 14 cm⁻¹ towards higher wavenumbers is observed, which is assigned to CO - CO interactions. The peak position of 2079 cm⁻¹ is almost identical to that of CO on the threefold Pd₁ termination (2080 cm⁻¹), where the molecules adsorb on-top of the isolated Pd atoms. Also the peak area ratio of 1:1.73 for (111)Pd₁:(100)Pd_α is in good agreement with the ratio of the surface area per molecule at full CO coverage of 1:1.75, derived from the sizes of the surface unit cells. However, one has to be careful in comparison of these numbers directly, as the IR absorption efficiency is strongly dependent on the CO dipole moment perpendicular to the surface.

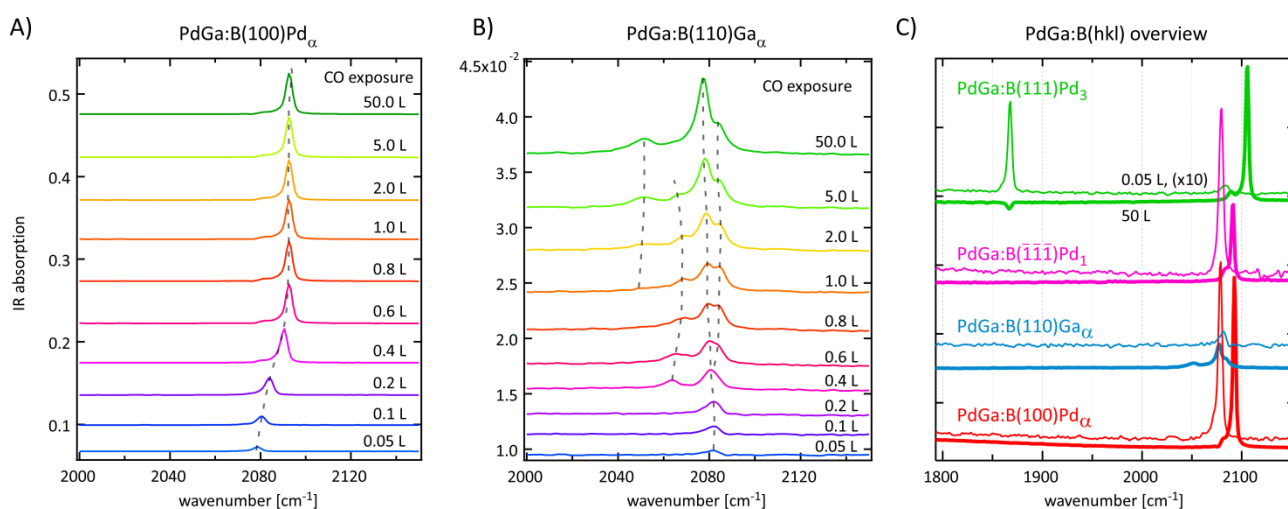


Figure 4.9 RAIRS adsorption spectra for CO on PdGa:B(100) and (110) in panel A) and B) respectively, as a function of CO exposure at 80 K. Note the much smaller y-scale for the (110) data. C) Overview of the FTIR data from the PdGa(hkl) surfaces. Spectra for exposures of 0.05 L (thin lines) are magnified by a factor of 10.

For CO adsorption on the PdGa:B(110)Ga_α termination, the IR absorption signal is much weaker for all coverages, as shown in Figure 4.9B and C. In contrast to the other investigated PdGa(hkl) surfaces, we observe a band of peaks at slightly lower wavenumbers of 2040 to 2090 cm⁻¹ with coverage-dependent intensities. Assuming adsorption on surface Pd atoms, the observed range of vibrational frequencies is indicative for CO on-top site configurations. Interestingly, peak heights for CO/PdGa(111) are still changing for exposures from 2 to 50 L, showing that deposition of CO from the gas phase is very inefficient on this surface and that the maximum occupation might not have been reached in the experiments.

To study the local adsorption geometry for CO and elucidate the origin of the peak shapes, LT-STM was performed after deposition at 77 K and 5 K for PdGa(100) and (110), respectively. Figure 4.10 shows STM images of single CO molecules on the (100) surface. For higher exposures, CO islands with the same lattice

periodicity as the (100) unit cell are observed. This comparably dense packing confirms the maximum occupation of 1 CO molecule per surface unit cell, which was suggested by the FTIR peak heights.

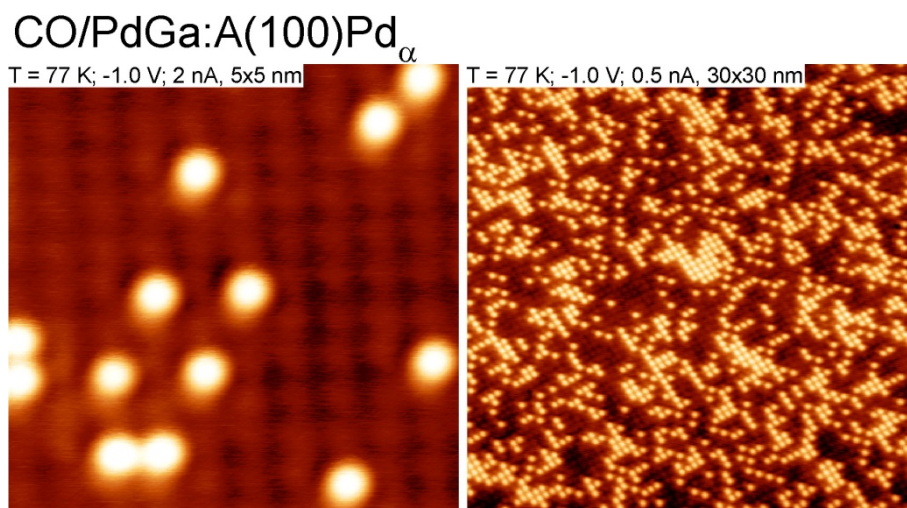


Figure 4.10 STM images of the (100) terminations after small (left) and large (right) exposure of CO at low temperatures (77 K). The molecules appear as round protrusions of high profile with respect to clean PdGa(100) surface. For higher coverages, we find one CO molecule per unit cell in the high density areas.

To identify the exact adsorption position of CO on PdGa:B(100)Pd_α, STM images were compared to a simulated STM image based on an iso-surface of the electron density, which was calculated by density functional theory. For the lowest energy adsorption configuration found by these computations, the CO molecule is located on-top of the outermost Pd atoms, in agreement with the CO vibrational frequencies⁸⁸ observed by RAIRS (cf. Figure 4.9). Alternative configurations on-top of other surface atoms yielded much weaker binding energies in DFT. The simulated STM image for this configuration is shown inside the green square in Figure 4.11, together with the atomic structure of the topmost Pd and Ga layers and the CO molecule.

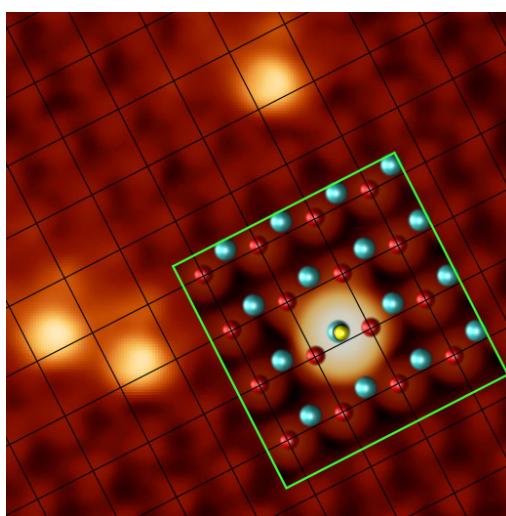


Figure 4.11 Identification of the adsorption site for CO on PdGa:A(100)Pd_α. STM image (4x4 nm) and STM simulation (in green box) of CO on are shown for a gap voltage of -0.1 V. The DFT optimized structure is shown in overlay with the STM simulation, revealing that the Ga atoms yield the highest topography in STM. The position of the CO molecule within the surface unit cell is the same for experiment and theory (C: black; O: yellow).

In experiment and simulation, the CO protrusions show a lateral offset with respect to the protrusions of the clean surface. Comparison of their position to the simulated STM image and the corresponding atomic structure reveals adsorption on-top of the outermost Pd atoms of the surface.

After the determination of the CO adsorption site on the (100) PdGa surface, we now turn our attention to the PdGa(110) surface, which showed a different behavior in the RAIRS experiments with respect to peak heights and position. Figure 4.12 shows STM images of the PdGa:A(110) surface after exposures to CO at 5 K. In the left image, the molecules appear as two lobed protrusions of low height with respect to the clean substrate atoms. This appearance differs from that of adsorbed CO on the other PdGa(hkl) surfaces, where CO appears with almost circular symmetry in STM. Particularly after large CO exposures, the molecules show a very different behavior, as can be seen in the right panel of Figure 4.12. The adsorbates arrange in chains along the $\langle -110 \rangle$ direction (green oval), or form checkerboard-like structures (red ovals). Both these phases have the same density of 0.5 CO molecules per surface unit cell, which might be one reason for the weak IR absorption signal that is seen after large CO exposures for this surface. Based on the STM images, we find no occupation of the vacancy defects that are present on this surface.

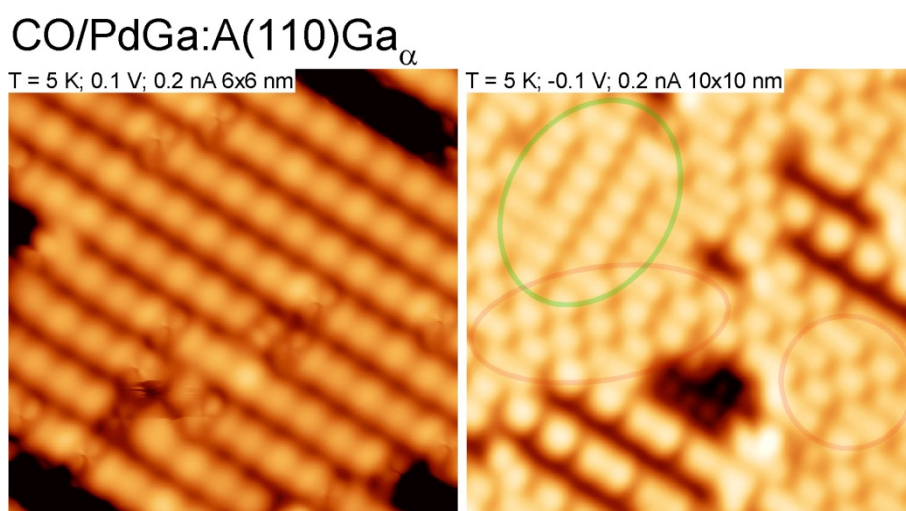


Figure 4.12 STM images of PdGa:A(110) after exposure to CO. Two lobes of low height are seen per molecule in the left panel, while they appear dark in the right panel. At higher coverages (right panel) molecular interactions lead to the formation of linear arrangements (green oval) or a checkerboard patterns (red ovals) of low areal density.

To determine the adsorption site for CO on the PdGa:A(110)Ga_α surface, the substrate atomic structure is shown as overlay in the STM image of single CO adsorbates in Figure 4.13. For the superposition, the ball model of the PdGa:A(110)Ga_α termination is aligned to the STM topography, such that the outermost Ga atoms (orange) are at the positions of the protrusions in the STM image. Previously, this particular alignment resulted in good agreement for the determination of the vacancy structure shown in Figure 3.11. Based on this alignment, the center of the two lobes of the molecules is close to atomic positions of the 2nd atomic layer (light green). These atoms are the outermost Pd atoms for this surface termination.

The origin for the peculiar STM topography might be a tilted arrangement of the linear CO molecule with respect to the surface plane. In a recent study of CO adsorbed on the reconstructed Cu(110)-(2 × 1)-O surface, exhibiting separated rows of alternating Cu and O as outermost layers, the molecules are reported to adsorb preferably with an angle of $\approx 45^\circ$ with respect to the surface plane.⁹⁹ The Cu-O rows serve as one-

dimensional templates with isolated Cu adsorption sites for CO. Upon exposure at 77 K, the surface saturates at a low CO coverage, while the CO molecules form widely separated chains perpendicular to the Cu-O rows of the substrate. The observed 8×1 superstructure is explained by tilted CO molecules that interact repulsively along the Cu-O rows, and attractively in the direction perpendicular to the substrate chains.

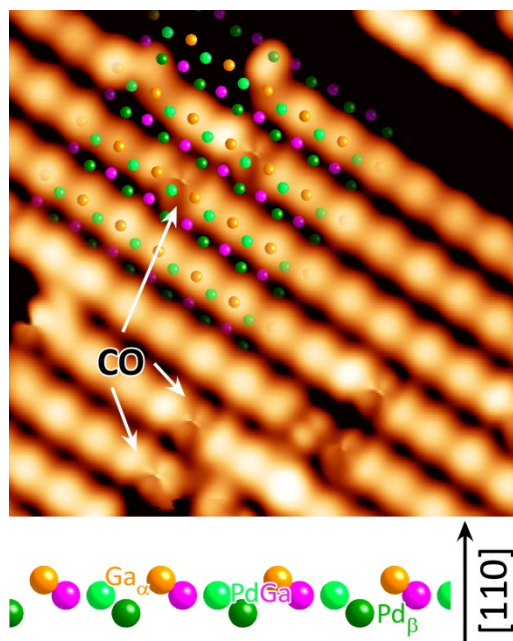


Figure 4.13 Identification of the adsorption site for CO on PdGa:A(110)Ga_α. The atomic surface structure of the surface termination is shown in overlay (cf. Figure 3.11) with the STM topography of single CO molecules, appearing as two lobes. Their apparent height is lower than that of the outermost surface atoms of Ga (orange). Dark areas are surface vacancy defects discussed in Chapter 3.2. The position of the CO molecules is found close to the outermost Pd atoms (light green).

In the case of CO/PdGa(110), a tilted CO geometry is consistent with the low IR absorption signal discussed above, as the dipole moment perpendicular to the surface is reduced. DFT computations on the CO adsorption energy as a function of tilting angle might contribute valuable information to the determination of the tilting angle. Experimentally, the adsorption geometry could be investigated using X-ray photoelectron diffraction, as the forward focusing effect for electrons emitted from the C1s core level, and scattered on the outer O atom, should yield an intensity maximum in the direction of the C-O bond axis.¹⁰⁰

In summary, the CO adsorption experiments have contributed important information to the understanding of site-isolation and ensemble effects on the different facets of the PdGa compound. By STM and FTIR, we revealed that CO-CO interactions are almost completely suppressed on the PdGa:A(111)Pd₁ and the (100)Pd_α surfaces, while they are reduced to a small number of nearest neighbors on the A(-1-1-1)Pd₃ surface. Interestingly, we find strong CO-CO interactions on the (110) surface and the formation of a CO overstructure with low molecular density. This is possibly due to CO adsorbing in a tilted fashion, creating long-ranged dipole-dipole interactions.⁹⁹ The fact that we observe such a wealth of well-defined effects on the different facets of one and the same material evidences the benefit of using PdGa single crystal surfaces as model structures to study adsorption and catalysis. In the next chapter, we follow this path and investigate the structural effect of different surface termination on the adsorption of small hydrocarbons.

Chapter 5 Reaction centers for acetylene semi-hydrogenation on Pd₃ and Pd₁

To approach the initial motivation for the investigations on the intermetallic compound PdGa we extend our studies to the reactants and the product of the semi-hydrogenation of acetylene. Therein, the main focus lies on the threefold PdGa surfaces, which serve as model structures for single atomic (PdGa:A(111)Pd₁), and three-atomic (PdGa:A(-1-1-1)Pd₃) ensembles of surface Pd, respectively. As discussed in the previous chapter, the two surface terminations have shown clear differences in CO adsorption, which is assigned to the ensemble effect of the different Pd sites. Here, we aim to enlighten the specific influence of these distinctly different Pd ensemble structures on the binding of the molecules that are involved in the semi-hydrogenation reaction. It will be demonstrated, that also for the hydrocarbons, the local configuration of Pd atoms has a strong influence on molecular configurations and binding energies, which prospectively results in different catalytic properties for the two PdGa surfaces. This is corroborated by DFT computed binding energies and reaction barriers for the hydrogenation steps on the Pd₃ and Pd₁ surfaces.

We start with the determination of the adsorption position for the involved molecules, namely acetylene, hydrogen and ethylene, by LT-STM, together with DFT calculations to elucidate reaction barriers and energies for the semi-hydrogenation reaction. This work is summarized in the manuscript presented in Chapter 5.1, which is in accepted for publication in *The Journal of the American Chemical Society*. In Chapter 5.2, we focus on tip-induced motions of acetylene molecules on the adsorption sites of the Pd₃ surface. In the last part of the chapter, the electronic structure of the adsorbates is studied by means of XPS, revealing peculiar differences in the C1s core levels for the hydrocarbons adsorbed on the two surfaces.

5.1 Publication (in print): “Adsorption of Small Hydrocarbons on Pd Reaction Centers: The Road to Selective Hydrogenation on PdGa (111)”

J. Am. Chem. Soc. (2014), DOI: 10.1021/ja505936b

(Article reprinted with permission. Copyright © 2014, American Chemical Society)

Adsorption of Small Hydrocarbons on the threefold PdGa surfaces: The Road to Selective Hydrogenation

Jan Prinz*, Carlo A. Pignedoli, Quirin S. Stöckl,[†] Marc Armbrüster,[‡] Harald Brune,[‡] Oliver Gröning, Roland Widmer and Daniele Passerone*

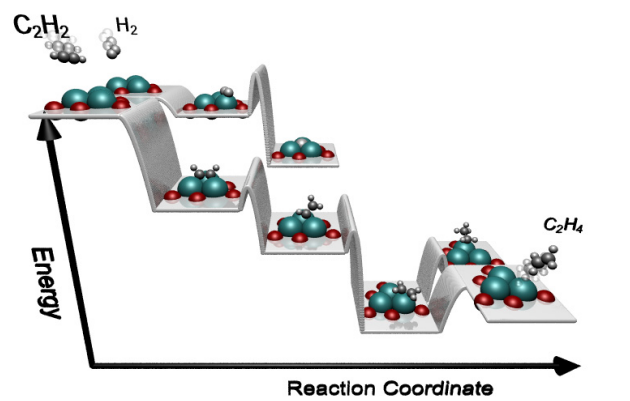
Empa, Swiss Federal Laboratories for Materials Science and Technology, nanotech@surfaces Laboratory, Ueberlandstrasse 129, 8600 Dübendorf, Switzerland.

[†] Empa, Swiss Federal Laboratories for Materials Science and Technology, Nanoscale Materials Science, Ueberlandstrasse 129, 8600 Dübendorf, Switzerland.

[‡] Max-Planck-Institut für Chemische Physik fester Stoffe, 01187 Dresden, Germany

[‡] Institute of Condensed Matter Physics, Ecole Polytechnique Fédérale de Lausanne (EPFL), Station 3, 1015 Lausanne, Switzerland.

ABSTRACT: Intermetallic compounds are promising class of materials as stable and selective heterogeneous catalysts. Here, the (111) and (-1-1-1) single crystal surfaces of the PdGa intermetallic compound were studied as model catalysts with regard to the selective hydrogenation of acetylene (C_2H_2) to ethylene (C_2H_4). The distinct atomic surface structures exhibit isolated active centers of single atomic, and three atomic Pd ensembles, respectively. For the two prototypal model catalyst surfaces, the adsorption sites and configurations for hydrogen (H_2), acetylene and ethylene were investigated by combining scanning tunneling microscopy (STM), temperature programmed desorption (TPD) and *ab-initio* modelling. The topmost Pd surface atoms provide the preferred adsorption sites for all studied molecules. The structural difference of the Pd ensembles has a significant influence on the adsorption energy and configuration of C_2H_2 , while the influence of the ensemble structure is weak for C_2H_4 and H_2 adsorption. To approach the question of catalytic performance, we simulated the reaction pathways for the heterogeneous catalytic hydrogenation of acetylene on the two surfaces by means of DFT. Due to the geometrical separation of the Pd sites on the surfaces, the steric approach of the reactants (H and C_2H_x) was found to be of importance to the energetics of the reaction. The presented study gives a direct comparison of binding properties of catalytic Pd on-top sites vs. threefold Pd hollow sites, and is therefore of major relevance to the knowledge based design of highly selective hydrogenation catalysts.



1. Introduction

Selective hydrogenations are a class of reactions essential in many pharmaceutical and petrochemical processes. It is of particular importance in the industrial production of polyethylene, where the removal of acetylene from the ethylene feedstock is pivotal to prevent poisoning of the polymerization catalyst.¹ The most efficient way to accomplish this purification is to convert the contaminant into the valuable reactant through catalytic semi-hydrogenation.² The "optimal" heterogeneous catalyst in this case maintains the same properties during the reaction (stability), enhances the transformation to ethylene (activity) and hinders further reaction to unwanted products like ethane or heavier hydrocarbon species (selectivity). The replacement of the primarily applied oxide supported pure Pd catalyst by bimetallic Pd-Ag alloys has yielded a significant increase in selectivity for this reaction.^{2,3} The increased selectivity is assigned to the formation of small, catalytically active Pd ensembles, embedded in the matrix of less active Ag. The separated ensembles of only a few atoms offer a reduced number of adsorption conformations for reactants and consequently increase selectivity by reducing the number of possible reaction pathways, which is known as the ensemble effect.⁴ Indeed, it was found that bimetallic catalysts often exhibit different reaction selectivity than their catalytically active monometallic constituents.⁵

In this respect, intermetallic compounds (IMC) have obtained increasing attention in the field of catalysis research, as the distinct crystal structure leads to well-defined surfaces that might exhibit small separated ensembles of active metal atoms with high areal density. They therefore offer the possibility to combine high catalytic selectivity with high activity.⁶⁻⁸ In recent experiments, PdGa IMCs were shown to be highly selective catalysts in the semi-hydrogenation of acetylene.^{3,9} While Pd is assumed to play the major role in the catalytic reaction, Ga is considered as the atomic spacer in between the active Pd sites. The crystal structure of PdGa exhibits a shell of 7 Ga atoms as nearest neighbors to each Pd atom and consequently the Pd atoms are spatially separated from each other.^{9,10} However, the question remains if, and to which extent, the bulk Pd separation leads to separated Pd reaction centers at the catalysts surfaces. As the catalytic experiments,^{3,9} evidencing high activity and selectivity, were performed on polycrystalline samples, the favorable catalytic properties can-

not be unambiguously related to specific atomic surface structures, *i.e.*, to the ensemble effect.

To gain more insight, we recently studied the atomic structures and the adsorption of CO on the threefold surfaces of the PdGa IMC.^{11,12} Here, we investigate the two polar (111) and (-1-1-1) terminations, exhibiting trimers of Pd atoms (Pd₃) and single atoms (Pd₁) on the outermost layers, respectively, with regard to the ensemble effect in the semi-hydrogenation of acetylene. We focus on the determination of the adsorption sites and configurations for hydrogen, acetylene and ethylene by means of scanning tunneling microscopy (STM) and density functional theory (DFT). We then propose a theoretical model for the catalytic reaction pathway towards ethylene and compare the mechanism for successive hydrogenations of acetylene on the two surfaces, focusing on barrier heights and binding energies for the reaction intermediates.

2. Methods

Details on crystal growth and UHV surface preparation and can be found in Refs.^{10,11,13} C₂H₂ (purity 99.6 %) from a solvent free container was cleaned by freeze-thaw cycling (77 K) before dosing. C₂H₄ and H₂ of purity 99.996 % (CANGas) were used without pre-cleaning. All gases were dosed by chamber backfilling through a leak valve. Effective exposure was achieved by removing the sample from the cold STM stage for a short time (20 s), which might lead to a slightly increased temperature during adsorption.

STM measurements were conducted using an Omicron low-temperature STM at a base pressure below 5×10^{-11} mbar and an etched Pt/Ir tip.

Computational parameters and methods were described in earlier publications.^{12,14,15} The well-established PBE parametrization was used for the DFT exchange correlation functional.¹⁵ Reaction barriers were computed using the Nudged Elastic Band (NEB) method (see SI for further details).¹⁶

3. Determination of Adsorption Sites

As a first step to answer the question of how the atomic surface structure of PdGa is influencing the catalytic semi-hydrogenation of acetylene, we identify the favored adsorption sites of the reactants and of the product. To this end, we performed low temperature STM measurements on the threefold PdGa surfaces after exposure to hydrogen, acetylene and ethylene, respectively. The molecules were dosed on the cold surfaces (5 K for C₂H₂ and H₂ to reduce molecular motion, and enable adsorption, respectively; 77 K for C₂H₄) by backfilling of the chamber. Submonolayer coverages were achieved after an exposure of the surfaces to about 0.05 L for all molecules. Figure 1 shows STM images of the PdGa:A(-1-1-1)Pd₃ (abbreviated as Pd₃) and PdGa:A(111)Pd₁ (Pd₁) surfaces after exposure to molecular hydrogen at 5 K.

The atomic structures of the clean substrates have been determined and discussed in an earlier publication¹¹ and are superimposed as ball models in the insets. While the top layer of the Pd₃ termination exhibits one trimer of Pd atoms per unit cell, the Pd₁ termination exhibits only one isolated Pd atom per unit cell. In both cases these Pd ensembles are well separated from their nearest Pd neighbors and arranged in a hexagonal pattern with a lattice constant of 0.69 nm (see also ball models in Figure 2). In STM, the Pd atoms appear as bright protrusions on the two surfaces.¹¹ In the STM images of Figure 1, single H₂ molecules can easily be distinguished and their adsorption position within the unit cell is identified from the superposition with the atomic structure. For both surfaces, the application of tunneling voltages larger than about 100 mV leads to immediate desorption of all adsorbates in the vicinity of the tip. This, and the fact that deposition at 77 K is not possible, indicates a rather weak physisorption of the adsorbate on the surface.

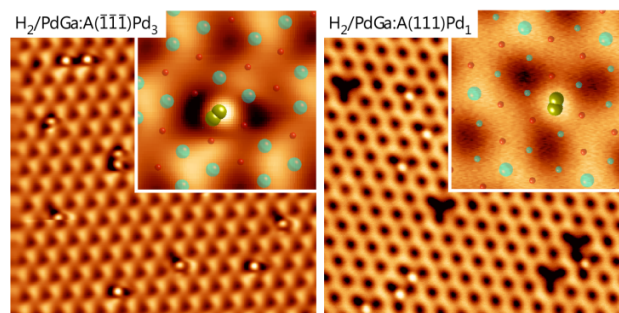


Figure 1: STM images (10×10 nm) of H₂ adsorbed at $T = 5$ K on PdGa:A(-1-1-1)Pd₃ (left) and on PdGa:A(111)Pd₁ (right). The hexagonal periodicity of the topmost atomic layers of the two threefold surfaces is visible. Insets show a magnified section (1.5×1.5 nm) of a single molecule. The superimposed atomic ball models show the lowest energy adsorption configurations as determined by DFT (Pd: cyan, Ga: red, H: yellow). For clarity, the atoms of the terminating layers and H are drawn with enlarged radii. In the right panel, the surface vacancy defects typical for the Pd₁ termination¹¹ appear as dark, threefold features. (Tunneling parameters: left: -5 mV, 1 nA; right: 5 mV, 20 pA).

On Pd₃, the H₂ molecules appear off center with respect to the protrusions marking the Pd trimer centers. Furthermore, three symmetrically equivalent such off-centered sites are found. Upon applying higher tunnel voltages transitions from one position to another is observed, as well as hopping to neighboring surface unit cells. A series of images of the tip induced hopping of the molecules is shown in the supporting information. Also two hydrogen molecules are occasionally observed on the same Pd trimer. From the off centered appearance and the overlay with the DFT optimized structure we identify the H₂/Pd₃ adsorption position as on-top site of one Pd atom of the trimer.

In the right-hand panel of Figure 1, the molecules appear as bright protrusion centered on the isolated Pd atoms of the Pd₁ termination. Other adsorption sites were not observed. Also on this surface, molecular hopping can be triggered by scanning with higher voltages, or by applying voltage pulses (≈ 90 mV) to the tunnel junction close to the molecules.

To achieve a more detailed understanding of the adsorption properties, we used DFT to compute the energetically most stable adsorption sites for the relevant molecules. The resulting configurations are summarized for Pd₃ and Pd₁ in the left- and right-hand panels of Figure 2, respectively.

The DFT results for the molecular hydrogen adsorption are in agreement with the observations from the STM experiments. For H₂ on Pd₃ and Pd₁, the energetically most favored sites are on-top of the Pd atoms of the topmost layer in both cases, with an average Pd-H distance of 1.90 Å and the H-H molecular axis almost parallel to the surface plane.¹¹ The binding energies are small, with -0.25 eV (Pd₃) and -0.29 eV (Pd₁). For Pd₃, the molecule binds slightly off-centered on one of the Pd atoms of the trimer, with the molecular axis pointing away from the trimer center. For the case of atomic hydrogen, the energetically favored adsorption positions are the threefold hollow site of the Pd trimer for Pd₃, and the threefold hollow site of the subsurface Pd trimer for Pd₁. The positions of the features seen by STM clearly coincide with the theoretically favored position of the H₂, and not with that of the H adsorption site. Therefore, we find that H₂ dissociation does not occur at 5 K, which is further supported by the tip induced desorption at low tunnel voltages of > 90 mV. Furthermore, it is noteworthy that H₂ behaves differently than CO regarding adsorption on the Pd trimer on Pd₃. For H₂ only Pd on-top site adsorption is present for Pd₃ and Pd₁, while for CO the Pd₃ trimers allow for hollow site adsorption at low coverages.¹² This might well be due to the upstanding adsorption configuration of the dipolar CO mol-

ecule, while the two H atoms in H_2 are identically charged and thus the molecule prefers a flat lying orientation.

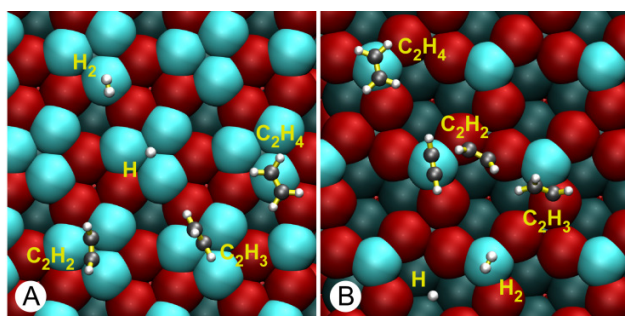


Figure 2: Summary of the DFT optimized, minimum energy adsorption configurations for various molecules on the Pd_3 (A) and the Pd_1 (B) surfaces, respectively. (Pd: cyan, Pd(sub-surface): dark cyan, Ga: red, C: black). Most adsorption sites are located on the topmost Pd atoms.

Figure 3 shows STM images of adsorbed C_2H_2 molecules on the two threefold $PdGa$ surfaces. As in the H_2 case, acetylene is found to bind preferably to the Pd centers of the topmost layer. Single molecules are easily distinguishable, however, their STM topographies are very different on the two surfaces. While on Pd_3 , a single molecule appears as two protruding lobes, a single, almost circular feature is seen on Pd_1 .

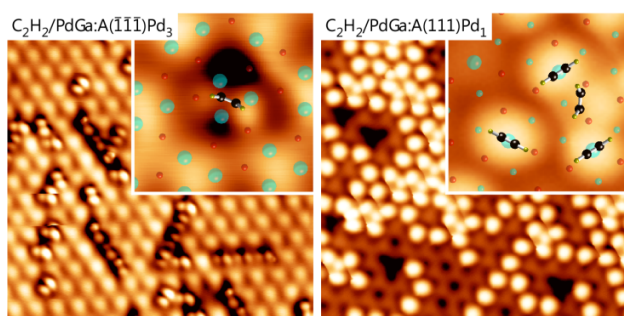


Figure 3: STM images (10×10 nm) of acetylene (C_2H_2) adsorbed at $T = 5$ K on Pd_3 (left) and Pd_1 (right). While in the former case, the molecules have a two-lobed appearance, a round shape is found in the latter. For C_2H_2/Pd_1 (right panel), two different adsorption sites are occupied. (Tunneling parameters: left: 5 mV, 50 pA; right: 5 mV, 10 pA).

For C_2H_2/Pd_3 we find three symmetrically equivalent orientations of the molecule that are characterized by 120° rotations of the two-lobe feature around the center of the Pd trimer. Transitions between these orientations can be induced by increasing the tunneling voltage, ultimately leading to a threefold symmetric shape for $V_T > 0.2$ V, since the frequency of the rotation can no longer be resolved by STM, as shown in Figure 4. Analysis of the transition frequency as a function of gap voltage, yields a barrier of 32 meV for the rotation, but also for lower gap voltages infrequent rotation is observed. Occasionally, a correlated alignment of the rotational state between neighboring adsorbates is detected (see Figure 3), leaving the molecules slightly more stable against tip induced rotation. This can be seen in an STM video added as supporting information to this article. Accordingly, full site isolation is not established for C_2H_2 adsorbed the Pd_3 trimers, as molecular orientations are not completely independent. The weak collective arrangement can be disturbed by increasing the tunneling voltage, but is partially reestablished after recording of a few images with reduced voltages. In the supporting information, a series of images illustrates the distortion and re-arrangement of adsorbed C_2H_2 on Pd_3 . Similar electron induced rotation has been reported for C_2H_2 on $Pd(111)$.¹⁷ However, in contrast to the close-

packed single element metal surface, the site separation on the intermetallic $PdGa$ surface does not allow for tip induced diffusion of C_2H_2 molecules to a neighboring Pd_3 site, since hopping was never observed for the applied tunneling conditions ($V_T \leq 2$ V, $I_T \leq 10$ nA).

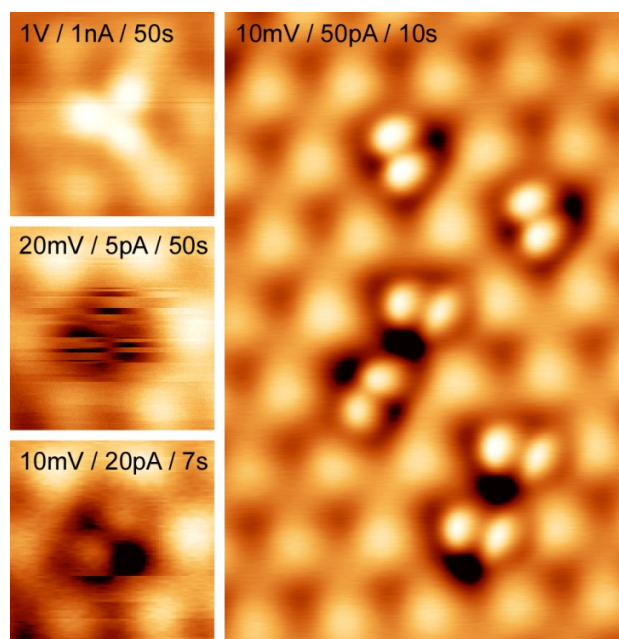


Figure 4: The STM appearance of C_2H_2 adsorbed on $PdGa:A(-1-1-1)Pd_3$ strongly depends on the applied tunneling conditions. Values given in each panel are tunnel voltage/tunnel current/approx. time to scan the molecule. In the top left panel, the electron induced molecular rotation between the three states is too fast to be resolved by the STM, leading to a threefold appearance. To resolve the molecular orientation, a low tunneling voltage and current (middle and bottom panel), and a fast scan speed (bottom and right panel) have to be chosen. In the right panel, the three symmetrically equivalent molecular orientations are identified.

The superposition of the DFT computed adsorption geometry and the STM topography in the inset of the left panel in Figure 3 reveals excellent agreement between theory and experiment. The comparison shows that the two bright lobes are located at the positions of the hydrogen atoms of the acetylene molecule, which is adsorbed on the Pd trimer in a slightly asymmetric π /di- σ bonding configuration¹⁸, as found by DFT. Each of the two carbon atoms forms a σ -bond to one atom of the Pd trimer, and the π orbital of the molecule forms a bond to the third Pd atom of the trimer, leading to a tilt of the C-H bonds and a shift of the C-C axis towards the center of the trimer. The two H-C-C bond angles are 130.5° and 128.5° , indicating that the hybridization of the C atoms has changed from sp to sp^2 . The C-C triple bond, typical of the gas phase, is reduced to a double bond (signaled by an increase of the bond length from 121 to 134 pm), resulting in an overall adsorption energy of -1.17 eV. While the bonding geometry is comparable to literature data of C_2H_2 on $Pd(111)$, the binding energy is significantly larger on the single element surface (-1.78 eV).^{19,20}

For C_2H_2/Pd_1 , the STM image in the right panel of Figure 3 reveals the existence of two different adsorption sites. The most abundant site is on the topmost Pd_1 atom. Less frequently observed is the adsorption in the center of three occupied on-top Pd sites, on top of Ga atoms. Please note, that the surface atomic structures shown in all figure insets are well-defined, and their angular orientations are carefully matched with the structure determination by low energy electron diffraction (LEED-I(V)).¹¹

Hence, we find the alternative site for C_2H_2/Pd_1 located on the Ga trimer of the second atomic layer, as can be seen from the superposition of the atomic surface structure (see right inset in Figure 3). The comparison to the DFT relaxed atomic structure of the single molecule, *i.e.*, without the neighboring Pd on-top sites occupied, does not yield full agreement with the STM image as DFT suggests an off-center adsorption. However, we cannot exclude that the round shapes of the molecules on C_2H_2/Pd_1 , as seen by STM, are due to fast rotation, or hopping, between iso-energetic configurations.

In order to achieve stable imaging for C_2H_2/Pd_1 , such as in Figure 3, it is necessary to reduce the tunnel current to about 10 pA. After continuously imaging an area with increased tunnel current (≈ 50 pA), some of the interstitial adsorbates disappear and reappear at an unoccupied on-top Pd site in the vicinity, confirming that the two observed features are of the same molecular species (for details see supporting information). We found that the adsorption energies computed by DFT for C_2H_2 in the two different adsorption sites of Pd_1 are similar, in agreement with the fact that both types are observed in experiment. The experimental observation that adsorbates can be transferred more easily from the interstitial to the Pd-top site than the other way around suggests that the latter is slightly more stable. In the on-top Pd site, C_2H_2 is π -bonded and has an adsorption energy of -0.61 eV with angles of 162° for both C-C-H bonds. The interstitial adsorption configuration is π /di- σ bonded to two Ga atoms of the 2nd and one Pd atom of the 3rd layer (Figure 2B), yielding an almost equivalent adsorption energy of 0.60 eV with C-C-H bond angles of 122° and 123° for the two H.

The different bonding characters of acetylene in the different π or σ bonding configurations on the two surfaces are reflected in the DFT computed C-C bonding distances of 124 pm for π -bonded C_2H_2 on the outermost Pd atoms of Pd_1 ; 135 pm for the σ -bond to the 2nd layer Ga atoms on Pd_1 ; and 134 pm for the σ -bond to the Pd_3 trimers (for comparison: 121 pm in the gas phase). Other possible adsorption sites were found to have considerably lower adsorption energies. The significant binding energy difference of acetylene bound to Pd_3 (-1.17 eV) and Pd_1 (-0.61 eV) is noteworthy, particularly in view that this difference occurs for two opposed surfaces of the same crystal. The origin of this effect lies in the size and configuration of the topmost atomic Pd ensembles on the two surfaces, as their electronic structures are almost identical.¹¹ Hence, as presented earlier for CO ¹², we observe a strong ensemble effect for C_2H_2 adsorbed on the threefold intermetallic PdGa surfaces.

Finally, we turn our attention to the product of the acetylene semi-hydrogenation, *i.e.* ethylene C_2H_4 . STM images after adsorption at 77 K are shown in Figure 5. On Pd_3 the molecules are off-centered with respect to the Pd trimer and almost on-top of a single Pd atom of the Pd trimer. This is in agreement with the energetically favored configuration found by DFT, as shown in the left inset in Figure 5. The binding energy amounts to -0.69 eV, with a C-C bond distance of 138 pm and with the C-C axis slightly tilted by 6° with respect to the surface plane (see Figure 2A). In STM we see evidence for some of the trimers being occupied by two molecules, with each appearing as a protrusion almost on-top the single Pd atoms of the trimer (see supporting information). Calculations show, that if two C_2H_4 are placed on the same trimer, they repel each other, yielding a reduced total binding energy of -0.50 eV per molecule. The occurrence of three C_2H_4 per trimer was never observed in STM, which indicates a limitation of the total coverage due to steric hindrance.

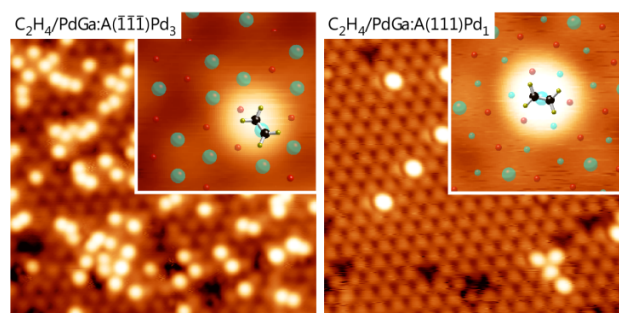


Figure 5: STM images (10×10 nm) of ethylene (C_2H_4) adsorbed at $T = 77$ K on Pd_3 (left) and Pd_1 (right). The molecules appear as round protrusions on both surfaces. On Pd_1 , the features are found on-top of the isolated Pd atoms, while on Pd_3 , they show a lateral offset with respect to the Pd trimer centers. The inset for Pd_3 reveals that the features coincide with the positions of one of the Pd atoms in the trimer. Dark areas in the bottom of the left panel are due to contaminants. (Tunneling parameters: left: -100 mV, 100 pA; right: -175 mV, 200 pA).

For the adsorption of C_2H_4 on Pd_1 , STM reveals round protrusions, centered on the single Pd atoms of the topmost layer. This configuration is very similar to the one of acetylene on this surface described above. However, also for higher coverages of ethylene (not shown), interstitial adsorbates are not seen in our experiments. DFT yields a binding energy of -0.73 eV for the case of C_2H_4 in a π -bonded conformation on-top of the Pd atoms, with the C-C axis parallel to the surface plane and a slight distortion of the C-C-H bonds to 168° . Notably, in both studied cases of C_2H_4 on Pd_3 and Pd_1 , the bonding configurations are different from that on the clean $Pd(111)$ surface, where C_2H_4 is reported to adsorb preferably in a di- σ bridge position between two neighboring Pd atoms, yielding a binding energy of -0.64 eV.²¹

Table 1: Adsorption energies in eV determined by DFT for some of the adsorbed species presented in Figure 2.

	Pd_3	Pd_1
H_2	-0.25	-0.29
$H+H$	-1.01	-0.51
C_2H_2	-1.17	-0.61 (-0.60)
C_2H_4	-0.69	-0.73

In Table 1, adsorption energies for hydrocarbons and hydrogen are summarized. The overview of the energetically most favorable bonding sites shown in Figure 2 reveals that on Pd_3 , molecules and reaction intermediates (discussed later in the text) bind preferentially to the Pd trimers. On Pd_1 , also bonding to Ga atoms is observed for some cases (alternative site for C_2H_2 , and C_2H_3), which was not indicated by the adsorption of CO used as a test molecule in an earlier study.¹² Remarkably, a recent DFT study revealed that also on $PdGa(210)$ C_2H_2 and C_2H_3 bind preferentially with at least one σ bond to a Ga atom of the surface.²² As the electronic structures of the Pd_1 , Pd_3 and $PdGa(210)$ surfaces are approximately equivalent,¹¹ this effect is ascribed to the geometrical arrangements of the surface atoms, which are rather open structures for Pd_1 and $PdGa(210)$ but rather dense in the Pd_3 case. Accordingly, the Pd_3 termination seems to provide a special case, in which the Pd trimers of the topmost layer are packed dense enough to prevent the bond of the hydrocarbons to the 2nd layer of Ga atoms.

To test the accuracy of the computed binding energies given above, we performed temperature programmed desorption (TPD) for acetylene, which yielded the largest differences in binding

energy between the two surfaces. The desorption curves are presented in Figure 6.

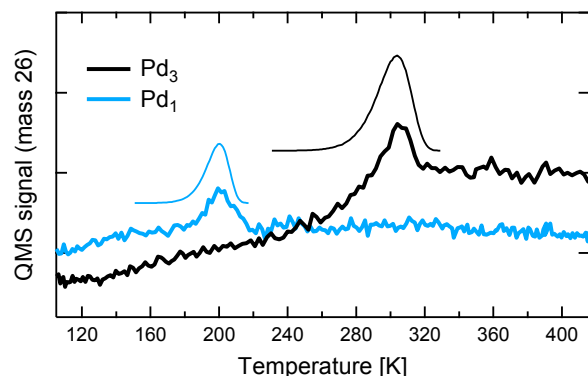


Figure 6: C_2H_2 desorption (mass 26) during a TPD ramp (6 K/s) for Pd_3 and Pd_1 , after exposure to 0.1 Langmuir at 77 K. The fitted peaks (thin lines above the experimental data) correspond to binding energies of -0.52 and -0.80 eV for Pd_1 and Pd_3 , respectively, and were obtained from the Redhead equation.²³

The peak positions in the TPD data confirm the DFT result that Pd_3 binds C_2H_2 significantly stronger than Pd_1 . Assuming first order desorption, we derive a binding energy ratio of 1.5 from the two desorption temperatures. From simulation of the desorption process based on the theory by Redhead²³ (1st order, desorption attempt frequency: 1×10^{13} Hz, ramp: 6 K/s), we find desorption energies of 0.52 and 0.80 eV for C_2H_2 on Pd_1 and Pd_3 . While in the first case, agreement with DFT is acceptable (DFT: 0.61 eV), the desorption energy in the latter case is with 0.8 eV smaller in experiment than in theory (DFT: 1.17 eV). This might be due to different desorption attempt frequencies for acetylene bound in a π /di- σ , or a π configuration, leading to a peak-shift in the experiment. However, we cannot exclude that the discrepancy is caused by an overestimation of the σ bond to the Pd_3 trimers by the DFT method. Nevertheless, the ratio of the desorption temperatures on the two surfaces of 1.54 is in reasonably good agreement with the ratio of the DFT computed adsorption energies of 1.92. The increase of the background signal with temperature in Figure 6 is assigned to desorption from the sample holder.

4. DFT Study on the Semi-hydrogenation of Acetylene

To address the performance of the two model catalysts we extend the theoretical analysis towards the reaction pathway of the semi-hydrogenation of acetylene. The very good agreement of theory and experiment in the determination of the adsorption sites and configurations, warrants the extension of the DFT analysis to reaction barriers and binding energies of the molecules and reaction intermediates involved in the selective hydrogenation, $C_2H_2 + H_2 \rightarrow C_2H_4$. To reveal trends in activity and selectivity for the different structures of Pd_3 and Pd_1 , we compare the reaction barrier heights as summarized in Figure 7. The energy step diagram is to be read from left to right, with the total energies relative to the initial condition of C_2H_2 and H_2 in the gaseous state. For the exact geometric reaction pathway the reader is referred to the supporting information.

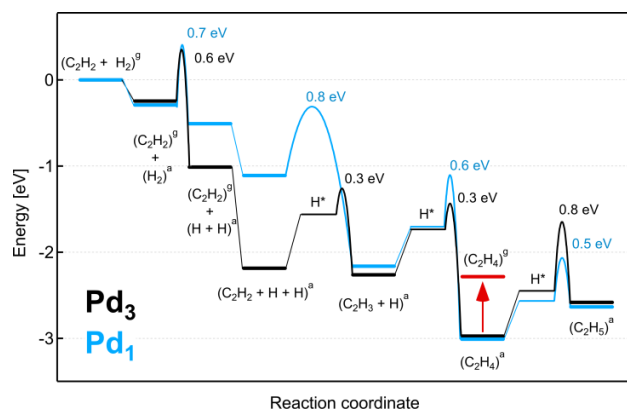


Figure 7: DFT computed energies of the intermediate states (horizontal lines) and barrier heights (inverted parabolas) for the semi-hydrogenation of acetylene on the two surface terminations Pd_3 and Pd_1 . Metastable hydrogen diffusion steps (see main text for details) are indicated by “H*”. The superscript “g” and “a” signals the gaseous and adsorbed state of a molecule, respectively. Figure 2 shows the respective bonding geometries and numerical values of energy differences are given in the text.

For the cases of surfaces with separated active sites as investigated here, the reactants bind at much larger distances from each other than on single element metal surfaces. Thus, the approach of the reactants to a nearby metastable position (marked H* in Figure 7) has to be considered explicitly, and the respective energetic cost has to be taken into account. In our analysis, we split the hydrogenation reactions into two parts: The first step involves the hydrogen transport from the most favorable adsorption site to a metastable adsorption position close to the hydrocarbon (H*). The second step represents the actual hydrogenation reaction barrier, which was calculated (inverted parabolas in Figure 7) using NEB starting from the hydrogen in the metastable position (see supporting information for details).

The first step considered in the DFT approach is the adsorption and dissociation of H_2 , yielding comparable energies and barriers, which might be rate limiting for the overall reaction on the two surfaces. For atomic hydrogen the most preferred site is a hollow site on a Pd trimer¹¹, as shown in Figure 2. On Pd_1 , this site belongs to the 3rd atomic layer which is strongly coordinated by the substrate atoms, resulting in a lower hydrogen adsorption energy as compared to Pd_3 . Given the very small distance between the layers of 143 pm, the H atom is still available for hydrogenation reactions. For the first hydrogenation step, namely the transformation of acetylene into C_2H_3 (vinyl), we consider the two acetylene configurations shown in Figure 2.

On the Pd_3 surface, the hydrogen approach (to H*) is endothermic by 0.7 eV. The subsequent hydrogenation process requires overcoming a barrier of 0.3 eV, which results in a total reaction barrier of 1.0 eV.

On the Pd_1 surface, where two degenerate C_2H_2 adsorption positions exist (compare Figure 2B), the barrier for hydrogenation of acetylene bound in the π /di- σ conformation, *i.e.*, partially bound to subsurface Ga, is lower (barrier height: 0.8 eV) than for hydrogenation from the π bonded, *i.e.*, on-top Pd position (barrier height 1.1 eV). For simplicity, only the first case is drawn in the energy step diagram in Figure 7. The main reason for the lower barrier from the π /di- σ conformation is that hydrogen is supplied directly from its energetically most favored position, such that no endothermic hydrogen diffusion to a metastable position is required.

For C_2H_3 on Pd_3 , the most favored adsorption conformation exhibits a tilted C-C bond with respect to the surface plane, with the

lower C atom close to the center of the Pd hollow site. Similar geometries were found by theory and experiment for Pd(111).^{19,24} The conformation is very different on Pd₁, where the C-H group relaxes to a bridge site position between the topmost Pd and a subsurface Ga atom, while the C-H₂ group is tilted towards the topmost Pd atom. This situation is similar to that reported for C₂H₃ on PdGa(210).²²

The next step of the reaction is hydrogenation of vinyl towards ethylene. This reaction requires overcoming barriers of 0.8 eV and 1.1 eV for Pd₃ and Pd₁, respectively, including the hydrogen diffusion to the metastable position (H*, endothermic by 0.5 eV for both surfaces).

As presented within the discussion on the LT-STM results, ethylene adsorbs in π -bonded conformations on-top of Pd atoms of the terminating layer for both surfaces and the binding energies amount to -0.73 eV on Pd₁ and -0.69 eV on Pd₃ (see red line in Figure 7). Once formed, the question arises whether ethylene would leave the surface (beneficially affecting selectivity) or remain and undergo further hydrogenation (compromising selectivity). The crucial parameter for this step is the barrier height for further hydrogenation.

For the transformation to ethyl (C₂H₃) on Pd₁ we find an endothermic process (by 0.38 eV). The endothermic hydrogen diffusion to the metastable site (H*, 0.4 eV) and the subsequent hydrogenation reaction barrier (0.5 eV) result in a total barrier of 0.9 eV. This value is only marginally higher than the desorption energy of ethylene (0.73 eV) on this surface; hence we cannot exclude the further transformation to ethyl. On Pd₃, on the contrary, the barrier for further hydrogenation of ethylene is instead 1.3 eV (including 0.8 eV for the hydrogen approach). This is almost double compared to the ethylene binding energy (-0.69 eV), making desorption much more likely.

To compare the two threefold PdGa surfaces with respect to their efficiency as catalysts, the energy step diagram shown in Figure 7 should be interpreted with regard to the following criteria: a) acetylene and hydrogen (the reactants) have a sufficiently high binding energy to allow hydrogenation on the surface; b) hydrogen dissociation is thermodynamically favorable on the surface; c) the hydrogenation process of acetylene has a high yield resulting from low reaction barriers; and d) there exist mechanisms hindering a further hydrogenation of ethylene and avoiding the formation of heavier hydrocarbons.

In almost all of the criteria named above, the Pd₃ is superior to the Pd₁ termination; adsorption energy of acetylene is larger (a), hydrogen dissociation is more exothermic (b), and the barrier towards (over-) hydrogenation to C₂H₃ is higher (d). Furthermore, if a situation of excess hydrogen is considered, all favored hydrogen adsorption sites, and the metastable sites can be considered to be dynamically occupied on both surfaces. As a consequence, the hydrogenation will mostly start from the metastable positions, closer to the hydrocarbon. This leads to a considerable decrease of the barrier heights (and thus increase in activity) for the hydrogenation steps (c) which is much more pronounced on Pd₃ as compared to Pd₁ (cf. Figure 7). Additionally, on Pd₁, the binding energy for ethylene (-0.73 eV) is found larger than for acetylene (-0.61 eV). As a consequence, the catalytic surface would become inactive due to ethylene poisoning, in particular when used in ethylene rich streams as purification catalyst.

Our DFT results are in general agreement with the very recently published investigation of the semi-hydrogenation on PdGa surfaces by Krajci and Hafner.²⁵ Furthermore, our DFT results compare to those found for the same reaction on the (210) surface of the PdGa compound.²² However, two differences should be pointed out; first, the binding energy of atomic hydrogen is much stronger for the threefold surfaces (Pd₃: E_{b,H} = -0.51 eV, Pd₁: -0.25 eV, PdGa(210): E_{b,H} = -0.06 eV), which is assigned to

the Pd hollow sites that are present on Pd₃ and Pd₁. And secondly, the barriers towards further hydrogenation to C₂H₃ are lower on the (210) surface as compared to Pd₃ (Pd₃: 0.8 eV, Pd₁: 0.5 eV, PdGa(210): 0.5 eV). In comparison to DFT simulations of the reaction on the close-packed Pd(111) surface by Sheth et al.¹⁹, the intermetallic Pd₃ surface yield lower reaction barriers for the considered hydrogenations towards ethylene and should thus yield higher activity (Pd(111): 0.68 eV, 0.88 eV, and 0.72 eV for the step towards C₂H₃, C₂H₄ and C₂H₅, respectively). However, quantitative comparison to the different *ab-initio* results have to be done with care, as the different computational parameters and the choice of exchange functionals may alter the results.

5. Conclusions

We compared the PdGa:A(111) and (-1-1-1) model catalyst surfaces exhibiting separated single Pd atoms (Pd₁) and Pd trimers (Pd₃) respectively, with regard to the adsorption of small hydrocarbons. In the combined STM and DFT study, we found that the single (Pd₁) and three-atomic (Pd₃) Pd ensembles which provide the lowest energy adsorption sites for CO¹², also play the major role in the bonding of H₂, C₂H₂, and C₂H₄. However, for the single atomic Pd sites of Pd₁, the Ga atoms of the 2nd layer are involved in C₂H₃ bonding and in the 2nd favorite adsorption site for C₂H₂. DFT and TPD reveal a weaker π -bond of acetylene to the single atomic Pd sites, as compared to the π /di- σ bonding to the Pd trimers on Pd₃. Also the binding energy of atomic hydrogen is significantly higher on Pd₃ than on Pd₁, while it is similar for molecular hydrogen and ethylene.

Based on the agreement of experiment and quantum chemical calculations of the adsorption, we expanded the DFT study to compute the reaction step energies and barriers heights for the semi-hydrogenation reaction pathway of acetylene towards the desired product ethylene. We found that the hydrogen approach towards the hydrocarbon plays a crucial role to the energetics of the reaction, leading to reduced reaction barriers for one of the threefold PdGa surfaces (namely Pd₃) in the case of hydrogen excess. This is attributed to the terminating Pd layer, consisting of atomic trimers, which allow for binding of both reactants simultaneously in a metastable configuration. If the hydrogen is supplied from the energetically most favored H adsorption site, the barrier heights for the reaction steps were found similar on the two surfaces, except for the step towards ethyl (C₂H₃), where the barrier on Pd₃ is larger compared to that for Pd₁, enhancing selectivity.

The comparison of three- and single Pd atom catalytic ensembles presented here reveals that the surface structure on the smallest possible length scale has a strong influence on the binding properties and on the catalytic reaction pathways. This opens the possibility to design improved catalysts by the choice of idealized surface atomic structures. As in the case of the PdGa surfaces, an experimental confirmation of the computed selectivity and activity differences would corroborate this approach.

Associated Content

Supporting Information

STM images on tip induced diffusion and reorientation of adsorbed molecules, as well as details on the DFT method and the computed reaction pathways are given. This material is available free of charge via the Internet at <http://pubs.acs.org>.

Web enhanced Objects

An STM video of 30 s (taken over a period of 4 hours), resolving the molecular rotation of single C₂H₂ molecules on the Pd₃ trimers is available in the HTML version of the paper.

Author Information

Corresponding Author

Daniele.Passerone@empa.ch; Jan.Prinz@empa.ch

Acknowledgements

We gratefully acknowledge funding by the Swiss National Science Foundation under the contract 200021-129511 and support by the Swiss National Supercomputing Center (CSCS). We thank Karl Heinz Ernst, and the members of the COST Action CM0904 for fruitful discussions.

References

- (1) Molnar, A.; Sarkany, A.; Varga, M. *J. Mol. Catal. A: Chem.* **2001**, *173*, 185.
- (2) Borodzinski, A.; Bond, G. C. *Catal. Rev.: Sci. Eng.* **2008**, *50*, 379.
- (3) Armbrüster, M.; Kovnir, K.; Behrens, M.; Teschner, D.; Grin, Y.; Schlögl, R. *J. Am. Chem. Soc.* **2010**, *132*, 14745.
- (4) Sachtler, W. M. H. *Catal. Rev.: Sci. Eng.* **1976**, *14*, 193.
- (5) Allison, E. G.; Bond, G. C. *Catal. Rev.: Sci. Eng.* **1972**, *7*, 233.
- (6) Kovnir, K.; Armbrüster, M.; Teschner, D.; Venkov, T. V.; Jentoft, F. C.; Knop-Gericke, A.; Grin, Y.; Schlögl, R. *Sci. Technol. Adv. Mater.* **2007**, *8*, 420.
- (7) Piccolo, L. *Chem. Commun.* **2013**, *49*, 9149.
- (8) Armbrüster, M.; Kovnir, K.; Friedrich, M.; Teschner, D.; Wowsnick, G.; Hahne, M.; Gille, P.; Szentmiklosi, L.; Feuerbacher, M.; Heggen, M.; Girgsdies, F.; Rosenthal, D.; Schlögl, R.; Grin, Y. *Nat. Mater.* **2012**, *11*, 690.
- (9) Kovnir, K.; Armbrüster, M.; Teschner, D.; Venkov, T. V.; Szentmiklosi, L.; Jentoft, F. C.; Knop-Gericke, A.; Grin, Y.; Schlögl, R. *Surf. Sci.* **2009**, *603*, 1784.
- (10) Armbrüster, M.; Borrmann, H.; Wedel, M.; Prots, Y.; Giedigkeit, R.; Gille, P. *Z. Kristallogr. - New Cryst. Struct.* **2010**, *225*, 617.
- (11) Prinz, J.; Pignedoli, C. A.; Stoeckl, Q. S.; Armbrüster, M.; Brune, H.; Gröning, O.; Widmer, R.; Passerone, D. *submitted to J. Am. Chem. Soc.* **2014**.
- (12) Prinz, J.; Gaspari, R.; Stoeckl, Q. S.; Gille, P.; Armbrüster, M.; Brune, H.; Gröning, O.; Pignedoli, C. A.; Passerone, D.; Widmer, R. *J. Phys. Chem. C* **2014**, *118*, 12260–12265.
- (13) Gille, P.; Ziemer, T.; Schmidt, M.; Kovnir, K.; Burkhardt, U.; Armbrüster, M. *Intermetallics* **2010**, *18*, 1663.
- (14) VandeVondele, J.; Krack, M.; Mohamed, F.; Parrinello, M.; Chassaing, T.; Hutter, J. *Comput. Phys. Commun.* **2005**, *167*, 103.
- (15) Perdew, J. P.; Burke, K.; Ernzerhof, M. *Phys. Rev. Lett.* **1997**, *78*, 1396.
- (16) Henkelman, G.; Uberuaga, B. P.; Jonsson, H. *J. Chem. Phys.* **2000**, *113*, 9901.
- (17) Dunphy, J. C.; Rose, M.; Behler, S.; Ogletree, D. F.; Salmeron, M.; Sautet, P. *Phys. Rev. B: Condens. Matter Mater. Phys.* **1998**, *57*, 12705.
- (18) Ibach, H.; Lehwald, S. *J. Vac. Sci. Technol.* **1978**, *15*, 407.
- (19) Sheth, P. A.; Neurock, M.; Smith, C. M. *J. Phys. Chem. B* **2003**, *107*, 2009.
- (20) Sesselmann, W.; Woratschek, B.; Ertl, G.; Kuppers, J.; Haberland, H. *Surf. Sci.* **1983**, *130*, 245.
- (21) Neurock, M.; van Santen, R. A. *J. Phys. Chem. B* **2000**, *104*, 11127.
- (22) Krajci, M.; Hafner, J. *J. Catal.* **2012**, *295*, 70.
- (23) Redhead, P. A. *Vacuum* **1962**, *12*, 274.
- (24) Stacchiola, D.; Calaza, F.; Zheng, T.; Tysoe, W. T. *J. Mol. Catal. A: Chem.* **2005**, *228*, 35.
- (25) Krajci, M.; Hafner, J. *J. Catal.* **2014**, *312*, 232.

5.1.1 Supplementary information for the publication "Adsorption of Small Hydrocarbons on the threefold PdGa surfaces: The Road to Selective Hydrogenation"

In the following supporting information we will define the PdGa:A(-1-1-1)Pd₃ surface, terminated by three Pd atoms as Pd₃ and the PdGa:A(111)Pd₁ surface, terminated by one Pd atom as Pd₁.

1. STM of small molecular adsorbates on the PdGa(111) surfaces

Tip induced hopping of H₂:

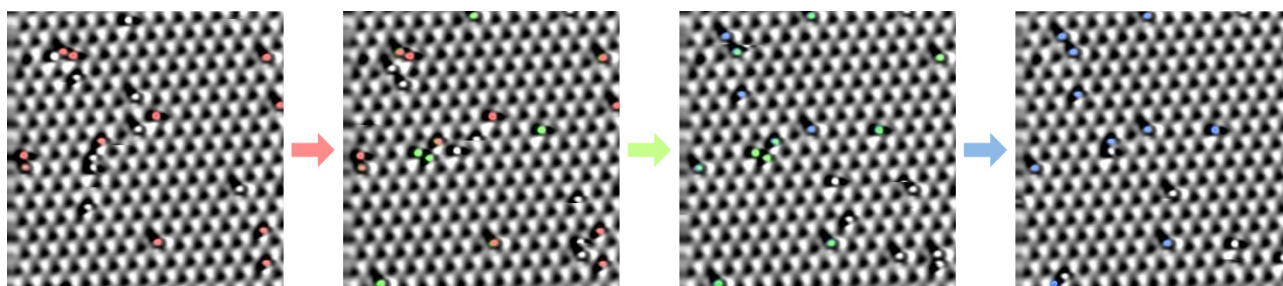


Figure 5.1 Hopping of H₂ molecules on the Pd₃ surfaces at 5K. Images were taken in upwards scan with a period of 1 minute. As a guide to the eye, those molecules that maintain their position in two subsequent images are color coded. (10 x 10 nm, tunnel parameters: - 5 mV, 1nA)

Collective alignment of neighboring C₂H₂ on Pd₃:

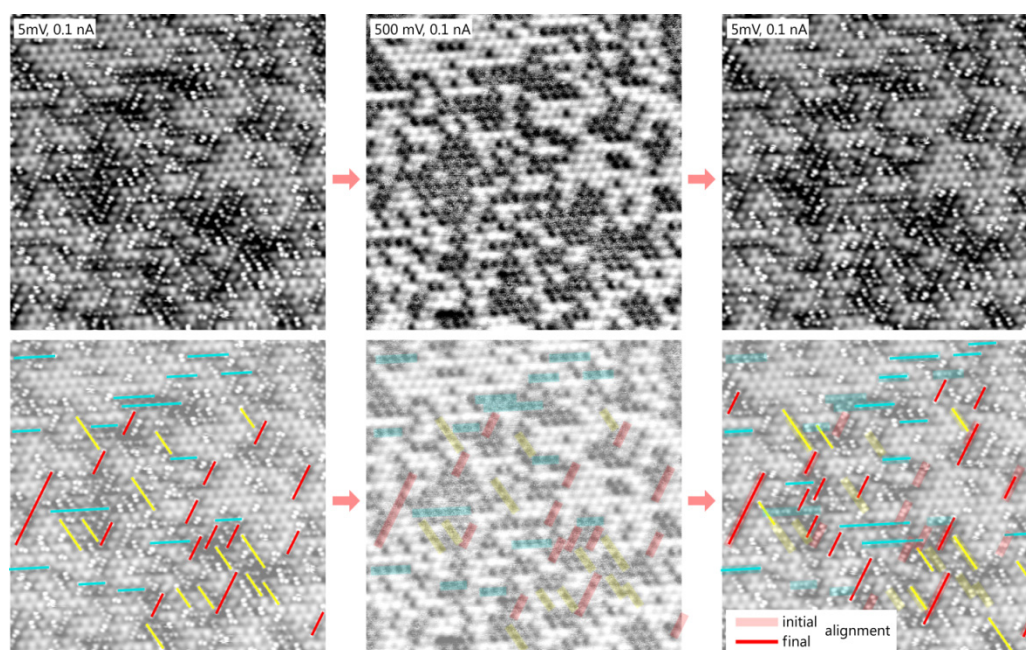


Figure 5.2 STM images of the collective alignment of C₂H₂ molecules at 5K. Top: Three subsequent STM images (20 x 20 nm) of C₂H₂ molecules on PdGa:A(-1-1-1)Pd₃ at 5 K. Bottom: alignments of three or more adsorbates are marked with colored lines, color coded for the three symmetry-equivalent directions. Center: Increasing the tunnel voltage from 5 mV to 500 mV leads to a re-arrangement of the collective orientations.

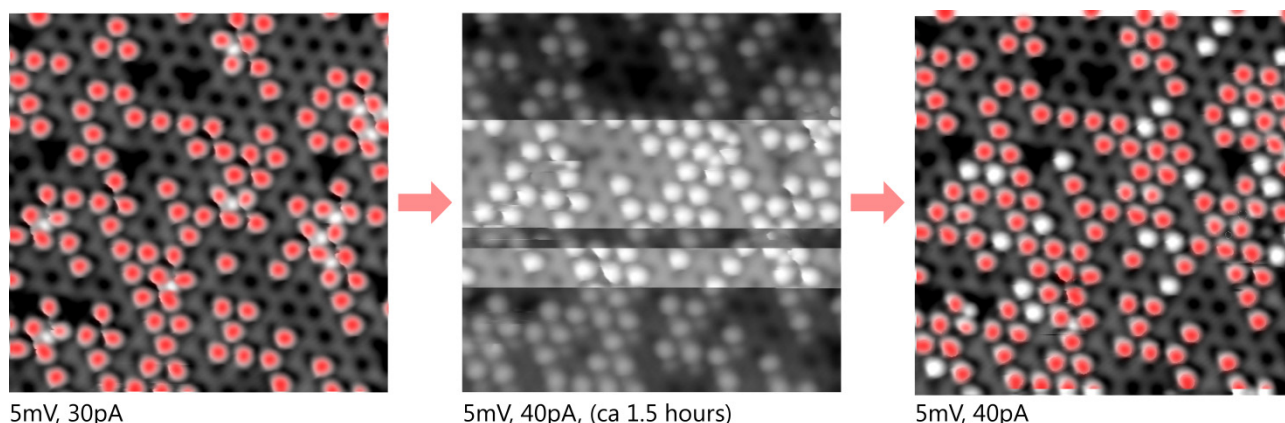
Tip induced change of adsorption site of C₂H₂ on Pd₁:

Figure 5.3 Tip induced relaxation of C₂H₂ adsorbed in the interstitial adsorption site on Pd₁. A slight increase in tunneling current (30 pA → 40 pA) first leads to unstable imaging conditions and tip changes (center). After scanning the same area for about 1.5 hours, conditions have stabilized and almost all interstitial adsorbates have disappeared. Instead the number of on-top adsorbed C₂H₂ has increased. Protrusions that were present initially are marked in red.

Steric repulsion of neighboring C₂H₄ molecules on Pd₃:

For neighboring C₂H₄ molecules on Pd₃, a slight shift is observed with respect to the position found for a single molecule on the Pd trimer. The STM images in overlay with the DFT structures are shown below.

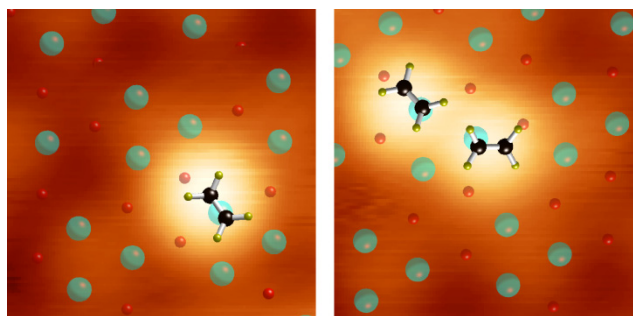


Figure 5.4 Steric repulsion of neighboring C₂H₄ molecules adsorbed on the same Pd trimer on PdGa:A(-1-1-1)Pd₃. DFT optimized geometries are superimposed. The adsorption energy per molecule accounts to 0.69 eV and 0.50 eV for the left and right case, respectively.

2. Details on bonding conformations and reaction pathways calculated by DFT

Details on the computational methods:

All calculations were performed in the mixed Gaussian plane wave approach as implemented in the CP2K code (<http://www.cp2k.org>). The substrate was modeled in the repeated slab geometry. Test performed on slabs thicker than 23/24 atomic layers confirm that the thickness of our slab is appropriate. Norm conserving pseudopotentials of the Goedecker type were employed.⁸⁹ Semicore 4s and 4p states of Pd, as well as

3d semicore states of Ga, were treated in the valence. A cutoff of 600 Ry was used for the representation of the charge density in plane waves. We used the PBE parameterization for the exchange correlation functional.⁹⁰

The Nudged Elastic Band method:

NEB calculations were performed in the "Climbing Image" scheme.¹⁰¹ Every reaction path was split in order to contain a single transition state per NEB simulation. According to the complexity of the NEB simulation we employed 10 to 31 images in the path. To increase precision for the determination of the total energies separate DFT relaxations were performed for the metastable positions of hydrogen.

Particular care was dedicated to the creation of the initial guess for each NEB simulation: starting from a given equilibrium geometry a series of consecutive constrained optimizations, where the distance between a H atom and a C atom in an adsorbed molecule was varying, allowed to select snapshots of a minimally biased reaction sequence. NEB procedure was then iterated until convergence of the barrier to 0.1 eV was reached.

3. Details on DFT computed hydrocarbon adsorption geometries

C₂H₂ adsorption on Pd₃:

In this case, the adsorbate is bound in a π /di- σ bond-configuration to the Pd trimer, with an energy of 1.17 eV. The C-C-H bonds are slightly asymmetrically tilted with 49.5° and 51.5°, resulting in a different height of the H atoms above the surface plane. Also for this surface we tested a π /di- σ configuration to Ga (similar to the one found for Pd₁), shown in the inset below, yielding an unfavorable adsorption energy of 0.3 eV.

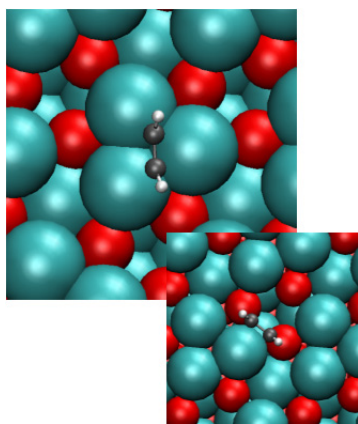


Figure 5.5 DFT optimized geometries of C₂H₂ on Pd₃. Top: The favored adsorption configuration is very similar to the one found on Pd(111). The inset shows the adsorption on the Ga atoms of the 2nd layer, similar to that found for Pd₁ (see later, Figure 5.6). However, on Pd₃ this configuration yields an adsorption energy of only 0.3 eV, and is thus unfavorable.

C₂H₂ adsorption on Pd₁:

Acetylene binds on this surface with an on-top geometry where the C-C-H bond angle is rotated by 18° with respect to the linear configuration. The adsorption energy amounts to 0.61 eV. The adsorption energy for other tested configurations shown in the bottom left) amounts to 0.43 eV, whereas it is 0.60 eV for the di-sigma configuration shown in the bottom right. Given the almost perfect degeneracy of the on-top site and the di-sigma configuration to Ga, we will consider paths leading from both configurations to the C₂H₃ geometry (see below).

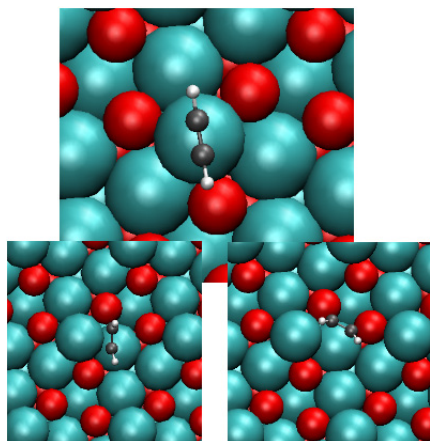


Figure 5.6 DFT optimized geometries of C_2H_2 on Pd_1 . Three different adsorption configurations exist, yielding adsorption energies of 0.61 eV, 0.43 eV and 0.60 eV for the situations shown in the top, bottom left, and bottom right panel, respectively.

C_2H_3 adsorption on Pd_3 :

The adsorption occurs on the trimer, and the configuration has a gain in energy of 0.076 eV with respect to C_2H_2 adsorption.

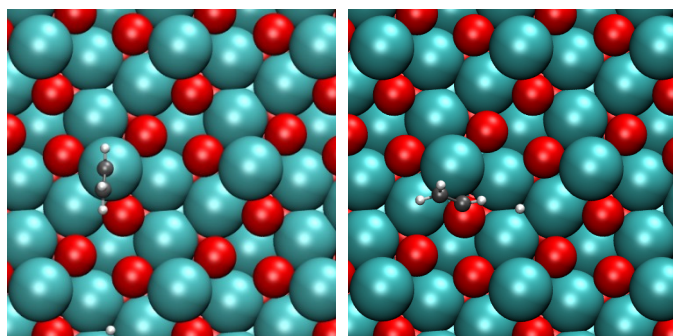


Figure 5.7 DFT optimized geometries of C_2H_3 on Pd_3 . The favored adsorption site after the first hydrogenation step is a bridge site between two Pd atoms of the trimer, yielding only a small energy gain of 0.076 eV with respect to C_2H_2 . The C-C axis of the C_2H_3 molecule is tilted with respect to the surface plane.

C_2H_3 adsorption on Pd_1 :

The configuration shown in the right panel is more stable by 0.66 eV compared to the on-top Pd position shown in the left panel. As for C_2H_2 , adsorption (see Figure 5.6), an adsorption site involving 2nd layer Ga atoms is identified for this surface.

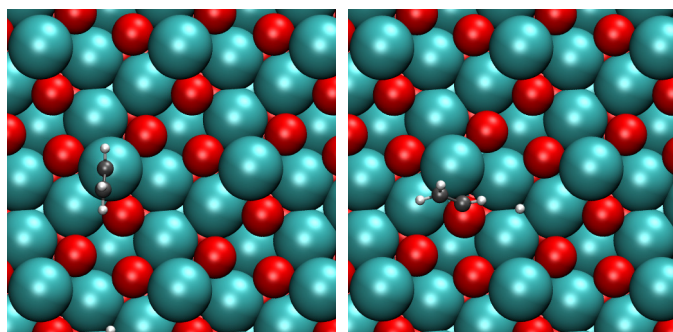


Figure 5.8 DFT optimized geometries of C_2H_3 on Pd_1 .

4. Details on NEB computed reaction barriers

$H_2 \rightarrow H + H$ on Pd_3 :

In this paragraph, all panels of this kind show the geometries at selected points of the trajectory (yellow symbols) on the left hand side, together with the reaction barrier on the right hand side. In the center panel, the path of hydrogen and hydrocarbons from the initial (white) to the final (black) state is presented.

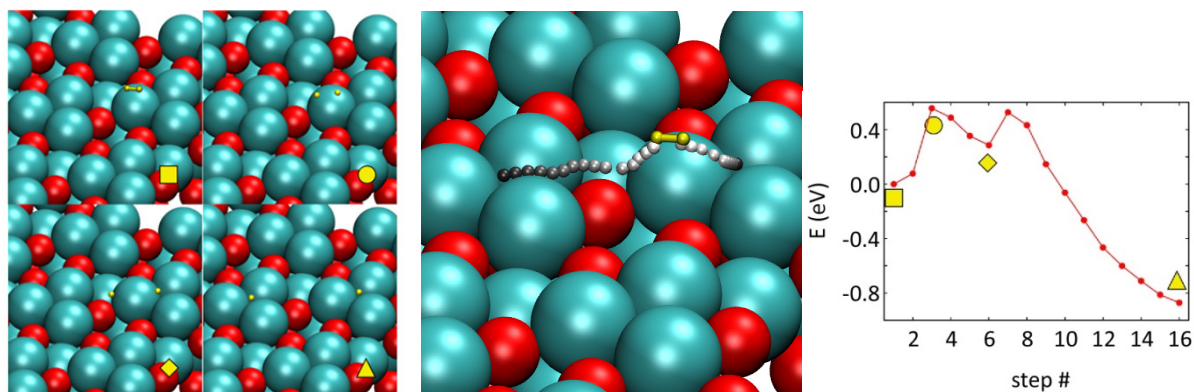


Figure 5.9 DFT reaction barrier for $H_2 \rightarrow H + H$ on Pd_3 . Hydrogen dissociation requires overcoming a barrier of 0.55 eV. The first minimum is due to one H atom in a metastable position.

$H_2 \rightarrow H + H$ on Pd_1 :

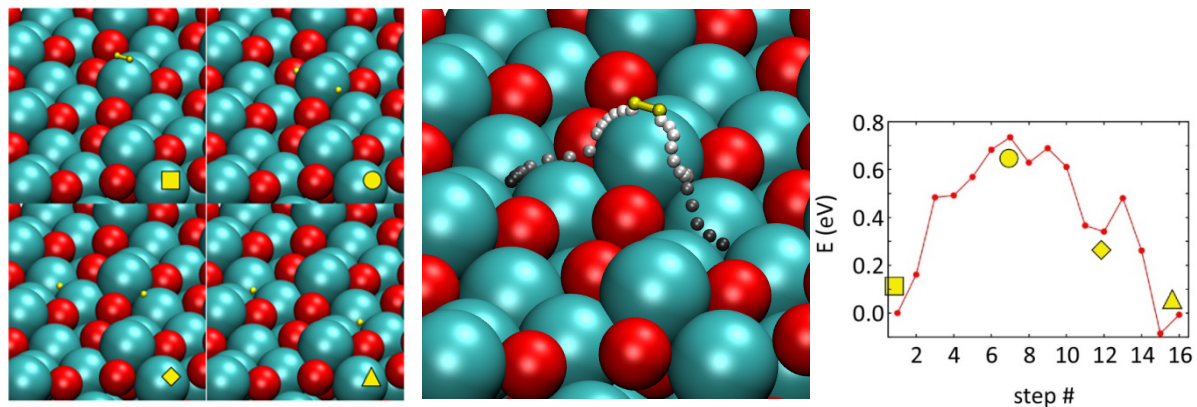


Figure 5.10 DFT reaction barrier for $H_2 \rightarrow H + H$ on Pd_1 . The barrier for hydrogen dissociation on Pd_1 is computed to 0.72 eV, with only a small gain in total energy.

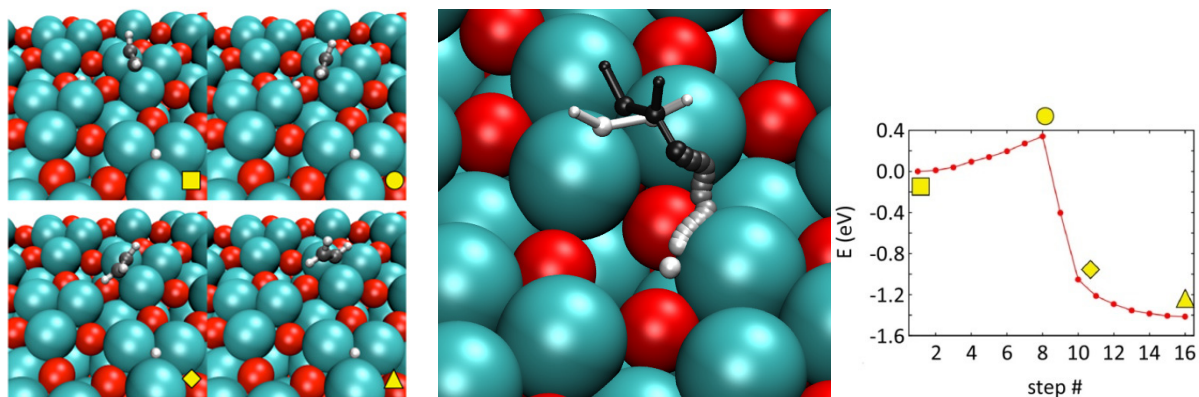
$C_2H_2 \rightarrow C_2H_3$ on Pd_3 :

Figure 5.11 DFT reaction barrier for $C_2H_2 \rightarrow C_2H_3$ on Pd_3 . The first hydrogenation step on Pd_3 requires a precedent endothermic (0.7 eV) approach of the atomic hydrogen towards the hydrocarbon (not shown in the graph) into a metastable position H^* . The hydrogenation barrier from the metastable hydrogen position is very low with 0.34 eV.

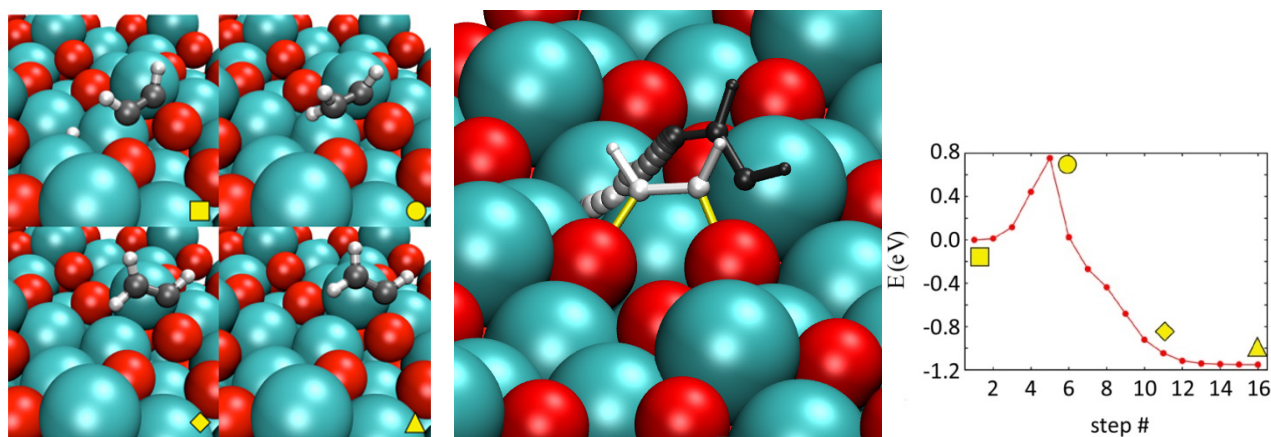
 $C_2H_2 \rightarrow C_2H_3$ on Pd_1 :

Figure 5.12 DFT reaction barrier for $C_2H_2 \rightarrow C_2H_3$ on Pd_1 . The first NEB simulated reaction connects the alternative π /di- σ Ga configuration for acetylene (Figure 5.6, bottom right panel) to the favorable adsorption geometry for C_2H_3 (Figure 5.8, right panel). As the hydrogen is supplied from the hollow site of the 3rd layer Pd trimer, no additional barrier is present for the hydrogen approach.

Alternative reaction barrier starting from the most preferred adsorption site for C_2H_2 on Pd_1 : The hydrogenation barrier amounts to 0.62 eV. The precedent hydrogen approach step (not shown) would cost additional 0.6 eV, which makes this reaction path less likely than the one from C_2H_2 in the π /di- σ Ga bridge state, shown in Figure 5.12.

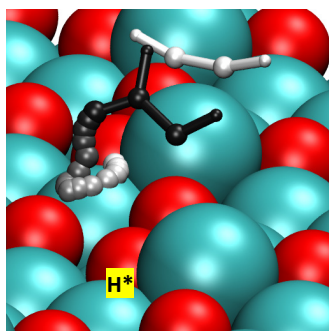


Figure 5.13 Alternative reaction pathway for $C_2H_2 \rightarrow C_2H_3$ on Pd_1 . The second NEB path is connecting the on-top π configuration for C_2H_2 (Figure 5.6, top panel) with the bridge site energetic minimum of C_2H_3 (Figure 5.8, right panel). (This reaction barrier is not shown in Figure 7 of the main text of the publication.)

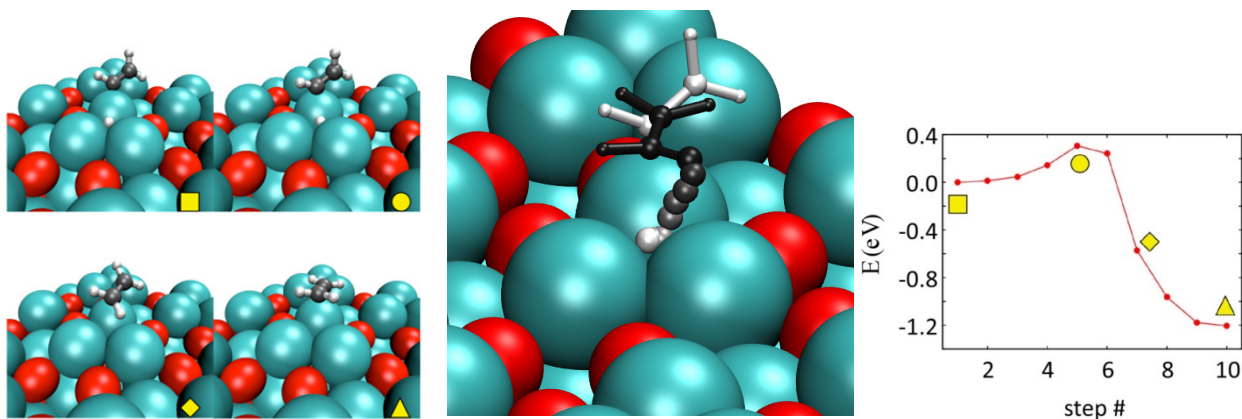
$C_2H_3 \rightarrow C_2H_4$ on Pd_3 :

Figure 5.14 DFT reaction barrier for $C_2H_3 \rightarrow C_2H_4$ on Pd_3 . To achieve hydrogenation, the hydrogen has to diffuse in an endothermic step (H^* , 0.5 eV) to the trimer hosting the vinyl (■). The co-adsorption on the same trimers leads to a shift of the vinyl from the preferred bridge site (Figure 5.7) to an on-top site position on Pd. The NEB presented above starts from this situation, yielding a reaction barrier of 0.3 eV for the hydrogenation step (●).

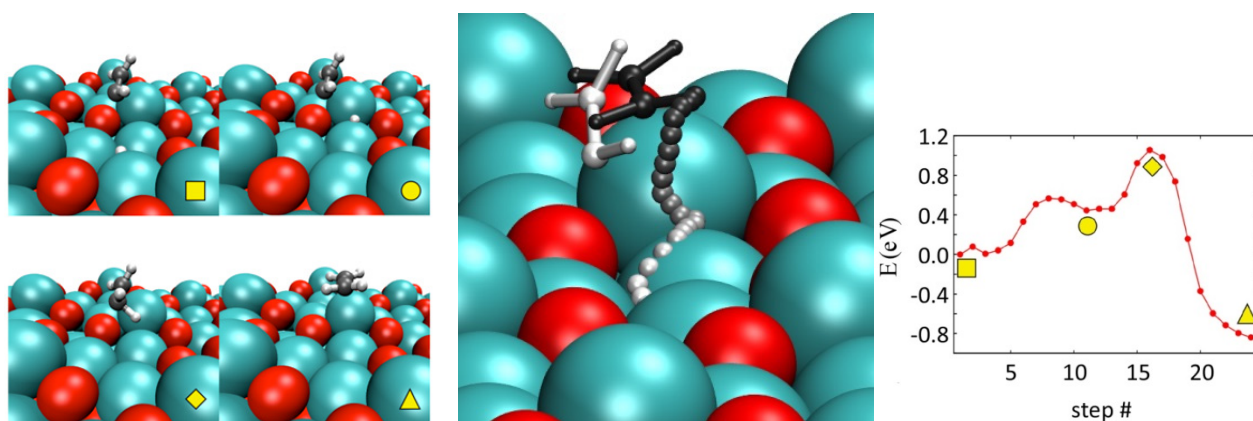
 $C_2H_3 \rightarrow C_2H_4$ on Pd_1 :

Figure 5.15 DFT reaction barrier for $C_2H_3 \rightarrow C_2H_4$ on Pd_1 . In this case, we split the NEB in two different calculations to test the diffusion of atomic hydrogen. To reach the metastable position (●), an initial barrier of 0.6 eV has to be overcome. The following the attack of the vinyl fragment yields a further barrier of 0.6 eV leading to the more stable ethylene state on-top of the outermost Pd atom (▲).

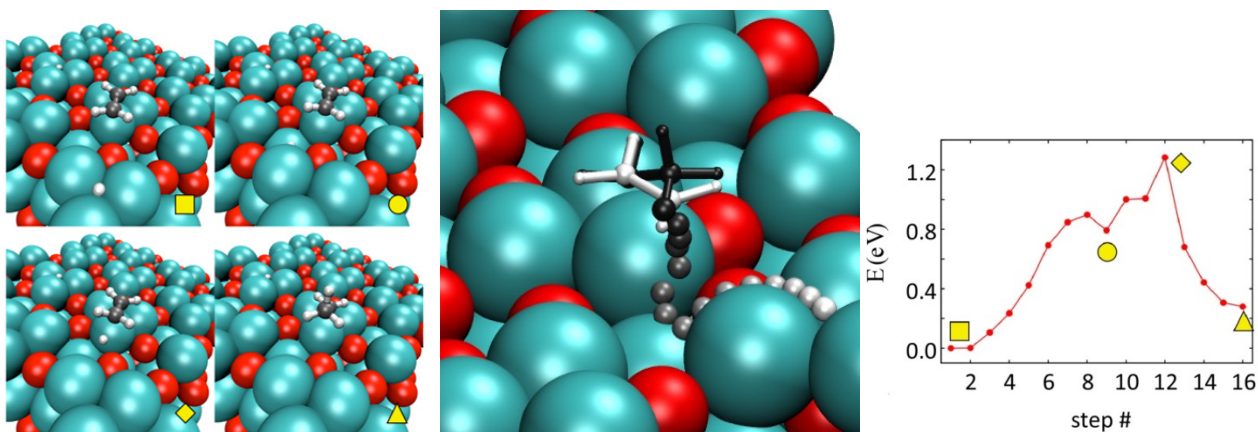
$C_2H_4 \rightarrow C_2H_5$ on Pd_3 :

Figure 5.16 DFT reaction barrier for $C_2H_4 \rightarrow C_2H_5$ on Pd_3 . Also here we consider the two processes in the NEB, starting with an approach of the hydrogen atom from the absolute minimum (■) to a metastable position of hydrogen (H^* , 0.8 eV) and the subsequent hydrogenation step to C_2H_5 with a total barrier height of 1.3 eV.

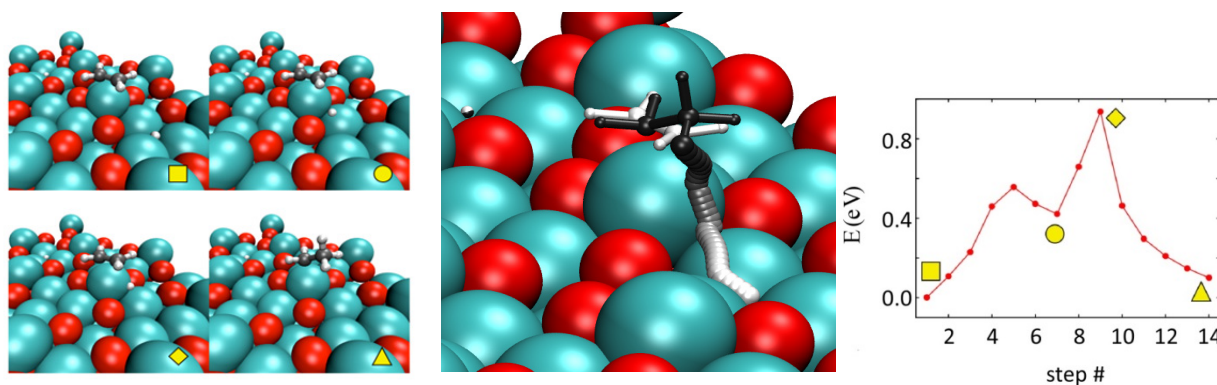
 $C_2H_4 \rightarrow C_2H_5$ on Pd_1 :

Figure 5.17 DFT reaction barrier for $C_2H_4 \rightarrow C_2H_5$ on Pd_1 . Also for Pd_1 , we include the hydrogen approach in the NEB simulation. The total barrier amounts to 0.9 eV, including the diffusion of H to the metastable position (●) at 0.4 eV, and the subsequent hydrogenation step with a barrier of 0.5 eV. As explained in the manuscript, desorption of ethylene (which has a lower adsorption energy of 0.73 eV) is likely to occur before the barrier for transformation to C_2H_5 is overcome.

5.2 The C₂H₂ molecular rotor on Pd₃

Scanning probe methods allow the manipulation of single molecules or atoms on a surface by tip proximity or inelastic tunneling of electrons into single molecules.¹⁰²⁻¹⁰³ This opens the possibility to investigate the adsorbate-surface bond on the atomic level, which is not only important for research on model catalysts, but also for the understanding of mechanical processes on the length-scale of single molecules, *e.g.* molecular movements and diffusion on surfaces.¹⁰⁴ Motions of molecules have been studied on various transition metal surfaces by means of LT-STM.^{115, 117} In the context of this work, Wilson Ho and co-workers performed in-depth studies on the rotational motion of acetylene on Cu(100).¹⁰⁵ If the STM tip is placed above a single C₂H₂ molecule, they evidenced a sudden increase in the molecular rotation rate as a function of tunnel gap voltage at 358 meV. The rotational motion of C₂H₂ is excited by relaxation of the C-H stretch bond (357 meV) into bending vibrations. A more recent computational study,¹⁰⁶ identifies the origin for the rotational motion as a combination of C-H stretch mode relaxation and overtone ladder climbing by multi-electron excitations of the hindered rotational mode. These experiments, allow insight into energy barriers for mechanical motions and lifetimes of different vibrational states of acetylene bound to the Cu substrate.

Rotation of acetylene has also been observed on Pd(111)¹⁰⁷⁻¹⁰⁸, where the molecules adsorb with the C-C axis parallel to the surface plane, with a π /di- σ bond and the center of the C-C axis in the threefold hollow sites. The H atoms are tilted with respect to the C-C axis, pointing away from the surface. As stated in Chapter 5.1, this situation is very similar to adsorption of C₂H₂ on the threefold Pd₃ termination. Both surfaces, Pd₃ and Pd(111), offer three degenerate adsorption configurations per hollow site for C₂H₂ and switching between these different orientations has been observed for Pd(111). By monitoring the rotational frequency as a function of temperature, Dunphy *et al.*¹⁰⁸ determined the rotation barrier to 113 meV. Matsumoto *et al.*¹⁰⁷ reported that the effect can be triggered by the STM tip, using a gap voltage of 100 meV, while no rotation is observed for 50 mV with the same tunnel current (1 nA).

To investigate the origin of the rotational motion of single C₂H₂ molecules on the Pd trimers of the Pd₃ surface (see Figure 4 of Chapter 5.1), the gap voltage- and current-dependency of the rotational frequency is investigated, and discussed with regard to literature data of C₂H₂ on Pd(111). For this purpose single molecules on Pd₃ were investigated by LT-STM at 5 K. The STM tip was located atop a C₂H₂ adsorbate, while keeping the tunnel current constant and the feedback loop activated. The stepwise rotational motion between three degenerated states (Figure 5.18a) led to a change in the apparent height of the molecule underneath the tip. As the tip height (z) was constantly regulated to maintain the current setpoint, the rotation results in a z profile as a function of time, $z(t)$, where three distinct levels are discernible. A typical $z(t)$ profile is shown in Figure 5.18b. By analysis of a large number of $z(t)$ profiles, the switching frequency f was determined as a function of gap voltage (Figure 5.18c), showing a sudden enhancement of rotation around 30-35 meV. The number of rotations per electrons, or the “rotational yield”, is obtained by normalization of the switching frequency to the tunnel current. An exponential increase is visible in the logarithmic representation of the rotation yield (Figure 5.18d) showing the onset of the excited rotation at 32 meV.

The dependency of the rotational frequency f on the tunnel current I (Figure 5.18e), allows to extract the number of electrons N contributing to the excitation.¹⁰³ For multi-excitation processes the relation is $f \propto I^N$. The linear increase of the rotational frequency with tunnel current, indicates that a single electron inelastic tunnel process is responsible for the excitation, as all curves shown in Figure 5.18e can be fitted using $N=1$. The absence of multi excitation-, or ladder climbing- processes, shows that the relaxation rate of a poten-

tially excited vibrational state, leading to rotation, is larger than the excitation rate, which is defined by the tunnel current.

The representation in Figure 5.18f indicates that the excitation probability is independent on the electric field; a smaller tip-sample separation, i.e. larger current, leads to higher fields across the molecule, but no change in the rotational yield.¹⁰³ The comparison of Figure 5.18f to the respective data for C₂H₂ on Pd(111) (FIG. 3 in Ref. ¹⁰⁵) reveals that the number of rotations per electron is about 1000 times larger on the inter-metallic surface. Furthermore, the necessary tunnel currents to excite these rotations are much lower for C₂H₂ on Pd₃, revealing that rotation is more efficiently excited on Pd₃ compared to Pd(111).

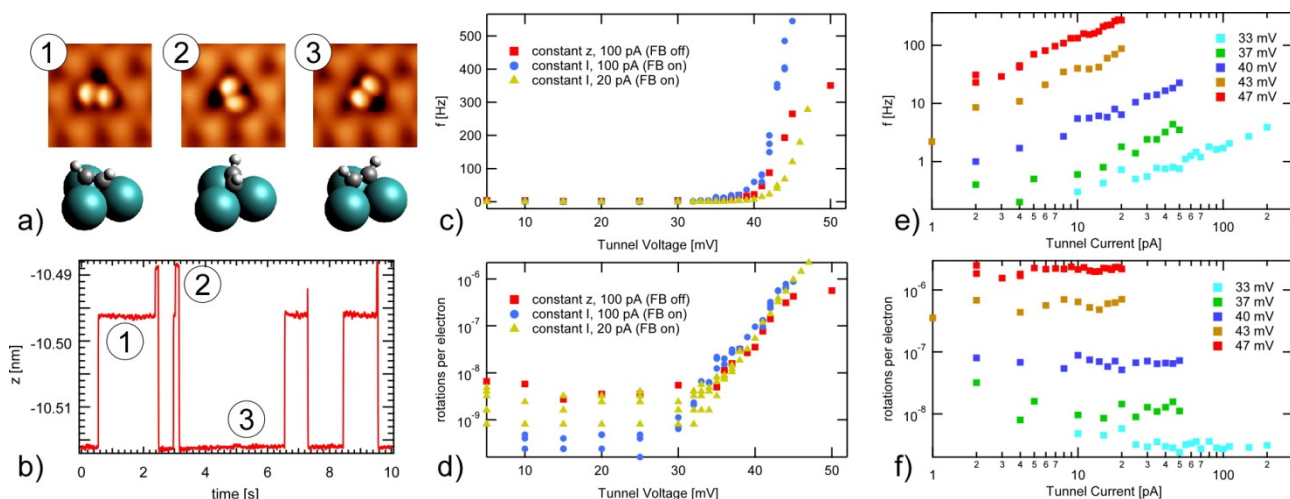


Figure 5.18 Rotational motion of the acetylene on the Pd₃ trimer. a) Three degenerate adsorption configurations can be observed by STM and switching between them can be monitored as a function of time (b). The rotation rate (c) and the rotational yield (d) increase exponentially with the gap voltage around 32 meV, while the number of rotations per electron is independent of tunnel current(d, f). The linear increase of the rotational frequency with tunnel current (e) indicates a single electron process for the excitation.

The threshold voltage for rotation on Pd₃ of 32 mV is much lower compared to the C₂H₂ rotational barrier on Cu(100) and Pd(111), of 358 and 113-100 meV, respectively.^{105, 107-108} While in the case of C₂H₂ on Cu(100) the assignment to the relaxation of the C-H vibrational stretch mode is evident (ν_{CH} : 2880 cm⁻¹ – 357 meV), the origin for rotation on Pd(111) was not explained in detail. However, literature values from electron energy loss spectroscopy¹⁰⁹ show that relaxation of C-H rocking modes of C₂H₂ might be responsible for the rotation on Pd(111), as the reported energies are in the range of 100 meV ($\rho_{CH(sym)}$: 673 cm⁻¹ – 84 meV; $\rho_{CH(asym)}$: 870 cm⁻¹ – 108 meV). Since the energy barrier for rotation of C₂H₂ on Pd₃ is much lower than those of the internal vibrational modes of C₂H₂, it is plausible that the rotation is excited directly by the inelastic tunnel processes of a single electron, as suggested by the data in Figure 5.18.

Another plausible pathway for rotation might be the excitation of a vibrational C-Pd stretch mode and its relaxation into the rotational motion of the molecule. The energies associated to the C-M (metal) stretch mode are typically in the range of 50-57 meV for a –CCH₃ hydrocarbon species on different transition metals.¹¹⁰ It is reasonable that this value might be reduced for adsorption on the intermetallic surface due to the ligand effect of Ga and the presence of the intact acetylene molecule.

An explanation for the highly efficient excitation of the molecular motion can be derived from the PdGa surface chirality. As the Pd(111) surface exhibits mirror symmetry, vertical motion of C₂H₂ is completely decoupled from rotation and clockwise and anticlockwise rotation are energetically equivalent. This is not the case for the chiral Pd₃ surface. Here, the surface asymmetry is expected to lead to a saw tooth-like potential energy as a function of rotational angle, with three minima over the range of 360° of rotation. This can lead to a molecular ratchet and one-way rotation of the molecules.¹¹¹ Furthermore, the rotational angle of the C-C axis yielding the lowest binding energy might depend on the height of the molecule above the surface. This would lead to efficient coupling of C-M vibrational motion and C₂H₂ rotation in one rotational direction. A preferred sense of rotation is indeed observed in most measurements (cf. Figure 5.18b).

In conclusion, by analysis of the C₂H₂ rotational frequency, the very different energetics for molecular rotation on Pd₃ and Pd(111) was demonstrated. In comparison, Pd₃ offers isolated adsorption sites and hopping to neighboring trimers is suppressed, while at the same time the barrier for rotation on the trimer is reduced. These effects are assigned to the site-isolation and the ligand effect of Ga, respectively.

5.3 XPS studies of acetylene and ethylene on the threefold PdGa surfaces

To investigate the electronic structure of adsorbed hydrocarbons on Pd₃ and Pd₁ we performed XPS during molecule deposition at 80 K. The shape and increase of the C1s level was monitored as a function of deposition time during the exposure of 1 Langmuir over 30 min. A typical dataset is shown in the left panel of Figure 5.19 for C₂H₂ on Pd₃.

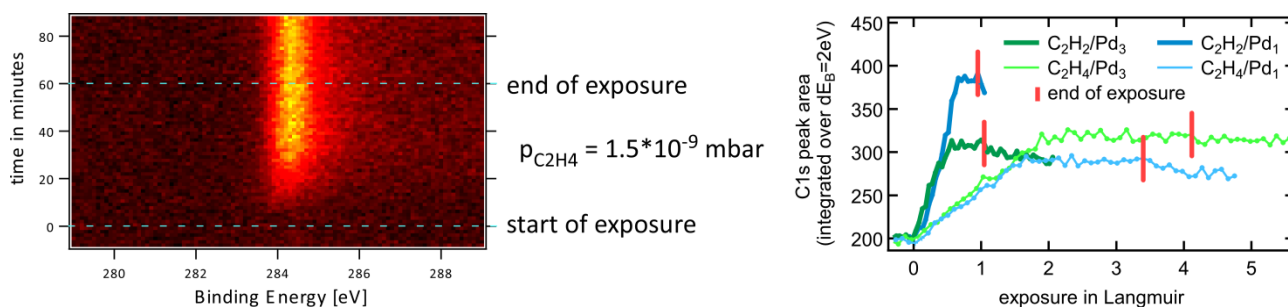


Figure 5.19 XPS spectra of the C1s peak as a function time for exposure of Pd₃ to C₂H₄ over 60 minutes. Right: Increase of the C1s peak areas during exposure of Pd₃ and Pd₁ to C₂H₂ and C₂H₄. The value for the peak area is obtained from the integration over a binding energy range of 2 eV.

The C1s peak area, shown as a function of exposure in Langmuir (L) in the right panel of Figure 5.19, is a measure for the amount of adsorbed carbon on the surface. The carbon coverage increases 4 times faster for exposure to C₂H₂ as for C₂H₄, which indicates a much lower sticking coefficient for the latter molecular species, independent of the substrate. Furthermore, the coverage increases linearly with exposure for all experiments until saturation is achieved. This behavior is indicative for a weakly bound adsorption precursor state^{98, 112} which allows for diffusion of the physisorbed molecules to an unoccupied adsorption site. Indeed for most data shown in Figure 5.19, a slight decrease in C1s peak area is observed shortly after deposition, showing desorption of molecules from the precursor state.

The larger saturation coverage for C₂H₂/Pd₁ that is apparent in the XPS data taken during molecule adsorption (Figure 5.19) is confirmed in the static spectra shown in Figure 5.20, taken after deposition with an integration time of 15 h. The total peak areas, given in the table below, are obtained from the sum of the fitted partial peaks (red lines in Figure 5.20). To ease comparability, also the relative total peak areas, normalized to C₂H₂/Pd₃, are given, showing that C₂H₂ saturation coverage on Pd₁ is about double with respect to Pd₃. This is in agreement to the STM observations presented in Chapter 5.1, where at high coverages two adsorption sites per surface unit cell were seen for Pd₁, while only one is present on Pd₃. The relative saturation coverages for C₂H₄ on the two surfaces are 1.26 and 0.89, for Pd₃ and Pd₁, respectively. This diverges from the number of adsorption sites per unit cell of 3 to 1, which was determined by STM. This is due to steric hindrance between C₂H₄ molecules bound to the same Pd₃ trimer (cf. Figure 5.4), which prohibits the full occupation of three molecules per trimer.

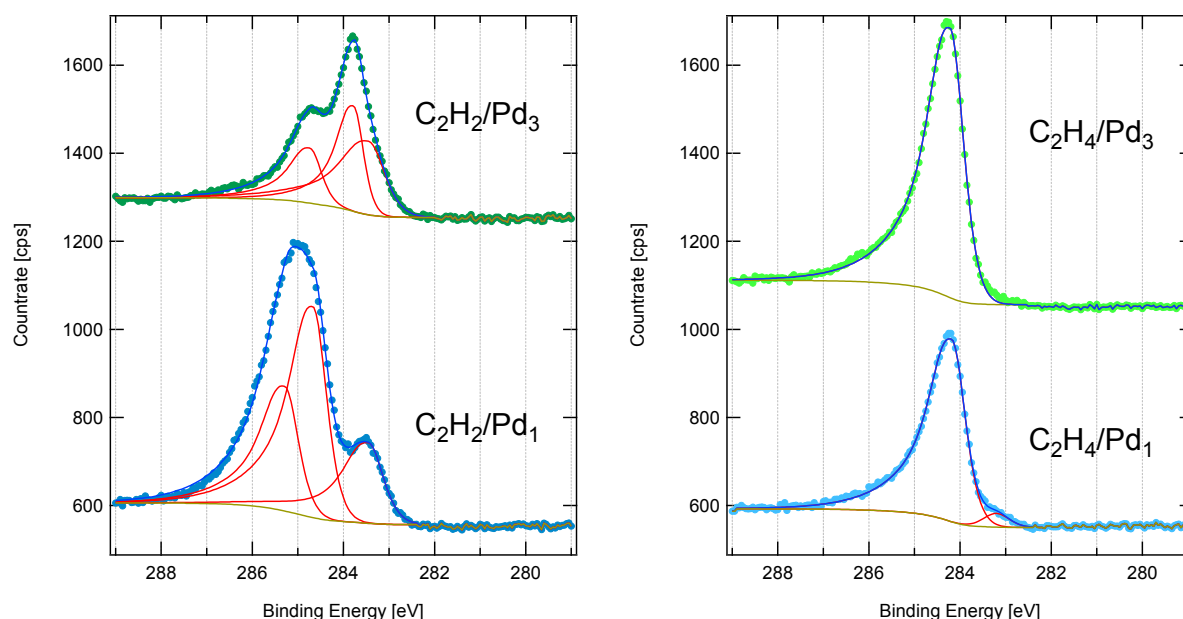


Figure 5.20 XPS spectra (round markers, same colors as in Figure 5.19) of the C1s level after deposition of C_2H_2 (left) and C_2H_4 (right) at 80 K to saturation coverage (integration time: 15 h). The results of the peak fitting are shown together with the data; Shirley-type background (brown), partial peaks (red), and envelope (blue). Numerical details are given in the table below. The shoulder at 283.46 eV for C_2H_2/Pd_1 is growing with measurement time due to X-ray degradation.

	C_2H_2/Pd_3	C_2H_2/Pd_1	C_2H_4/Pd_3	C_2H_4/Pd_1
Peak position [eV]	283.45	284.67		284.18
	283.78	285.29	284.21	283.20
	284.74	283.46		
FWHM	0.84	0.71		0.70
	0.51	0.71	0.70	0.66
	0.60	0.77		
Relative peak area	42 %	50 %		96 %
	36 %	30 %	100 %	4 %
	22 %	21 %		
Absolute total peak area	613	1232	772	546
Relative total peak area	1	2.01	1.26	0.89

Results of the C1s peak fitting shown in Figure 5.20.

We begin the discussion on the C1s peak shapes and components from the data on C_2H_4 adsorption. A single asymmetric peak is measured on both surfaces at binding energy 284.2 eV, which is ascribed to sp^2 hybridized carbon in the π -bonded C_2H_4 molecule on-top the Pd surface atoms. The asymmetric peak shape is due to vibrational excitation of the C-H bonds by photoelectrons, resulting in a peak towards higher binding energies about 0.4 eV apart from the main component, and giving about 40 % contribution to the overall intensity.¹¹³⁻¹¹⁴ For C_2H_4 on Pd_1 , the weak component (4%) at 283.20 eV is assigned to other carbon deposits.

In contrast to this straight forward interpretation, the C1s peak shapes detected for the C₂H₂ saturated surfaces are more complicated. On Pd₁, the main peak is fitted to two components at 284.67 and 285.29 eV (the shoulder at 283.45 eV is due to X-ray degradation and discussed below). Keeping in mind the results from DFT and STM, showing that two different adsorption sites exist for C₂H₂ on this surface, the presence of multiple peaks is explained by the differently coordinated carbon atoms bound to Pd or Ga. However, the available data does not permit a direct assignment of the components. Compared to C₂H₄, the positions of the main contributions are shifted by about 0.5 eV towards higher binding energies indicating a substantial difference in carbon ionization state for binding of acetylene and ethylene on Pd₁. With increasing X-ray exposure of the C₂H₂ over 15 h, the shoulder at 283.46 eV keeps growing, while the component at 285.29 eV decreases. This indicates a degradation of the molecules due to the X-ray photons or the photoelectrons emitted by the surface atoms.

For Pd₃, a double peak is observed, with an additional weak shoulder towards lower binding energies. Peak fitting yields good results for three components with 42, 36 and 22 % contribution at 283.45, 283.78 and 284.74 eV, respectively. This large spread of the C1s core level binding energies indicates a strong variation in the ionization state of different carbon atoms. Even though we identified an asymmetric π /di- σ bond of C₂H₂ to the Pd trimer of the surface by STM and DFT, with the two carbon atoms in slightly different configurations with the surface Pd atoms, the observed peak separation of about 1 eV is rather large. For comparison, the C1s peaks for CCH₃ bound to Pd(111) leads to a peak separation of 0.6 eV, due to the different ionization states of the inner and outer carbon atoms.¹¹³ As described above for ethylene, also for acetylene a contribution from vibrational excitation of the molecule is present, yielding a component shifted about 0.4 eV towards higher binding energies.¹¹⁵ However, since 1st (2nd) order vibrational excitations for C-H bonds commonly yield shifts of 0.4 eV (0.8 eV) and contributions of about 40 % (10 %), this does not explain the large separation and intensity of the side peak at 284.74 eV observed for C₂H₂/Pd₁. Even though only a very weak change of the C1s peak shape is observed as a function of time, we cannot exclude fast X-ray degradation leading to dehydrogenation and formation of other hydrocarbon species.

To study the influence of acetylene binding on the substrate atoms, we measured the Pd and Ga core levels before and after adsorption, shown in Figure 5.21. The Pd 3d core level of the clean Pd₃ termination exhibits a shoulder towards lower binding energies, which disappears upon adsorption of acetylene. Also for Pd₁, a small component of the Pd 3d peak towards lower energies disappears upon adsorption. In combination with the STM data discussed in Chapter 5.1, these observations are assigned to the outermost Pd atoms of the two surfaces, and their change in coordination upon binding of acetylene. This effect is more pronounced on Pd₃ than on Pd₁, due to the ratio of low coordinated surface Pd of 3:1. Variations in the Ga 3p core level peak shape are weak. The overall loss of intensity in the Ga peaks is assigned to the hydrocarbons “shielding” the emission from substrate Ga atoms.

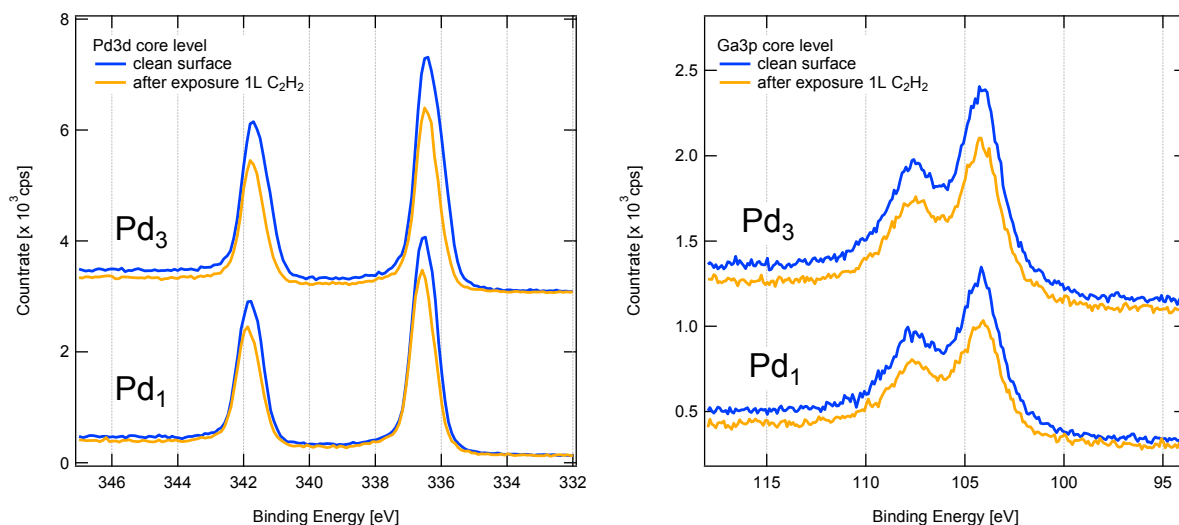


Figure 5.21 XPS of Pd 3d and Ga 3p core levels before and after adsorption of C₂H₂ at 80 K, taken at an angle of 70° from the surface normal direction. In the left/right, a pass energy of 100/200 eV was used.

To summarize the XPS investigations, a good agreement between the peak areas, i.e. carbon saturation coverages as measured by XPS, and our STM and DFT results is found. The variations observed for the Pd 3d core level upon adsorption of acetylene, confirm the involvement of surface Pd atoms in the bonding of the molecules. Peak positions and shapes of the C1s core levels for C₂H₄ are in-line with the picture of π -bonded molecules on-top the outermost Pd surface atoms on the Pd₃ and Pd₁ surfaces. For C₂H₂ adsorption, three matters do not allow for an unambiguous interpretation of the XPS data: Firstly, the appearance of two largely separated C1s peaks for Pd₃; and secondly, the fact that degradation of the molecules due to X-ray exposure cannot be excluded. A solution to this might be the use of low energy X-rays from synchrotron radiation, as the molecule degradation might be reduced and a better energy resolution can be obtained. Furthermore, by varying the excitation energy or the emission angle, valuable information on the adsorption geometry can be obtained, like C-C bond distance and angles with respect to the surface. Experiments on vibrational excitations using electron energy loss spectroscopy (EELS) or FTIR might help to further enlighten the adsorption configuration of acetylene on the intermetallic surfaces.

Chapter 6 Exploring enantioselectivity on intrinsically chiral intermetallic PdGa surfaces

Biochemical processes in the human body strongly rely on the correct stereoisomers of involved molecules. Therefore, the synthesis of stereopure chemicals is of tremendous importance to the fabrication of efficient and correctly functioning drugs. In this respect, the synthesis of a specific enantiomer, *i.e.* a stereoisomer with a specific stereogenic or chiral center, can be accomplished by means of homochiral catalysis. As enantiomerism is a purely geometrical property, *i.e.* the physiochemical properties of two enantiomers are exactly the same, an enantioselective reaction step in catalysis requires chiral binding centers. In homogeneous catalysis (Figure 6.1A), these binding centers may be provided by enantiopure molecules, which bind achiral reactants in a chiral configuration, leaving a specific site of the reactant exposed for the attack of a second reactant. This directs the reaction into a predefined chiral pathway which leads to enantioselective synthesis.

In heterogeneous catalysis, enantioselectivity is commonly achieved by using surface modifiers or auxiliaries.¹¹⁶⁻¹¹⁸ Typically, those are chiral molecules that are adsorbed on an achiral support. In the example shown in Figure 6.1B, the adsorbate complex and the surface form a chiral binding center for the achiral reactant. Similar to the case of homogeneous catalysis, the reactant binds in a predefined configuration to this chiral complex. In the example (Figure 6.1B), an enantiospecific hydrogenation of the reactant is achieved, through the hydrogen attack occurring from the side of the surface, not from the vacuum. With this procedure, the previously prochiral reactant is converted into a specific enantiomer of the product by addition of hydrogen to a defined site of the molecule and creation of a stereogenic center.

Recently, “naturally” chiral surfaces, *i.e.* surfaces that exhibit chiral features in the bare, adsorbent-free state, have been investigated with respect to chiral adsorption and enantioselective separation of racemic mixtures.¹¹⁹⁻¹²⁰ In the case of achiral crystals, the chirality is created by cutting of single crystals at low symmetry crystal planes. The resulting high-Miller index surfaces can exhibit chiral binding centers at atomic kink sites (Figure 6.1C), and in consequence might offer an energetically favorable binding for one of the enantiomers of the adsorbed racemat.

A different approach is based on the intrinsic chirality of materials, as present for example in minerals.¹²¹ In contrast to the heterogeneous methods discussed above, where the chirality is imparted by chiral modifiers or precise cutting of achiral single crystals, these materials are chiral in their bulk crystal structure, which might be projected to their surface (Figure 6.1D). In principle, the chirality is conserved also after grinding of these materials into powders, or after surface etching, which makes them prospectively interesting materials as industrial catalysts. Also some intermetallic compounds exhibit bulk chirality, which, to the best of our knowledge, has not yet been investigated with respect to enantioselectivity. Also the intermetallic compound PdGa exhibits a chiral crystal structure, as discussed in Chapter 2.1 while at the same time being

an active hydrogenation catalyst.²¹ The combination of a partially bound crystal structure, catalytic activity and bulk chirality of PdGa bears great potential for its application as enantioselective catalytic material.

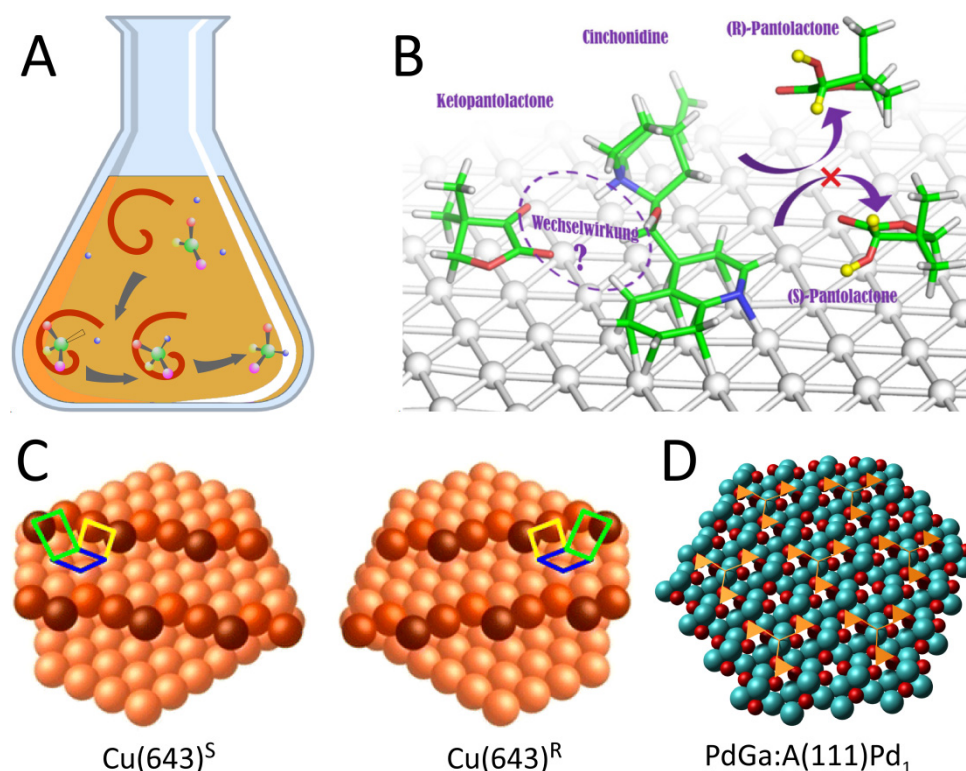


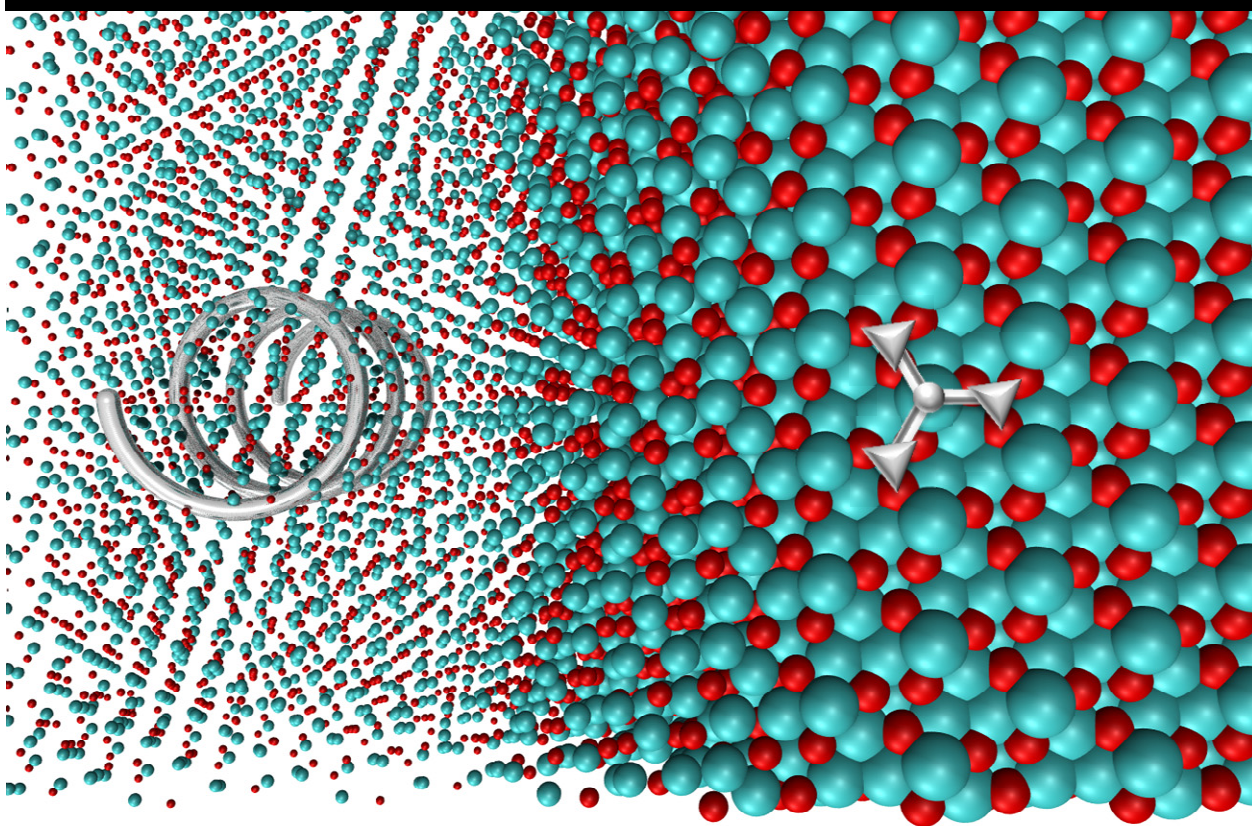
Figure 6.1 Different approaches to chiral synthesis of molecules. A) Homogeneous enantioselective catalysis is based on chiral molecules (red spirals) binding the non-chiral reactant (3-atomic molecule). A fourth atom (blue) connects on a well-defined site, defining the handedness of the product (4-atomic molecule) B) In heterogeneous catalysis, an adsorbed chiral auxiliary (Cinchonidine) binds an achiral reactant (Ketopantolactone), which is subsequently hydrogenated from the side of the substrate. (figure adapted from Ref. ¹²²) C) Kinks of single crystal surfaces offer chiral binding sites. (figure adapted from Ref. ¹¹⁹) D) Clean surface of a chiral intermetallic compound exhibiting chirality in every surface unit cell (structure indicated by orange triangles). The handedness is defined by the bulk enantiomer form of the compound.

In this chapter, we investigate the effect of the chiral binding centers on the adsorption of prochiral molecules, which is the pivotal step towards enantioselective reactions. The chiral structures of the different PdGa(hkl) surfaces are discussed in Chapter 3.3. For the threefold surfaces, the chirality is expressed in the atomic arrangement of the 2nd and 3rd outermost layers, consisting of Ga and Pd atoms, respectively. Due to its open surface structure, Pd₁ is expected to show an enhanced influence of surface chirality as these atomic layers are exposed.

We chose the prochiral molecule 9-Ethynylphenanthrene (9-EP) to probe the surface chirality on the Pd₁ surface, as elaborated in Chapter 6.1. By evaluation of a large number of molecules observed by LT-STM, we demonstrate a strong enantioselective adsorption for this molecule-substrate system. The results are summarized in a manuscript that is in preparation for submission as a Letter in the journal *Nature Materials*. In a second experiment, the more densely packed Pd₃ surface was tested for enantioselective 9-EP adsorption. The results are presented in Chapter 6.2. The Pd trimers of this surface termination lead to a different binding behavior of the adsorbates, compared to the single Pd atoms on Pd₁.

6.1 Publication (in preparation): "Room Temperature Enantioselective Adsorption on a Chiral Intermetallic Surface"

Enantioselectivity on PdGa
from bulk- to surface chirality



Room Temperature Enantioselective Adsorption on a Chiral Intermetallic Surface

Jan Prinz, Harald Brune+, Oliver Gröning, and Roland Widmer

Empa. Swiss Federal Laboratories for Materials Science and Technology, nanotech@surfaces Laboratory, Ueberlandstrasse 129, 8600 Dübendorf, Switzerland.

+ Institute of Condensed Matter Physics, Ecole Polytechnique Fédérale de Lausanne (EPFL), Station 3, 1015 Lausanne, Switzerland

Synthesis of enantiopure products is pivotal in the production of many pharmaceuticals, artificial flavors, agrochemicals, and materials for nonlinear optical devices. Chiral synthesis implies reactions that are asymmetric with regard to stereoisomerism¹²³⁻¹²⁴ and therefore requires chiral template surfaces to achieve enantioselective heterogeneous catalysis. To date, such surfaces are commonly obtained by imparting chirality to non-chiral metal surfaces via the adsorption of chiral molecular modifiers or auxiliaries.¹²⁵⁻¹²⁶ In the present study, we investigate the potential of intrinsically chiral surfaces of intermetallic compounds as novel materials for enantioselective catalysts. Their advantage is the significantly higher thermal and chemical stability, and therefore their extended application range for catalyzed chiral reactions.^{121, 127} We show that on the Pd₁ terminated PdGa(111) surface room temperature adsorption of a small prochiral molecule (9-Ethynylphenanthrene) leads to exceptionally high enantiomeric excess ratios of up to 98%. Our findings highlight the great potential of intrinsically chiral intermetallic compounds for the development of novel, enantioselective catalysts which can be operated at high temperatures and potentially also in harsh chemical environments.

In the investigation of stereochemical processes at surfaces the use of chiral metal substrates has been extremely scarce and mainly limited to self-assembled chiral molecular layers^{120, 126, 128} and vicinal surfaces exhibiting chiral kink sites at the step edges of atomic terraces^{119, 129-130}. Due to its non-centrosymmetric bulk structure of the space group P2₁3, the intermetallic compound PdGa exists in two enantiomeric forms A and B, which are denoted as PdGa:A and PdGa:B respectively.^{20, 28-29} PdGa has recently attracted considerable interest due to its high activity, selectivity and stability in the catalytic semi-hydrogenation of ethyne, which is an important step in the polyethylene production.²¹ Single crystals grown by the Czochralski method are available in cm³-sized monoliths³⁰ and all the low index surfaces (111), (-1-1-1), (100) and (110) can be prepared to show large single atomic terraces by standard ultra-high vacuum (UHV) preparation using sputtering and annealing cycles.^{28-29, 131} As no significant surfaces reconstructions occur²⁸⁻²⁹, the bulk chirality is maintained at all these surfaces, thus each surface unit cell exhibits a chiral atomic arrangement, as shown Figure 6.2. This means that a high density of chiral bonding centers is present on the bare surfaces, potentially leading to higher enantioselective catalytic activity compared to approaches based on the handedness of terrace step kink sites.^{119, 129-130}

PdGa:A(111) is terminated by an atomic layer containing one isolated Pd atom per surface unit cell²⁹ and accordingly this termination is denoted as Pd₁ (cf. Figure 6.2). These Pd atoms form a hexagonal lattice with a lattice constant of 0.69 nm and therefore the topmost layer of this surface is achiral. The structure of the 2nd and 3rd outermost surface layers, consisting of Ga and Pd trimers respectively, induces the surface chi-

rality, which is indicated by red and cyan triangles in Figure 6.2. The enantiomorph of the PdGa:A(111) (abbreviated A:Pd₁) is the PdGa:B(-1-1-1) surface (B:Pd₁). The relatively large size of the surface unit cell and the low density of the topmost Pd layer ensure that the chirality expressed in the deeper layers can still influence the molecular adsorption and reaction processes.

The effect of the intrinsic chirality of the A:Pd₁ and B:Pd₁ surfaces on enantioselective adsorption is investigated by deposition of the prochiral molecule 9-Ethynylphenanthrene (9-EP, see Figure 6.2). Prochirality is a property of planar molecules which possess in-plane but not out-of-plane mirror symmetry and are thus achiral. However, when deposited on a surface the molecule forms a chiral adsorbate complex by lying either "face-up" or "face-down", forming either enantiomer *R* or *S*. For achiral substrates, energetically equivalent adsorption sites for the *R* and *S* enantiomers are available, and thus they appear in equal abundance.¹³² To achieve an excess of one of the two enantiomeric forms, i.e., enantioselectivity, the substrate must exhibit chiral binding sites that promote the preferred adsorption into either *R* or *S* configuration.

In the present case, the prochiral 9-EP molecule exhibits two distinct moieties, an aromatic ring system, and an ethynyl end group, which allows for different binding mechanisms to the substrate. Previous studies on ethyne (C₂H₂) adsorption on the Pd₁ surface revealed the preferred binding of this unsaturated hydrocarbon on-top of the outermost Pd atoms.²⁹ In the case of 9-EP on Pd₁, the expectation is that the ethynyl group acts as anchor point to the outermost Pd atoms, while the asymmetric aromatic ring system acts as a probe for the surface chirality. As a consequence, the different surface chirality of A:Pd₁ and B:Pd₁, should each lead to an excess of one of the two enantiomers, *R* or *S*, respectively. By employing high resolution low temperature scanning tunneling microscopy (STM), we demonstrate enantioselectivity by determining the handedness for a large number of single molecular adsorbates for different adsorption and sample annealing conditions.

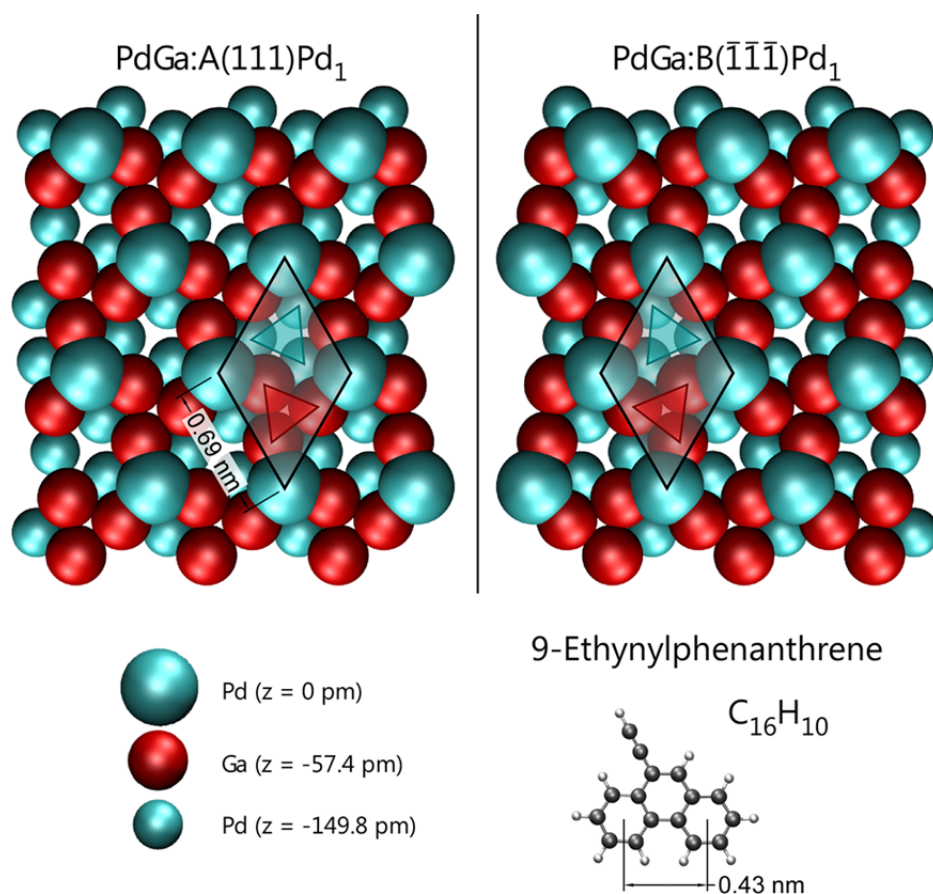


Figure 6.2 Surface structure of PdGa:A(111)Pd₁ and its enantiomorph B($\bar{1}\bar{1}\bar{1}$)Pd₁. The chiral arrangement within the hexagonal surface unit cell (black lozenge) is highlighted by the cyan and red triangle, representing the Pd and Ga trimers of the subsurface layers, respectively. Upon adsorption on a surface, the prochiral molecule 9-Ethynylphenanthrene forms a chiral adsorption complex.

Figure 6.3 shows high resolution STM images of 9-EP deposited at room temperature (RT) with sub-monolayer coverage, imaged at 5 K on A:Pd₁ and B:Pd₁ respectively. Single 9-EP molecules can easily be distinguished and appear in two predominant morphologies. The most relevant ones regarding enantioselectivity consist of three differently sized lobes in the STM topography (see Figure 6.3C). The handedness of these types can be inferred from the sense of rotation going from the largest to the smallest lobe¹³³, where the clockwise rotation from the large, over medium, to small protrusion is defined as *R*-, and the counter-clockwise sequence as *S*- enantiomer, as labelled in Figure 6.3A and B. For adsorption on A:Pd₁, shown in Figure 6.3A, the excess of the *R* enantiomer is evident (*R*:*S*=215:7), while *S* is predominant on B:Pd₁ (Figure 6.3B) (*R*:*S*=2:196). Due to the threefold symmetry of the substrate, each enantiomer appears with equal probability in three orientations which are rotated by 120° to each other. The 0°:120°:240° rotated orientations for the *R* and *S* enantiomers, are observed in quantities of 69:68:78, and 69:77:50, on the A:Pd₁ and B:Pd₁ surfaces, respectively. Alternatively, 60° rotated configurations with the centered phenanthrene ring atop a Ga trimer of the 2nd layer are observed. As the clockwise or anticlockwise rotations of these alternative adsorbates can still be identified, they are considered a sub group of the *R* and *S* enantiomers in this study (see supplementary information for more details). For deposition at RT, the statistical analysis of molecules in *R* and *S* configuration yields an enantiomeric excess *ee* ($ee = |R-S|/(R+S)$) of 0.94 and 0.98 on A:Pd₁ and B:Pd₁, respectively.

A third group of adsorbed 9-EP molecules is observed as brighter protrusions, which are molecules bound to surface vacancies (γ).²⁹ Very often three 9-EP molecules of undeterminable enantiomer type decorate the same vacancy and form a bright, triangular structure.

Figure 6.3C shows a zoom of two enantiomers. For the determination of the adsorption sites the surface atomic structure has been superimposed in Fig. 2D. Its in-plane position and orientation has been identified by using adsorbed CO molecules as markers for the top-most Pd atoms¹³⁴ and by determination of the crystallographic structure of the subsequent atomic planes using LEED-I(V) (low energy electron diffraction).¹³⁵ The combined information allows to unambiguously identify the topographic depression in the STM topography as the 3rd layer Pd trimer sites. For both enantiomers, the ethynyl-group is found atop the outermost Pd surface atoms, and the center phenanthrene ring atop a Pd trimer of the 3rd topmost atomic layer. Due to the surface chirality, the position of the two outer phenyl rings with respect to the underlying substrate atoms is slightly different for the *R* and *S* enantiomers, respectively. The resulting adsorption energy difference seems to be sufficient for driving the observed, very pronounced enantioselectivity.

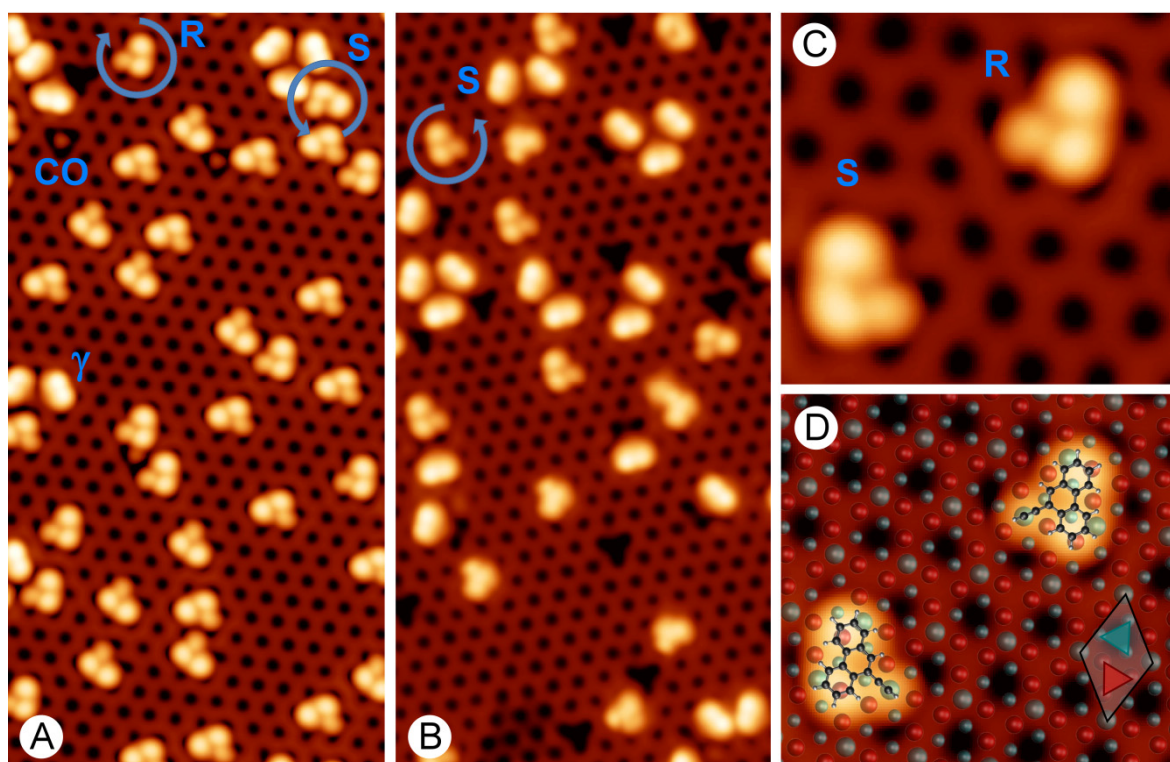


Figure 6.3 STM images (10x20 nm, 0.02 V, 2 nA, T = 5 K) of 9-EP adsorbed at room temperature on A) the PdGa:A(111)Pd₁ surface and B) the PdGa:B(-1-1-1)Pd₁ surface. The different adsorbates are identified as clockwise (R) and counterclockwise (S) adsorption conformation, vacancy pinned molecules (γ) and CO molecules. Some unoccupied vacancy defects (dark features) are visible in B. C) Zoom (3.8x3.5 nm) showing R and S enantiomers on A: Pd₁ D) The structure overlay allows to identify the adsorption position within the surface unit cell. (cf. Figure 6.2).

As the adsorption is carried out with the substrate at RT, but the determination of the enantiomeric excess is obtained from STM images measured at 5 K the question arises: At which temperature does the excess of the preferred enantiomer develop?

To elucidate this question temperature dependent adsorption and annealing experiments have been carried out. We deposited 9-EP on the A:Pd₁ sample at T=135 K to investigate if enantioselectivity is already achieved at the reduced available thermal energy of the substrate. The corresponding STM image in Figure 6.4A reveals the presence of a large variety of adsorption conformations, with a comparable amount of *R* and *S* enantiomers, meaning that no significant enantioselectivity is observed. Thus, the reaction mechanism is, at least partly, driven by the temperature of the substrate and the molecules shown in Figure 6.4A are frozen in a metastable adsorption state. Post-annealing of the sample prepared at low temperatures, to 300 K leads to an increase of the excess of *R* over *S* and after 80 minutes of post-annealing at RT an *ee* of 0.77 is observed. However, the very high enantioselectivity that is observed for room temperature deposition (Figure 6.3A and B) are not reproduced. Therefore even very long post-annealing is not as efficient as adsorption directly at the annealing temperature. This indicates that the adsorption process plays a role in overcoming the barrier for transformation to the energetically favored enantiomer of the adsorbate complex on the respective surface.

Higher annealing temperatures were tested to check whether enantioselectivity is maintained or whether new molecular species are formed on this catalytically active surface. To this end, we performed stepwise sequential post-annealing of the sample that showed high enantioselectivity after room temperature deposition (Figure 6.4B). Figure 6.4C shows the sample after 10 min post-annealing to 370 K, resulting in a slightly reduced enantioselectivity (*ee* = 0.83) as compared to sample after RT deposition. After further annealing to 490 K (Figure 6.4D), a large amount of the adsorbed molecules show a changed STM appearance, possibly due to dehydrogenation, which does not allow for unambiguous identification of the handedness. Furthermore, the formation of molecular dimers is observed, built from *R* and *S* enantiomers in racemic ratios, with the molecules connected through their ethynyl groups. For T > 490 K, almost all adsorbates have formed dimers and larger carbohydrate agglomerates, while the overall amount of adsorbed carbon is maintained (see supplementary information). In all experiments no significant decoration of step edges or kink sites was observed. STM experiments at room temperature (see supplementary information) revealed that only the molecules bound to surface vacancies (γ) are not diffusing, while other adsorbates are mobile and thus cannot be individually resolved by STM.

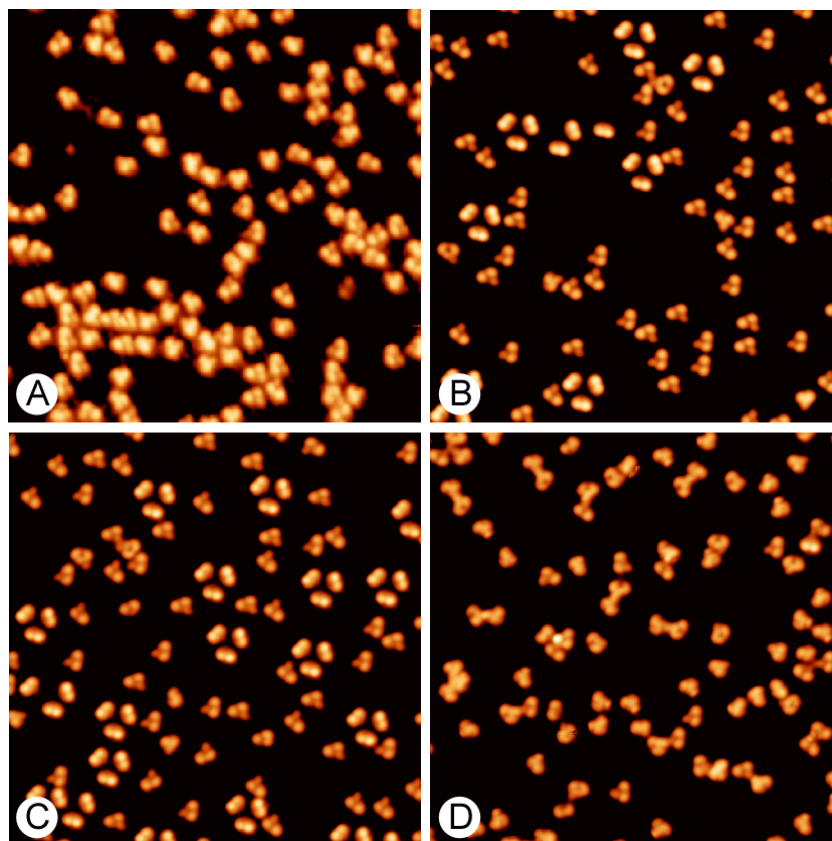


Figure 6.4 STM images ($T=5$ K, 20×20 nm, 0.2 V, 2 nA) of 9-EP after A) deposition at 135 K; and B) at 300 K. C) and D) show the same sample as in B after post-annealing for 10 minutes to 370 K and 490 K, respectively.

To quantify the enantioselectivity of the Pd_1 surface towards the adsorption of 9-EP, we evaluated and assigned a large number of adsorbates ($N \approx 400$) for each of the experiments performed at different adsorption and annealing temperatures. In every case all the absorbed molecules have been classified in the categories; R , S , γ , and *dimers*. 9-EP molecules whose adsorbate configuration cannot be unambiguously determined from their topographic appearance in STM, are classified as *unidentified*. The result is shown as vertical colored bars in Figure 6.5, representing the normalized fraction of adsorbate configurations R , S , γ and molecules that have formed dimers. Atop the bars, the amount of unidentifiable adsorbates is given for each experiment. Based on the temperature dependent quantities, a tentative phase diagram was constructed for the 9-EP species on $\text{A}:\text{Pd}_1$ (see background in Figure 6.5). The graph shows the transition from the racemic mixture of R and S enantiomers at low temperatures, over a region yielding high enantioselectivity situated around 300 - 350 K, to the formation of dimers for $T \gtrsim 450$ K. The appearance of γ type molecules, *i.e.* molecules pinned at vacancies, at higher substrate temperature is linked to the increase in mobility. ee is shown for each experiment as black marker with estimated errors for temperature and statistically computed errors for ee .

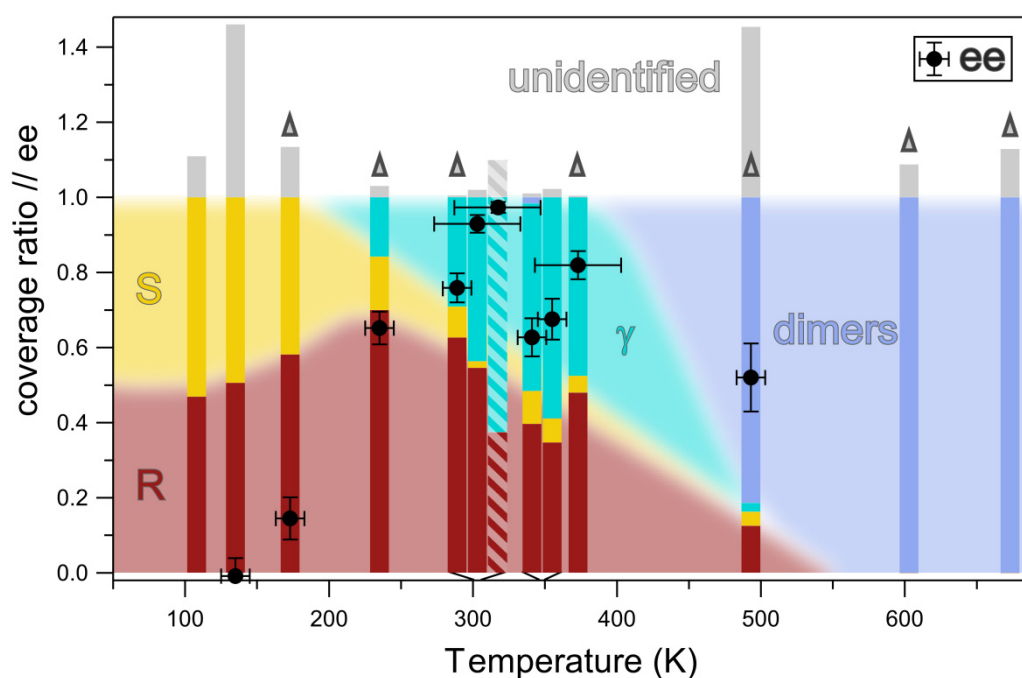


Figure 6.5 Phase diagram based on statistical evaluation of 9-EP molecules on Pd₁. Normalized abundances for the R and S enantiomers, as well as molecules pinned to surface vacancies (γ), and dimers. Annealed samples are marked by gray triangles. A phase-diagram, based on the data of the different adsorbate configuration ratios, is presented as background. All bars represent the A: Pd₁ surface apart from the striped one representing B: Pd₁ (colors for R and S are inverted for clarity). The enantiomeric excess (ee) is given for each experiment as black circles. Error propagation of the counting errors in the number of R and S enantiomers was used to compute the error for ee .

The data reveals that a temperature window of about ± 100 K around room temperature yields $ee > 0.6$. For room temperature deposition, we find a high ee of 0.98 ± 0.01 for B: Pd₁, while for the same experiment on the form A sample $ee = 0.94 \pm 0.02$ is observed. The remarkably strong enantioselective adsorption is in contrast to deposition of the same molecule on the achiral Cu(111) surface, where Bebensee et al. found equivalent quantities of R and S (Ref. ¹³³ and supplementary information therein).

Deposition of the molecules on the cold A: Pd₁ surface (135 K) and subsequent annealing to room temperature for 80 minutes results in $ee \approx 0.77 \pm 0.04$ (left bar for 300 K in Figure 6.5). Interestingly, the temperature onset, where enantioselectivity is observed, coincides with the occupation of surface vacancies (γ), indicating that the mobility of molecules might play a role in the enantioselective transformation from S to R. The reduction of ee for annealing temperatures above 400 K can be explained by the entropic disorder of the equilibrium occupation of a two level system with small energy difference (R and S). The fact that this reduction is still observed after cooling to 5 K with an estimated temperature ramp of about 1-5 K/s, shows that the molecules were “frozen” in their position during cool-down, which indicates a low frequency for the R to S transformation mechanism. The values for ee presented here are based on the evaluation of the observed amount of R and S enantiomers. However, one has to keep in mind the presence of the γ adsorbates, whose enantiomer form cannot be identified. A surface preparation free from vacancies might allow a more complete conversion of adsorbed 9-EP to the preferred enantiomer.

In conclusion, we have demonstrated remarkably high enantioselective adsorption of a prochiral molecule on the bare, chiral surface of an intermetallic compound at room temperature. The adsorption of 9-Etynylphenanthrene on the A(111) surface and its mirror symmetric equivalent the B(-1-1-1) surface of

PdGa has shown enantiomeric excess of 0.94 and 0.98 for the *R* and the *S* enantiomorphs, respectively. By studying the temperature dependence of the process we showed that the racemic molecule mixture, formed by adsorption of the 9-EP at temperatures below 120 K, is efficiently transformed to an almost enantiopure ensemble at room temperature.

This observation shows that the bulk chirality of PdGa can be expressed sufficiently strong at its surfaces to yield highly enantioselective processes. In combination with the catalytic properties of intermetallic compounds in general and PdGa in particular, this opens the perspective of chiral heterogeneous catalysis under operation conditions beyond the ones allowed by catalyst surfaces based on functionalization with organic, chiral modifiers.

Methods

All experiments were performed in an ultra-high vacuum chamber with a base pressure below $5 \cdot 10^{-11}$ mbar. Sample preparation was performed by sputter and annealing cycles (sputtering: Ar^+ , 1 keV; annealing: 20 min at 870 K). An Omicron low-temperature STM was used for the measurements at 5 K. 9-EP (97 %) was purchased from Sigma Aldrich and used without further purification. Deposition was performed in UHV by exposing the clean sample surface for a few seconds (2-10 s) to a crucible held at 300 K and containing a small amount of molecules. To prevent vacuum contamination, the crucible was located in a separately pumped chamber behind a gate valve, which was opened during deposition only.

Acknowledgements

We gratefully acknowledge discussions with Karl-Heinz Ernst and funding by the Swiss National Science Foundation under Contract 200021-129511.

6.1.1 Supplementary information for the publication "Adsorption of Small Hydrocarbons on the threefold PdGa surfaces: The Road to Selective Hydrogenation"

1. 60° rotated adsorbate types R^* and S^* :

The adsorbate types marked with an asterisk adsorb with the centered phenanthrene ring atop the Ga trimer of the 2nd outermost layer, instead of the common alignment of the center phenanthrene ring atop of the Pd trimer in the 3rd outermost layer. The binding configuration is depicted in Figure 6.6.

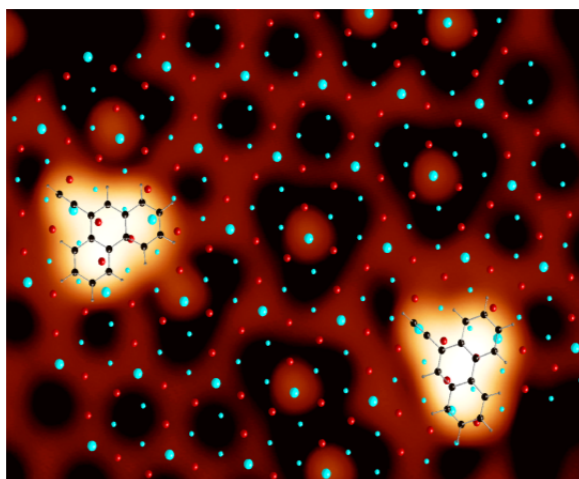


Figure 6.6 STM topography in overlay with the DFT optimized structure of a R^* and S^* adsorbate (left and right, respectively) on A:Pd_1 after adsorption at 108 K. CO molecules appear as smaller protrusions, surrounded by a dark triangle.

2. Room temperature STM images of adsorbed 9-EP molecules :

After room temperature deposition of the molecules on Pd_1 the surface was imaged in a VT-STM (Omicron) at room temperature, as shown in the left panel of Figure 6.7. Only threefold γ species, and a few dimers are seen in the STM image. After subsequent cooling of the same sample to 77 K, a higher coverage is observed. Accordingly, the fast molecular diffusion at room temperature could not be resolved by STM, and the only species visible in STM are the molecules that are pinned to the vacancies.

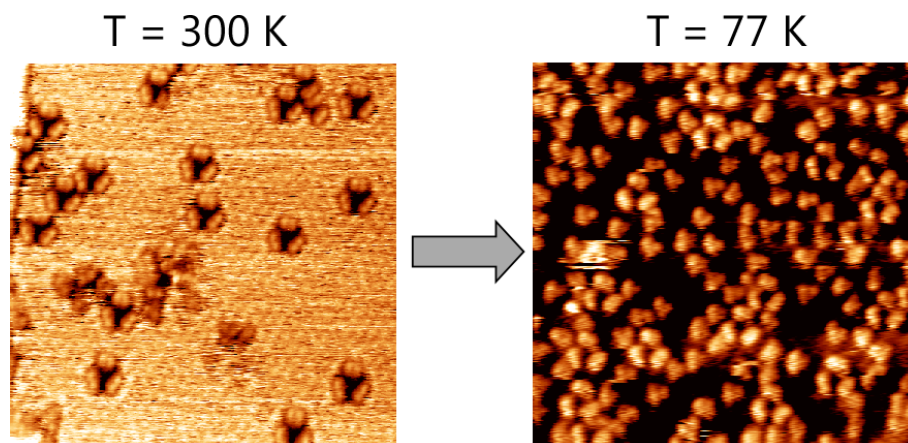


Figure 6.7 STM images of 9-EP on Pd_1 at room temperature, and after cooling to 77K (left: 0.5 V, 2 nA; right: -0.8 V, 0.05 nA).

3. Statistics on enantiomer abundances upon annealing:

Deposition of 9-EP at room temperature on A:Pd₁, leads to a high enantioselectivity, as presented in the main text. In this supplementary paragraph, we demonstrate the abundances of the different adsorbate species after subsequent annealing of this sample preparation to four higher temperatures. As enantioselectivity is not the focus here, the *R* and *S* enantiomers are summarized in the same group of adsorbates, which is shown in the most left of the 6 sections in Figure 6.8. When going from 300 K to 670 K, the number of identified *R+S* enantiomers per surface area decreases, reaching zero at 570 K. The total number of the vacancy pinned molecules (γ) shows the same behavior. While the number of these molecules is strongly reduced at 470 K, the amount of unidentified adsorbates and dimers increase at this temperature. The number of unidentified molecules decreases again at 570 K, which indicates that the unidentified species of single 9-EP molecules seem to be a pre-state to the formation of dimers. The dimers contain two 9-EP molecules in a racemic ratio.

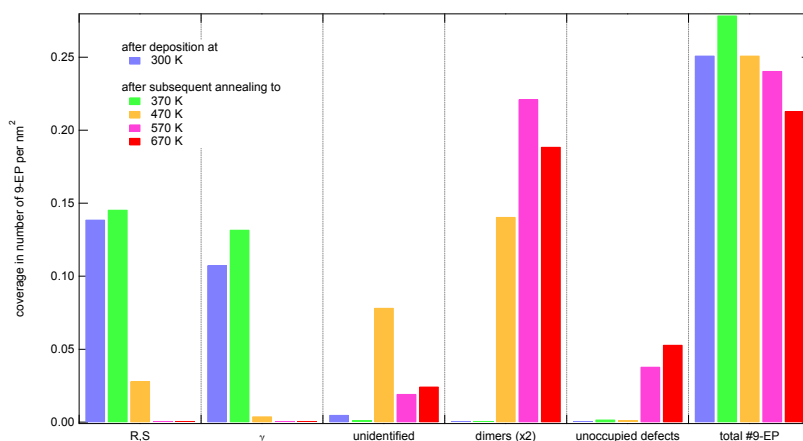


Figure 6.8 Evolution of the different 9-EP species upon annealing of the same sample.

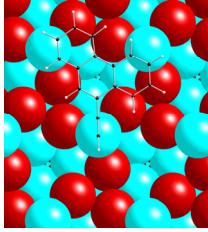
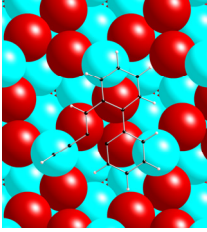
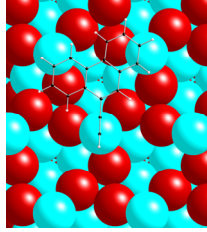
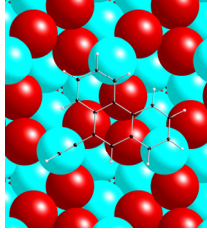
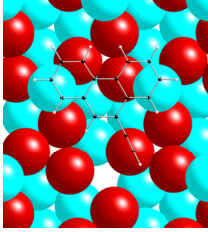
Upon annealing to 570 K, the surface vacancy defects appear in the STM images. These defects are occupied by molecules for lower temperatures, and therefore not directly detectable by STM. The number of unoccupied defects is shown in Figure 6.8. in the 2nd section from the right, revealing that the defects are still occupied at 470 K, while the number of γ adsorbates is almost zero. Therefore, the defects must be covered by either the dimers, or the unidentified adsorbates. Annealing to 570 K, leads to an increase in the number of dimers and the unoccupied defects. While the abundances of the different species change with annealing temperature, the total amount of adsorbates remains comparably stable. This indicates conversion between the species, and the absence of thermal desorption of molecules.

Together with the findings presented in the main text, the redistribution of the molecules into different adsorbate species suggests the following, hypothetical reaction pathway for the formation of the dimers: After adsorption at 300 K, thermal diffusion and the dissipation of the landing energy leads to occupation of the most stable adsorption sites, and thus to the γ type adsorbates. Upon annealing to 470 K, the γ type adsorbates are altered (possibly dehydrogenated) at the vacancy defects, and thus appearing unidentifiable. In the same annealing step, two of the mostly threefold occupied vacancies connect to form a dimer and diffuse away from the vacancy defect, while the third unidentifiable molecule remains at the vacancy

defect, but is lacking a partner to form a dimer. Further annealing to 570 K enables diffusion of molecules (*R*, *S* and maybe even the unidentifiable ones at the vacancies), such that almost all molecules are bound in dimers, leaving from the defects. Annealing to 670 K leads to small carbon agglomerates of several dimers which cannot be distinguished in the STM images and thus fall into the category of unidentified adsorbates.

4. DFT adsorption energies and configurations

DFT computed adsorption energies of 9-Ethynylphenanthrene on Pd₁ for different binding conformations and Pd-C bond distances for the three Pd atoms of the outermost layer involved in the bonding.

	<i>R</i>	<i>R</i> *	<i>S</i>	<i>S</i> *	<i>γ</i>
E_B in eV	-2.5181 	-2.3781 	-2.5028 	-2.3712 	-2.177/-2.173 
Pd-C_{1st/2nd} in Å	2.216/2.435 2.677/2.635 2.577/2.561	2.217/2.515 2.580/2.716 2.596/2.720	2.219/2.464 2.606/2.529 2.536/2.667	2.208/2.469 2.589/2.682 2.720/2.860	2.237/2.926(Ga-C) 2.498/2.506 2.437/2.505
Avg Pd-C	2.326 2.656 2.569	2.366 2.648 2.658	2.342 2.568 2.602	2.339 2.636 2.790	2.582 2.502 2.471

6.2 Adsorption of 9-Ethynylphenanthrene on the threefold Pd₃ termination

To investigate the surface chirality of the Pd₃ surface we followed the approach applied to Pd₁ and investigated the adsorption of prochiral 9-EP molecules by LT-STM. In contrast to Pd₁, the surface offers threefold Pd hollow sites on the outermost atomic layer. This potentially leads to a stronger bond of the alkyne-group ($\text{-C}\equiv\text{C-H}$) of the molecule to the substrate, similar to the stronger bond of C₂H₂ on Pd₃ compared to Pd₁ (Chapter 5.1).

The experiment was performed as follow; the molecules were deposited with the sample at room temperature which was then cooled-down to 5 K for the LT-STM measurements. Subsequently, annealing was performed in 3 steps at different temperatures, with intermediate STM measurements at 5 K.

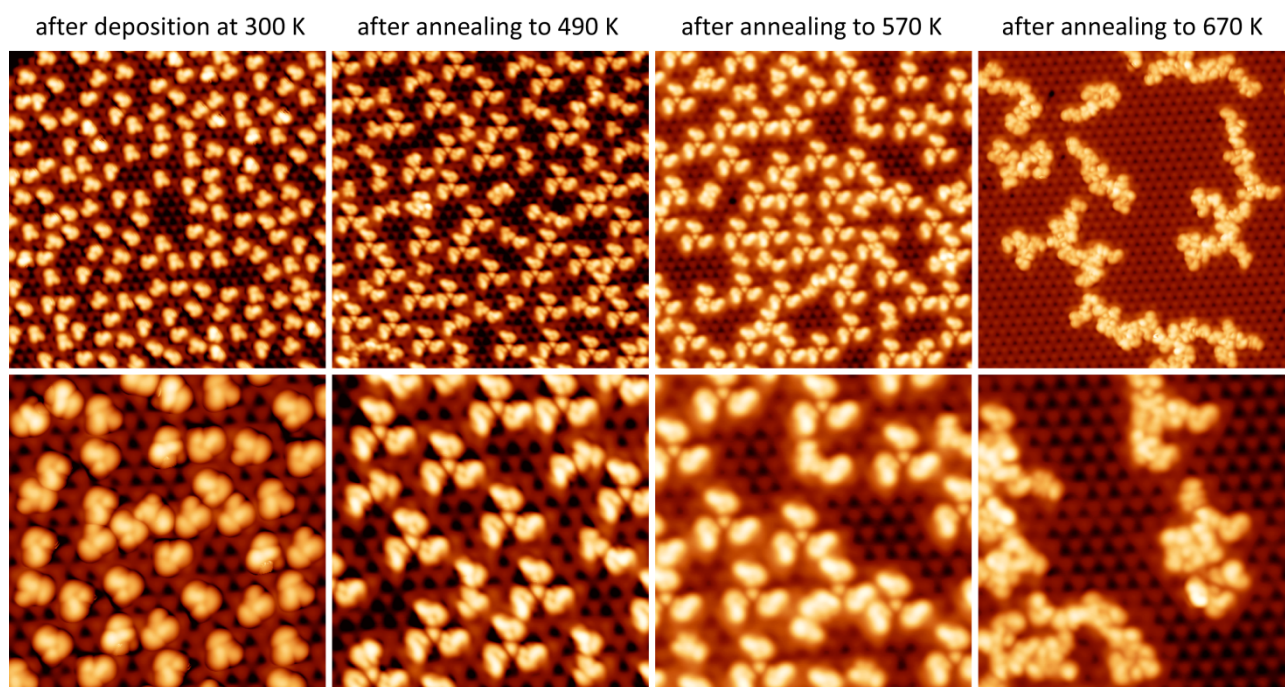


Figure 6.9 Adsorption of prochiral 9-EP on PdGa:A(-1-1-1)Pd₃. The LT-STM images ($T = 5\text{ K}$, Top: $20\times 20\text{ nm}$, bottom: $10\times 10\text{ nm}$) were taken after deposition at room temperature (left) and subsequent annealing for 80 minutes to the different temperatures (from left to right). (The gap voltage is 20 mV for all images. The tunnel current was adapted for each image depending on imaging and tip stability between 1 and 10 nA).

In the STM images on the left hand side of Figure 6.9, taken after deposition at 300 K, most molecules appear as three-lobed shapes, similar to adsorption on Pd₁. Also here, two different enantiomer forms of the adsorbate complex can be identified by their sense of rotation (which will be defined in the next paragraph), and each of them appears in three different rotational orientations due to the symmetry of the substrate. However, in the case of Pd₃, no enantioselectivity is observed after adsorption at room temperature. Furthermore, we find a repulsion of the molecules, as directly neighboring adsorbates are almost never observed. This situation is different after annealing to 490 K, which leads to an ordering of the molecules into trimer groups, with almost all of the molecules flipped into one of the two possible enantiomers. Consequently, also for adsorption the Pd₃ surface we observe a high enantiomeric excess, even though in a different way than on the Pd₁ termination. The molecular trimers remain stable up to annealing to 570 K, while higher annealing to 670 K leads to larger hydrocarbon agglomerates on the surface. Even though

some topographic features are frequently seen after the 670 K annealing step, the general disordered appearance of the adsorbates does not allow for identification of enantiomers.

The STM topography of isolated molecules on Pd₃ before annealing is shown in overlay with the undistorted molecular structure and the substrate atomic structure in the top panels of Figure 6.10. *R* and *S* enantiomers are named according to clockwise-, and anti-clockwise-rotation when going from the largest to the smallest appearing part of the molecule. In contrast to 9-EP adsorption on Pd₁, adsorption on Pd₃ seems to lead to a distortion of the molecules. This is concluded from the comparison of the STM appearance and the ball model of the unperturbed molecule, which does not match well. In particular for the *R* enantiomer the alkyne-group of the molecule appears much shorter in the STM image. However, this interpretation has to be taken with care, as the local electronic density, probed by STM, might differ from the molecular structure. For both enantiomers forms, the preferred adsorption site involves binding to atoms of 2 to 3 neighboring unit cells. A dominant binding center, like the isolated Pd atom on Pd₁, cannot be identified after room temperature adsorption of 9-EP on Pd₃.

The molecular trimer groups, formed after annealing to 490 K, contain three *R* type enantiomers, which is concluded from comparison of the STM appearance to the isolated molecules (cf. top and bottom panels in Figure 6.10). The groups show a peculiar protrusion in the symmetric center. A possible explanation is that the outermost H atoms of the acetylene group are elevated from the surface after the three carbon atoms bind to the Pd atoms of the substrate. This hypothesis is to be evaluated in future experiments. Nevertheless, we again find the outermost Pd atoms as the active centers on the PdGa surface, which is in agreement with the adsorption of carbon monoxide and hydrocarbons presented in Chapter 4 and Chapter 5 of this thesis, respectively.

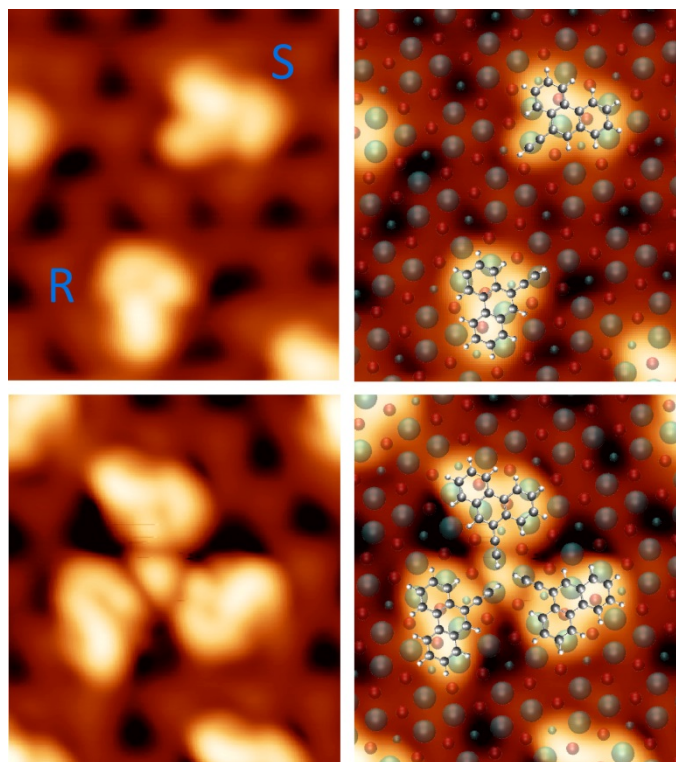


Figure 6.10 Identification of the adsorption site for 9-EP on Pd₃ by STM. Sections of STM images after adsorption at 300 K (top) and after annealing to 490 K (bottom). On the right hand side, the STM images are shown in overlay with the atomic surface structure of the Pd₃ termination and the unperturbed 9-EP molecule (not DFT optimized). *R* and *S* enantiomers are identified according to the clockwise or anti-clockwise appearance of the largest to smallest lobe, similar to the adsorption study on Pd₁ presented in the previous chapter.

In summary, we have demonstrated highly enantioselective adsorption on the threefold Pd₁ and Pd₃ surfaces of the chiral intermetallic compound PdGa. Due to structural differences in the outermost layers of the surface terminations, the enantioselectivity develops at higher temperatures for Pd₃, as compared to the Pd₁ surface. The findings validate that chiral intermetallic compounds are indeed promising materials for chiral synthesis by heterogeneous catalysis. Even though a chiral reaction was not demonstrated, the highly selective adsorption process is the first step towards enantioselective reactions on intrinsically chiral intermetallic compounds.

Chapter 7 Conclusions and Outlook

This thesis reports on a surface science study on low-Miller index surfaces of the intermetallic compound PdGa. The main motivation was to develop a deeper understanding of how the surface atomic structure affects the adsorption of small molecules on intermetallic compounds, and thereby to contribute to the knowledge-based design of new heterogeneous catalysts. The choice of PdGa as a model catalyst was based on two particular features of its bulk crystal structure, namely Pd site-isolation and chirality. While the isolation of active Pd sites is the potential reason for the outstanding performance of PdGa as a stable and selective semi-hydrogenation catalyst for acetylene,^{21, 23} the combination with its surface chirality might offer the possibility to design highly enantioselective catalysts.

The surface terminations of five single crystal PdGa surfaces were determined, namely PdGa(111), (-1-1-1), (100), (110) and (210). The obtained information of the different PdGa surface structures opens the door for *ab-initio* simulations on adsorption and reactions on these PdGa surfaces. Our results of the structural determination and CO adsorption reveal that the Pd site-isolation of the bulk crystal structure is indeed maintained at the surfaces, but it is expressed to varying degrees, ranging from isolated single Pd atoms in the topmost surface layer (PdGa:A(111)Pd₁), to rugged chains of Pd atoms (PdGa:A(210)Pd_α). Probing of the site-isolation by CO adsorption revealed that intermolecular interactions are completely suppressed for (111)Pd₁ and (100)Pd_α, while they are strongly reduced for (111)Pd₃, but present on (110)Ga_α. The Pd₁ termination of the (111) surface exhibits the largest isolation of Pd sites with a distance of 0.7 nm between the outermost Pd atoms. This is more than double compared to the Pd-Pd distance in bulk PdGa. These separated single atoms are the favored adsorption sites for CO, C₂H₂ and C₂H₄ on this surface.

The peculiar arrangement of the threefold Pd₁ and Pd₃ terminations, featuring single Pd atoms and Pd trimer groups, respectively, showed a striking difference in the adsorption of acetylene. While the single Pd atoms lead to π -bonded acetylene, adsorption on the Pd trimers resulted in a strong π /di- σ bond of the molecule to the surface. On the other hand, the adsorption configurations of H₂ and C₂H₄ are similar on the two surfaces. Both molecules are weakly bound, and located on-top a Pd atom of the outermost atomic layer with the main molecular axes (C-C and H-H, respectively) parallel to the surface plane. For the Pd₃ termination, these are promising conditions to achieve high selectivity, as the reactant is strongly bound in comparison to the product, which is weakly bound to the surface. Catalytic experiments, comparing selectivity and activity of the PdGa- to Pd single crystal surfaces, could give direct insights into the performance of the site-isolated intermetallic surfaces for various heterogeneous reactions. In such experiments the structural ensemble effect and the ligand effect, caused by the alloying with Ga, may influence the reaction. In the comparison of the PdGa surfaces among each other, this ensemble effect should be largely decoupled from the ligand effect of Ga, as the electronic structures are approximately the same for the two terminations. The catalytic experiments on single crystal surfaces could be achieved by employing a small volume reactor, attached to the UHV chamber, which allows for reproducible preparation of surfaces.

The (100), (110) and (210) surface, showing atomic chains on their surface, have not been investigated with respect to hydrocarbon adsorption. The comparably small isolation of the Pd sites on these surface along the $\langle 001 \rangle$ direction might enable the guided formation of linear polymers or “molecular wires” from small hydrocarbons, upon annealing on the catalytic PdGa surfaces.

The intrinsic bulk chirality of the PdGa crystal structure is maintained in the outermost atomic layers for all low-Miller index surfaces, *i.e.* none of the surfaces exhibits a mirror plane. The surface chirality of the threefold PdGa surfaces leads to highly enantioselective adsorption of prochiral molecules. For room temperature deposition of 9-Ethynylphenanthrene, an enantiomeric excess of up to 0.98 was observed. This effect is temperature-, and surface structure-dependent. The challenge of future experiments will be to transform the enantioselective adsorption into a chiral surface reaction and to synthesize chiral molecules.

In summary, PdGa exhibits isolated and chiral Pd sites on its low-Miller index surface terminations. This leads to the separation of adsorbed molecules on the surfaces and to enantioselective adsorption. The atomic structure and coordination of the Pd sites have a strong influence on molecular adsorption strength and configuration. The results provide original insights of molecular binding to intermetallic surfaces and might contribute to a rational design of selective catalysts based on well-defined intermetallic compounds.

References

1. Piringer, O. G.; Baner, A. L., *Plastic Packaging: Interactions with Food and Pharmaceuticals*. Wiley: **2008**.
2. Molnar, A.; Sarkany, A.; Varga, M., *Hydrogenation of carbon-carbon multiple bonds: chemo-, regio- and stereo-selectivity*, J. Mol. Catal. A: Chem. **2001**, 173 (1-2), 185-221, and references therein.
3. Borodzinski, A.; Bond, G. C., *Selective Hydrogenation of Ethyne in Ethene-rich Streams on Palladium Catalysts, Part 2: Steady-state Kinetics and Effects of Palladium Particle Size, Carbon Monoxide, and Promoters*, Catal. Rev.: Sci. Eng. **2008**, 50 (3), 379-469.
4. Borodziński, A.; Bond, G. C., *Selective Hydrogenation of Ethyne in Ethene-Rich Streams on Palladium Catalysts. Part 1. Effect of Changes to the Catalyst During Reaction*, Catal. Rev.: Sci. Eng. **2006**, 48 (2), 91-144.
5. Ertl, G.; Freund, H. J., *Catalysis and Surface Science*, Phys. Today **1999**, 52 (1), 32-38.
6. Bocklein, S.; Gunther, S.; Wintterlin, J., *High-Pressure Scanning Tunneling Microscopy of a Silver Surface during Catalytic Formation of Ethylene Oxide*, Angew. Chem., Int. Ed. **2013**, 52 (21), 5518-5521.
7. Herbschleb, C. T.; Bobaru, S. C.; Frenken, J. W. M., *High-pressure STM study of NO reduction by CO on Pt(100)*, Catal. Today **2010**, 154 (1-2), 61-67.
8. Somorjai, G. A., *Surface Science and Catalysis*, Science **1985**, 227 (4689), 902-908.
9. Miller, D. J.; Oberg, H.; Kaya, S.; Casalongue, H. S.; Friebel, D.; Anniyev, T.; Ogasawara, H.; Bluhm, H.; Pettersson, L. G. M.; Nilsson, A., *Oxidation of Pt(111) under Near-Ambient Conditions*, Phys. Rev. Lett. **2011**, 107 (19).
10. Conrad, H.; Ertl, G.; Koch, J.; Latta, E. E., *Adsorption of Co on Pd Single-Crystal Surfaces*, Surf. Sci. **1974**, 43 (2), 462-480.
11. Schwegmann, S.; Over, H.; DeRenzi, V.; Ertl, G., *The atomic geometry of the O and CO+O phases on Rh(111)*, Surf. Sci. **1997**, 375 (1), 91-106.
12. Wintterlin, J.; Volkening, S.; Janssens, T. V. W.; Zambelli, T.; Ertl, G., *Atomic and macroscopic reaction rates of a surface-catalyzed reaction*, Science **1997**, 278 (5345), 1931-1934.
13. Baddeley, C. J.; Lee, A. F.; Lambert, R. M.; Giessel, T.; Schaff, O.; Fernandez, V.; Schindler, K. M.; Theobald, A.; Hirschmugl, C. J.; Lindsay, R.; Bradshaw, A. M.; Woodruff, D. P., *Photoelectron diffraction study of a catalytically active overlayer: C₂H₂ on Pd{111}*, Surf. Sci. **1998**, 400 (1-3), 166-175.
14. Lee, A. F.; Wilson, K.; Middleton, R. L.; Baraldi, A.; Goldoni, A.; Paolucci, G.; Lambert, R. M., *In situ observation of a surface chemical reaction by fast X-ray photoelectron spectroscopy*, J. Am. Chem. Soc. **1999**, 121 (34), 7969-7970.
15. Tysoe, W. T.; Nyberg, G. L.; Lambert, R. M., *Photoelectron-Spectroscopy and Heterogeneous Catalysis - Benzene and Ethylene from Acetylene on Palladium (111)*, Surf. Sci. **1983**, 135 (1-3), 128-146.
16. Tysoe, W. T.; Nyberg, G. L.; Lambert, R. M., *Selective Hydrogenation of Acetylene over Palladium in Ultra High-Vacuum*, J. Phys. Chem. **1986**, 90 (14), 3188-3192.
17. Bond, G. C.; Dowden, D. A.; Mackenzie, N., *The Selective Hydrogenation of Acetylene*, Trans. Faraday Soc. **1958**, 54 (10), 1537-1546.
18. Zafeirotos, S.; Piccinin, S.; Teschner, D., *Alloys in catalysis: phase separation and surface segregation phenomena in response to the reactive environment*, Catal.: Sci. Technol. **2012**, 2 (9), 1787-1801.
19. Armbrüster, M., *Intermetallic Compounds in Catalysis*. In *Encyclopedia of Catalysis*, John Wiley & Sons, Inc.: **2011**.
20. Armbrüster, M.; Borrmann, H.; Wedel, M.; Prots, Y.; Giedigkeit, R.; Gille, P., *Refinement of the Crystal Structure of Palladium Gallium (1:1), PdGa*, Z. Kristallogr. - New Cryst. Struct. **2010**, 225 (4), 617-618.
21. Armbrüster, M.; Kovnir, K.; Behrens, M.; Teschner, D.; Grin, Y.; Schlögl, R., *Pd-Ga Intermetallic Compounds as Highly Selective Semihydrogenation Catalysts*, J. Am. Chem. Soc. **2010**, 132 (42), 14745-14747.
22. Kovnir, K.; Armbrüster, M.; Teschner, D.; Venkov, T. V.; Jentoft, F. C.; Knop-Gericke, A.; Grin, Y.; Schlögl, R., *A new approach to well-defined, stable and site-isolated catalysts*, Sci. Technol. Adv. Mater. **2007**, 8 (5), 420-427.
23. Kovnir, K.; Armbrüster, M.; Teschner, D.; Venkov, T. V.; Szentmiklosi, L.; Jentoft, F. C.; Knop-Gericke, A.; Grin, Y.; Schlögl, R., *In Situ Surface Characterization of the Intermetallic Compound PdGa - A Highly Selective Hydrogenation Catalyst*, Surf. Sci. **2009**, 603 (10-12), 1784-1792.

24. Osswald, J.; Giedigkeit, R.; Jentoft, R. E.; Armbrüster, M.; Girgsdies, F.; Kovnir, K.; Ressler, T.; Grin, Y.; Schlögl, R., *Palladium-gallium intermetallic compounds for the selective hydrogenation of acetylene - Part I: Preparation and structural investigation under reaction conditions*, J. Catal. **2008**, 258 (1), 210-218.
25. Osswald, J.; Kovnir, K.; Armbrüster, M.; Giedigkeit, R.; Jentoft, R. E.; Wild, U.; Grin, Y.; Schlögl, R., *Palladium-Gallium Intermetallic Compounds for the Selective Hydrogenation of Acetylene - Part II: Surface Characterization and Catalytic Performance*, J. Catal. **2008**, 258 (1), 219-227.
26. Klanjšek, M.; Gradisek, A.; Kocjan, A.; Bobnar, M.; Jeglic, P.; Wencka, M.; Jaglicic, Z.; Popcevic, P.; Ivkov, J.; Smontara, A.; Gille, P.; Armbrüster, M.; Grin, Y.; Dolinsek, J., *PdGa intermetallic hydrogenation catalyst: an NMR and physical property study*, J. Phys.: Condens. Matter **2012**, 24 (8).
27. Wulff, G., *Zur Frage der Geschwindigkeit des Wachstums und der Auflösung der Krystallflächen*, Z. Kristallogr. Min. **1901**, 34, 449-530.
28. Rosenthal, D.; Widmer, R.; Wagner, R.; Gille, P.; Armbrüster, M.; Grin, Y.; Schlögl, R.; Gröning, O., *Surface Investigation of Intermetallic PdGa(-1-1-1)*, Langmuir **2012**.
29. Prinz, J.; Pignedoli, C. A.; Stoeckl, Q. S.; Armbrüster, M.; Brune, H.; Gröning, O.; Widmer, R.; Passerone, D., *Adsorption of Small Hydrocarbons on the threefold PdGa surfaces: The Road to Selective Hydrogenation*, J. Am. Chem. Soc. (in print, DOI: 10.1021/ja505936b) **2014**.
30. Gille, P.; Ziemer, T.; Schmidt, M.; Kovnir, K.; Burkhardt, U.; Armbrüster, M., *Growth of Large PdGa Single Crystals from the Melt*, Intermetallics **2010**, 18 (8), 1663-1668.
31. Davisson, C.; Germer, L. H., *Diffraction of Electrons by a Crystal of Nickel*, Phys. Rev. **1927**, 30 (6), 705-740.
32. Van Hove, M. A.; Weinberg, W. H.; C.-M., C., *Low-Energy Electron Diffraction*. Springer Verlag: 1986.
33. Tong, S. Y., *Theory of Low-energy Electron Diffraction*. Pergamon Press: **1975**.
34. Image on elemental scattering process adapted from:
http://eaps4.iap.tuwien.ac.at/~WERNER/qes_tut_elscat.html
35. Barbieri, A.; Van Hove, M. A. *private communication*
36. Somorjai, G. A., *Chemistry in Two Dimensions: Surfaces*. Cornell University Press: **1981**.
37. Rous, P. J.; Pendry, J. B.; Saldin, D. K.; Heinz, K.; Muller, K.; Bickel, N., *Tensor Leed - a Technique for High-Speed Surface-Structure Determination*, Phys. Rev. Lett. **1986**, 57 (23), 2951-2954.
38. Rous, P. J., *The Tensor Leed Approximation and Surface Crystallography by Low-Energy Electron-Diffraction*, Prog. Surf. Sci. **1992**, 39 (1), 3-63.
39. Pendry, J. B., *Reliability Factors for Leed Calculations*, J. Phys. C: Solid State Phys. **1980**, 13 (5), 937-944.
40. Van Hove, M. A., *Atomic-scale structure: From surfaces to nanomaterials*, Surf. Sci. **2009**, 603 (10-12), 1301-1305.
41. Pussi, K.; Diehl, R. D., *Low-Energy Electron Diffraction*. In *Characterization of Materials*, John Wiley & Sons, Inc.: **2012**.
42. Pentcheva, R.; Moritz, W.; Rundgren, J.; Frank, S.; Schrupp, D.; Scheffler, M., *A combined DFT/LEED-approach for complex oxide surface structure determination: Fe3O4(001)*, Surf. Sci. **2008**, 602 (7), 1299-1305.
43. Vogt, J.; Weiss, H., *LEED and PIRS structure analysis of physisorbed molecules on insulators: Monolayer C2D2/KCl(100)*, Phys. Rev. B: Condens. Matter Mater. Phys. **2008**, 77 (12), -.
44. Wiesendanger, R., *Scanning Probe Microscopy and Spectroscopy: Methods and Applications*. Cambridge University Press: **1994**.
45. Binnig, G.; Rohrer, H., *Scanning Tunneling Microscopy*, Surf. Sci. **1983**, 126 (1-3), 236-244.
46. Binnig, G.; Rohrer, H.; Gerber, C.; Weibel, E., *7x7 Reconstruction on Si(111) Resolved in Real Space*, Phys. rev. Lett. **1983**, 50 (2), 120-123.
47. Gross, L., *Recent advances in submolecular resolution with scanning probe microscopy*, Nat. Chem. **2011**, 3 (4), 273-278.
48. Repp, J.; Meyer, G.; Stojkovic, S. M.; Gourdon, A.; Joachim, C., *Molecules on insulating films: Scanning-tunneling microscopy imaging of individual molecular orbitals*, Phys. Rev. Lett. **2005**, 94 (2).
49. Simmons, J. G., *Electric Tunnel Effect between Dissimilar Electrodes Separated by a Thin Insulating Film*, J. Appl. Phys. **1963**, 34 (9), 2581-&.
50. Bardeen, J., *Tunnelling from a Many-Particle Point of View*, Phys. Rev. Lett. **1961**, 6 (2), 57-&.
51. Chen, C. J., *Theory of Scanning Tunneling Spectroscopy*, J. Vac. Sci. Technol., A **1988**, 6 (2), 319-322.
52. Tersoff, J.; Hamann, D. R., *Theory of the Scanning Tunneling Microscope*, Phys. Rev. B: Condens. Matter Mater. Phys. **1985**, 31 (2), 805-813.
53. Blyholder, G., *Molecular Orbital View of Chemisorbed Carbon Monoxide*, J. Phys. Chem. **1964**, 68 (10), 2772-&.

54. Fohllisch, A.; Nyberg, M.; Hasselstrom, J.; Karis, O.; Pettersson, L. G. M.; Nilsson, A., *How carbon monoxide adsorbs in different sites*, Phys. Rev. Lett. **2000**, 85 (15), 3309-3312.
55. Günzler, H.; Gremlich, H. U., *IR Spectroscopy: An Introduction*. Wiley: **2002**.
56. Lam, R. B.; Wieboldt, R. C.; Isenhour, T. L., *Practical Computation with Fourier-Transforms for Data-Analysis*, Anal. Chem. **1981**, 53 (7), A889-&.
57. King, D. A., *Thermal Desorption from Metal-Surfaces*, Surf. Sci. **1975**, 47 (1), 384-402.
58. Stuve, E. M.; Madix, R. J.; Brundle, C. R., *Co Oxidation on Pd(100) - a Study of the Coadsorption of Oxygen and Carbon-Monoxide*, Surf. Sci. **1984**, 146 (1), 155-178.
59. Habenschaden, E.; Kupperts, J., *Evaluation of Flash Desorption Spectra*, Surf. Sci. **1984**, 138 (1), L147-L150.
60. Miller, J. B.; Siddiqui, H. R.; Gates, S. M.; Russell, J. N.; Yates, J. T.; Tully, J. C.; Cardillo, M. J., *Extraction of Kinetic-Parameters in Temperature Programmed Desorption - a Comparison of Methods*, J. Chem. Phys. **1987**, 87 (11), 6725-6732.
61. Redhead, P. A., *Thermal desorption of gases*, Vacuum **1962**, 12 (5), 274.
62. Feigerle, C. S.; Desai, S. R.; Overbury, S. H., *The Kinetics of Co Desorption from Ni(110)*, J. Chem. Phys. **1990**, 93 (1), 787-794.
63. Kirstein, W.; Kruger, B.; Thieme, F., *Co Adsorption Studies on Pure and Ni-Covered Cu(111) Surfaces*, Surf. Sci. **1986**, 176 (3), 505-529.
64. Ratner, B. D.; Castner, D. G., *Electron Spectroscopy for Chemical Analysis*. In *Surface Analysis – The Principal Techniques*, John Wiley & Sons, Ltd: **2009**; pp 47-112.
65. Rous, P. J.; Pendry, J. B., *The Theory of Tensor Leed*, Surf. Sci. **1989**, 219 (3), 355-372.
66. Vanhove, M. A.; Moritz, W.; Over, H.; Rous, P. J.; Wander, A.; Barbieri, A.; Materer, N.; Starke, U.; Jentz, D.; Powers, J. M.; Held, G.; Somorjai, G. A., *Fitting Dozens of Coordinates by Leed - Automated-Determination of Complex Surface-Structures*, Surf. Sci. **1993**, 287, 428-431.
67. Van Hove, M. A.; Weinberg, W. H.; Chan, C. M., *Low-Energy Electron Diffraction*. Springer Verlag: Heidelberg, **1986**.
68. Fiorentini, V.; Methfessel, M., *Extracting convergent surface energies from slab calculations*, J. Phys.: Condens. Matter **1996**, 8 (36), 6525-6529.
69. Boettger, J. C.; Smith, J. R.; Birkenheuer, U.; Rosch, N.; Trickey, S. B.; Sabin, J. R.; Apell, S. P., *Extracting convergent surface formation energies from slab calculations*, J. Phys.: Condens. Matter **1998**, 10 (4), 893-894.
70. Moll, N.; Kley, A.; Pehlke, E.; Scheffler, M., *GaAs equilibrium crystal shape from first principles*, Phys. Rev. B: Condens. Matter Mater. Phys. **1996**, 54 (12), 8844-8855.
71. Sanna, S.; Schmidt, W. G., *Lithium niobate X-cut, Y-cut, and Z-cut surfaces from ab initio theory*, Phys. Rev. B: Condens. Matter Mater. Phys. **2010**, 81 (21).
72. Qian, G. X.; Martin, R. M.; Chadi, D. J., *1st-Principles Study of the Atomic Reconstructions and Energies of Ga-Stabilized and as-Stabilized GaAs(100) Surfaces*, Phys. Rev. B: Condens. Matter Mater. Phys. **1988**, 38 (11), 7649-7663.
73. Giannozzi, P.; Baroni, S.; Bonini, N.; Calandra, M.; Car, R.; Cavazzoni, C.; Ceresoli, D.; Chiarotti, G. L.; Cococcioni, M.; Dabo, I.; Dal Corso, A.; de Gironcoli, S.; Fabris, S.; Fratesi, G.; Gebauer, R.; Gerstmann, U.; Gougoussis, C.; Kokalj, A.; Lazzeri, M.; Martin-Samos, L.; Marzari, N.; Mauri, F.; Mazzarello, R.; Paolini, S.; Pasquarello, A.; Paulatto, L.; Sbraccia, C.; Scandolo, S.; Sclauzero, G.; Seitsonen, A. P.; Smogunov, A.; Umari, P.; Wentzcovitch, R. M., *QUANTUM ESPRESSO: a modular and open-source software project for quantum simulations of materials*, J. Phys.: Condens. Matter **2009**, 21 (39).
74. Perdew, J. P.; Burke, K.; Ernzerhof, M., *Generalized gradient approximation made simple*, Phys. Rev. Lett. **1996**, 77 (18), 3865-3868.
75. Vanderbilt, D., *Soft Self-Consistent Pseudopotentials in a Generalized Eigenvalue Formalism*, Phys. Rev. B: Condens. Matter Mater. Phys. **1990**, 41 (11), 7892-7895.
76. J. VandeVondele; M. Krack; F. Mohamed; M. Parrinello; T. Chassaing; Hutter, J. <http://cp2k.berlios.de/>
77. VandeVondele, J.; Hutter, J., *Gaussian basis sets for accurate calculations on molecular systems in gas and condensed phases*, J. Chem. Phys. **2007**, 127 (11).
78. Rohlfing, M.; Temirov, R.; Tautz, F. S., *Adsorption structure and scanning tunneling data of a prototype organic-inorganic interface: PTCDA on Ag(111)*, Phys. Rev. B: Condens. Matter Mater. Phys. **2007**, 76 (11).
79. Lang, N. D., *Spectroscopy of Single Atoms in the Scanning Tunneling Microscope*, Phys. Rev. B: Condens. Matter Mater. Phys. **1986**, 34 (8), 5947-5950.
80. Rosenthal, D.; Widmer, R.; Wagner, R.; Gille, P.; Armbrüster, M.; Grin, Y.; Schlögl, R.; Gröning, O., *Surface Investigation of Intermetallic PdGa(I I I)*, Langmuir **2012**, 28 (17), 6848-6856.

81. Roudgar, A.; Gross, A., *Local reactivity of thin Pd overlayers on Au single crystals*, J. Electroanal. Chem. **2003**, 548, 121-130.
82. Angyan, J. G.; Loos, M.; Mayer, I., *Covalent Bond Orders and Atomic Valence Indexes in the Topological Theory of Atoms in Molecules*, J. Phys. Chem. **1994**, 98 (20), 5244-5248.
83. Gaspari, R. Linking structure and function at the surface of selected metal-based solids through atomistic simulations. Doctoral Thesis, ETH Zürich, 2012.
84. Krajci, M.; Hafner, J., *The (210) surface of intermetallic B20 compound GaPd as a selective hydrogenation catalyst: A DFT study*, J. Catal. **2012**, 295 (0), 70-80.
85. Zhong, D. Y.; Franke, J. H.; Podiyanchari, S. K.; Blomker, T.; Zhang, H. M.; Kehr, G.; Erker, G.; Fuchs, H.; Chi, L. F., *Linear Alkane Polymerization on a Gold Surface*, Science **2011**, 334 (6053), 213-216.
86. Hoffmann, F. M., *Infrared Reflection-Absorption Spectroscopy of Adsorbed Molecules*, Surf. Sci. Rep. **1983**, 3 (2-3), 107-192.
87. Ma, Y. S.; Diemant, T.; Bansmann, J.; Behm, R. J., *The Interaction of CO with PdAg/Pd(111) Surface Alloys-A Case Study of Ensemble Effects on a Bimetallic Surface*, Phys. Chem. Chem. Phys. **2011**, 13 (22), 10741-10754.
88. Rupprechter, G., *Sum Frequency Generation and Polarization-Modulation Infrared Reflection Absorption Spectroscopy of Functioning Model Catalysts from Ultrahigh Vacuum to Ambient Pressure*, Adv. Catal. **2007**, 51, 133-263.
89. Goedecker, S.; Teter, M.; Hutter, J., *Separable Dual-space Gaussian Pseudopotentials*, Phys. Rev. B: Condens. Matter Mater. Phys. **1996**, 54 (3), 1703-1710.
90. Perdew, J. P.; Burke, K.; Ernzerhof, M., *Generalized Gradient Approximation Made Simple*, Phys. Rev. Lett. **1997**, 78 (7), 1396-1396.
91. Krajci, M.; Hafner, J., *Structure and Chemical Reactivity of the Polar Three-fold Surfaces of GaPd: A Density-functional Study*, J. Chem. Phys. **2013**, 138 (12), 124703.
92. Shin, H.; Pussi, K.; Gaudry, E.; Ledieu, J.; Fournée, V.; Villaseca, S. A.; Dubois, J. M.; Grin, Y.; Gille, P.; Moritz, W.; Diehl, R. D., *Structure of the Orthorhombic Al₁₃Co₄(100) Surface Using LEED, STM, and ab initio Studies*, Phys. Rev. B: Condens. Matter Mater. Phys. **2011**, 84 (8).
93. Wang, Y. M.; Wong, K. W.; Lee, S. T.; Nishitani-Gamo, M.; Sakaguchi, I.; Loh, K. P.; Ando, T., *Surface Structure of C(100)-(2x1)-H Studied by a Quantitative LEED Analysis*, Phys. Rev. B: Condens. Matter Mater. Phys. **1999**, 59 (15), 10347-10350.
94. Weinberg, W. H.; Comrie, C. M.; Lambert, R. M., *Kinetics of Adsorption of Co on Group-VIII Transition-Metals*, J. Catal. **1976**, 41 (3), 489-493.
95. Dell'Angela, M.; Anniyev, T.; Beye, M.; Coffee, R.; Fohlsch, A.; Gladh, J.; Katayama, T.; Kaya, S.; Krupin, O.; LaRue, J.; Mogelhof, A.; Nordlund, D.; Norskov, J. K.; Oberg, H.; Ogasawara, H.; Ostrom, H.; Pettersson, L. G. M.; Schlotter, W. F.; Sellberg, J. A.; Sorgenfrei, F.; Turner, J. J.; Wolf, M.; Wurth, W.; Nilsson, A., *Real-Time Observation of Surface Bond Breaking with an X-ray Laser*, Science **2013**, 339 (6125), 1302-1305.
96. Feibelman, P. J.; Hammer, B.; Norskov, J. K.; Wagner, F.; Scheffler, M.; Stumpf, R.; Watwe, R.; Dumesic, J., *The CO/Pt(111) puzzle*, J. Phys. Chem. B **2001**, 105 (18), 4018-4025.
97. Mancera, L. A.; Behm, R. J.; Gross, A., *Structure and Local Reactivity of PdAg/Pd(111) Surface Alloys*, Phys. Chem. Chem. Phys. **2013**, 15 (5), 1497-1508.
98. Cassuto, A.; King, D. A., *Rate Expressions for Adsorption and Desorption-Kinetics with Precursor States and Lateral Interactions*, Surf. Sci. **1981**, 102 (2-3), 388-404.
99. Feng, M.; Cabrera-Sanfelix, P.; Lin, C. W.; Arnau, A.; Sanchez-Portal, D.; Zhao, J.; Echenique, P. M.; Petek, H., *Orthogonal Interactions of CO Molecules on a One-Dimensional Substrate*, ACS Nano **2011**, 5 (11), 8877-8883.
100. Wesner, D. A.; Coenen, F. P.; Bonzel, H. P., *X-Ray Photoelectron Diffraction Study of Perpendicular and Tilted Co on Clean and Potassium-Modified Ni(110)*, Phys. Rev. B: Condens. Matter Mater. Phys. **1989**, 39 (15), 10770-10780.
101. Henkelman, G.; Uberuaga, B. P.; Jonsson, H., *A climbing image nudged elastic band method for finding saddle points and minimum energy paths*, J. Chem. Phys. **2000**, 113 (22), 9901-9904.
102. Bartels, L.; Meyer, G.; Rieder, K. H., *Basic steps of lateral manipulation of single atoms and diatomic clusters with a scanning tunneling microscope tip*, Phys. Rev. Lett. **1997**, 79 (4), 697-700.
103. Stipe, B. C.; Rezaei, M. A.; Ho, W., *Inducing and viewing the rotational motion of a single molecule*, Science **1998**, 279 (5358), 1907-1909.
104. Grill, L.; Rieder, K. H.; Moresco, F.; Rapenne, G.; Stojkovic, S.; Bouju, X.; Joachim, C., *Rolling a single molecular wheel at the atomic scale*, Nat. Nanotechnol. **2007**, 2 (2), 95-98.
105. Stipe, B. C.; Rezaei, M. A.; Ho, W., *Coupling of vibrational excitation to the rotational motion of a single adsorbed molecule*, Phys. Rev. Lett. **1998**, 81 (6), 1263-1266.

106. Shchadilova, Y. E.; Tikhodeev, S. G.; Paulsson, M.; Ueba, H., *Rotation of a Single Acetylene Molecule on Cu(001) by Tunneling Electrons in STM*, Phys. Rev. Lett. **2013**, 111 (18).
107. Matsumoto, C.; Kim, Y.; Okawa, T.; Sainoo, Y.; Kawai, M., *Low-temperature STM investigation of acetylene on Pd(111)*, Surf. Sci. **2005**, 587 (1-2), 19-24.
108. Dunphy, J. C.; Rose, M.; Behler, S.; Ogletree, D. F.; Salmeron, M.; Sautet, P., *Acetylene structure and dynamics on Pd(111)*, Phys. Rev. B: Condens. Matter Mater. Phys. **1998**, 57 (20), 12705-12708.
109. Gates, J. A.; Kesmodel, L. L., *Thermal Evolution of Acetylene and Ethylene on Pd(111)*, Surf. Sci. **1983**, 124 (1), 68-86.
110. Marinova, T. S.; Kostov, K. L., *Adsorption of Acetylene and Ethylene on a Clean Ir(111) Surface*, Surf. Sci. **1987**, 181 (3), 573-585.
111. Echeverria, J.; Monturet, S.; Joachim, C., *One-way rotation of a molecule-rotor driven by a shot noise*, Nanoscale **2014**, 6 (5), 2793-2799.
112. Taylor, J. B.; Langmuir, I., *The evaporation of atoms, ions and electrons from caesium films on tungsten*, Phys. Rev. **1933**, 44 (6), 0423-0458.
113. Sandell, A.; Beutler, A.; Jaworowski, A.; Wiklund, M.; Heister, K.; Nyholm, R.; Andersen, J. N., *Adsorption of acetylene and hydrogen on Pd(111): formation of a well-ordered ethylidyne overlayer*, Surf. Sci. **1998**, 415 (3), 411-422.
114. Andersen, J. N.; Beutler, A.; Sorensen, S. L.; Nyholm, R.; Setlik, B.; Heskett, D., *Vibrational fine structure in the C 1s core level photoemission of chemisorbed molecules: Ethylene and ethylidyne on Rh(111)*, Chem. Phys. Lett. **1997**, 269 (3-4), 371-377.
115. Ramsvik, T.; Borg, A.; Worren, T.; Kildemo, M., *Hybridisation and vibrational excitation of C₂H₂ on Co(0001)*, Surf. Sci. **2002**, 511 (1-3), 351-358.
116. Ernst, K. H., *Molecular chirality at surfaces*, Phys. Status Solidi B **2012**, 249 (11), 2057-2088.
117. Roy, S.; Pericas, M. A., *Functionalized nanoparticles as catalysts for enantioselective processes*, Org. Biomol. Chem. **2009**, 7 (13), 2669-2677.
118. Forster, M.; Raval, R., *Chiral Expression by Organic Architectures at Metal Surfaces: the Role of Both Adsorbate and Surface in Inducing Asymmetry*. In *Model Systems in Catalysis*, Rioux, R., Ed. Springer New York: **2010**; pp 97-115.
119. Gellman, A. J.; Huang, Y.; Feng, X.; Pushkarev, V. V.; Holsclaw, B.; Mhatre, B. S., *Superenantioselective Chiral Surface Explosions*, J. Am. Chem. Soc. **2013**, 135 (51), 19208-19214.
120. Weissbuch, I.; Lahav, M., *Crystalline Architectures as Templates of Relevance to the Origins of Homochirality*, Chem. Rev. **2011**, 111 (5), 3236-3267.
121. Hazen, R. M.; Sholl, D. S., *Chiral selection on inorganic crystalline surfaces*, Nat. Mater. **2003**, 2 (6), 367-374.
122. Illustration: Prof. A. Baikers Group / ETH Zürich.
http://www.ethlife.ethz.ch/archive_articles/120823_katalyse_per/index_EN.
123. Vineyard, B. D.; Knowles, W. S.; Sabacky, M. J.; Bachman, G. L.; Weinkauff, D. J., *Asymmetric Hydrogenation - Rhodium Chiral Bisphosphine Catalyst*, J. Am. Chem. Soc. **1977**, 99 (18), 5946-5952.
124. Noyori, R.; Hashiguchi, S., *Asymmetric transfer hydrogenation catalyzed by chiral ruthenium complexes*, Acc. Chem. Res. **1997**, 30 (2), 97-102.
125. Sugimura, T., *Heterogeneous Enantioselective Hydrogenation on Metal Surface Modified by Chiral Molecules*. In *Handbook of Asymmetric Heterogeneous Catalysis*, Wiley-VCH: **2008**; pp 357-382.
126. Weissbuch, I.; Addadi, L.; Lahav, M.; Leiserowitz, L., *Molecular Recognition at Crystal Interfaces*, Science **1991**, 253 (5020), 637-645.
127. Mallat, T.; Orglmeister, E.; Baiker, A., *Asymmetric catalysis at chiral metal surfaces*, Chem. Rev. **2007**, 107 (11), 4863-4890.
128. Fasel, R.; Parschau, M.; Ernst, K. H., *Amplification of chirality in two-dimensional enantiomorphous lattices*, Nature **2006**, 439 (7075), 449-452.
129. Jenkins, S. J.; Pratt, S. J., *Beyond the surface atlas: A roadmap and gazetteer for surface symmetry and structure*, Surf. Sci. Rep. **2007**, 62 (10), 373-429.
130. Ahmadi, A.; Attard, G.; Feliu, J.; Rodas, A., *Surface reactivity at "chiral" platinum surfaces*, Langmuir **1999**, 15 (7), 2420-2424.
131. Prinz, J.; Gaspari, R.; Pignedoli, C. A.; Gille, P.; Armbrüster, M.; Brune, H.; Gröning, O.; Passerone, D.; Widmer, R., *The surface atomic structures of PdGa(100) and (110)*, (in preparation, 2014).
132. Xu, W.; Kelly, R. E. A.; Gersen, H.; Laegsgaard, E.; Stensgaard, I.; Kantorovich, L. N.; Besenbacher, F., *Prochiral Guanine Adsorption on Au(111): An Entropy-Stabilized Intermixed Guanine-Quartet Chiral Structure*, Small **2009**, 5 (17), 1952-1956.

133. Bebensee, F.; Bombis, C.; Vadapoo, S. R.; Cramer, J. R.; Besenbacher, F.; Gothelf, K. V.; Linderoth, T. R., *On-Surface Azide-Alkyne Cycloaddition on Cu(111): Does It "Click" in Ultrahigh Vacuum?*, J. Am. Chem. Soc. **2013**, *135* (6), 2136-2139.
134. Prinz, J.; Gaspari, R.; Stoeckl, Q. S.; Gille, P.; Armbrüster, M.; Brune, H.; Gröning, O.; Pignedoli, C. A.; Passerone, D.; Widmer, R., *Ensemble Effect Evidenced by CO Adsorption on the 3 -Fold PdGa Surfaces*, J. Phys. Chem. C **2014**, *118* (23), 12260–12265.
135. Prinz, J.; Gaspari, R.; Pignedoli, C. A.; Vogt, J.; Gille, P.; Armbrüster, M.; Brune, H.; Gröning, O.; Passerone, D.; Widmer, R., *Isolated Pd Sites on the Intermetallic PdGa(111) and PdGa(-1-1-1) Model Catalyst Surfaces*, Angew. Chem., Int. Ed. **2012**, *51* (37), 9339-9343.

Curriculum Vitae

Jan Prinz

jnprinz@gmail.com
Date of Birth: 24.09.1983
Nationality: German

Work experience and education

Empa Dübendorf, nanotech@surfaces laboratory, in collaboration with
EPF Lausanne (EPFL), Switzerland, Nov 2010 – Oct 2014
PhD Studies in Physics: "Surface Science Investigations on Structure and Binding Centers of Intermetallic PdGa Surfaces"

Materials Physics, Uppsala University, Sweden, Apr 2009 - Sep 2010
Diploma Thesis Project: "Hydrogen in Thin Metal Films as seen by Electron and Light Scattering"

Exchange Semester (Erasmus), EPF Lausanne (EPFL), Switzerland, Aug 2008 - Apr 2009

Karlsruhe Institute of Technology (KIT), Germany, Apr 2004 - Apr 2010
Diplomstudiengang in Physics (German Master Studies), Diploma thesis in collaboration with Uppsala University, Sweden

Balthasar Neumann Technikum, Trier, Germany, 2000 – 2003
Technical High School

Publications

- Prinz, J.; A.; Brune, H.; Gröning, O.; Widmer, R.; "Highly Enantioselective Molecule Adsorption at Room Temperature on a Chiral Intermetallic Surface", *in preparation for submission to Nat. Mater.* (**2014**).
- Prinz, J.; Pignedoli, C.; Passerone, D.; Widmer, R.; Gröning, O.; "Adsorption of Small Hydrocarbons on Pd Reaction Centers: The Road to Selective Hydrogenation on PdGa(111)", *J. Am. Chem. Soc. (accepted 2014)*, DOI: 10.1021/ja505936b
- Prinz, J.; Gaspari, R.; Stöckl, Q.S.; A.; Gille, P.; Armbrüster, M.; Brune, H.; Gröning, O.; Pignedoli, C.; Passerone, D.; Widmer, R.; "Ensemble effect evidence by CO adsorption on the threefold PdGa surfaces", *J. Phys. Chem. C* **2014**, *118*, 12260
- Prinz, J.; Gaspari, R.; Pignedoli, C. A.; Vogt, J.; Gille, P.; Armbrüster, M.; Brune, H.; Gröning, O.; Passerone, D.; Widmer, R.; "Isolated Pd Sites on the Intermetallic PdGa(111) and PdGa(-1-1-1) Model Catalyst Surfaces", *Angew. Chem., Int. Ed.* **2012**, *51*, 9339.
- Armbrüster, M.; Behrens, M.; Cinquini, F.; Föttinger, K.; Grin, Y.; Haghofer, A.; Klötzer, B.; Knop-Gericke, A.; Lorenz, H.; Ota, A.; Penner, S.; Prinz, J.; Rameshan, C.; Révay, Z.; Rosenthal, D.; Rupprechter, G.; Sautet, P.; Schlögl, R.; Shao, L.; Szentmiklósi, L.; Teschner, D.; Torres, D.; Wagner, R.; Widmer, R.; Wowsnick, G.; "How to Control the Selectivity of Palladium-based Catalysts in Hydrogenation Reactions: The Role of Subsurface Chemistry", *ChemCatChem* **2012**, *4*, 1048.
- Prinz, J.; Palsson, G. K.; Korelis, P. T.; Hjörvarsson, B.; "Combined light and electron scattering for exploring hydrogen in thin metallic films", *Appl. Phys. Lett.* **2010**, *97*.

Scientific presentations

- "Surface science studies on structures and adsorption sites of single crystalline PdGa surfaces as model catalysts in acetylene semi-hydrogenation", *oral contribution*, 4th International Symposium of Intermetallic Compounds in Catalysis (COST), Santa-Margherita (Italy), **2014**
- "Isolated Pd Sites on PdGa Model Catalyst Surfaces", *oral contribution*, Joint Meeting of the Swiss and Austrian Physical Society, Linz (Austria), **2013**
- "The Effect of Active-Site Separation on Molecular Adsorption and Reaction Pathways demonstrated on PdGa Single Crystal Surfaces", *oral contribution*, 3rd International Symposium of Intermetallic Compounds in Catalysis (COST), Chania (Greece), **2013**
- "Investigating the Surface Reactivity of PdGa Model Catalysts Using Probe Molecules", *invited talk*, MolCH Meeting, Bern (Switzerland), **2013**
- "Structure and active site-isolation of PdGa model catalyst surfaces", *invited talk*, SPLDS Workshop, Pont-a-Mousson (France), **2013**
- "Molecules on the PdGa single crystal surfaces", *oral contribution*, Pd days of the Fritz-Haber Institute, Bad Schandau (Germany), **2012**
- "Separated Pd sites on the low indexed surfaces of PdGa catalysts", *oral contribution*, ICN+T conference, Paris (France), **2012**
- "Surface Science Investigations of Intermetallic PdGa Catalysts", *invited talk*, Workshop: Heterogeneous Catalysis @ EMPA, Dübendorf (Switzerland), **2012**
- "Separated Pd sites on the low Miller index surfaces of PdGa catalysts", *poster presentation*, SAOG Meeting, Fribourg (Switzerland), **2012**
- "CO adsorption on PdGa(111) and (-1-1-1) and first insights into PdGa(110) surfaces", *oral contribution*, Pd days of the Fritz-Haber Institute, Obergurgl (Austria), **2011**
- "Surface Structure Determination of Intermetallic Pd-Ga Catalysts", *poster presentation*, 1st International Symposium on Intermetallic Compounds in Methanol Steam Reforming, Berlin (Germany), **2011**
- "Surface Termination of Intermetallic Pd-Ga Catalysts", *poster presentation*, Meeting of the Swiss Physical Society, Lausanne (Switzerland), **2011**

Acknowledgements

First of all, I would like to thank my thesis directors, Harald Brune and Roland Widmer, for giving me the opportunity to follow this PhD project and for their guidance throughout my years as their PhD student. I really appreciate Harald's interest in the project and the inspiring discussions on results and new approaches. Despite the physical distance of EPFL and Empa, we had a valuable exchange, which is also thanks to him having no problem in traveling across Switzerland to pay us a visit. A big "Thank You!" goes to Roland, who did not only show me the best way to run experiments and conduct science, but also taught me a lot about Switzerland and its fine cultural variations. I appreciated the numerous possibilities to visit conferences and meetings abroad, and especially the dive we had in the Mediterranean Sea. I would also like to thank Oliver Gröning, for his general guidance and the time he spared to answer my countless questions on the physics of things, Igor programming, or just to share his biking experiences.

I am grateful to the additional jury members Günther Rupprechter, Karl-Heinz Ernst, Marco Grioni and Olivier Schneider for reading and evaluating my work. I thank Peter Gille and Marc Armbrüster for the provision of the single crystal samples and the fruitful meetings in the frame of the COST action CM0904 at beautiful places all over Europe. I further appreciate the open and friendly atmosphere at the "Pd-Days" initiated by the Fritz-Haber Institute Berlin, to which we were invited.

Further gratitude is devoted to all the people at the nanotech@surfaces laboratory at Empa Dübendorf. I had a great time sharing the labs and working with you and enjoyed the coffee breaks filled with scientific and non-scientific discussions. Special thanks are devoted to:

Carlo Pignedoli and Daniele Passerone, for computations and insights from their world and the exchange of results on a large number of cheerful lunch-, coffee-, and tea breaks. - Thanks for enduring the hard times I gave you with my demands on PdGa.

Carlo again, for taking me to a wonderful flight over Zurich, and for daring to try the "fresh" snow with me in Andermatt.

Roberto Gaspari, for computations and for showing me the bright sides of town.

Roman Fasel, for advice and opinions on my project and for keeping up an open and constructive atmosphere in our lab.

Pierangelo Gröning, for his genuine interest in my work and for enlightening conversations on the history of our lab equipment.

Thomas Dienel, for all help and advice I received from him and for contributing to, and maintaining the incredible stability of the new "Qplus" instrument.

Lukas Rotach, for his fast technical solutions whenever they were needed.

Quirin Stöckl, for the fruitful collaboration and help with the FTIR and TDS setups.

Andreas Bliersbach for the exchange of ideas on experiments and life, mostly combined with uplifting coffee breaks and cakes.

Simon Bonanni and Wolfgang Harbich, for entrusting their precious "sniffer" instrument to me.

The whole group at the EPFL, for always welcoming their "lost" PhD student.

The "PhD-Symposium 2012" organization committee and Anne Satir; it was a lot of fun, and an honor to work with you!

I finally want to thank my friends in Zurich and at home, as well as my family, for supporting me in whichever way they could. This holds in particular for Ylva, who volunteered to listen to hours of sometimes incomplete science talks and did an excellent good job in keeping spirits up in the tough times.